The Variability of Atmospheric D/H Fractionation on Mars

by

E. M. Cangi

B.S. Theatre Arts, University of Oregon, 2010

B.S. Physics, University of Oregon, 2017

M.S. Astrophysical & Planetary Sciences, University of Colorado Boulder, 2019

A thesis submitted to the
Faculty of the Graduate School of the
University of Colorado in partial fulfillment
of the requirements for the degree of
Doctor of Philosophy
Department of Astrophysical and Planetary Sciences
2023

Committee Members:
Michael Chaffin, Chair
David Brain
Nick Schneider
Bruce Jakosky
Lauren Blum

Cangi, E. M. (Ph.D., Astrophysics & Planetary Science)

The Variability of Atmospheric D/H Fractionation on Mars

Thesis directed by Research scientist Michael Chaffin

Water, a key requirement for life, once shaped the martian surface in huge amounts, but today is only a small fraction of the planet's volatile inventory. Mars' high D/H (deuterium/hydrogen) ratio, 4-6× the Earth value, suggests that much of the missing water has escaped to space; H, the less massive isotope, more easily escapes the planet's gravity. However, estimates of water loss from atmospheric models are typically a factor of $\sim$4 lower than geomorphological estimates. Much literature has focused on H escape, with less emphasis on D escape and the fractionation factor (the relative escape efficiency of D compared to H), despite the importance of the D/H ratio to understanding of the water cycle of Mars.

To approach these problems, I have developed the most comprehensive photochemical model, named bluejay, of the martian atmosphere to date, which I use in this thesis to explore D and H escape and water loss from Mars. The first chapter covers how the thermal Jeans escape fractionation factor varies with temperature and atmospheric water, revealing it to be smaller than in previous studies and hinting at the importance of non-thermal D escape. In the second chapter, I present the first predictions of the deuterated ionosphere and photochemical non-thermal D escape, and identify the driving chemical reactions. Finally, I investigate the response of the D/H ratio and escape to seasonal variations, finding that both thermospheric temperatures and mesospheric water induce large changes in the atomic D/H ratio within a Mars season due to dynamical differences of H and D.

Even with the inclusion of non-thermal D escape, modeled integrated water loss is still lower than geomorphological estimates by a factor of $\sim$3, indicating a future need to better understand past epochs and additional avenues for water loss. Nevertheless, these results present the most detailed look at the deuterated atmosphere of Mars thus far. The work here also provides a baseline for future photochemical modeling investigations, as bluejay may continue to be used to study Mars or other rocky bodies with atmospheres.

Dedication

To anyone else who ever took a risk and had it pay off many times over.

And to my mom, Casey Cangi, who didn't live to see me complete my PhD, but who I'm sure knew I'd make it through.

Acknowledgements

Thank you to the following close collaborators: Mike Chaffin, for stellar advising, sharing my concern for presentation, always making sure I felt comfortable to speak my mind, and endless patience. Dave Brain, for being the absolute realest, always making time, and your ongoing support of the four of us in APS who lost parents in 2020. Bruce Jakosky, for valuing student input, and for the many science discussions, especially the ones on the ski lift! Bethan Gregory, Gwen Hanley, Andréa Hughes, Margaret Landis, and Neesha Schnepf for the sticker charts, mentoring, conference-buddying, knowledge-sharing, pet sitting, excursions, lunches, dinners, and more.

Thank you also to my coauthors; the Brain & Chaffin groups; the faculty, staff, & past and present grad students of the APS and Geology departments; the entire MAVEN team; my past and present mentors and colleagues at the University of Oregon; my family: Jerry & Casey (1954-2020) Cangi, Mike & Debbie Cangi, Karen DeCotis, Denise & Rusty McCauley; and my many friends and colleagues across the country and from all different parts of my life who don't fit into the above categories and have supported me in some way: Gabe Barello, Desi Beardmore, Brittany Brown & Daniel Mundra, Drew Camron, Rosa Wallace Everson, John Gemperline, Matt Gentry, Meli & Ryan Hull, Megan Mitchell, Jason & Rhiannah Shirley.

As someone with a theatre degree, I would be remiss if I didn't acknowledge some of the media that inspired me and brought me joy during the pursuit of this PhD. Despite their importance in our society—movies, TV, music, books, visual art, photography—the arts are often denigrated as a career path, poorly paid, or even expected to be created, distributed, and performed for free. The arts not only add aesthetic enjoyment to our lives; they also form a space and place in which we

engage with narrative to make inroads into understanding the universe and the human experience—rather similar to science, actually. This thesis and its contents was written to a soundtrack of ambient and downtempo, jazz, bluegrass, and synthpop. I would also like to specifically acknowledge the Cowboy Bebop soundtrack by The Seatbelts for getting me through my undergraduate physics homework, and the “Lofi Hip Hop Beats to Study/Relax to” YouTube stream by ChilledCow for enabling the writing of chapter 2. Many parts were also written on the patio at Trident Books in Boulder, CO, or to the many sounds of MyNoise.net, one of the best websites on the internet. Finally, the Star Trek franchise, and its belief in the deep-seated goodness of humanity and its vision of a future in which equity and justice co-exist with technological progress and exploration, was a significant source of inspiration and motivation.

Materially, this work was supported by multiple sources of funding, including:

- Mars Data Analysis Program (MDAP) grant #NNX14AM20G
- The National Science Foundation Graduate Research Fellowship Program (NSF GRFP) under Grant No. DGE 1650115. Any opinions, findings, and conclusions or recommendations expressed in this material are those of the author(s) and do not necessarily reflect the views of the National Science Foundation
- The NASA Future Investigators in NASA Earth and Space Science and Technology (FINESST) Program (Grant #80NSSC22K1326)
- The Mars Atmosphere and Volatile EvolutioN (MAVEN) Imaging UltraViolet Spectrograph (IUVS) team

Contents

Chapter

Appendix

Tables

Table

Figures

Figure

Chapter 1

Introduction

Of all the outstanding mysteries in the human experience, few come close to approaching the gravity of one particular question: “are we alone in the universe?” We are self-evident proof that life can arise in the universe; it is natural that we should wonder about other kinds of life elsewhere, perhaps very alien, or perhaps rather similar to us. Earth is presently the only known an inhabited planet, so we naturally approach the question of whether life can or does exist on other planets by beginning with our own solar system.

As far as we understand it, life requires three key things: a source of energy, access to the biogenic elements, and a solvent for chemical reactions, expected to be water due to its chemical properties and importance on Earth (Domagal-Goldman et al. 2016). The first two are fairly easy: the star itself provides boundless energy, and the planets cache the biogenic elements that were originally formed deep in the interior of the star. Water, however, is trickier. Stray too far from the sun, and the low condensation temperature of water (273 K, 0°C) means that surface water will typically only be found in ice form, as on Titan, where the temperatures are so low that water ice behaves almost like a rock on Earth. Orbiting close to the sun, as Mercury does, means that typical planetary surface temperatures are so high that any exposed ice or liquid water outside shadowed regions (Slade et al. 1992) would not persist. Earth sits happily inside the “Goldilocks zone” of our sun: the narrow orbital band in which average planetary surface temperature is “just right” to enable liquid water to be available for life, conservatively estimated to be 0.95-1.37 AU, with the “continuously [over the age of the solar system] habitable zone” a smaller 0.95-1.15 AU

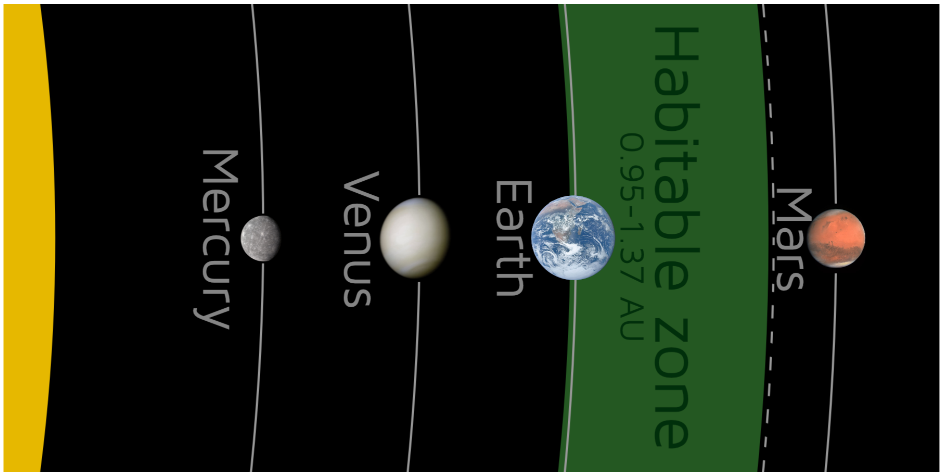

Figure 1.1: The habitable zone of our solar system, along with the mean orbits of the terrestrial inner solar system planets. The perihelion distance of Mars is shown by the dashed line. Mercury photo credit: NASA/Johns Hopkins University Applied Physics Laboratory/Arizona State University/Carnegie Institution of Washington; Mars photo credit: ESA & MPS for OSIRIS Team MPS/UPD/LAM/IAA/RSSD/INTA/UPM/DASP/IDA.

(Kasting et al. 1993). It's not true that liquid water can only exist within the habitable zone of a star system—Enceladus' plumes are a clear counter example—but it is a likely place to look. Our nearest neighbors, Venus (semi-major axis $a = 0.723$ AU) and Mars ($a = 1.53$ AU), are both outside the habitable zone, although Mars at closest approach to the sun (1.38 AU) does approach the outside edge of the habitable zone (Figure 1.1).

Mars has captured the human imagination as a potentially habitable world for generations. In 1877, Schiaparelli mapped the "canali" of Mars (Figure 1.2); Percival Lowell continued the work in the early 20th century, eventually concluding that the "canals" (a mistranslation; "canali" means "channels") were filled with water and indicative of intelligent life on Mars (Lowell 1908). Later observations with the Mariner missions of course revealed no such canals or intelligence, but rather a dry and arid surface, albeit one that had once been shaped by vast quantities of water (Figure 1.3)—just not through the use of great aquifers once imagined to exist there.

Although there are no great canals filled with water and no martian agriculturalists to use them, the possibility of future human exploration and of extant life in tiny habitable niches on Mars has driven an ongoing fascination with the planet, prompting investment in exploration, both

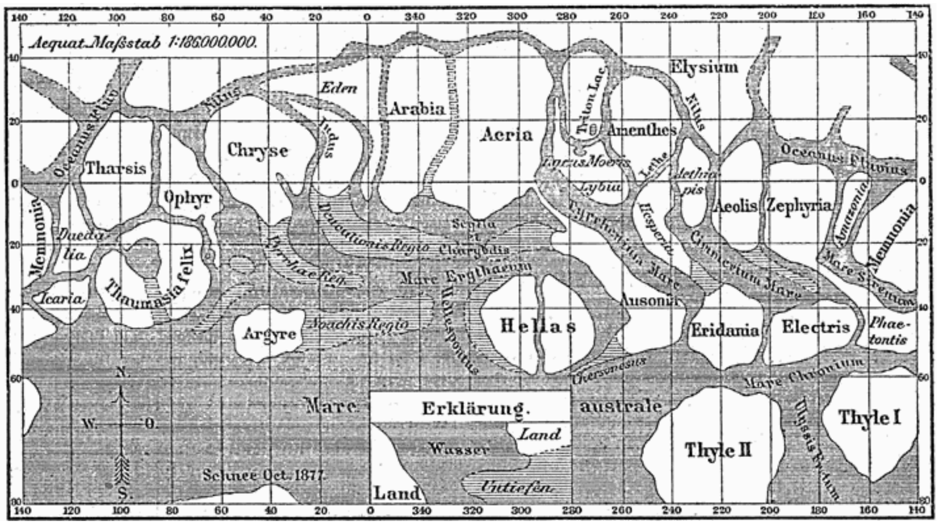

Figure 1.2: 1877 map of Mars as drawn by Giovanni Schiaparelli. Image in the public domain.

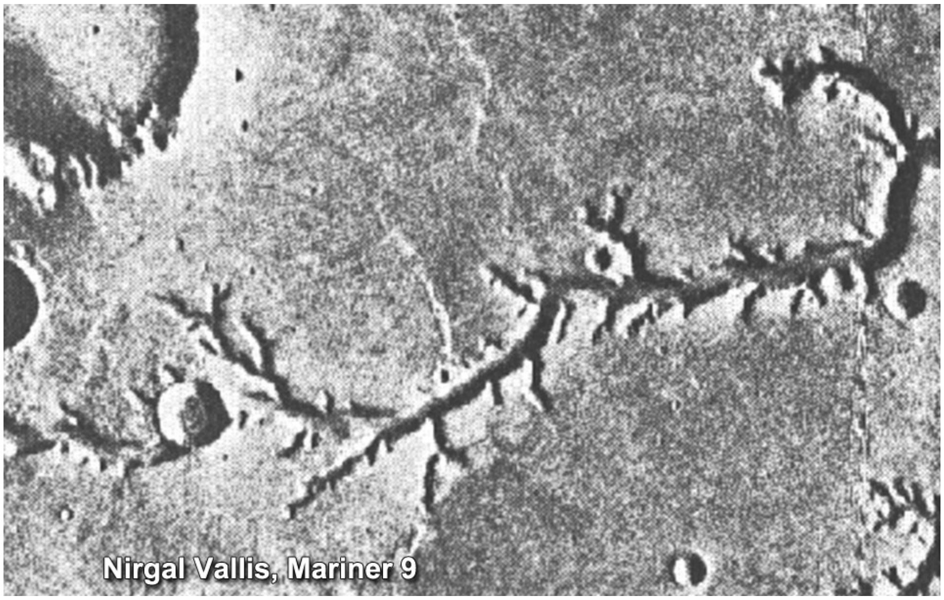

Figure 1.3: Mariner 9 photograph of Nirgal Vallis; while not an intelligently-designed canal, it is one among many pieces of evidence that water once flowed on Mars, here in the form of groundwater sapping (M. H. Carr 2012). Image credit NASA/JPL-Caltech.

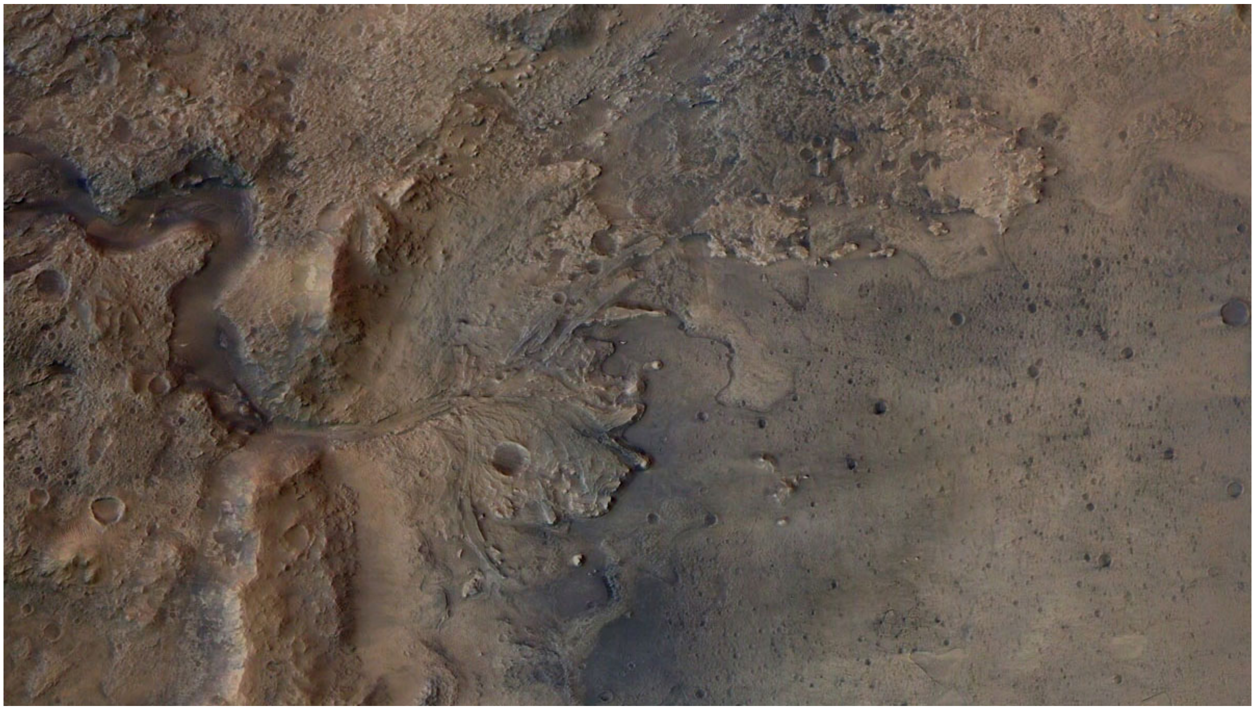

(a) Fluvial channel leading to delta in Jezero Crater, from the Mars Express orbiter's HRSC instrument. Image credit ESA/DLR/FU-Berlin.

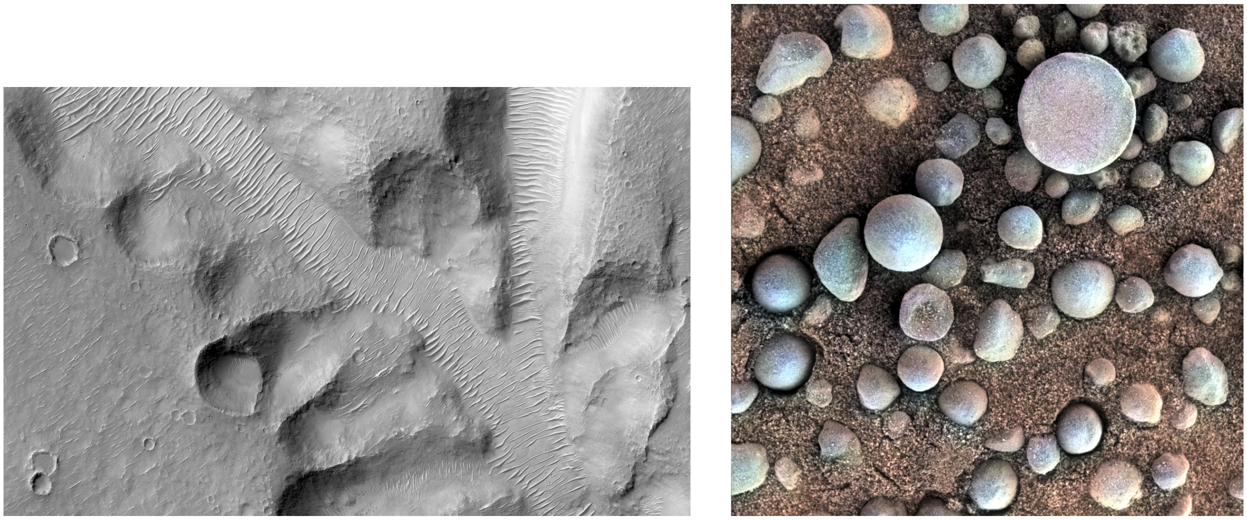

(b) Nirgal Vallis photographed by the Mars Reconnaissance Orbiter HiRISE instrument. Image credit NASA/JPL-Caltech/Univ. of Arizona.

(c) Hematite concretions ("blueberries") photographed by the Curiosity Rover. Image credit NASA/JPL-Caltech/Cornell/USGS.

Figure 1.4: Examples of martian surface features indicating a history of aqueous alteration.

ground-based and space-based. By the early 1970s, the planetary science community began to converge on the idea that water may have been stable on the surface at some past time (Sagan 1971), and that water, rather than lava flows, was responsible for carving many of the channels (McCauley et al. 1972; M. H. Carr 1979). The evidence supporting the importance of liquid water in shaping the surface of Mars over geological time has since only strengthened. Geomorphological analysis has revealed many water-formed features (Masson et al. 2001, and references therein), such as catastrophic flood/outflow channels (Baker et al. 1974, 1979; Pacifici et al. 2009; Chapman et al. 2010), ancient lakes and deltas (Fassett et al. 2008) such as Jezero Crater (Figure 1.4a), and dendritic valley networks (M. H. Carr 1995; Hynek et al. 2010) like Nirgal Vallis (Figure 1.4b). Modern missions have detected materials known to form in the presence of water across the planet, including phyllosilicates (Poulet et al. 2005; Bibring et al. 2006; Bandfield 2008; Bishop et al. 2008; Mustard et al. 2008; Ehlmann et al. 2009, 2011), fluvial conglomerates (Williams et al. 2013), jarosite (Elwood Madden et al. 2004), and hematite concretions (Figure 1.4c), or "blueberries" (Squyres et al. 2004). Results from the new Perseverance rover at Jezero Crater are presently coming in at the time of writing of this thesis; early results (Scheller et al. 2022) support the hypothesis that aqueous environments were present there in the past (Goudge et al. 2017).

But there is a problem: the present-day surface conditions of Mars cannot support liquid water (Ingersoll 1969). Unlike the life-enabling "thin blue line" (Figure 1.5a) of Earth's atmosphere as described by NASA (Dunbar 2023), the atmosphere of Mars today is more like a "faint red smudge." With a surface pressure just 0.6% that of Earth (6 millibars compared to 1000 millibars), and mean temperatures well below the freezing point of water, flowing water on Mars today is unlikely. This contradiction suggested another theory: That the atmosphere of Mars was once much thicker than it is today.

How did the martian atmosphere become so thin, and how does it relate to water loss? There are two main possibilities for where the missing atmosphere and water went: down into the surface, or out to space. Some water certainly ended up on the surface: residual water exists today as ice in the polar caps (Figure 1.6), ground ice, and subsurface hydrated minerals (Lasue et al. 2013). Table

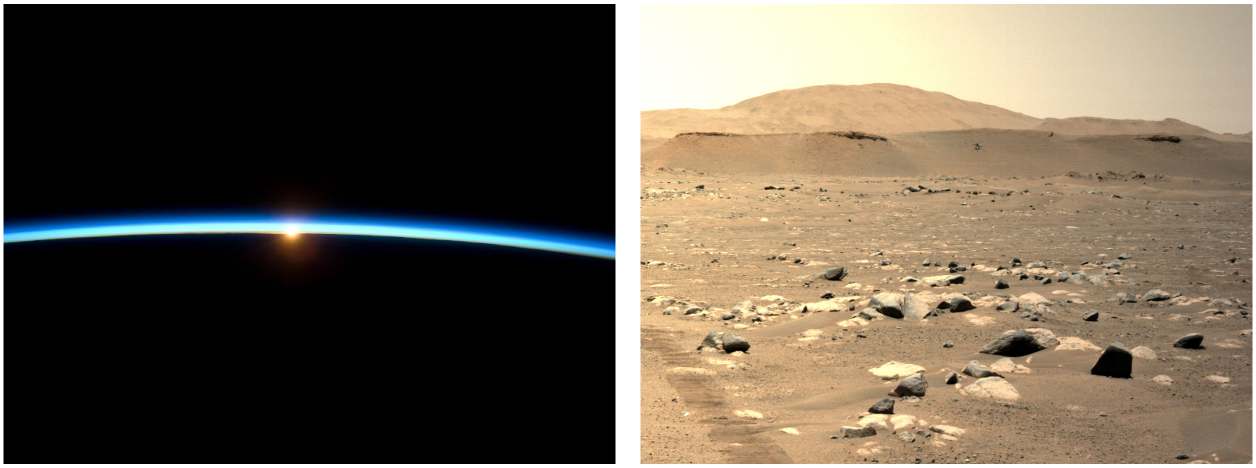

(a) Earth's atmosphere as photographed by the crew of the International Space Station during the STS-129 mission. Credit: NASA

(b) The comparatively thin atmosphere of Mars and the Ingenuity helicopter in the midground, as photographed by the Perseverance rover. Credit: NASA/JPL-Caltech

Figure 1.5: Comparison photographs of the atmospheres of Earth and Mars.

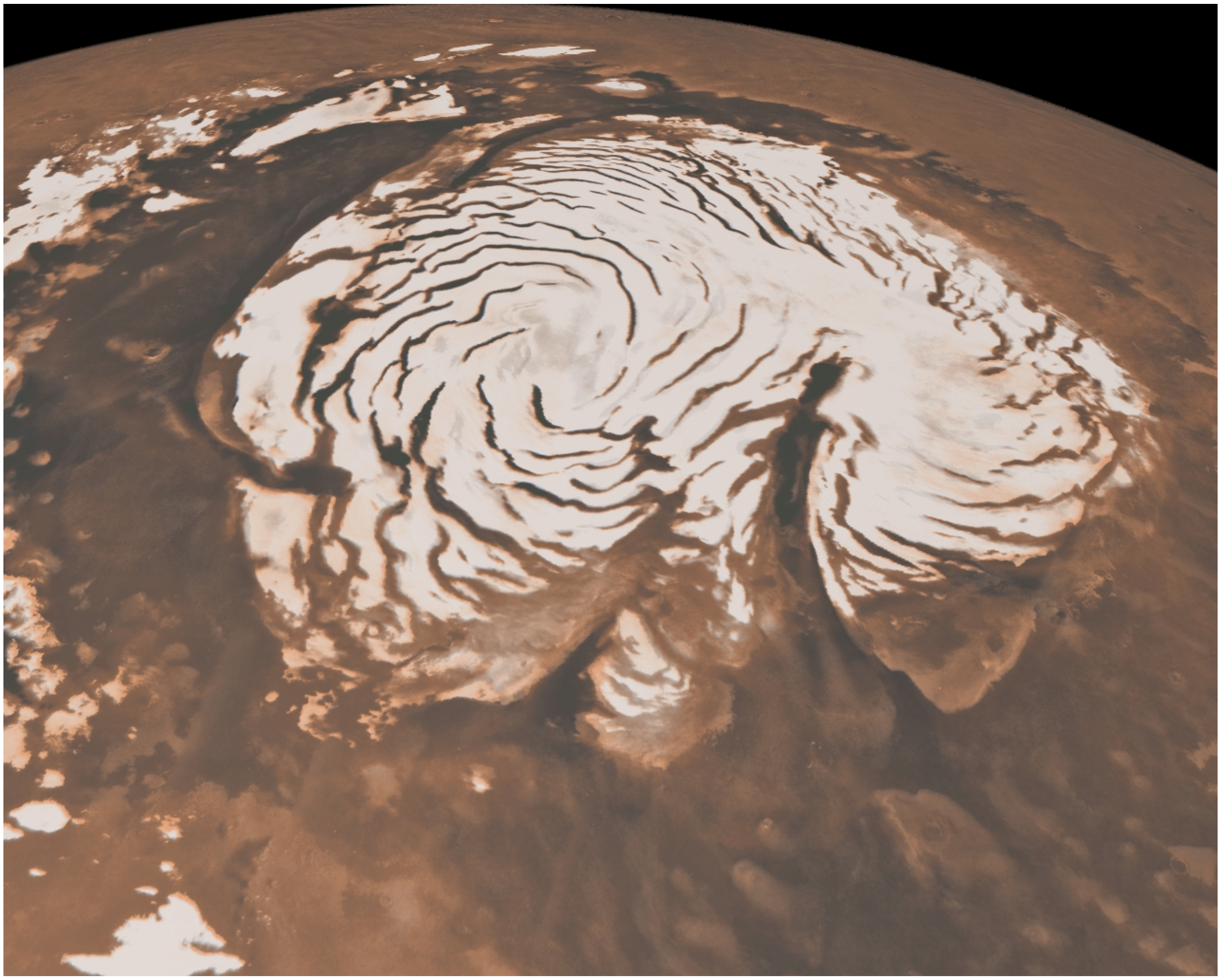

Figure 1.6: The north polar cap of Mars, as photographed by the Mars Global Surveyor mission. Credit: NASA/JPL-Caltech/MSSS

Sink		m GEL	Ref
Polar caps	North	8.3–11.7	Lasue et al. (2013, and references therein)
	South	11–15.9	
Hydrated minerals		130–260	Wernicke et al. (2021)
Crustal water		400–1000	Jakosky et al. (2022)

Table 1.1: Water remaining on Mars today in m GEL. The wide range of crustal water is uncertain, and may not all have been/is part of the present-day exchangeable reservoir.

1.1 contains a brief summary of these quantities today in m global equivalent layer, or GEL, a unit describing the depth of a planet-wide ocean containing the same amount of water. Several pieces of evidence also point to loss to space as a major water sink. The first piece of evidence is visible with the naked eye in a reasonably dark sky. The strongly oxidized surface of Mars, which gives it its characteristic red color, suggests past interaction with an excess of liberated oxygen atoms, possibly sourced from water (Lammer et al. 2003b). Dissociation of CO_2, the primary atmospheric constituent, is another possible source of oxygen atoms, but if this were the main source, we would expect to see far more carbonate deposits on the surface than we do (Ehlmann et al. 2014).

Ground-based observations revealed the strongest piece of evidence for atmospheric escape: the D/H ratio enhancement.

1.1 The D/H Ratio and Atmospheric Escape

One of the longest standing pieces of evidence for water loss to space via atmospheric escape of H is the enrichment of heavy isotopes in several species, typically measured with respect to Earth values. Isotope ratios become enriched when the two isotopes respond differently to some process; this differential response is called fractionation. In planetary atmospheres, escape to space is a commonly occurring fractionating process, as the mass difference of isotopes shows up in their gravitational potential. This results in a preferential loss of the lighter isotope and a build up of the heavier isotope; Table 1.2 shows several isotope enrichments on Mars, including nitrogen ($^{15}N/^{14}N$), oxygen ($^{18}O/^{16}O$), argon ($^{40}Ar/^{36}Ar$ and $^{38}Ar/^{36}Ar$), and, importantly, hydrogen, which is explicitly written $^{2}H/^{1}H$, but is more often referred to as the D/H (deuterium to hydrogen) ratio.

Isotopes	× Earth val.	Comment	Ref
D/H	5.8 ± 2.6	Canada-France-Hawaii Telescope	Owen et al. (1988)
	5.2 ± 0.2	NASA Kuiper Airborne Observatory	Bjoraker et al. (1989)
	5.5 ± 2	Kitt Peak Fourier Transform Spectrometer	V. Krasnopolsky et al. (1997)
	5.95 ± 1.08	Mars Science Lab/Curiosity Rover	Webster et al. (2013)
	4.0–0.6, +0.8	SOFIA disk average, L_s 127	Encrenaz et al. (2018)
	4.5–0.6, +0.7	SOFIA disk average, L_s 304	Encrenaz et al. (2018)
	5–7	Polar cap sublimation	Villanueva et al. (2022)
$^{18}O/^{16}O$	0.943 ± 0.09974	Viking Neutral Mass Spectrometer	Biemann et al. (1976)
	1.031 ± 0.0057	Phoenix Lander	Niles et al. (2010)
	1.048 ± 0.005	MSL / Curiosity	Webster et al. (2013)
$^{15}N/^{14}N$	1.36-1.74	Viking NMS	Biemann et al. (1976)
	1.62 ± 0.16	Viking NMS	Nier et al. (1977)
	1.572 ± 0.082	MSL / Curiosity	M. H. Wong et al. (2013)
$^{38}Ar/^{36}Ar$	1.26 ± 0.03	MSL/Curiosity	Atreya et al. (2013)
$^{40}Ar/^{36}Ar$	10.1 ± 1.7	Viking NMS	Owen et al. (1977)
	6.4 ± 1.0	MSL/Curiosity	Mahaffy et al. (2013)

Table 1.2: Measured enrichments of several isotope systems on Mars. Measurements are quoted in multiples of the Earth value. For D/H and O, this corresponds to Vienna Standard Mean Ocean Water (VSMOW). The enrichment of noble gases like argon is also evidence of atmospheric escape.

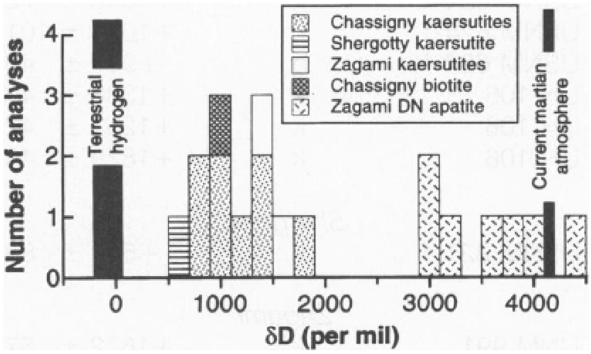

Figure 1.7: Elevated D/H ratios of various parts of an SNC meteorite, as measured by Leshin Watson et al. (1994) (their Figure 2).

On Mars, water is the primary reservoir of H and D, so changes in the D/H ratio encode changes in water loss, as over long time periods, the more efficient escape of H leads to retention of D and an enhancement of the D/H ratio in water.

The first detection of atmospheric D/H on Mars was made by Owen et al. (1988), by resolution of the 3.7 μm HDO absorption line. Follow up observations were made by Bjoraker et al. (1989). These early data showed that the atmosphere was enriched on average by a factor of 6 compared to the telluric value, suggesting past hydrogen escape and thus desiccation. This measurement was determined to be consistent with the existing geological models of martian surface evolution (M. H. Carr 1990), with the caveat that exchange with near-surface or subsurface water, via floods or volcanism, could have periodically reset the atmospheric D/H ratio, while also leaving signatures of the event in the polar caps. At this time, however, the D/H ratios of various water reservoirs on Mars were unknown.

Later, Leshin Watson et al. (1994) measured the D/H ratio in the SNC (Shergottites, Nakhlites, Chassignites) meteorites, which are believed to have a Mars origin due to their composition. They found large D/H values similar to that measured in the atmosphere, implying that the meteorites were sourced from an exchangeable near-surface reservoir (not from deep in the planet's interior), and that said reservoir may have achieved a high D/H earlier than expected. Additional detections followed of atomic D (V. A. Krasnopolsky et al. 1998) and molecular HD

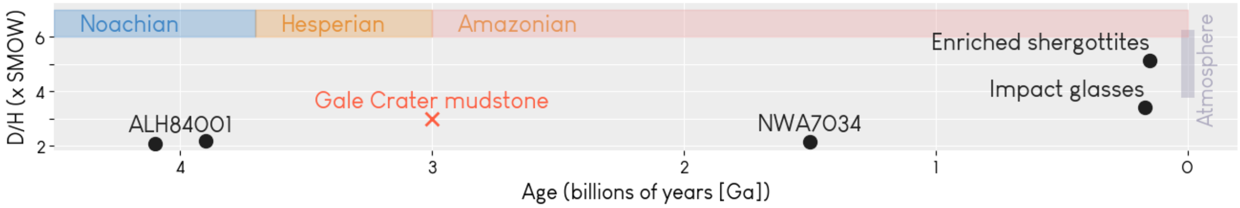

Figure 1.8: Martian D/H ratios as recorded in meteorites (dark gray circles) and a mudstone at Gale Crater (coral-colored x, Mahaffy et al. 2015a). Data adapted from Barnes et al. (2020), their Figure 2. See Table 1.2 for a summary of the atmospheric measurements.

(V. A. Krasnopolsky et al. 2001) in the atmosphere, enabling additional calculations. At the time of writing, aided by decades of Mars landers, orbiters, and observation campaigns, we now have a large number of D/H measurements and detections of HDO, D, and HD. These measurements encompass lab measurements of the D/H in meteorites (Hallis 2017, and references therein), an in situ measurement of a Gale crater mudstone, aged 3.3 Ga (Mahaffy et al. 2015a), and atmospheric measurements from surface assets (Hallis 2017), Earth-based observing campaigns (Villanueva et al. 2015; Encrenaz et al. 2018), and most recently, the ESA Trace Gas Orbiter (Aoki et al. 2019; Vandaele et al. 2019; Villanueva et al. 2022) and MAVEN IUVS (Chaufray et al. 2021a). The ensemble of D/H ratio measurements at multiple ages in the rock record (Figure 1.8) made it clear that D/H has steadily increased over geological time, supporting the hypothesis that water has escaped to space.

The story so far has answered some major questions about the escape of the martian atmosphere and the desiccation of the surface, but what we know so far also points to new questions. Most work so far has focused mainly on H escape, but the D/H ratio is critical to understanding water loss. To complete the puzzle of Mars water loss, we cannot neglect the D escape piece. We now know that H escape is not constant, and is sensitive to seasonal changes and drivers, particularly dust events and the seasonal cycle (see Section 1.2.2.2). What about D escape? What are the implications for the D/H ratio, the fractionation factor, and total water loss over time? This thesis addresses some of the questions around D escape, adding to our knowledge of the history of water on Mars.

1.2 Atmospheric escape

1.2.1 Processes

The retention of any atmosphere on a planet is a constant balancing act between the pull of gravity and the kinetic energy of atmospheric gasses, which can gain energy—and thus velocity which may allow them to escape the planet—through a variety of processes. Escape is an umbrella term encompassing these processes, the relative importance of which vary based on the atom or molecule (generally, "species") under consideration. The heavier the species, the more tightly bound to the planet by gravity it is, and the more energy it will require to escape; as mass goes up, escape likelihood goes down.

Atmospheric escape occurs in two primary flavors: thermal and non-thermal.

Thermal escape includes escape of atoms with velocities that fall above the planetary escape velocity in the high-energy tail of the Maxwell-Boltzmann distribution (Figure 1.9c). This type of escape is divided into thermal Jeans escape (Jeans 1925; Hunten 1973), which controls loss of minor, light atmospheric constituents (Figure 1.9a), and hydrodynamic escape (Figure 1.9b), which occurs when light gases making up $\gtrsim 10\%$ of an atmosphere flow out to space like a fluid, dragging heavier particles along in their wake (Hunten et al. 1987; Gronoff et al. 2020). The division between the two regimes is identified by the value of the Jeans parameter,

$$\lambda_{\mathrm{J}} = \frac{\mathrm{GMm/r}}{\mathrm{kT}} = \frac{\mathrm{v}_{\mathrm{esc}}^2}{\mathrm{v}_{\mathrm{th}}^2}, \tag{1.1}$$

representing a ratio of the gravitational energy to the thermal energy (escape velocity to the most probable velocity of the Maxwell-Boltzmann distribution). For an atomic gas (e.g., H), thermal Jeans escape occurs when the parameter exceeds $\lambda \sim 3$, with a transition region from $\lambda = 2-3$ and hydrodynamic escape occurring below $\lambda = 2$; for a diatomic gas, the transition region is $\lambda = 2.4-3.6$ (Volkov et al. 2011). Both are fractionating processes, although hydrodynamic escape fractionates the heavier molecules rather than the light ones which form the bulk of the fluid flow (Zahnle et al.

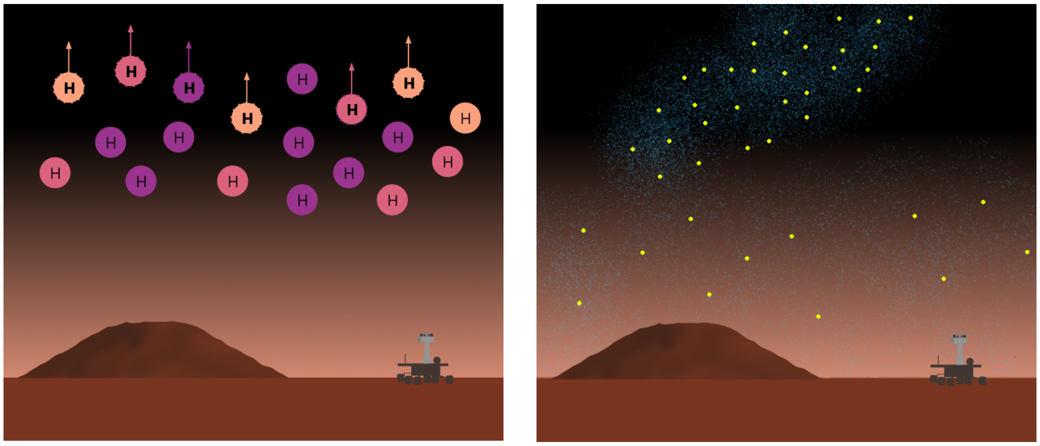

(a) For light, minor species in a planetary atmosphere in local thermodynamic equilibrium, Jeans escape is the operative escape process. Under Jeans escape, a small fraction of particles are moving fast enough to exceed escape velocity. Their velocities are in the high-energy tail of the Maxwell-Boltzmann distribution (panel c).

(b) Hydrodynamic escape, in which a light species (blue) makes up a significant fraction of the atmosphere (1-10%) and flows out to space, entraining heavier particles (yellow dots) along the way. This process may have been present on early Mars, with neutral H forming the wind and entraining and fractionating noble gases.

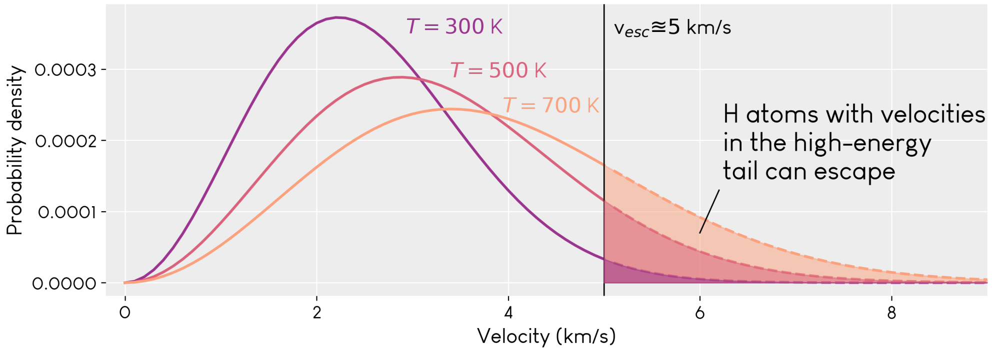

(c) Maxwell-Boltzmann distribution for three different temperatures. As temperatures increase, the relative amount of atoms in the high-energy tail (above escape velocity) increases.

Figure 1.9: Thermal escape processes in planetary atmospheres.

1990). Hydrodynamic escape may have been active on early Mars (Yoshida et al. 2020; Cassata et al. 2022), while Jeans escape is ongoing today.

Non-thermal escape (Figure 1.10), on the other hand, occurs when a species gains extra energy through other methods, many of which involve ion interactions, which occur at much higher temperatures than neutral-neutral reactions. It includes:

- Ion pickup and outflow (Figure 1.10a), which describes the outflow of planetary ions according to influence from magnetic and electric fields (e.g. Luhmann 1990; Schunk et al. 2009; Inui et al. 2018; Maes et al. 2021; Pickett et al. 2022; Dong et al. 2023);
- Sputtering (Figure 1.10a), when ions, usually O^+, accelerated by the solar wind collide with other neutral atmospheric particles and literally knock them out of the atmosphere and into space (Luhmann et al. 1992; Jakosky et al. 2017);
- Photochemical escape (Figure 1.10b), in which photochemical processes, especially below the exobase, impart extra energy to neutrals produced through dissociative recombination, charge exchange, and ion-neutral reactions (Lillis et al. 2017; Gronoff et al. 2020; Lo et al. 2021);
- Charge exchange of a solar wind ion and a planetary neutral (Figure 1.10c), which creates an energetic neutral atom and a new ion. The ENA can then continue into past the bow shock with the same velocity and energy as the solar wind, imparting excess heat and energy. The new ion may escape along electric field lines (Deighan et al. 2018).
- Impact erosion, when large amounts of the atmosphere are ejected when a large impactor hits the planet (e.g. Schlichting et al. 2015). Smaller impactors may also actually deliver volatiles, so that that the net effect on the atmosphere is not always certain.

On Mars, escape of the lightest neutral species, such as H, tends to be dominated by thermal escape processes, while larger ions and D escape mostly non-thermally; the balance of escape type between H and D will be addressed in Chapter 3 of this thesis, which implements ion-neutral

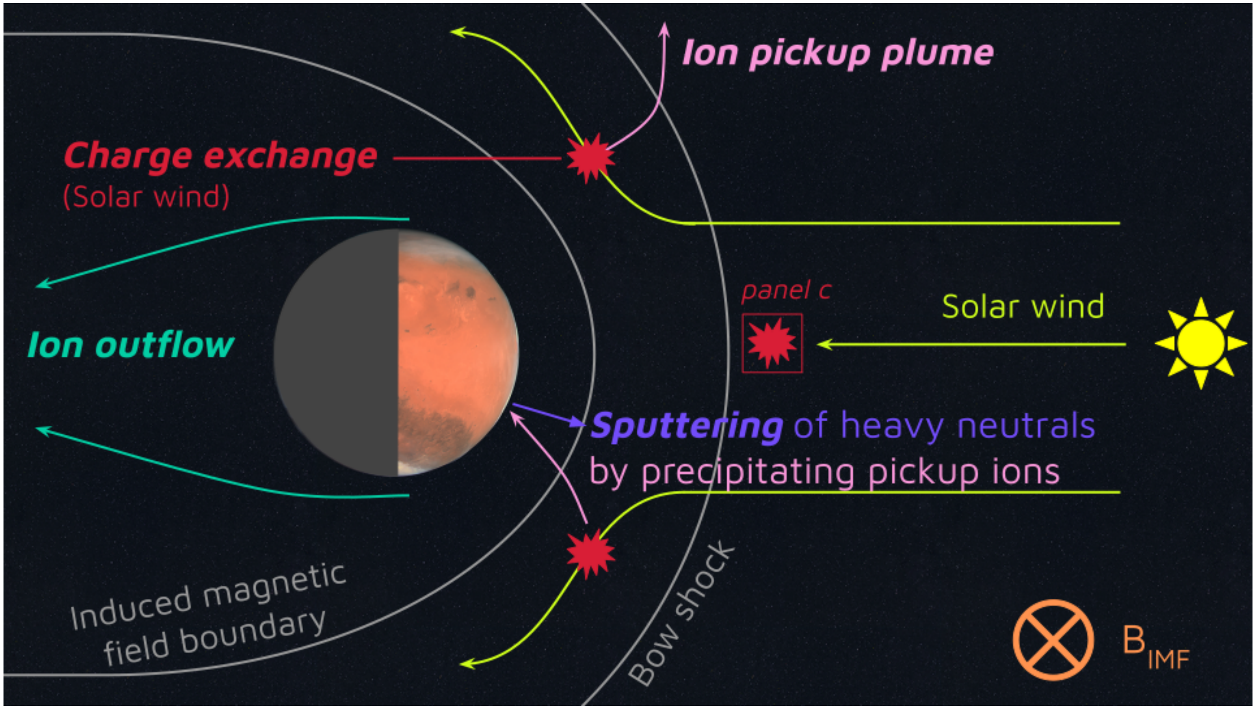

(a) The solar wind stimulates a pickup ion plume, tailward outflow, sputtering due to precipitating pickup ions, and escape of energetic neutrals created in charge exchange reactions (panel c). Adapted from Hughes et al. (2019) and Ramstad et al. (2023).

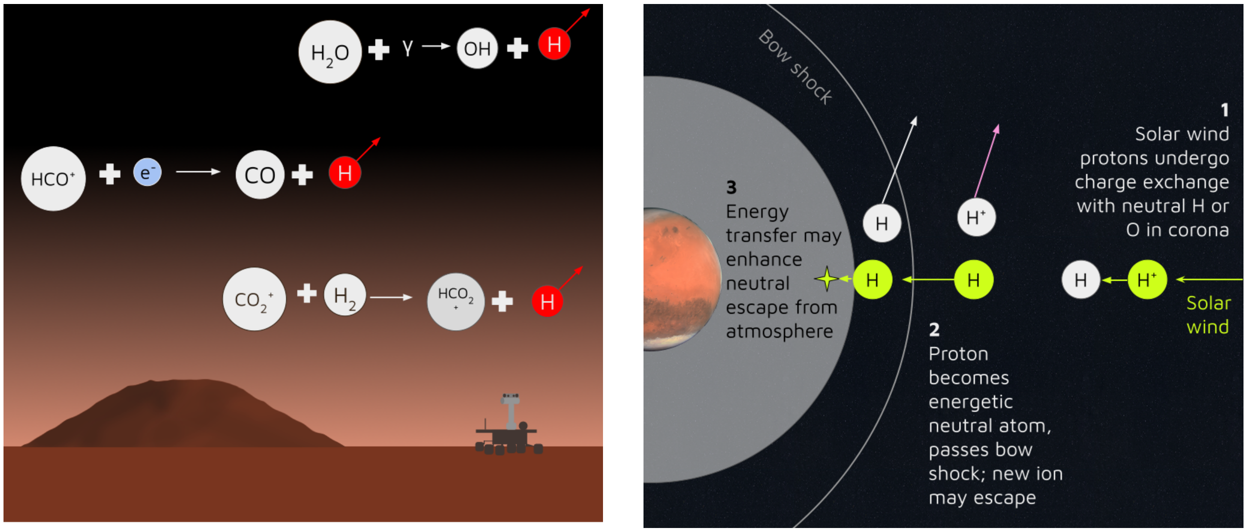

(b) Lower down in the collisional atmosphere, bi-molecular, termolecular, and photochemical reactions can produce suprathermal ("hot") atoms when excess energy from an ion-neutral reaction is deposited in a produced atomic H or D.

(c) Charge exchange reactions, in which solar wind protons or helium ions react with coronal H or O. The newly created ion can escape, and the neutral H continues into the atmosphere, where it can induce heating and may enhance neutral escape.

Figure 1.10: Non-thermal escape of ions and neutral particles created in ionospheric processes at Mars.

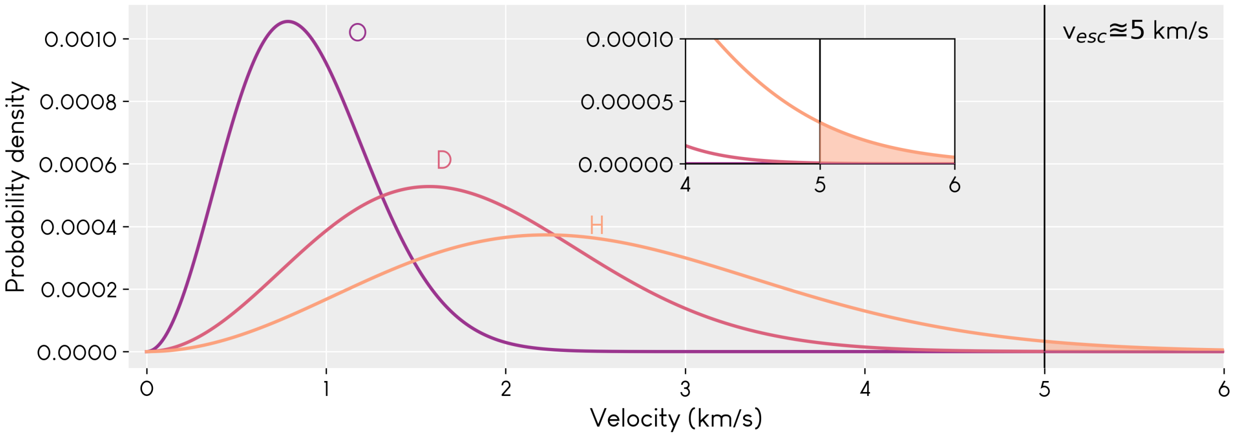

Figure 1.11: Maxwell-Boltzmann distributions for H, D, and O at 300 K. For species more massive than H and D, thermal escape is negligible due to the lack of particles in the high-energy tail above escape velocity.

processes as a source of hot H and D which can then escape non-thermally, falling under the photochemical escape umbrella. This thesis does not include ion outflow (which depends heavily on 3D magnetohydrodynamics), impact erosion (due to its stochastic nature), or interactions with the solar wind (due to this being most important above the bow shock (Halekas et al. 2017), which is far above the upper boundary of the photochemical model used here). Collision of H and D with hot oxygen (O) is also not included; H collision with hot O is well characterized at Mars (Nagy et al. 1990; Deighan et al. 2015; Lee et al. 2015), but is more easily modeled in collisional/kinetic models. Hot O has been shown to be an important process in non-thermal escape of hot H from Mars (Shematovich 2013); the escaping fraction of hot D has also been calculated using a kinetic model for Mars (Shizgal 1999), but the resulting escape fluxes have not been modeled.

1.2.2 Modeling and measurements of escape

Over the last several decades, escape of many species has been modeled at Mars; since the start of the MAVEN mission, observationally-derived escape rates have become commonplace in the literature. Given that Mars' escape velocity is approximately 5 km/s, most atmospheric atoms and molecules must escape non-thermally, as species larger than D do not have well-populated high-energy tails in their Maxwell-Boltzmann distributions (see Figure 1.11). H and D, due to their low masses, are unique in that thermal escape can make up a non-negligible (for D) or dominant (for H) share of their escape. In the 20th century, most work was done as modeling studies or with ground-based observations. A combination of these early studies, plus modern observations from Mars orbiters such as Mars Express and MAVEN, have provided us with the wealth of knowledge about the Mars upper atmosphere that we have today.

1.2.2.1 Escape of CO_2-derived atoms and ions

As the atmosphere of Mars is 95% CO_2, many escape studies have focused on escape of its products. The escape of O^+ and O_2^+ ions in particular have been studied extensively, as O_2^+ is the principal ionospheric ion. Modelers using 3D MHD and hybrid models to model loss of O^+, O_2^+, and CO_2^+ have obtained total loss rates of 2×10^{23} - 5×10^{24} s^{-1} (e.g. Ma et al. 2007; Boesswetter et al. 2010). These values were consistent with findings from the Mars Express ASPERA-3 instrument (Barabash et al. 2007). Later, MAVEN observations agreed, indicating a total $O^+ + O_2^+$ loss value of 5×10^{24} s^{-1} (Jakosky et al. 2018).

Ion escape is not the only source of loss for oxygen species, although it is an important one. Photochemical escape, in which hot neutral O atoms are produced in ion-involved reactions, is the dominant source (Jakosky et al. 2018), with total loss initially calculated by models to be $1.4 - 2.1 \times 10^{26}$ s^{-1} (Fox et al. 2009a); later models and the MAVEN mission converged on a smaller value of $1 - 9 \times 10^{25}$ s^{-1} (Gröller et al. 2014; Deighan et al. 2015; Lee et al. 2015; Lillis et al. 2017; Rahmati et al. 2018). As mentioned, hot O also contributes to hot H and D escape (Shizgal 1999; Shematovich 2013).

Atomic carbon (C) is a minor constituent in the atmosphere, with densities on the order of 10^5 cm^{-3} (Lo et al. 2022), but its escape is of interest because of its source in CO_2. H and O escape on Mars receive a lot of attention in research because of their ties to water and water loss, but O can also be sourced from CO_2. Through the odd hydrogen cycle (M. B. McElroy et al. 1972; Liu et al. 1976), the abundance of O_2 in the atmosphere controls the escape rates of both O and H. In long-term equilibrium, H and O escape will balance in a 2:1 ratio, stemming from their ratio in water. On shorter timescales and in the real atmosphere, which may not be in equilibrium, this ratio does not necessarily hold. Thus, an understanding of the exact amount of the escape of H, O, and C is thus extremely useful for developing insight into the photochemistry of the atmosphere. Carbon escape at Mars has been both modeled (Fox et al. 2001a; Fox 2004; Gröller et al. 2014; Lo et al. 2020) and derived from observations (Cui et al. 2019; Lo et al. 2022), with total escape rates in the range of 10^5-10^6 cm^{-2}s^{-1}. Because the work in this thesis mostly concerns equilibrium modeling and uses a fixed oxygen escape rate $\sim 10^8$, carbon escape is not included; the effect to the calculations of H and D escape is expected to be negligible.

1.2.2.2 H and D escape

H escape has been extensively studied at Mars. After two teams observed strong short-term variation in the H corona around Mars using the Hubble Space Telescope (Clarke et al. 2014) and the SPICAM instrument onboard Mars Express (Chaffin et al. 2014), the connection to water loss was identified by Chaffin et al. (2017). They demonstrated that water supplied into the mesosphere can drive seasonal changes in H escape in a matter of weeks. The generally agreed upon present-day escape rate for H typically falls between $1 - 11 \times 10^8$ cm^{-2}s^{-1}, which includes some seasonal variations (Jakosky et al. 2018, and references therein). These values have been derived from photochemical modeling (Yung et al. 1988; Kass et al. 1999; V. Krasnopolsky 2000; V. A. Krasnopolsky 2002; Zahnle et al. 2008; Chaffin et al. 2017; V. A. Krasnopolsky 2019, and Cangi et al. 2020 (chapter 2)), 3D GCM (general circulation model; see section 1.5) modeling (AlMaazmi et al. 2019; Chaufray et al. 2021b), and derivation from mission data, especially MAVEN (Halekas 2017; Chaffin et al. 2018; Rahmati et al. 2018; Stone et al. 2020). H escape can be enhanced by thermospheric winds (Gu et al. 2022), space weather events (Mayyasi et al. 2018), seasonal variation (Rahmati et al. 2017), gravity waves (Yiğit 2021; Yiğit et al. 2021), and dust storms (Heavens et al. 2018; Aoki et al. 2019; Vandaele et al. 2019; A. A. Fedorova et al. 2020; Stone et al. 2020; Chaffin et al. 2021; Holmes et al. 2021; Villanueva et al. 2021).

By comparison, D escape has received significantly less attention. It was initially studied with a photochemical model by Yung et al. (1988) around the same time that the D/H ratio of the Mars atmosphere was first measured by Owen et al. (1988). Yung et al. (1988)'s model was a primarily neutral model with only a few fixed-density ion species. While the work established D escape in the literature, many avenues were left open to explore. Measurements of HDO and D in the Mars atmosphere were obtained by V. Krasnopolsky et al. (1997) and V. A. Krasnopolsky et al. (1998), and these measurements were used to guide later photochemical models. V. Krasnopolsky (2000), V. A. Krasnopolsky et al. (2001), and V. A. Krasnopolsky (2002, 2015) include thermal and non-thermal escape of D and HD in their photochemical models, but without an extensive deuterated chemical network and deuterated ions. The non-thermal escape they calculate only considers the escape of H and D ions above the ionopause that are produced due to charge exchange with the solar wind, electron impact ionization, and photoionization. Other researchers have also modeled isotope effects on condensation, cloud formation, dust grain adsorption, and other processes involving HDO (Fouchet et al. 2000; Bertaux et al. 2001; Moores et al. 2011b), but without studying the direct impact on escape.

1.3 The fractionation factor: comparing escape efficiencies of D and H

At its heart, the fractionation factor is a quantity we define to capture the differential escape of H and D from Mars. It also serves as a proportionality factor when we define a coupled system of differential equations to describe this escape (Chamberlain et al. 1987):

$$\frac{dD}{dt} = -fAD \tag{1.2}$$

$$\frac{dH}{dt} = -AH \tag{1.3}$$

Here, D and H are their number densities, the left-hand sides represent the change in abundance due to escape, A is a proportionality constant, and f is the fractionation factor, which has a range [0,1] and represents the efficiency of dD/dt compared with dH/dt. "Fractionation" essentially means "how different is the behavior of the heavier isotope compared to the lighter isotope?" This leads to the canonical definition of $f = 1$ as "no fractionation" (the isotopes behave similarly, with no mass-dependent effects) and $f = 0$ as "maximum fractionation" (the abundance of the lighter isotope, but not the heavier isotope, can change over time). Although these definitions are somewhat non-intuitive, they are the ones we are stuck with. Since we have defined these equations to represent the planetary abundances of the isotopes H and D, $f = 0$ represents a scenario in which H can escape, but D is completely retained on the planet, manifesting as a nullification of equation 1.2.

We can see that f is simply the relative rate of change of the D/H ratio, normalized by the total abundance:

$$f = \frac{\frac{\mathrm{d}D}{\mathrm{d}t}}{\frac{\mathrm{d}H}{\mathrm{d}t}} \frac{1}{D/H} \tag{1.4}$$

Since we use the escape rates of D and H as a proxy for water loss from the planet, we normalize with the abundance of water at the surface and replace the derivatives with the escape fluxes:

$$\mathrm{f} = \frac{\phi_{\mathrm{D}}/\phi_{\mathrm{H}}}{[\mathrm{HDO}]_{\mathrm{s}}/2[\mathrm{H_2O}]_{\mathrm{s}}} = \frac{\phi_D/\phi_H}{R_{dh}} \tag{1.5}$$

With ϕ representing the escape flux (encompassing both thermal and non-thermal escape), and [X] representing the abundance of a species, with $[\mathrm{X}]_s$ indicating that the abundance is at the surface.

If the ratio of fluxes approaches the D/H ratio in water, then $f = 1$, and both D and H escape proportionately to their abundances; there is no mass-dependent fractionation effect at all. On the other hand, if the physical characteristics of Mars were such that D was completely unable to escape to space, then $\phi_D \to 0$, and $f = 0$; this is the case with the highest fractionation, where D would be completely retained on the planet. In theory, it is possible that there could be some process leading to $f > 1$—all that would be required is for the D/H ratio of escaping atoms to be larger than the D/H ratio in water at the surface—but thus far such a value has not been calculated in any studies or from real data. In reality, D/H fractionation is somewhere between 0 and 1, as both atoms can escape from Mars.

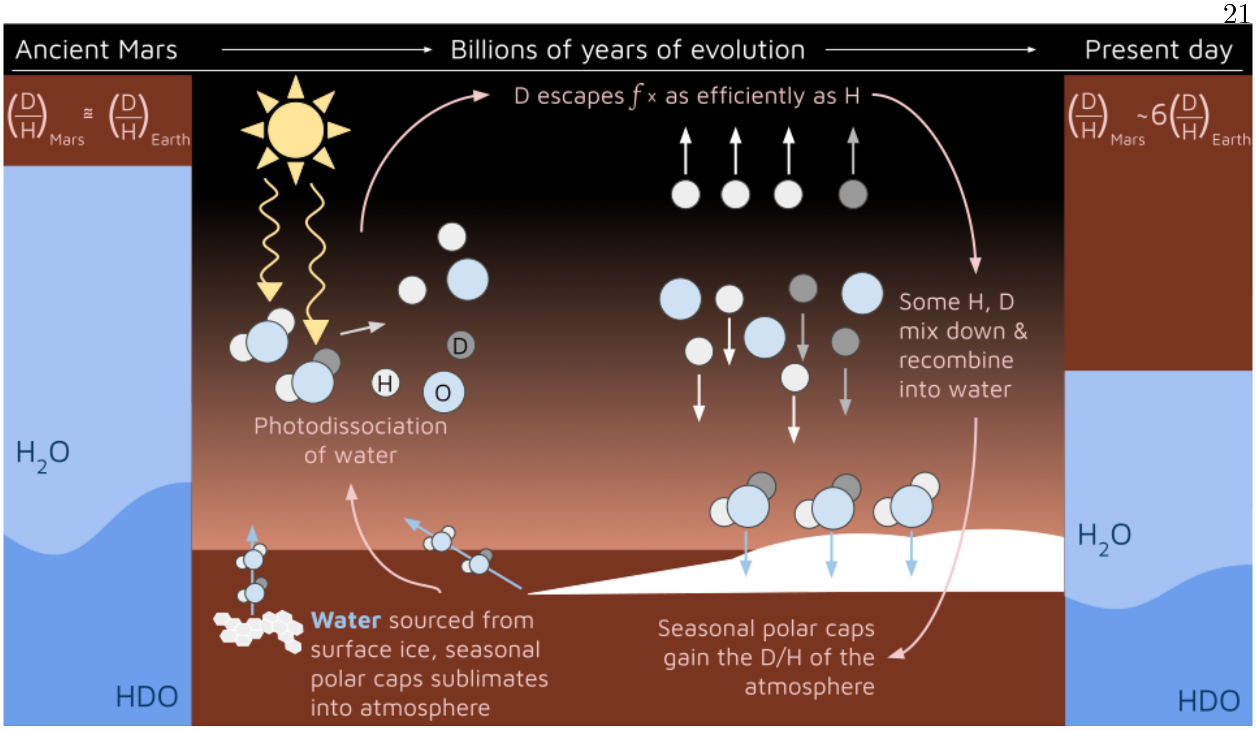

Figure 1.12: The fractionating nature of D and H escape leads, over long timescales, to a relative enhancement of the D/H ratio in water compared to Earth. The D/H ratio of ancient Mars is typically assumed to be similar to the ratio on Earth in the present day.

A summary of calculated fractionation factors is shown in Table 1.3, and the general effect of the fractionation factor on the D/H inventory of Mars is shown in Figure 1.12. In the first photochemical modeling study of D/H on Mars, Yung et al. (1988) calculated $f = 0.32$, based on neutral chemistry and an exospheric temperature $T_{exo} = 364$ K, based on highly uncertain Mariner data roughly 100 K higher than temperatures measured by MAVEN (e.g. Stone et al. 2018; Thiemann et al. 2018; Jain et al. 2023). They also performed a small sensitivity study to determine which processes available in the model have the largest effect on f, and concluded that the most important factors are (in order of most to least) the differences in isotope masses, effusion velocities, molecular diffusion, and finally branching ratios and rates of deuterated reactions.

Several studies in the late 1990s and early 2000s also calculated the fractionation factor. V. A. Krasnopolsky et al. (1998) used observations of D Ly α in conjunction with a radiative transfer model and a photochemical model to derive densities of H_2 and HD and escape rates of D

f	**Reference**	**Note**
0.32	Yung et al. (1988)	Neutral only model, assumed present water inventory 0.2 m GEL, thermal escape only
0.02	V. A. Krasnopolsky et al. (1998)	Based on detection of atomic D with the Hubble Space Telescope
0.016, 0.135	V. Krasnopolsky (2000)	Two models of eddy diffusion
0.055, 0.082, 0.167	V. A. Krasnopolsky (2002)	$T_{exo} = 200, 270, 350$
0.002	E. M. Cangi et al. (2020)	Thermal escape only

Table 1.3: Existing calculated values of the fractionation factor. Note that to determine non-thermal escape velocities, V. A. Krasnopolsky et al. (1998) calculates charge exchange with the solar wind, photoionization, and electron impact ionization. Later papers (V. Krasnopolsky 2000; V. A. Krasnopolsky 2002) which calculate f do not describe the non-thermal processes accounted for, but are likely the same as V. A. Krasnopolsky et al. (1998). Some additional later papers spearheaded by V. A. Krasnopolsky (2006, 2010, 2019) focus on Mars, but do not mention the fractionation factor. V. A. Krasnopolsky (2010) contains the most explicit description of included non-thermal processes in their model, with references to earlier papers in which various methods were developed.

and H, calculating $f = 0.02$. Two possible fractionation factors were proposed by V. Krasnopolsky (2000) in an attempt to reconcile a difference in the ratio HD/H_2 / HDO/H_2O as calculated by V. A. Krasnopolsky et al. (1998) and Yung et al. (1988), but neither was deemed to be preferred because the assumptions used to calculate each value disagreed with either the Mariner 9 data or the understanding of kinetic differences between the D and H isotopes (Fouchet et al. 2000; Bertaux et al. 2001). V. A. Krasnopolsky (2002) also calculated f for three different exospheric temperatures (200 K, 270 K, and 350 K), with $f = 0.082$ for $T_{exo} = 270$ K being the largest value in agreement with more modern measurements of exospheric temperatures.

The fractionation factor is very sensitive to the total escape of both H and D, which occurs through loss of both the atomic form and the molecular forms, and for both thermal and non-thermal escape:

$$f \sim \frac{\phi_D}{\phi_H} \tag{1.6}$$

$$\phi_{\mathrm{D}} = \phi_{\mathrm{D}}^{\mathrm{thermal}} + \phi_{\mathrm{D}}^{\mathrm{nonthermal}} + \phi_{\mathrm{HD}}^{\mathrm{thermal}} + \phi_{\mathrm{HD}}^{\mathrm{nonthermal}} \tag{1.7}$$

$$\phi_{\mathrm{H}} = \phi_{\mathrm{H}}^{\mathrm{thermal}} + \phi_{\mathrm{H}}^{\mathrm{nonthermal}} + 2\phi_{\mathrm{H2}}^{\mathrm{thermal}} + 2\phi_{\mathrm{H2}}^{\mathrm{nonthermal}} + \phi_{\mathrm{HD}}^{\mathrm{thermal}} + \phi_{\mathrm{HD}}^{\mathrm{nonthermal}} \tag{1.8}$$

Similarly, the total integrated water loss depends sensitively on the value of f. This relationship is discussed more in the following section.

1.4 Rayleigh fractionation and integrated water loss

Solving the system of equations defined by equations 1.2 and 1.3, we can derive the equation of Rayleigh fractionation (also sometimes called Rayleigh distillation), which links the change in a given species abundance over time with a change in its isotope ratio and the fractionation factor f. We begin by dividing the equations:

$$\frac{\mathrm{d}H}{\mathrm{d}D} = \frac{H}{fD}$$

Using the identity $\mathrm{d}\ln x = \frac{1}{x}\mathrm{d}x$:

$$\frac{H\mathrm{d}\ln H}{D\mathrm{d}\ln D} = \frac{1}{f}\frac{H}{D}$$
$$\mathrm{d}\ln D = f\mathrm{d}\ln H \tag{1.9}$$

Now, we can define $R \equiv \frac{H}{D}$ and substitute in equation 1.9:

$$\begin{aligned}\mathrm{d}\ln R &= \mathrm{d}\ln(H/D) = \ln(\mathrm{d}H/\mathrm{d}D) = \mathrm{d}\ln H - \mathrm{d}\ln D\\ &= \mathrm{d}\ln H - f\mathrm{d}\ln H\\ \mathrm{d}\ln R &= (1-f)\mathrm{d}\ln(H)\end{aligned}$$

By integrating and cleverly choosing $C_1 = \ln\frac{1}{R_0}$ and $C_2 = \ln\frac{1}{H_0}$ to represent values at some reference time $t = 0$, we can derive the final Rayleigh fractionation equation:

$$\begin{aligned}\ln R + C_1 &= (1-f)\left(\ln H + C_2\right)\\ \ln\frac{R}{R_0} &= (1-f)\left(\ln\frac{H}{H_0}\right)\\ \exp\left[\ln\frac{R}{R_0}\right] &= \exp\left[(1-f)\left(\ln\frac{H}{H_0}\right)\right] = \left(\exp\left[\ln\frac{H}{H_0}\right]\right)^{(1-f)}\\ \frac{R}{R_0} &= \frac{H}{H_0}^{1-f}\\ \frac{H/D}{(H/D)_0} &= \frac{H}{H_0}^{1-f}\\ \frac{D/H}{(D/H)_0} &= \frac{H_0}{H}^{1-f}\end{aligned} \tag{1.10}$$

By manipulating equation 1.10 so that H is a proxy for water abundance, and using R_{dh} from equation 1.5 such that $R_{dh} = D/H$ (since D/H is typically measured in water on Mars), we can obtain a similar expression that gives us the total integrated water loss from Mars (E. M. Cangi et al. 2020):

$$W_{\text{lost}} = W(t)\left(\left(\frac{R_{dh}(t)}{R_{dh}(t=0)}\right)^{1/(1-f)} - 1\right), \tag{1.11}$$

Where W represents water (H_2O and HDO), with $W(t)$ representing the water inventory at a given time t and W_{lost} represents the total water lost from Mars since $t = 0$; $(t = 0)$ represents primordial Mars (about 4.5 billion years ago). The relationships described by Equations 1.5 and 1.11 can be visualized in a variety of ways for a variety of assumptions about their inputs, as shown in Figure 1.13.

There are a few assumptions implicit in the definition of Rayleigh fractionation. First, we have assumed that the inventory of a given gas, such as H, decreases steadily over long time periods proportionately to its abundance. This is a reasonable enough assumption, but over short time frames on real Mars, it may not hold; for example, volcanic outgassing, catastrophic floods, or other release of juvenile water onto the surface and into the exchangeable reservoir could briefly change the D/H ratio. More importantly, in order to complete our derivation, we have assumed that the fractionation factor is constant in time; part of the outcome of this thesis is that this is not correct, although the goodness of the assumption over geological time is yet unknown. Rayleigh fractionation represents water loss based on mean conditions, so it serves well enough for an estimate.

1.4.1 Evolving estimates of water loss

Initial D/H studies obtained very small present-day water inventories, from 0.2–9 m GEL (Yung et al. 1988; Kass et al. 1999), mostly due to assumption that today's escape rates are representational of all of Mars' history, and due to a lack of observational confirmations. Geologists have since determined through geomorphological analysis of the martian surface that many surface features must have been formed by huge quantities of water, as discussed previously. Given all of the evidence, estimations of water loss range from 500 m GEL (global equivalent layer; the depth of a planet-wide ocean containing all of the water in question) up to as high as 2600 m GEL (Lunine et al. 2003; Lasue et al. 2013).

Models which calculate atmospheric escape, however, regularly come up short of this, as shown in Figure 1.13c. It is yet unclear whether the difference is made up through emplacement of

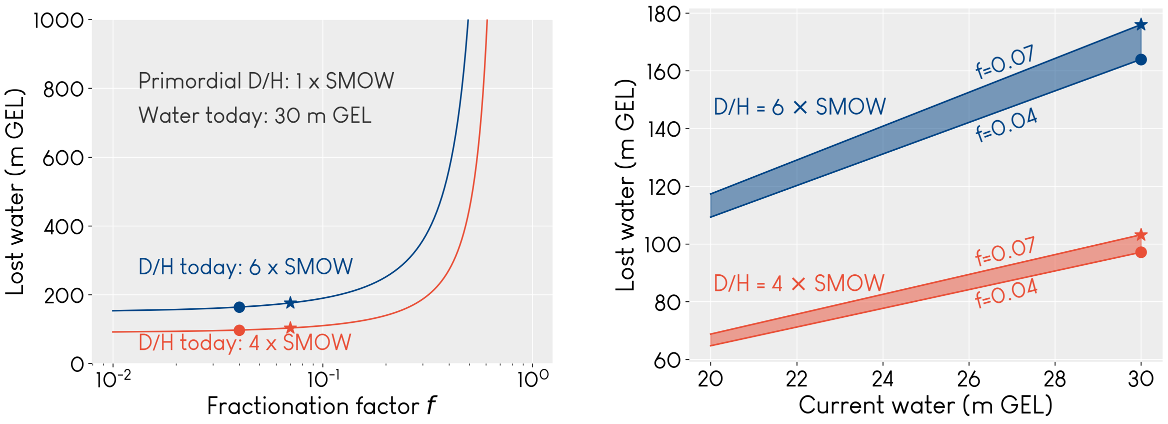

(a) Dependence of water loss on f. In this panel, current water inventory is assumed to be 30 m GEL (Lasue et al. 2013). Total water loss is insensitive to f if $f < 0.1$, but increases rapidly as $f \to 1$.

(b) Lost water as a function of the present-day inventory in the exchangeable reservoir. The shaded areas are bounded by $f = [0.04, 0.07]$ (see Chapter 3), and the slope of the lines is the parenthetical portion of equation 1.11.

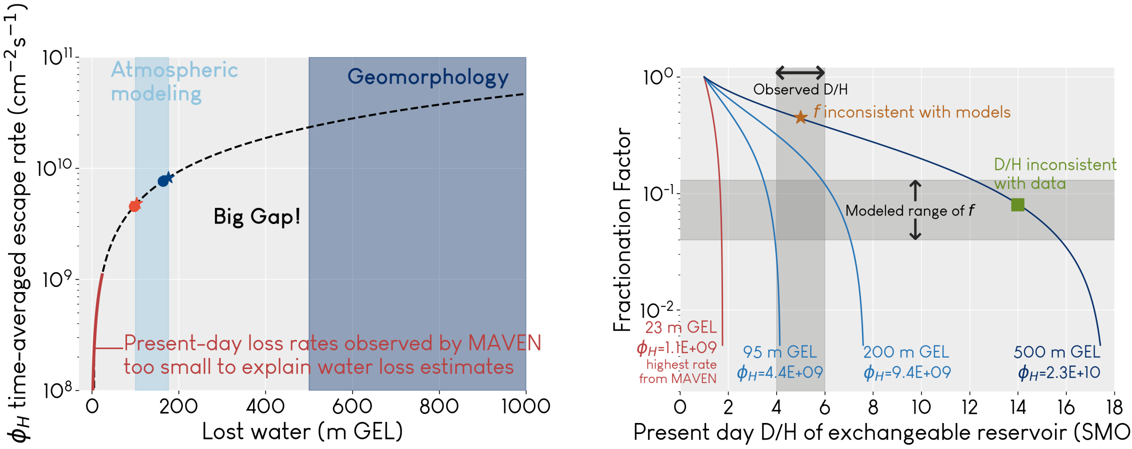

(c) Required time-averaged escape rate of H as a function of total water lost. Atmospheric models and geomorphology studies disagree on the total, and the present-day escape rates from MAVEN are not consistent with either group.

(d) Contours show total water loss and associated ϕ_H. In order to match the geomorphology escape estimates, either the D/H ratio is inconsistent with observations, or f is inconsistent with modeling.

Figure 1.13: Several ways of visualizing Equation 1.11. The star and circle points represent the same solutions to Equation 1.11, plotted in the three different panels. In all panels, the primordial D/H value is assumed to be equal to the Earth value. Values of f are for the total (thermal & non-thermal) fractionation factor, and are from chapter 3 results.

water into a subsurface, non-exchangeable reservoir, loss to space through unquantified pathways, or a mix of the two. Recent works suggest that a significant amount of water could exist in hydrated minerals (Scheller et al. 2021; Wernicke et al. 2021), though the time of emplacement, concurrent planetary conditions, and implications for resurfacing are unknown. One approach to elucidating this question is to attempt to thoroughly characterize atmospheric escape modes; this is the approach that this thesis takes, through the use of photochemical modeling to understand the subtle differences in the atmospheric chemistry and dynamics of H and D.

1.5 Photochemical modeling

Many models of planetary atmospheres take the form of one-dimensional photochemistry, or three-dimensional "General Circulation Models" (GCMs; sometimes also expanded to "Global Climate Models"). Complementary in nature, they tend to be used to achieve different ends.

Photochemical modeling, the approach used in this thesis, is a one-dimensional modeling approach where the spatial dimension is either altitude or pressure. A given run of a photochemical model begins with an initial condition, a few boundary conditions at the top and bottom of the modeled atmosphere, and a coupled system of differential equations from gas-phase bimolecular and termolecular chemistry and photochemistry (chemistry stimulated by photons). Because of the complexity of chemical systems which involve many different species with different behaviors, the systems of equations quickly become a huge network of lengthy, coupled, stiff equations which require careful choice of integrators to solve. Photochemical models have the advantage of being very useful for careful study of the dominance of different chemical pathways, understanding how transport and chemistry differ at different levels of the atmosphere, and being relatively computationally cheap and easy to run on a personal computer. Because photochemical models are not able to consider differences in the atmospheric structure and behavior across the planet, they are most often used to examine the mean-field behavior of an atmosphere; they can be thought of as producing the atmospheric equivalent of "end-member cases", that is, they explore the most reasonable and feasible range of atmospheric states, given some inputs. A schematic of the photochemical

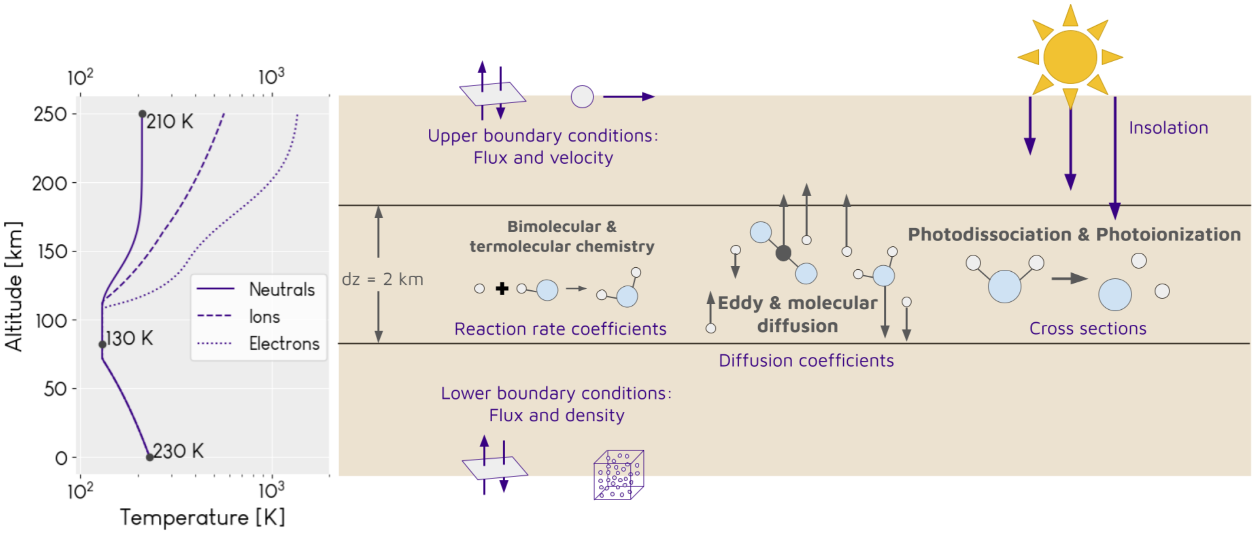

(a) The basic structure and inputs of a photochemical model. Processes are shown in bold brown text, and the altitude discretization in brown text. Inputs are shown in indigo. A third input, which is not pictured, is an initial guess for the density profile for every species in the atmosphere. Boundary conditions may be defined for each species, and some species have more than one boundary condition. See Table 1.5 for a description of the boundary conditions used in the chapters of this thesis.

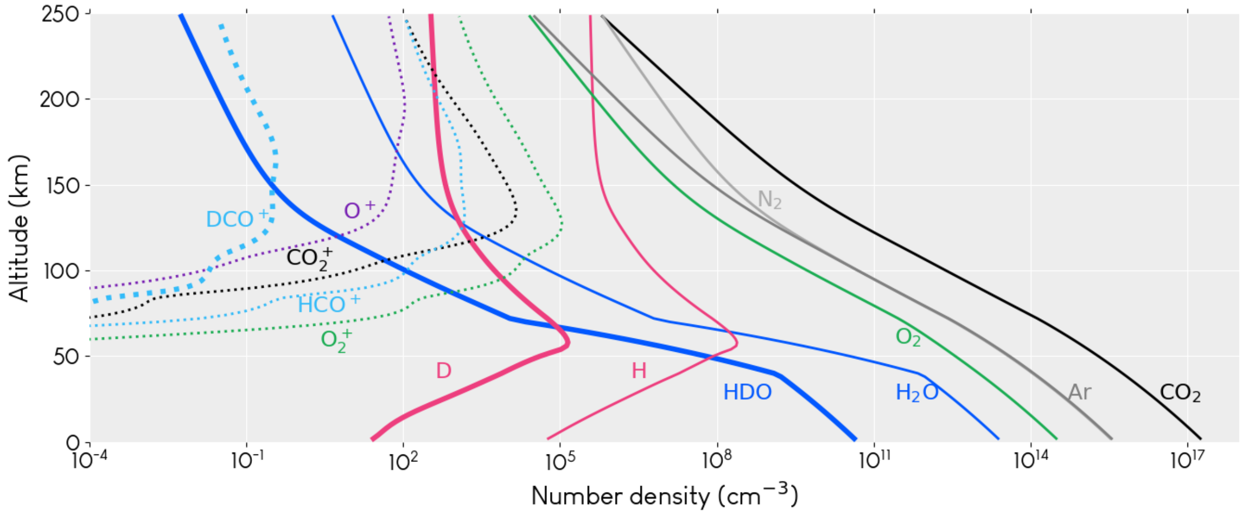

(b) Example output of a photochemical model: species number densities by altitude. Some photochemical models have pressure as the vertical coordinate; this thesis uses altitude. Ions are shown in dotted lines, neutrals in solid lines, and deuterated species, which are emphasized in this thesis, are shown with a thick line. The species shown here are only a selection of the total included species.

Figure 1.14: Schematic of the photochemical model developed and used in this thesis.

model developed and used for this thesis is shown in Figure 1.14.

In contrast, GCMs solve the 3D fluid or MHD equations and are effective at modeling large-scale circulation (hence the name) and climate patterns. On Mars, they are also the models most likely to implement parameterization of dust and cloud microphysics. They often also include some photochemistry, but are too computationally demanding to enable a high-resolution, detailed study of chemical interactions of a large number of species.

Both 3D GCMs and 1D photochemical models can inform us about atmospheric evolution over time, and both can be used to assimilate data from spacecraft missions to examine atmospheric responses to specific impulses and drivers.

1.5.1 Photochemical modeling at Mars and elsewhere

Photochemical modeling was first used on Mars to solve the problem of the stability of the atmosphere by (M. B. McElroy et al. 1972). The fast dissociation of CO_2 and slow recombination of CO + O would seem to imply that a CO_2 atmosphere should not be stable in the presence of incoming solar radiation. The solution was the odd hydrogen cycle as the catalyst of CO + O recombination. Further photochemical work explored the relationship between H and O escape (Liu et al. 1976), the eddy diffusion rates (Kong et al. 1977), possible early evolution scenarios (M. B. McElroy et al. 1977; Deighan 2012), and the history of water loss as encoded in the D/H ratio (Yung et al. 1988; Kass et al. 1999). Much research also focused on varying model parameters such as diffusion constants, reaction rate coefficients, boundary conditions, and so forth, and comparing the results with data from the Mariner and Viking missions, in attempts to understand the processes likely to be occurring in the atmosphere (e.g. V. A. Krasnopolsky et al. 1979; Nair et al. 1994).

Ionospheric chemistry has also been studied with photochemical models. Molina-Cuberos et al. (2002) considered ion-neutral reactions in the lower atmosphere. In the upper atmosphere and ionosphere, topics have included carbon escape (Fox et al. 2001a; Fox 2004; Lo et al. 2020, 2021, 2022), the importance of H_2 (Fox 2003), oxygen escape (Fox 2009; Fox et al. 2009b), the chemistry of H-bearing (protonated) ions (Matta et al. 2013; Fox 2015) and water-group ions (Fox et al. 2015), and the impacts of certain important rate coefficients (Fox et al. 2017, 2021). Photochemical models have also been applied to early Mars to explore nitrogen chemistry (Adams et al. 2021).

A robust photochemical model lends itself easily to adaptation to other planets. Photochemistry has also been used to study Venus (Yung et al. 1982; Fox et al. 2001b; Liang et al. 2009; Yung et al. 2009; V. A. Krasnopolsky 2012; X. Zhang et al. 2012; V. A. Krasnopolsky 2013; Bierson et al. 2020), Titan (V. A. Krasnopolsky 2014; M. L. Wong et al. 2015; Dobrijevic et al. 2016; Vuitton et al. 2019), Io (Kumar 1982; M. C. Wong et al. 1996, 2000; Moses et al. 2002; Smyth et al. 2004), Triton (V. A. Krasnopolsky et al. 1995), and Pluto (M. L. Wong et al. 2015, 2017; V. A. Krasnopolsky 2020).

1.5.2 Methodology of photochemical models

A photochemical model solves the standard production and loss (continuity) equation for each species:

$$\frac{\partial n_i}{\partial t} = -\frac{d\Phi_i}{dz} + P_i - L_i \tag{1.12}$$

Here, the change in a species density n over time is the sum of the rate of diffusive flux and the rate of chemical production and loss. The left side of the equation becomes the quantities which we solve for at each timestep of the model, and are used to update the primary tracked quantity, the species number density.

1.5.2.1 Chemistry

P_i and L_i represent the production and loss of species i due to photochemical interactions. Each term depends on the densities of reactants, making an atmospheric system become quite complicated very quickly. As an example, consider a simple pair of equations:

$$\mathrm{CO_2 + h\nu \rightarrow CO + O} \qquad J_1 \tag{1.13}$$

$$\mathrm{CO + O \rightarrow CO_2} \qquad k_1 \tag{1.14}$$

where J_1 and k_1 are rate coefficients, units $\mathrm{s^{-1}}$ and $\mathrm{cm^3s^{-1}}$ respectively. From this most basic chemical system of the Mars atmosphere, we can write the differential equations for the rates of change of each species listed (chemistry only—i.e., $P_i - L_i$):

$$\left.\frac{dn_{\mathrm{CO2}}}{dt}\right|_{\mathrm{chem}} = k_1 n_{\mathrm{CO}} n_{\mathrm{O}} - J_1 n_{\mathrm{CO2}}$$
$$\left.\frac{dn_{\mathrm{CO}}}{dt}\right|_{\mathrm{chem}} = J_1 n_{\mathrm{CO2}} - k_1 n_{\mathrm{CO}} n_{\mathrm{O}}$$
$$\left.\frac{dn_{\mathrm{O}}}{dt}\right|_{\mathrm{chem}} = J_1 n_{\mathrm{CO2}} - k_1 n_{\mathrm{CO}} n_{\mathrm{O}}$$

Chemical production is represented by the positive terms, and loss by the negative terms. These terms fill in the P and L terms in equation 1.12, and are calculated in every atmospheric grid cell of width Δz.

1.5.2.2 Transport

In 1D photochemistry, complex fluid dynamics are typically not modeled. Horizontal transport is not possible due to the dimensionality of the model. Thus, In photochemical models, vertical transport is usually parameterized using a variety of diffusion methods, including eddy, molecular, and ambipolar diffusion, which are captured in the diffusion coefficients K (eddy) and D (molecular and ambipolar). The 1D diffusion equation is (Banks et al. 1973; Chaffin et al. 2017):

$$\Phi = -(D+K)\frac{\partial n}{\partial z} - n\left[D\left(\frac{1}{H_s} + \frac{1+\alpha}{T}\frac{dT}{dz}\right) + K\left(\frac{1}{H_a} + \frac{1}{T}\frac{dT}{dz}\right)\right] \tag{1.15}$$

Where ϕ is the upward flux, n is the density, D the molecular diffusion coefficient, K the eddy diffusion coefficient, z is altitude, H_s is the species-specific scale height, α the thermal diffusion factor, T the temperature H_a the mean scale height of the atmosphere. Equation 1.15 must be discretized for computation, so we can define a flux ϕ_i from a cell with density n_i into the cell above with density n_{i+1}, in a model where the altitude grid has a step size of Δz:

$$\phi_i = -(D+K)\frac{n_{i+1}-n_i}{\Delta z} - \left[D\left(\frac{1}{H_s}+\frac{1+\alpha}{T}\frac{dT}{dz}\right)+K\left(\frac{1}{H_a}+\frac{1}{T}\frac{dT}{dz}\right)\right]\left(\frac{n_{i+1}-n_i}{2}\right) \tag{1.16}$$

Grouping terms and assigning the large square parenthetical to the symbol $\square$:

$$\phi_i = n_{i+1}\left(-\frac{D+K}{\Delta z}-\frac{\square}{2}\right)+n_i\left(-\frac{D+K}{\Delta z}-\frac{\square}{2}\right) \tag{1.17}$$

Now, to get it into the correct units so that we can incorporate it into equation 1.12, we take the negative of its derivative with respect to z:

$$\left.\frac{\partial n}{\partial t}\right|_{\text{transport}} = -\frac{\partial \phi}{\partial z} = -\frac{(\phi_i-\phi_{i-1})}{\Delta z} \tag{1.18}$$

And the final expression that can be incorporated into equation 1.12 is:

$$\begin{aligned}\left.\frac{\partial n}{\partial t}\right|_{\text{transport}} = -\frac{\partial \phi}{\partial z} = n_{i+1}\left(\frac{D_i+K_i}{\Delta z^2}+\frac{\square_i}{2\Delta z}\right)+n_i\left(\frac{-D_i+K_i}{\Delta z^2}+\frac{\square_i}{2\Delta z}\right)\\ + n_i\left(-\frac{(D_{i-1}+K_{i-1})}{\Delta z^2}-\frac{\square_{i-1}}{2\Delta z}\right)+n_{i-1}\left(\frac{D_{i-1}+K_{i-1}}{\Delta z^2}-\frac{\square_{i-1}}{2\Delta z}\right)\end{aligned} \tag{1.19}$$

The first two terms represent the transport at the upper boundary of the grid cell, and the second two the transport at the lower boundary of the cell.

Once discretized, these equations can be solved using a variety of differential equation integrators. The system is stiff, so the choice of integrator should account for this; for the purposes of this thesis, I use a custom Gear method first implemented by Chaffin et al. (2017). As the equations are solved, the model produces a final output in the form of species number densities vs. altitude. Typically, photochemical modeling results show the altitude or pressure on the y-axis, while the x-axis shows either the mixing ratio or the number density. This provides an intuitive “vertical profile” view of the atmosphere.

The parameters of the photochemical model used for this thesis are given in Tables 1.4 and 1.5.

	Chapter 2	Chapter 3 & Chapter 4
Neutrals	Ar, CO, CO_2, D, DO_2, DOCO, H, H_2, H_2O, H_2O_2, HD, HDO, HDO_2, HO_2, HOCO, N_2, O, $O(^1D)$, O_2, O_3, OD, OH	Same as left, plus: C, DCO, HCO, N, NO, $N(^2D)$
Ions	CO_2^+	ArD^+, ArH^+, Ar^+, CH^+, CO_2^+, CO^+, C^+, DCO_2^+, DCO^+, DOC^+, D^+, H_2DO^+, H_2D^+, H_2O^+, H_2^+, H_3O^+, H_3^+, HCO_2^+, HCO^+, HDO^+, HD^+, HNO^+, HO_2^+, HOC^+, H^+, N_2D^+, N_2H^+, N_2^+, NH^+, NO^+, N^+, O_2^+, OD^+, OH^+, O^+
Fixed background species	CO_2^+, H_2O, HDO, Ar, N_2	Ar
Spatial grid	0-250 km, dz=2 km	0-250 km, dz=2 km
SZA	60°(Dayside mean)	60°(Dayside mean)
Chemistry	110 reactions: 24 photodissociation, 83 neutral-neutral, 3 ion-neutral	606 reactions: 33 photodissociation, 29 photoionization, 147 neutral-neutral, 397 ion-neutral
Electron density	None	Quasineutral (sum of ion density)
Photochemical equilibrium	None	Optional (not used)
Escape types	Thermal Jeans escape	Thermal: Jeans escape; Non-thermal: photochemical
Escaping species	H, D, H_2, HD, O	H, D, H_2, HD, O

Table 1.4: Basic parameters of the photochemical model used in this thesis. Substantial upgrades were made to the model between Chapters 2 and 3.

1.5.3 bluejay, a fully coupled ion-neutral photochemical model

A substantial amount of the work of this thesis went into developing a model that could be used to address the research questions described below in Section 1.6. Most of the details of this work are also available in chapters 2–3, but the highlights will be repeated here for clarity and to set the stage. The model, bluejay, was not named until chapter 3 was accepted for publication, so after this section, the name will not appear until that chapter.

For chapter 2, I extended the model originally built by Chaffin et al. (2017) to incorporate deuterium chemistry. This was sufficient to do simulations of neutral chemistry and study the fractionation factor for neutral Jeans escape.

In order to model non-thermal escape sourced from Mars' ion-neutral reactions, bluejay needed to support a self-consistent ionosphere (previous versions had only parameterized a background profile of CO_2^+). Because I wanted to capture the behavior of H and D from the surface to the exobase, it also needed to be able to model from 0–250 km. The fact that H is already a minor species, and D even more minor than that, demanded as high a degree of accuracy as possible for the calculation. Much of the development of bluejay between chapters 2 and 3 consisted of:

- hunting down ionospheric reactions, especially for deuterated species, for which not many are available;
- incorporating ambipolar diffusion, which is a straightforward equation but required the addition of the polarizability constant; and
- addressing the calculation challenges of ions and neutrals (see Figure 1.14b), since ion densities fall to near zero below about 80 km, posing problems for floating point arithmetic and the numerical stability of bluejay.

All of the above modifications, plus the large number of species and reactions, meant that bluejay became computationally intensive, even for a 1D model; a typical size of the chemical Jacobian matrix, which is used to invert the system of equations to obtain a solution, is 6×10^7

Species	Surface density (cm^{-3})	Surface flux (cm^{-2}s^{-1})	Upper boundary flux[a] (cm^{-2}s^{-1})	Upper boundary velocity[b] (cm/s)
CO_2	2.1×10^{17}	-	0	-
Ar	$2.0 \times 10^{-2}(n_{\mathrm{CO2}})$	-	0	-
N_2	$1.9 \times 10^{-2}(n_{\mathrm{CO2}})$	-	0	-
H_2O	$1.3 \times 10^{-4}(n_{\mathrm{CO2}})$	-	0	-
HDO[c]	$R_{dh}(1.3 \times 10^{-4})(n_{\mathrm{CO2}})$	-	0	-
O	-	0	1.2×10^{8}	-
H	-	0	$\phi = \mathrm{P_{esc} r_H}$	$\mathrm{v_{eff,H}}$
D	-	0	$\phi = \mathrm{P_{esc} r_D}$	$\mathrm{v_{eff,D}}$
H_2	-	0	$\phi = \mathrm{P_{esc} r_{H2}}$	$\mathrm{v_{eff,H2}}$
HD	-	0	$\phi = \mathrm{P_{esc} r_{HD}}$	$\mathrm{v_{eff,HD}}$

[a] O escape is fixed at the value indicated. H, D, H_2 and HD fluxes are calculated as the production rate r of suprathermal atoms and their probability of escape P (Gregory et al. 2023a), which is a function of the overhead atmospheric column at any given moment. See Chapter 3 for more.

[b] The effusion velocity (Hunten 1973) is multiplied by the density of each species at the exobase to calculate the thermal escape.

[c] Density boundary condition is the same as H_2O, multiplied by R_{dh}, the D/H ratio ($5.5(1.6 \times 10^{-4})$).

Table 1.5: Boundary conditions used in this thesis

elements. Much work also thus went into improving its efficiency and speed: vectorization of functions, optimization of metaprogramming (auto-created code; mostly used for symbolic algebra to solve the system of equations), creating the most efficient and accurate possible chemical Jacobian, and optimizing use of built-in functions and data types.

By the end of peer review for chapter 3, it was becoming awkward to constantly refer to “the model”. Many name candidates were proposed before settling on bluejay. The short story can be read in the README file of the GitHub repository E. M. Cangi et al. (2022).

No significant updates to bluejay occurred between chapters 3 and 4, except for an adjustment to timesteps saved in order to simulate a seasonal cycle while obtaining output at specified cadences (one second, one minute, one hour, half a day, one day, and then every week until the end of a season).

1.5.3.1 Key inputs and outputs of bluejay

Key inputs are listed below. As with any open-source software, all are technically modifiable, but an asterisk (*) designates the inputs that are easiest to modify without significant code-wrangling.

- *Temperatures at the surface, mesosphere, and exobase (which control the functional form of the temperature profile)
- *Water vapor mixing ratio at the surface
- *Amount and altitude of extra water parcels
- *Solar input (flux as a function of wavelength)
- Photodissociation and ionization cross sections
- Molecular diffusion coefficients
- Neutral polarizability

- Escape probability of hot atoms
- *Chemistry reaction rate coefficients

Key outputs and analysis capabilities as used in this thesis are as follows.

- Species densities by altitude
- Thermal escape of neutral H, D, H_2, HD
- Non-thermal escape of suprathermal, neutral H, D, H_2, HD

In addition to these quantities, model output can also be used to calculate the fractionation factor and the total reaction rates for each included chemical reaction. In principle, this means that the fate of atoms like H and D that do not escape can also be characterized—i.e., the rate of recombination into water or other species, although this rate of reincorporation will not be discussed in this thesis.

1.6 Research questions of this thesis

The overarching themes of this thesis are as follows:

(1) What are the controls on the value of the D/H fractionation factor and its variability?

(2) Could the discrepancy in integrated water loss calculated by photochemical models and geomorphological assessments be resolved with a better understanding of D escape?

(3) What is the relative balance of thermal and non-thermal escape of D and H under present atmospheric conditions?

Each of the chapters of this thesis are an individual paper that I wrote during my time in the PhD program, and collectively address the questions above. Here, the research questions are collected for ease of reference.

Chapter 2 research questions

- How does the temperature in different parts of the atmosphere affect the D/H fractionation factor?
- How does the total water vapor content of the atmosphere affect the D/H fractionation factor?

Chapter 3 research questions

- What is the make up of the deuterated ionosphere, and how does it compare to the H-bearing ionosphere?
- What is the balance of thermal and non-thermal escape of H and D?
- What are the dominant mechanisms that control production of non-thermal ("hot") D?
- Is the non-thermal escape of deuterium large enough to close the gap between water loss estimates by atmospheric models and geomorphological studies?

Chapter 4 research questions

- How do temperatures and water vapor affect the atomic D/H ratio?
- How does the atomic D/H ratio vary throughout the martian year?
- How do H and D escape vary throughout the martian year?

Chapter 2

Higher Martian Atmospheric Temperatures at All Altitudes Increase the D/H Fractionation Factor and Water Loss

The contents of this chapter were originally published as E. M. Cangi et al. (2020).

Two small citation errors in the published paper have been replaced below:

- The original paper cited Lammer et al. (2003a) and M. D. Smith (2004) for the mean atmospheric water abundance of 10 precipitable micrometers. The correct citation is Jakosky et al. (1982) and M. D. Smith (2004).
- The original paper cited Lammer et al. (2003a) for the water loss used in Figure 2.9. The correct citation is Lammer et al. (2003b) for the low end (12 m GEL) and Lammer et al. (2003a) for the high end (34 m GEL).

One descriptive error has been corrected also: the original paper claimed that Lammer et al. (2003a) assumed 3.3–15 m GEL for the current water inventory. Actually, this was a calculation result of the paper, and what they assumed was the aforementioned 12–34 m GEL of lost water.

2.1 Abstract

Much of the water that once flowed on the surface of Mars was lost to space long ago, and the total amount lost remains unknown. Clues to the amount lost can be found by studying hydrogen (H) and its isotope deuterium (D), which are produced when atmospheric water molecules H_2O and HDO dissociate. The difference in escape efficiencies of H and D (which leads to an enhanced D/H

ratio) is referred to as the fractionation factor f. Both the D/H ratio and f are necessary to estimate water loss; thus, if we can constrain the range of f and understand what controls it, we will be able to estimate water loss more accurately. In this study, we use a 1D photochemical model of the neutral Martian atmosphere to determine how f depends on assumed temperature and water vapor profiles. We find that the exobase temperature most strongly controls the value of f for thermal escape processes. When we include estimates of non-thermal escape from other studies, we find that the tropopause temperature is also important. Overall, for the standard Martian atmosphere, $f = 0.002$ for thermal escape, and $f = 0.06$ for thermal + non-thermal escape. We estimate that Mars has lost at minimum 66-122 m GEL of water. Importantly, our results demonstrate that the value of f depends critically on non-thermal escape of D, and that modeling studies that include D/H fractionation must model both neutral and ion processes throughout the atmosphere.

2.2 The D/H Fractionation Factor and Loss of Martian Water to Space

The surface of Mars is marked with ample evidence of its wetter past. Today, water on Mars exists only in the polar caps, subsurface ice, and atmosphere, but geomorphological and geochemical evidence points to significant alteration of the surface by liquid water. The presence of compounds like jarosite and hematite indicate past pooling and evaporation (Klingelhöfer et al. 2004; Squyres et al. 2004), while substantial evidence of hydrated silicates supports the theory that ancient river deltas, lake beds, catastrophic flood channels, and dendritic valley networks were formed by water (M. H. Carr et al. 2010; Ehlmann et al. 2014, and references therein). Because the contemporary Martian climate cannot support liquid water on the surface, Mars must have once had a thicker and warmer atmosphere. The Mars science community generally agrees that the atmosphere has escaped over time, with a significant amount integrated atmospheric escapethis has effectively desiccated the planet (Jakosky et al. 2018).

A significant indicator of this loss of water to space is the elevated D (deuterium, ^{2}H or D) to H (hydrogen, ^{1}H) ratio, which we will abbreviate as R_{dh}. Because water (either as H_2O or HDO) is the primary reservoir of both H and D, when we talk about the D/H ratio, we are thus usually referring to D/H measured in water:

$$R_{dh} = \frac{\text{D in HDO}}{\text{H from HDO} + \text{H from H}_2\text{O}} = \frac{[HDO]}{[HDO] + 2[H_2O]} \approx \frac{[HDO]}{2[H_2O]} \tag{2.1}$$

Here, $[X]$ represents a molecule's abundance; H sourced from HDO is negligible compared to H sourced from H_2O. This ratio evolves according to differential escape of D and H; D, being twice as massive as H, is less likely to escape. This difference can be characterized as a relative efficiency, the fractionation factor f:

$$f = \frac{\phi_{\text{D}}/\phi_{\text{H}}}{[HDO]_s/2[H_2O]_s} = \frac{\phi_{\text{D}}/\phi_{\text{H}}}{R_{dh,s}} \tag{2.2}$$

where ϕ represents fluxes to space, and the s subscript specifies the near-surface atmospheric reservoir, which approximates the total amount in the atmosphere. As it represents efficiency of D escape, f takes on values between 0 and 1. When f is 0, D is completely retained on the planet, and cumulative water loss must have been lower than for $f \neq 0$. When $f = 1$, the *ratio* of escaping to retained atoms is the same for both D and H, and there is no mass effect on the escape rates. In this scenario, no amount of escape is sufficient to change the D/H ratio in any species. In practice, f is somewhere in between these extremes.

Over geologic time, this fractionation manifests as an enhancement of the D/H ratio compared to the Earth ratio of 1.6×10^{-4} (Yung et al. 1988), called SMOW (for the measured source, Standard Mean Ocean Water). A planet's D/H ratio is often quoted as a multiple of the Earth value. At present, multiple measurements put the global mean R_{dh} on Mars between 4 and 6 × SMOW (Owen et al. 1988; Bjoraker et al. 1989; V. Krasnopolsky et al. 1997; Encrenaz et al. 2018; Vandaele et al. 2019), with some variations occurring on local spatial and temporal scales (Villanueva et al. 2015; Clarke et al. 2017; Encrenaz et al. 2018; Clarke et al. 2019; Villanueva et al. 2019). This is most commonly interpreted as evidence for significant escape to space of H.

To estimate the integrated amount of water lost, one can use current estimates of the Martian water inventory, R_{dh}, and f with the Rayleigh distillation equation for H (Yung et al. 1998):

$$R_{dh}(t) = R_{dh}(t=0)\left(\frac{[H](0)}{[H](t)}\right)^{1-f}, \tag{2.3}$$

where $t = 0$ can be arbitrarily chosen. Because we use R_{dh} and because water is the primary reservoir of H on Mars, [H] is commonly replaced with total water W (W = [H_2O] + [HDO]). Then $W(0)$, the total water on Mars at some point in the past $t = 0$, is the sum of the water budget at time t and the total water lost: $W(0) = W(t) + W_{textlost}$. Substituting W for [H] and rearranging equation 2.3, we obtain an expression for water lost from Mars:

$$W_{\text{lost}} = W(t)\left(\left(\frac{R_{dh}(t)}{R_{dh}(0)}\right)^{1/(1-f)} - 1\right) \tag{2.4}$$

Most of the inputs to Equation 2.4 are well-described. The current D/H ratio of exchangeable water (the atmosphere, seasonal polar caps, ground ice, and water adsorbed in the regolith), $R_{dh}(t)$, is $4 - 6\times$ SMOW as mentioned (we use 5.5 in this study). $R_{dh}(0)$ is usually taken to be that at Mars' formation, when it would have been similar to the Earth's D/H ratio (Geiss et al. 1981); R_{dh} at other points in time can be obtained from meteorite samples (Usui et al. 2012, e.g.) or in-situ analysis (Mahaffy et al. 2015a, e.g.). The current water inventory in exchangeable reservoirs, $W(t)$, is estimated to be between 20-30 m GEL (global equivalent layer), the depth of water if the entire exchangeable inventory were rained onto the surface (Zuber et al. 1998; Plaut et al. 2007; Lasue et al. 2013; Villanueva et al. 2015; M. Carr et al. 2019).

Prior studies estimated the fractionation factor f, but its range of values under all plausible scenarios has been largely unexplored. Yung et al. (1988) used a 1D photochemical model to calculate a first value of $f = 0.32$ which has been frequently referenced in the years since. They explored the effects of certain chemical reactions on f, but did not test other parameters. V. A. Krasnopolsky et al. (1998) obtained $f = 0.02$ by combining Hubble Space Telescope observations with a radiative transfer and 1D photochemical model. Later, V. Krasnopolsky (2000) followed up with another study that tested the effects of two different models of eddy diffusion, finding values of $f = 0.135$ and $f = 0.016$. Two years later, V. A. Krasnopolsky (2002) found 3 values for f, depending on whether the solar cycle was at minimum ($f = 0.055$), maximum ($f = 0.167$), or mean ($f = 0.082$), represented in the model by variation of the exobase temperature and non-thermal escape flux. Our goal is to advance this body of work by performing the first systematic parameter-space study of the fractionation factor with respect to the assumed atmospheric temperature and water vapor profiles.

2.3 Building Our 1D Photochemical Model

To best capture the mean behavior of the Martian atmosphere over long time scales, we use a 1D photochemical model, extended from the original developed by Chaffin et al. (2017) to include D chemistry. The model uses standard photochemical techniques described in other studies (V. Krasnopolsky 1993; Nair et al. 1994; Chaffin et al. 2017), with the addition of the D-bearing species D, HD, HDO, OD, HDO_2, DO_2, and DOCO. The chemical reactions for D-bearing species came from several sources, including past papers (Yung et al. 1988, 1989; Cazaux et al. 2010; Deighan 2012), NASA publications (Sander et al. 2011), and online databases (D. McElroy et al. 2013; Manion et al. 2015; Wakelam et al. 2019). The full list of chemical reactions and reaction rates, as well as details on implemented photochemical cross sections (Barfield et al. 1972; Nee et al. 1984; B.-M. Cheng et al. 1999; B. M. Cheng et al. 2004) and diffusion coefficients (Banks et al. 1973), is given in Appendix A. Photodissociation is driven by solar UV irradiation data from SORCE/SOLSTICE and TIMED/SEE (Woods et al. 2019), appropriate for solar mean conditions and scaled to Mars' orbit. For our primary input, we construct temperature and water vapor profiles designed to represent end-member states of the atmosphere, such that we fully constrain the range of plausible fractionation factor values.

A run of the model consists of the following steps: (1) loading the temperature and water vapor profiles, (2) establishing an initial condition of species number densities, (3) establishing boundary conditions (Table A.3), and (4) stepping forward over 10 million years of simulation time until the atmosphere reaches chemical equilibrium, which is achieved when the combined escape flux of atomic H and D ($\phi_{\mathrm{H}} + \phi_{\mathrm{D}}$) is twice that of the escape flux of atomic O (ϕ_O). (This stoichiometric balance is required because H and D are primarily sourced from water.) The model output comprises species number densities by altitude. By multiplying the H- and D-bearing atomic and molecular species densities by their thermal effusion velocities (Hunten 1973), we can calculate ϕ_{H} and ϕ_{D}:

$$\phi_{\mathrm{H}} = n_{\mathrm{H}}v_{\mathrm{H}} + 2n_{\mathrm{H_2}}v_{\mathrm{H_2}} + n_{\mathrm{HD}}v_{\mathrm{HD}} \tag{2.5}$$

$$\phi_{\mathrm{D}} = n_{\mathrm{D}}v_{\mathrm{D}} + n_{\mathrm{HD}}v_{\mathrm{HD}} \tag{2.6}$$

These fluxes are then used to calculate f according to equation 2.2.

A limitation of our model is that we do not include a full ionosphere. Instead, we approximate it by including a static profile of $\mathrm{CO_2^+}$ (Matta et al. 2013), enabling the primary H-producing ion reaction in the Martian atmosphere; a similar tactic was used by Yung et al. (1988). Without a full ionosphere, we are not able to model non-thermal escape of H or D, as most non-thermal processes depend on ions. In an effort to estimate the relative importance of non-thermal processes to the fractionation factor, we estimate non-thermal effusion velocities for our model conditions, scaled from V. A. Krasnopolsky (2002), described further in Section 2.4.

2.3.1 Reproductions of Past Studies

Before proceeding with our study, we attempted to reproduce the results by Yung et al. (1988) and V. A. Krasnopolsky (2002). Their original results and our reproductions are shown in Figure A.3. We achieved very good agreement with the results by Yung et al. (1988), finding $f = 0.26$ versus their $f = 0.32$. The small difference is due to the only two differences between the model by Yung et al. (1988) and ours. First, Yung et al. (1988) manually fix their photodissociation rates, whereas our model calculates them. Second, they adopt the water profile used by Liu et al. (1976), fixing it below 80 km and allowing it to vary above, whereas we fix it throughout the atmosphere. Our results for f were consistent with V. A. Krasnopolsky (2002) for solar maximum, but comparatively low for solar mean and minimum. We expect that this is because their model includes an ionosphere, allowing them to model non-thermal escape. To account for this, we added their results for non-thermal escape of D to our results for thermal escape, resulting in a slight overestimate instead of an underestimate. This change was a first hint at the importance of non-thermal escape to f. The remaining discrepancy is due to other significant model differences, irreconcilable without rewriting our model; for example, their model atmosphere has its lower bound at 80 km, while ours is at the surface. This difference in model extent means that our two models also have significant differences in temperature structure and boundary conditions.

2.3.2 Model input: Temperature and Water Vapor Profiles

Our temperature and water vapor vertical profiles remain fixed for the duration of a simulation. This allows us to examine the mean behavior of the atmosphere over long time scales.

2.3.2.1 Temperature Profiles

The piecewise temperature profile is modeled with equation 2.7. The general form is based on measurements by the Viking orbiters (Seiff 1982), and similar models have been used in other studies (e.g. M. B. McElroy et al. 1977; Nair et al. 1994; V. A. Krasnopolsky 2010). In the lower atmosphere, the temperature decreases with altitude according to the dry adiabatic lapse rate Γ. At the tropopause (altitude z_t), temperature reaches a minimum and remains isothermal in the mesosphere. Above the mesopause (120 km), upper atmospheric density is low enough that UV heating is efficient, causing the temperature to increase rapidly with altitude.

$$T = \begin{cases} T_{\text{exo}} - (T_{\text{exo}} - T_{\text{tropo}}) \exp\left(-\frac{(z-120)^2)}{(8T_{\text{exo}})}\right) & z > 120 \text{ km} \\ T_{\text{tropo}} & z_t < z < 120 \text{ km} \\ T_{\text{surf}} + \Gamma z & z < z_t \end{cases} \tag{2.7}$$

We constrain this modeled profile with the temperatures at the surface (T_{surf}), tropopause (T_{tropo}), and exobase (T_{exo}). Constraining the temperature at these three points requires either Γ or z_t to vary; if they are both fixed, the profile will be over-constrained and discontinuous. We allow z_t to vary as it does in reality (e.g. Forget et al. 2009) exactly what sets its altitude is less well defined than the dynamics of gas and dust, on which Γ depends. We use $\Gamma = -1.4$ K/km, which is slightly lower than the standard dry adiabatic lapse rate due to warming effects from suspended dust (Zahnle et al. 2008).

For the first part of the study, we constructed a standard temperature profile representing current conditions on Mars, as well as 6 alternate profiles intended to represent plausible climate extrema driven by changing planetary obliquity throughout the last ~10 million years of Mars' history, the maximum time over which obliquity evolution can be analytically predicted. (On longer time scales, the obliquity evolves chaotically, making precise definition of climate parameters impossible (Laskar et al. 2004).) We used the Mars Climate Database (MCD) (Millour et al. 2018) to obtain values for T_{surf} ($z = 0$), T_{tropo} ($z = 100$ km), and T_{exo} ($z = 250$ km) for different times of sol (local times 03:00, 09:00, 15:00, 21:00), Mars latitude (90°N, 45°N, 0°, 45°S, 90°S), and L_s (90°and 270°), then compared the mean temperatures across each of these parameters with data from multiple missions to ensure consistency. The surface temperature was compared with the Curiosity Rover (Audouard et al. 2016; Vasavada et al. 2016; Savijärvi et al. 2019), Mars Global Surveyor Thermal Emission Spectrometer (TES) (M. D. Smith 2004), and the Spirit/Opportunity Rovers' Mini-TES (M. D. Smith et al. 2006); the exobase temperature was compared with MAVEN data from multiple instruments (Bougher et al. 2017; Stone et al. 2018; Thiemann et al. 2018). The mean temperatures formed the standard profile, shown in Figure 2.1a. Figure 2.1b shows the 6 alternate profiles, in which we varied one of T_{surf}, T_{tropo}, or T_{exo} by ±25% of the standard value. This variation covers most values observed by current missions, as well as temperatures calculated (R. D. Wordsworth et al. 2015) for obliquities of ~25–45°predicted for the last 10 million years (Laskar et al. 2004). A table with the control temperatures for each profile is available in Appendix A. Together, the standard and alternate temperature profiles represent end-member cases for the Martian atmosphere.

In addition to these select profiles, we also created a larger set of temperature profiles with finer variation in each of T_{surf}, T_{tropo}, or T_{exo} to examine the details of how each parameter affects

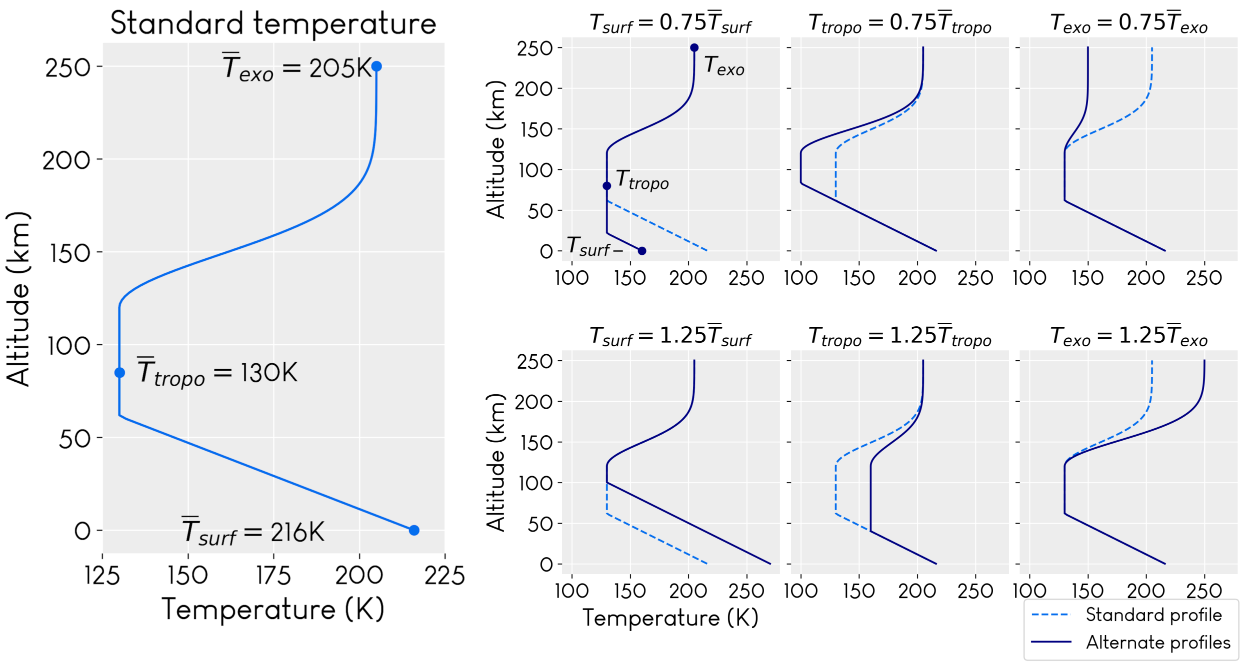

Figure 2.1: a) Our standard temperature profile used in the model, and b) alternate temperature profiles representing plausible climate extrema due to obliquity variations. Profiles are created by modifying the standard temperatures $\overline{T}_{\text{surf}}$, $\overline{T}_{\text{tropo}}$, or $\overline{T}_{\mathbf{exo}}$ by ±25%. We do not consider effects of CO_2 condensation for cold temperatures, although this would be important in real atmospheres. These profiles, along with the standard profile, are used to obtain the results in Figure 2.4. Table A.4 gives specific values for T_{surf}, T_{tropo}. T_{exo}.

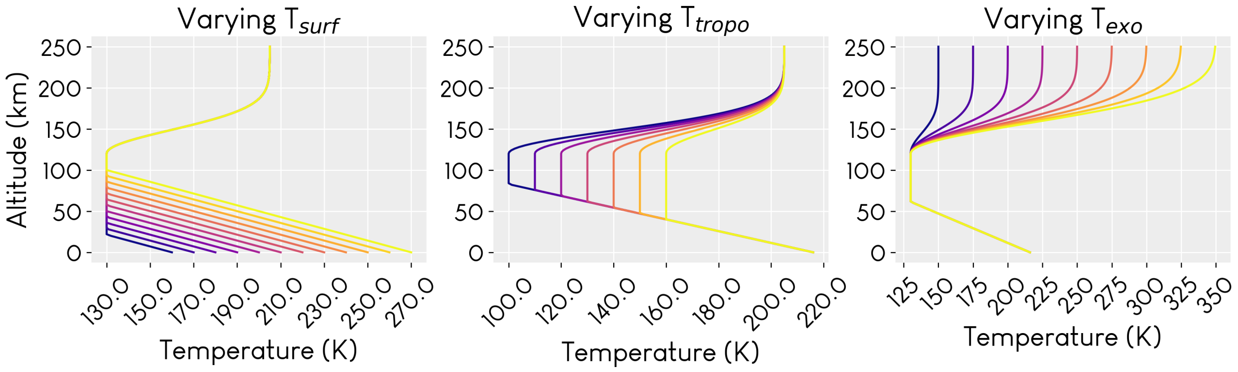

Figure 2.2: The full range of temperature profiles tested. Each panel represents a set of profiles in which one of the specifiable temperatures was varied. Results from the simulations using these profiles are shown in Figure 2.5. Each color represents a different profile.

f. This set of temperature profiles is shown in Figure 2.2.

2.3.2.2 Water Profiles

H_2O and HDO profiles used in the model are shown in Figure 2.3. We require that the profiles have total water content (H_2O + HDO) equal to 1, 10, 25, 50, or 100 pr μm (precipitable micrometers), with H_2O making up most of the share. Higher concentrations of water vapor would require a supersaturated atmosphere; while there is observational evidence of supersaturation at upper altitudes in specific cases (Maltagliati 2011; A. A. Fedorova et al. 2020), our model does not include it. We use the 10 pr μm profile to represent the long-term standard atmosphere, a value in agreement with observations (Jakosky et al. 1982; M. D. Smith 2004), although more recent observations (Heavens et al. 2018; Vandaele et al. 2019) and modeling (Shaposhnikov et al. 2019) suggest that local water vapor concentrations can reach higher values, up to 150 pr μm, on very short timescales, particularly during dust storms. We assume that the lower atmosphere is well-mixed, such that the water vapor mixing ratio is constant. At the hygropause, usually between 25 and 50 km (V. Krasnopolsky 2000; Heavens et al. 2018), water begins to condense, and its mixing ratio follows the saturation vapor pressure curve until it becomes negligible in the upper atmosphere (Heavens et al. 2018). Although HDO preferentially condenses compared to H_2O (Montmessin et al. 2005), it never approaches saturation in our model atmosphere, allowing us to use the same empirical saturation vapor pressure equation (Marti et al. 1993) for both H_2O and HDO. This is helpful, as no empirical equation for HDO exists, and the enthalpies of HDO under Mars-like conditions are very sparsely studied.

Although observations (Villanueva et al. 2015) and modeling (Fouchet et al. 1999; Bertaux et al. 2001) have shown that atmospheric D/H varies between 1-10× SMOW depending on the species it is measured in, altitude, and latitude/longitude, we tested these variations and determined that they had no effect on our results. We therefore multiply the initial profiles of H-bearing species by the D/H ratio of 5.5× SMOW to create the D-bearing profiles. The number densities of H_2O and HDO remain fixed during the simulation to represent the standard water abundance, though they are used to calculate chemical reaction rates.

2.4 Results: Temperature Variations and Non-thermal Escape Critical to Understanding the Fractionation Factor

Figure 2.4 shows the range of the fractionation factor as a function of each temperature and water vapor parameter, using the temperature profiles in Figure 2.1 and the water vapor profiles in Figure 2.3. Results for the broad range of temperatures shown in Figure 2.2 are discussed in Section 2.4.1.

For thermal escape only, we find that f is 1-3 orders of magnitude lower than the original value by Yung et al. (1988). The primary reason for this difference is the exobase temperature (they use 364 K, while we use a maximum of 250 K, which is more consistent with modern measurements). Other minor differences are as described in Section 2.3.1 Details of the dependence of f on each parameter are discussed in sections 2.4.1 and 2.4.2.

Because our model does not include an ionosphere, we do not model the effects of non-thermal escape processes (e.g. sputtering, photochemical escape), and only model thermal escape. This makes it difficult to compare with other studies which do include non-thermal escape (e.g. V. A. Krasnopolsky 2002). In order to compare with that study, we must estimate v_{nt}, the non-thermal escape velocity, which is not part of our model. To do so, we calculated the ratio of thermal to non-thermal effusion velocities ($r = v_t/v_{nt}$) for H, H_2, D, and HD in the model used by V. A. Krasnopolsky (2002). We then divided our v_t by the ratio r to get an estimate of non-thermal effusion velocities v_{nt} at the temperatures modeled by V. A. Krasnopolsky (2002): 200 K, 270 K, and 350 K. We extrapolated this estimate down to 150 K, the lowest temperature in our model, by fitting a 2nd order polynomial to the estimates for v_{nt}, allowing us to estimate the role that non-thermal escape plays in setting f for the temperature profiles shown in Figure 2.1. Though the estimation method is imperfect, it provides a rough estimation while avoiding unphysical velocity values at low temperatures, and gives values of f are consistent with V. Krasnopolsky (2000) and V. A. Krasnopolsky (2002), as well as more recent observations using MAVEN/IUVS (Clarke et al.

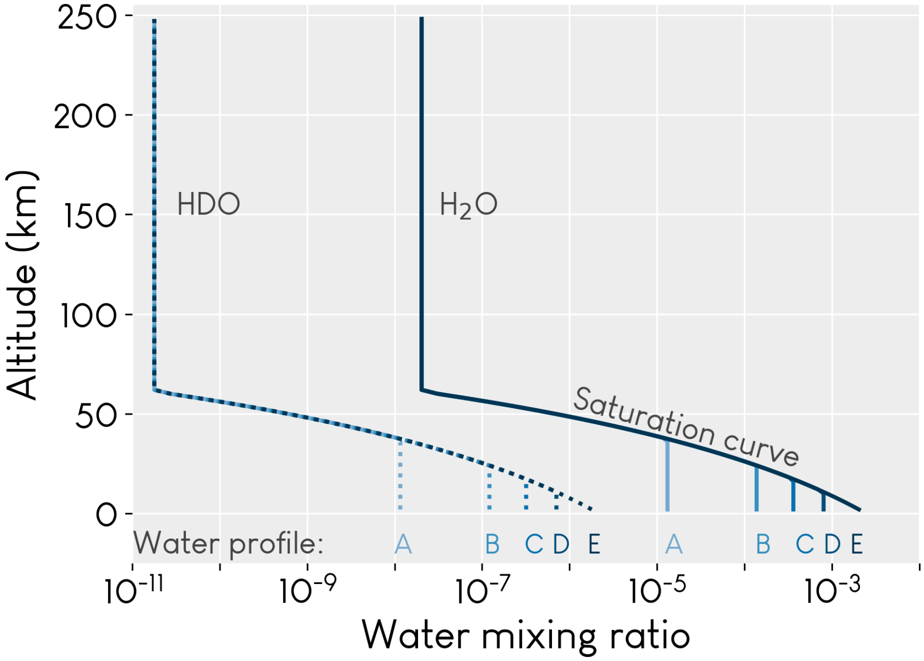

Figure 2.3: Water vapor profiles used in our model. A single profile, e.g. A, comprises both H_2O (solid lines) and HDO (dotted). Profiles are constrained by requiring that $[H_2O]+[HDO] = 1$ pr μm (profile A), 10 (B), 25 (C), 50 (D), or 100 (E) and that the HDO profile is equal to 5.5 × SMOW × the H_2O profile. Profiles differ in the well-mixed lower atmosphere and are the same once they reach the saturation vapor pressure curve. Water vapor in the mesosphere and upper atmosphere is negligible on average over long time scales, like those we model, although it may change on short time scales (see text). Profile B (10 pr μm) is used for our standard atmosphere.

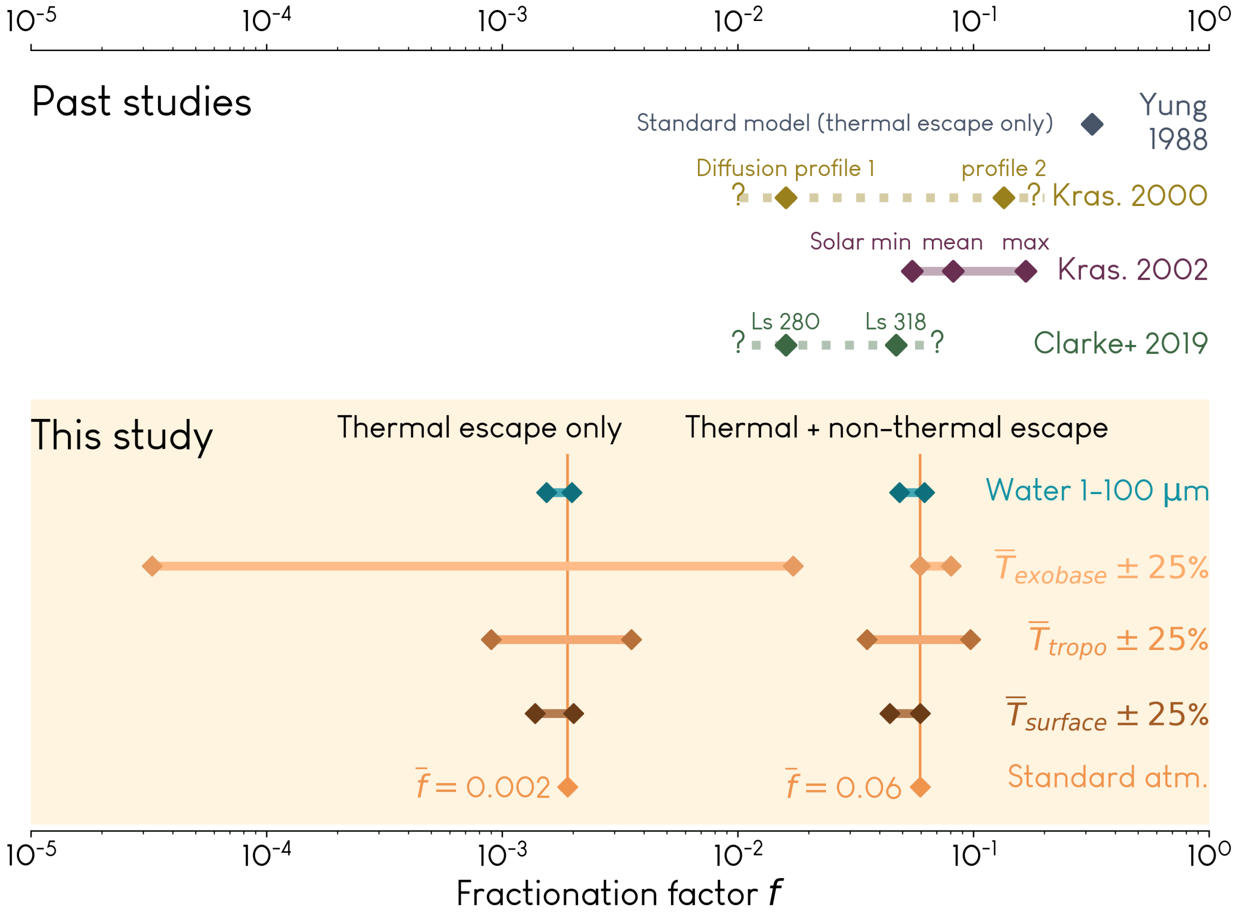

Figure 2.4: Results for the fractionation factor from this study (lower panel) and in past studies (upper panel). Bars represent the approximate range. Dotted lines with question marks indicate a study where the cases chosen did not necessarily represent end-member cases, so the true range is uncertain. Details of the dependence of f on temperatures and water vapor (orange and blue bars in lower panel) are shown in Figures 2.5 and 2.7. A numerical table of our results is available in Table A.5.

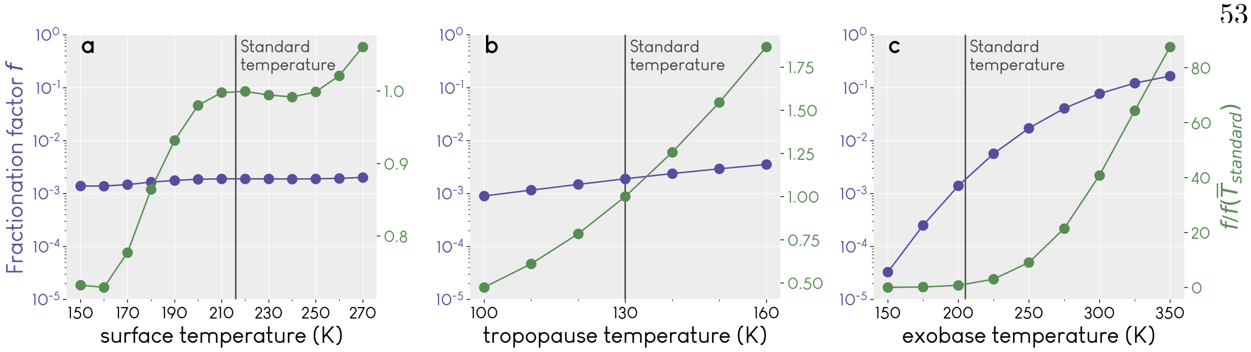

Figure 2.5: Dependence of the fractionation factor f on changes in the surface, tropopause, and exobase temperatures. The standard value of each is marked by a black vertical line. The left (purple) axis shows the value of f, while the right (green) axis shows the relative change of f with respect to that calculated for the standard temperature.

2019). Notably, our highest value of f is approximately a factor of 3 larger than the lowest, in agreement with V. A. Krasnopolsky (2002). In future work beyond the scope of this paper, we plan to directly model non-thermal contributions, enabling a better model comparison.

2.4.1 Fractionation Factor for Thermal Escape Strongly Controlled by Exobase Temperature

Figure 2.5 shows in detail how f varies with each temperature parameter for the modeled thermal escape only. This approach allows us to focus on what we can learn about f from our model, and refrain from drawing any strong conclusions about specific effects introduced by non-thermal escape before we can fully model it. The results show that an increase in temperature in any part of the atmosphere leads to an increase of f (less fractionation). The effect is small when the temperature increase occurs in the lower atmosphere, and dramatic when the change occurs at the exobase. Understanding this behavior requires examining the temperature-dependent behavior of H, D, H_2, and HD abundances and the escape fluxes ϕ_D and ϕ_H. This information is shown in Figure 2.6, where we plot these values for each simulation, normalized to the simulation with the standard atmosphere.

As a function of both surface and tropopause temperature, ϕ_D most closely tracks the abundance of atomic D at the exobase. Per equation 2.2, f depends directly on ϕ_D, inversely on ϕ_H, and

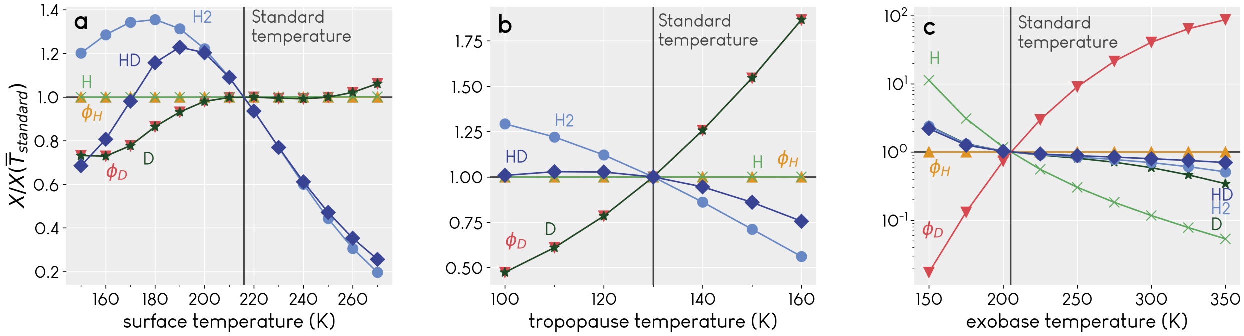

Figure 2.6: Change in exobase abundances of H- and D-bearing species or escape fluxes (ϕ) as a function of temperature for thermal escape only. ϕ_{H} and ϕ_{D} are calculated as in equations 2.5 and 2.6. In panels a and b, ϕ_{D} (and thus f in Figure 2.5a and b) closely tracks the abundance of atomic D. In panel c, changes in the abundance of H, D, H_2 and HD are caused by both escape to space and supply by diffusion from below. D is not diffusion limited, so ϕ_{D} responds more strongly to temperature forcing than H. Note the linear y-scale in panels a and b and the log scale in panel c. In all panels, ϕ_{H} is on the order of $\sim 10^8$ cm^{-2}s^{-1}, but differences between simulations are on the order of 10, making the relative variation of $\phi_{\mathrm{H}} \approxeq 1$.

inversely on $R_{dh,s}$. $R_{dh,s}$ is constant, and any reduction of ϕ_H is offset by an increase in ϕ_D because stoichiometric balance requires that $\phi_\mathrm{H} + \phi_\mathrm{D} = 2\phi_O$. This change is many orders of magnitude smaller than ϕ_H and thus not visible in Figure 2.6, but comparable to ϕ_D, making it easily visible. The increase of f with T_tropo is thus primarily because the higher temperatures in the mesosphere and thermosphere enable greater transport of D upwards. This response is possible because D is not diffusion-limited. Moderate increases in ϕ_D are a by-product of this effect (see Figure A.6), as the escaping population is proportional to the upper-atmospheric abundance of D. Transport into the mesosphere may also be slightly enhanced by increased T_surf, but the main role of T_surf is to drive the chemical reaction rates in the dense lower atmosphere, where they dominate over transport in controlling species abundances.

In contrast, the exobase temperature T_exo has a far greater effect on the value of f, with values ranging from 10^{-5} to 10^{-1}. This is unsurprising, as f directly depends on ϕ_D. Because thermal populations are assumed to be Maxwellian, we take the velocity in equations 2.5 and 2.6 to be the effusion velocity, which depends directly on T_exo. As T_exo rises, the warmer thermosphere to enable enhanced vertical transport of D. Escape of D is enhanced enough that ϕ_D no longer closely tracks the abundance of atomic D. To compensate for the increased loss of D while maintaining stoichiometric balance, ϕ_H must decrease by a negligible amount (see Figure A.7).

2.4.2 Fractionation Factor Depends Weakly on Water Vapor Column Abundance

The fractionation factor as a function of total water vapor is shown in Figure 2.7a, and the comparison of abundances and fluxes of H- and D-bearing species in Figure 2.7b. As in the previous section, the increase of f with additional water vapor is correlated with an increased abundance of D at the exobase, but also HD. The total water vapor has little effect on f, likely because the absolute abundance of water changes neither the D/H ratio in water or the processes by which it is fractionated. The small variation with respect to water vapor thus reflects the influence of minor differences in H_2O and HDO chemical and photochemical reactions. In order to more fully characterize the effects of water vapor on f, the model will have to be modified to allow variable

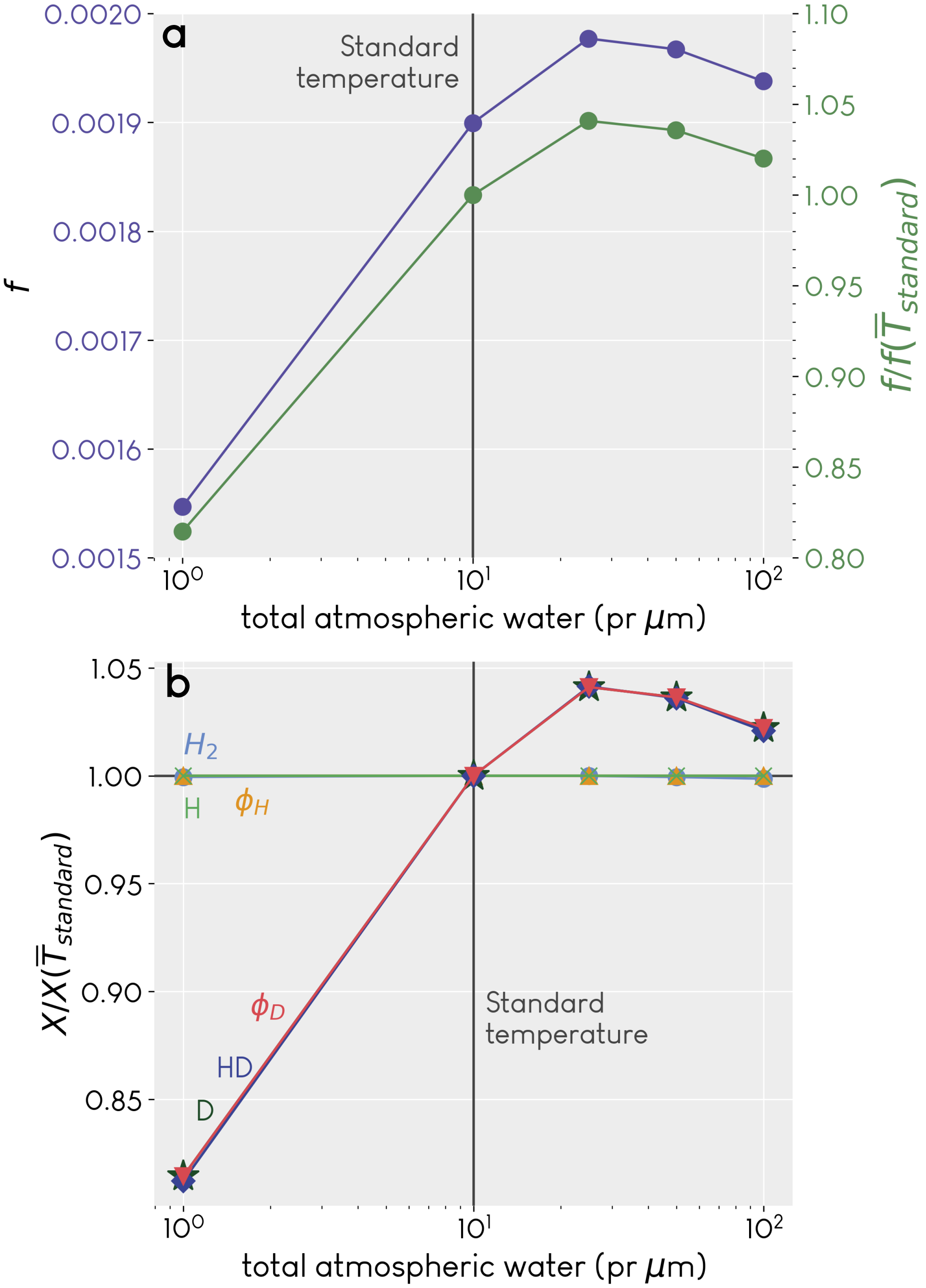

Figure 2.7: a) Fractionation factor f as a function of water vapor column abundance, shown for concentrations of 1, 10, 25, 50, and 100 pr μm, for thermal escape only. b) Same as Figure 2.6, but as a function of water vapor. Here, ϕ_D and f track the abundances of both D and HD.

water vapor profiles.

2.4.3 Mapping Fractionation Factor Results to Integrated Water Loss

We can determine the magnitude of water loss on Mars by using our results for f as input to Equation 2.4. These results are shown in Figure 2.8. In order to use Equation 2.4 to plot past water loss, we must set values for the current water inventory $W(t)$, the current D/H ratio $R_{dh}(t)$, and the ancient Martian D/H ratio, $R_{dh}(0)$.

For $W(t)$, we use the aforementioned range 20-30 m GEL for the current exchangeable water budget of Mars . Exchangeable water is water that is able to move between surface deposits and the atmosphere; its D/H ratio increases due to escape to space. Non-exchangeable water, being unaffected by escape to space, would have its original D/H value.

For $R_{dh}(0)$, we follow Kurokawa et al. (2014) and Villanueva et al. (2015) and use 1.275 × SMOW, in agreement with the measurement of D/H in the 4.5 billion year old melt inclusions in the Martian meteorite Yamato 980459 (Usui et al. 2012). Finally, we use 5.5 × SMOW for $R_{dh}(t)$.

Using these values, we calculate the cumulative water lost to be between about 66 and 122 m GEL, depending on escape type and value of f. We compare these results with other estimates in the literature in the next section.

2.5 Discussion

Because f depends directly on the escape fluxes ϕ_{D} and ϕ_{H}, it is reasonable that the exobase temperature would most strongly affect f for thermal escape. Disturbances in the lower atmosphere that may otherwise affect f will be reduced in amplitude by the time they propagate to the upper atmosphere. A larger f at higher exobase temperatures also makes sense in the context of past work; the Mariner missions measured the exobase temperature to be 350 ± 100 K (Anderson et al. 1971), and Yung et al. (1988) used $T_{\text{exo}} = 364$ K to obtain $f = 0.32$ for thermal escape only. However, these original Mariner measurements were highly uncertain; more recent data (discussed previously) indicate that T_{exo} during solar mean and minimum is cold enough that f for

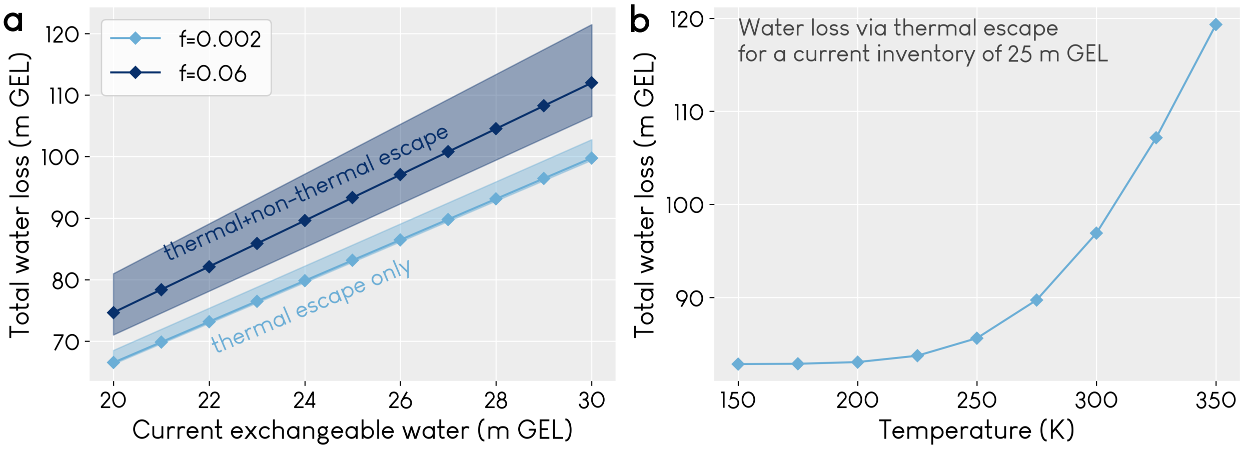

Figure 2.8: Water lost from Mars a) as a function of the current exchangeable water budget and the fractionation factor for the standard atmosphere (f=0.002 for thermal escape and f=0.06 for thermal and non-thermal together). The shaded regions represent the extrema of water loss, calculated for the extrema of f of each escape type from our results. The lower bound for thermal escape is close to that of the standard case because water loss is insensitive to f for f<0.01. b) as a function of exobase temperature and f for that temperature as calculated in the model. Water loss is calculated using Equation 2.4. Equation parameters are described in Section 2.4.3. Because we do not model non-thermal escape, the top line in panel a includes an approximation of the effect of non-thermal escape as described in the main text.

thermal escape is substantially smaller, and that non-thermal escape of D is critical to an accurate calculation of f.

The importance of T_{tropo} is also worth some discussion. In Figure 2.4, T_{tropo} appears to be the parameter with the greatest control over f for thermal + non-thermal escape together. It should be noted, however, that our estimates of non-thermal escape are approximate and extrapolated below 200 K, as described in Section 2.4. For the simulations that varied T_{surf} or T_{tropo}, each estimation of non-thermal escape was made assuming a constant value of T_{exo} (205 K). On the other hand, different values of T_{exo} were necessarily used in the simulations which tested the effects of varying it. This means that $f_{\text{thermal+nonthermal}}$ and f_{thermal} as a function of T_{tropo} appear to differ by a constant, whereas $f_{\text{thermal+nonthermal}}$ as a function of T_{exo} may be artificially large at temperatures below 200 K (see Figure A.5). Despite these uncertainties, T_{tropo} is still important to the value of f, as increased T_{tropo} also increases the temperature of the thermosphere, enabling greater upward transport and contributing to overall escape (see Figure A.6).

The relationship of ϕ_{D} from thermal escape to the abundances of atomic D and HD is not immediately obvious. In Figure 2.6a and b, ϕ_{D} most closely tracks the abundance of atomic D at the exobase because it is much more abundant than HD. In all of the simulations represented in these panels, the exobase temperature is 205 K, a value too low for escape of HD to contribute significantly to D loss. Only at high exobase temperatures (Figure 2.6c) or high concentrations of water (Figure 2.7b) does ϕ_{D} appear to track the HD abundance, indicating HD is abundant enough to contribute more to D loss. In general, in Figures 2.6 and 2.7b, an increase in ϕ_{D} is correlated with an increase in the abundance of D, except when T_{exo} increases and escape is dramatically enhanced. More abundant deuterium means more deuterium available to escape; in most cases, loss of deuterium (hydrogen) via D (H) dominates, but at high exobase temperatures, loss via the molecular form HD (H_2) can reach higher values, up to 5% (20%), as shown in Figure A.4.

A comparison of our results for water loss to those of other similar studies is shown in Figure 2.9. Overall, our results agree reasonably well with these other studies. Our results are a little lower than those by Villanueva et al. (2015), who assume a higher atmospheric D/H ratio (7-8 ×

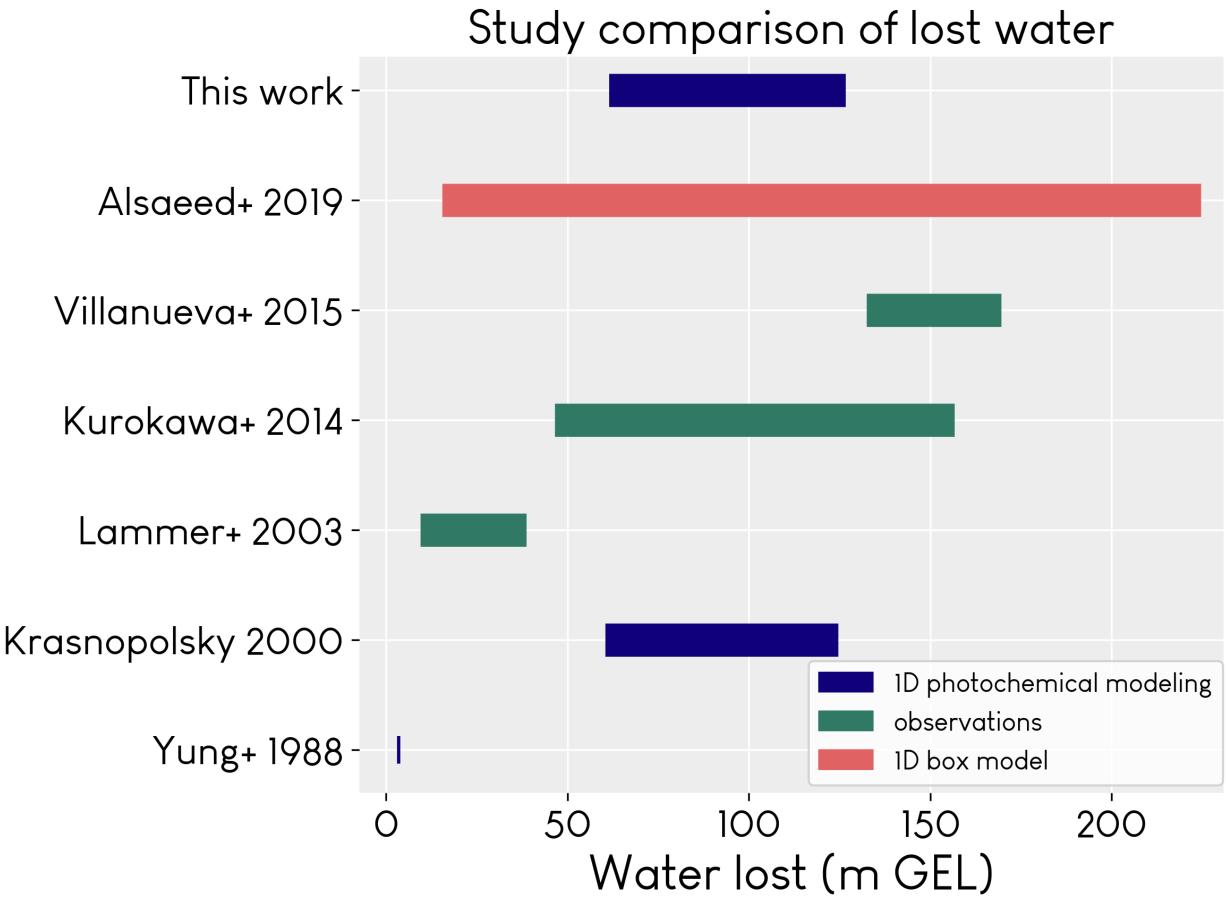

Figure 2.9: Estimates of water lost from Mars by various studies.

SMOW), and a little higher than Lammer et al. (2003a), who assume a higher D/H ratio for early Mars (1.2-2.6 × SMOW) and calculate a present-day water budget of 3.3-15 m GEL, based on the estimated integrated loss of 12 m GEL by Lammer et al. (2003b). Lammer et al. (2003a) extend their estimate of lost water up to 34 m GEL based on other studies also, and these values are those shown in Figure 2.9. The original study by Yung et al. (1988) is an outlier in this case because they were attempting to determine both the current water inventory and the amount lost, and did not have the benefit of the many Mars missions and observations that we have today. The recent work by Alsaeed et al. (2019) is unique compared to the other studies in this figure in that they allow water to be added to the atmosphere via volcanic outgassing, so that their results represent a large possible solution space and are less directly comparable than the other studies.

Our results for water loss also bring up an important point with regard to escape rates. It is common when estimating water loss on Mars to assume that the escape fluxes ϕ_H and ϕ_D are constant and that the water inventory decreases linearly with time. This is an often necessary but imperfect assumption due to the many unknowns involved, including historical rates of atmospheric escape and their evolution in light of Mars' chaotically evolving obliquity. Assuming linear loss with time (and neglecting ϕ_D, which is far slower than ϕ_H) gives $\phi_\mathrm{H} = W_{lost}/t$, where t is the time over which the water has been lost. Using our results for water loss, even the smallest amount lost (about 60 m GEL) requires an escape rate of $\sim 3 \times 10^9$ cm^{-2} s^{-1}, an order of magnitude higher than what we currently observe for escape rates of H from Mars (Jakosky et al. 2018). This is an indication that escape rates were likely higher in the past due to a variety of factors, especially in the context of a more UV-active young sun (Jakosky et al. 2018), or that surface interactions play a larger role that has been previously explored–e.g., with regard to oxygen deposition (Zahnle et al. 2008)–but not yet fully quantified.

As a way to gain insight about our results, we compared the concentrations of a few molecular species in our model with available measurements (Figures 2.10 and 2.11). The measurements we used were the inferred lower atmospheric abundance of $H_2 = 15 \pm 5$ ppm (V. A. Krasnopolsky et al. 2001); a global mean O_3 abundance of 1.2 μm-atm, extracted from maps by Clancy et al. (2016);

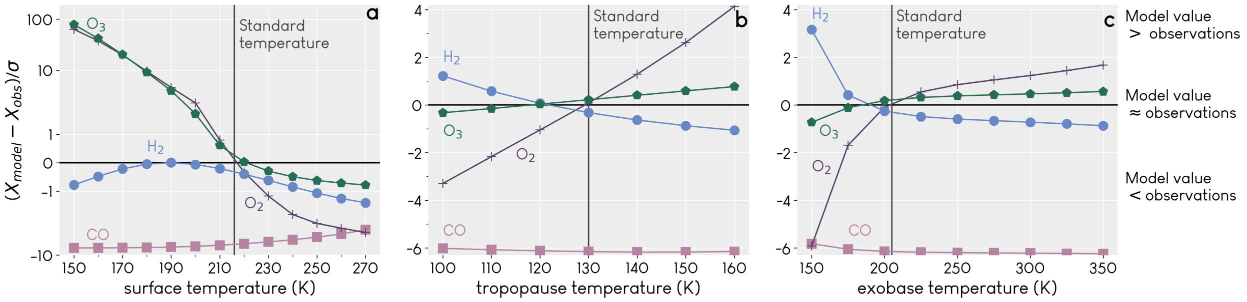

Figure 2.10: Comparison of model output values to measured values as a means of determining appropriateness of our temperature assumptions. See text for measurement citations. O_3 is measured in μm-atm. O_2 and CO are measured as the mixing ratio at the surface. H_2 is measured with the total abundance in ppm in the lower atmosphere (0-80 km). The y-axis is the difference between model output and measurement, weighted by the uncertainty in the measurement; the closer a point is to the 0 line, the more similar the model output and measurement.

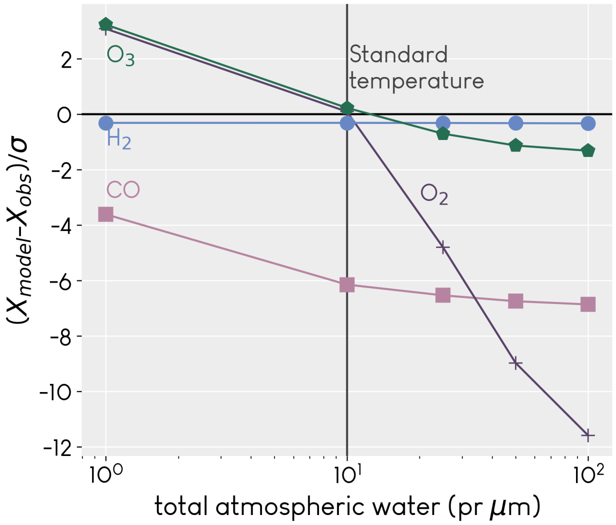

Figure 2.11: The same as Figure 2.10, but for model runs where we varied the water vapor content of the atmosphere.

and mixing ratios for O_2 and CO at the surface equal to $(5.8 \pm 0.8) \times 10^{-4}$ and $(1.61 \pm 0.09) \times 10^{-3}$ (Trainer et al. 2019). These comparisons indicate the model conditions which may be more similar or dissimilar to the current state of Mars. As one example, model results that used a particularly low temperature as input (for example, models with $T_{\mathrm{surf}} < 190$ or $T_{\mathrm{exo}} < 175$) diverge greatly from measurements of all molecular species. These model results thus represent a significant perturbation to the photochemical system as compared to modern Mars. It is also important to note that O_3 and O_2 are related, as O_3 is created and destroyed via interactions between O_2 and O. CO sticks out as an obvious problem; this is not surprising, as many photochemical models also have difficulty in reproducing the observed values (V. A. Krasnopolsky 2010). Some models come close (e.g. Zahnle et al. (2008)), usually only when another parameter changes significantly. Our model also underestimates CO, reaffirming the ongoing need for study in this area. Apart from CO, the difference between our model and measurements is mostly small, indicating that the standard atmosphere we chose was reasonable.

Our results represent a peri-modern global scenario; f has likely changed over time in ways that our model does not account for. In this work, we consider only the exchangeable reservoirs of water on Mars without including any type of surface deposition, which comprises multiple processes with potentially different fractionation factors. Fractionation may also vary on seasonal timescales, especially around the poles, as HDO preferentially condenses and may also have a different sublimation rate compared to H_2O. It has certainly varied over geological time scales. We run the model for 10 million years to equilibrium, though it would not necessarily have been in equilibrium throughout its 4.5 billion year history. This also means that atmospheric escape rates would not have been constant in time, although we assume them to be because their time evolution is unknown. Mars' chaotically evolving obliquity on time scales greater than 10 million years is a major reason for this lack of a definitive paleo-climate timeline. Characterization of escape rates through time is therefore a critical, but daunting, subject for future modeling efforts. On early Mars, the more UV-active young sun would have enhanced non-thermal escape rates (Jakosky et al. 2018), allowing f to grow larger due to the enhancement of ϕ_{D}. This is allowed even in long-term chemical equilibrium; when no D is present, $\phi_{\mathrm{H}} = 2\phi_O$, but when D is present, the requirement instead becomes $\phi_{\mathrm{H}} + \phi_{\mathrm{D}} = 2\phi_O$. For all these reasons, we expect that our results for water loss are a lower bound.

2.6 Conclusions

Our results in Figure 2.4 and Table A.5 show that if only thermal escape is considered, the exobase temperature has the strongest effect on the fractionation factor, whereas when non-thermal escape is included, the temperatures of the tropopause and exobase become comparably important (given the uncertainty in our non-thermal escape estimation). While the exobase and upper atmosphere have been the focus of many recent studies, the Martian mesosphere is less well-studied, but is worthy of future modeling and observational efforts. The tropopause temperature affects mesospheric chemistry, which is especially important considering the seasonal transport of water to these altitudes (Chaffin et al. 2017; Heavens et al. 2018; Shaposhnikov et al. 2019; A. A. Fedorova et al. 2020). Because T_{tropo} is the minimum temperature in the atmosphere, a larger value also implies a warmer thermosphere (see Figure 2.2), which may contribute to enhanced transport, especially above the homopause.

Our results also show how important non-thermal escape is to accurately calculate f. For thermal escape processes only, D is almost completely retained on Mars compared to H. This is especially true near solar maximum, when most atmospheric loss occurs as thermal escape of H. During solar mean and minimum, however, thermal escape of both D and H is lowenough that the non-thermal loss of D and HD becomes much more significant (V. A. Krasnopolsky et al. 1998; Gacesa et al. 2012). Figure 2.4 shows that including non-thermal escape increases f by an order of magnitude or more for all atmospheric conditions. Studies of only thermal escape are therefore not likely to provide a reasonable estimate of f. We therefore advise that future modeling studies that calculate f should include non-thermal escape; this will also enable better comparison with recent observationally-derived values of f (e.g Clarke et al. 2019).

In this study, we have neglected interaction with the planetary surface, which is certainly important due to the unknown D/H of surface ice and polar caps and fractionating effects on sublimation and deposition. Future work to understand the fractionation factor and atmospheric escape will need to link cross-disciplinary knowledge of surface and atmospheric processes. The history of water on Mars cannot be fully understood by only considering one or the other; they are inextricably linked. A more thorough understanding of exchange between different water reservoirs on and under the surface and in the atmosphere, as well as the variables affecting all types of atmospheric escape and water loss, will be instrumental in forming a more complete picture of the fractionation factor, and by extension water loss, on Mars.

Chapter 3

Fully coupled photochemistry of the deuterated ionosphere of Mars and its effects on escape of H and D

The contents of this chapter were originally published as E. M. Cangi et al. (2023).

3.1 Abstract

Although deuterium (D) on Mars has received substantial attention, the deuterated ionosphere remains relatively unstudied. This means that we also know very little about non-thermal D escape from Mars, since it is primarily driven by excess energy imparted to atoms produced in ion-neutral reactions. Most D escape from Mars is expected to be non-thermal, highlighting a gap in our understanding of water loss from Mars. In this work, we set out to fill this knowledge gap. To accomplish our goals, we use an upgraded 1D photochemical model that fully couples ions and neutrals and does not assume photochemical equilibrium. To our knowledge, such a model has not been applied to Mars previously. We model the atmosphere during solar minimum, mean, and maximum, and find that the deuterated ionosphere behaves similarly to the H-bearing ionosphere, but that non-thermal escape on the order of 8000-9000 $\mathrm{cm}^{-2}\mathrm{s}^{-1}$ dominates atomic D loss under all solar conditions. The total fractionation factor, f, is $f = 0.04$–0.07, and integrated water loss is 147–158 m GEL. This is still less than geomorphological estimates. Deuterated ions at Mars are likely difficult to measure with current techniques due to low densities and mass degeneracies with more abundant H ions. Future missions wishing to measure the deuterated ionosphere in situ will need to develop innovative techniques to do so.

3.2 Introduction

Mars is a natural laboratory to study how atmospheric escape shapes planetary habitability. It is now well established that a significant amount of the Mars atmosphere has been lost to space (e.g. Jakosky et al. 2018). This escape is fractionating—the relative escape efficiency is different for members of an isotope pair, such as deuterium (D) and hydrogen (H). Because on Mars, D and H are found primarily in water, D/H fractionation indicates a history of water loss (Owen et al. 1988). Understanding escape fractionation therefore contributes to understanding the long-term loss of the atmosphere and desiccation of the planet.

Geological studies indicate that Mars has likely lost 500+ meters global equivalent layer (GEL) of water (and references therein Lasue et al. 2013), but atmospheric modeling studies typically do not find the same result, instead arriving at a smaller number of 100-250 m GEL (V. Krasnopolsky 2000; V. A. Krasnopolsky 2002; Alsaeed et al. 2019; E. M. Cangi et al. 2020). A key step in retrieving water loss estimates from atmospheric models is to quantify both thermal and non-thermal escape.

Thermal escape includes hydrodynamic escape, which may have ocurred on early Mars and is not expected to significantly fractionate H and D (Hunten et al. 1987), but does fractionate more massive molecules (Zahnle et al. 1990; Yoshida et al. 2020; Cassata et al. 2022); and Jeans escape, in which a small fraction of particles escape because they have a thermal velocity in the high-energy tail of the Maxwellian velocity distribution, above planetary escape velocity. Non-thermal escape comprises all other processes that grant extra kinetic energy to atmospheric particles, then variously dubbed “suprathermal” or “hot”; most of these processes involve ion chemistry or interaction with ionsand include sputtering, interactions of the planetary ionosphere with the solar wind, and ion outflow. (Impact-driven escape also falls under the non-thermal category, but doesn’t specifically involve ions, and is not expected to be fractionating.) H escape has been well-studied at Mars with atmospheric models, observations from missions, and mixes of the two (V. A. Krasnopolsky 2002; Zahnle et al. 2008; Bhattacharyya et al. 2017; Halekas 2017; Mayyasi et al. 2018; Rahmati et al. 2018; AlMaazmi et al. 2019; V. A. Krasnopolsky 2019; Stone et al. 2020; Chaffin et al. 2021; Chaufray et al. 2021b; Holmes et al. 2021; Gu et al. 2022, and others). Thermal escape of D has also been modeled (Yung et al. 1988; Kass et al. 1999; E. M. Cangi et al. 2020), but non-thermal escape of D sourced from planetary ion-neutral reactions has not been modeled, despite indications that non-thermal escape is the dominant loss process of D (V. A. Krasnopolsky 2002, 2010; Gacesa et al. 2012). V. A. Krasnopolsky (2002, 2010) and V. A. Krasnopolsky et al. (1998) calculated non-thermal D escape velocities for a few select processes (solar wind charge exchange, electron impact ionization, and photoionization), but their model did not include a deuterated ionosphere, and so missed a portion of the production of hot atoms.

E. M. Cangi et al. (2020) used a 1D photochemical model of Mars' neutral atmosphere to calculate the D/H fractionation factor f as a function of atmospheric temperatures. The model only calculated thermal escape directly; non-thermal escape was approximated by scaling the non-thermal effusion velocities given by V. A. Krasnopolsky (2002) and multiplying them by the densities of H and D at the exobase. This estimation indicated that f is several orders of magnitude larger when non-thermal escape processes are considered, motivating a more complete calculation of non-thermal escape of H and D. Here, we present this more complete treatment. The key questions about the deuterated martian ionosphere that we address are as follows.

(1) What are the atmospheric densities of deuterated ions?

(2) What are the dominant production mechanisms of hot H and hot D, and are they analogous or dissimilar?

(3) What is the magnitude of non-thermal escape of D, and is it the dominant type of escape during quiet solar conditions?

(4) Can inclusion of non-thermal escape in the model yield an estimation of water loss similar to the amount calculated in geomorphological studies?

To answer these questions, we have substantially upgraded our existing 1D photochemical model, now named bluejay, of the martian atmosphere. Spanning from the surface to 250 km, it now includes a self-consistent ionosphere with deuterated ions, fully couples the ions and neutrals without assumption of photochemical equilibrium, and has only argon as a fixed background species. To our knowledge, it is the first photochemical model to do all of this in the Mars literature.

Past photochemistry studies have typically used several simplifications which improve computational speed and make it easier to model the chemistry of ions and neutrals, which have very different timescales of chemical reaction. Most recent ion-neutral photochemical models use one or more of three common approaches: (1) a fixed (either wholly or partially) background neutral atmosphere (Molina-Cuberos et al. 2002; Matta et al. 2013; Fox et al. 2015, 2017, 2021); (2) placing the lower boundary of the model near the bottom of the ionosphere (V. A. Krasnopolsky 2002; Matta et al. 2013; Fox et al. 2015; V. A. Krasnopolsky 2019; Fox et al. 2021); or (3) the assumption of photochemical equilibrium for chemically short-lived species (Banaszkiewicz et al. 2000; Vuitton et al. 2019) and/or neglect of ion diffusion (Dobrijevic et al. 2016). By building a model that does not use these approaches, we obtain a more complete understanding of the coupling of the lower to upper atmospheres, which has been recently shown to be key to understanding water transport, destruction, and escape during the Mars dusty season (Heavens et al. 2018; Aoki et al. 2019; Vandaele et al. 2019; A. A. Fedorova et al. 2020; Stone et al. 2020; Chaffin et al. 2021; Holmes et al. 2021; Villanueva et al. 2021). To accommodate the computational demands of the model, bluejay is built in Julia (Bezanson et al. 2017), a relatively new language designed specifically for numerical modeling.

We use our enhanced model to present the first theoretical analysis of D ion chemistry at Mars, which includes an updated quantification of non-thermal escape of D and H, the most critical reactions for production of hot H and D, and the implications for water loss.

3.3 Model description

Here we describe changes made to the 1D photochemical model as described by E. M. Cangi et al. (2020). In addition to the upgrades to physics and chemistry described below, this update incorporates computational improvements, such as extensive encapsulation, vectorization of functions, and performance tuning. The only species that we hold constant in our model is argon and lower atmospheric water (see Section 3.3.1.3).

The absolute tolerance is 1 $\times 10^{-12}$, or 1 ppt, and the relative tolerance is 1×10^{-6}. If the percent change of a value is above relative tolerance, the model continues performing Newton iterations to predict the species densities at the next timestep, and stops once it falls below the relative tolerance. This becomes problematic when the values solved for are near machine precision (for 64-bit floats), as happens for ions in the lower atmosphere. In this scenario, the model relies on the absolute tolerance instead, which represents a level below which we do not demand any numerical accuracy; thus, densities that are below 1 ppt may be less representative of the real atmosphere than densities above.

3.3.1 New features

3.3.1.1 Ion reaction network

Our updated model contains ∼600 total ion and neutral reactions. The deuterated reactions are shown in Table 3.1, and the non-deuterated reactions are available in Table B.2; rate coefficients of H-analogue reactions are generally the same as those used by Chaffin et al. (2017), Vuitton et al. (2019), and E. M. Cangi et al. (2020).

Scope of deuterated reactions: We define a deuterated analogue reaction as a reaction in which one H atom in one of the reactants has been replaced with D; for example, $D + O_2 \rightarrow DO_2$ instead of $H + O_2 \rightarrow HO_2$. We do not consider doubly deuterated reactions or species, e.g., we do not include reactions like $DO_2 + D \rightarrow OD + OD$ nor species like D_2O. The already very low relative abundance of D to H ($\sim 1 \times 10^{-3}$) means that doubly deuterated species and reactions will have an abundance lower by another factor of ∼1000, are thus expected to have a negligible effect on the atmospheric chemistry. Our deuterated reaction network includes all of the reactions shown in Table 3.1. The H-bearing analogues of the reactions in Table 3.1 contribute 99.99997% of the total column rate of all H-bearing reactions, meaning that most of the atmospheric chemistry of H has a deuterated analogue, so it is unlikely that we have accidentally biased our results against D production.

Table 3.1: Deuterated reactions used in the model. Reactions 1-6b: column rate ν in $cm^{-2}s^{-1}$. Reactions 7-125: rate coefficients in units of cm^3 $molecule^{-1}$ s^{-1} for bimolecular reactions and cm^6 $molecule^{-1}$ s^{-1} for termolecular reactions. BR = branching ratio; MS = mass scaling.

	Reaction		BR	MS	Rate coefficient	Ref
		Photodissociation and photoionization				
1	D	$\rightarrow D^+$			$\nu_{col} = 7.5 \times 10^{-12}$	†
2	DO_2	$\rightarrow OD + O$			$\nu_{col} = 6.9 \times 10^{-8}$	†
3a	HD	$\rightarrow HD^+$			$\nu_{col} = 6.2 \times 10^{-12}$	†
3b		$\rightarrow H + D$			$\nu_{col} = 3.8 \times 10^{-12}$	†
3c		$\rightarrow H^+ + D$			$\nu_{col} = 6.9 \times 10^{-13}$	†
3d		$\rightarrow D^+ + H$			$\nu_{col} = 6.9 \times 10^{-13}$	†
4a	HDO	$\rightarrow D + OH$			$\nu_{col} = 4.4 \times 10^{-10}$	C0499
4b		$\rightarrow H + OD$			$\nu_{col} = 4.4 \times 10^{-10}$	C0499
4c		$\rightarrow HD + O(^1D)$			$\nu_{col} = 5.6 \times 10^{-11}$	C0499
4d		$\rightarrow HDO^+$			$\nu_{col} = 3.3 \times 10^{-11}$	†
4e		$\rightarrow OD^+ + H$			$\nu_{col} = 6.4 \times 10^{-12}$	†
4f		$\rightarrow OH^+ + D$			$\nu_{col} = 6.4 \times 10^{-12}$	†
4g		$\rightarrow D^+ + OH$			$\nu_{col} = 2.9 \times 10^{-12}$	†
4h		$\rightarrow H^+ + OD$			$\nu_{col} = 2.9 \times 10^{-12}$	†
4i		$\rightarrow O^+ + HD$			$\nu_{col} = 3.8 \times 10^{-13}$	†
4j		$\rightarrow H + D + O$			$\nu_{col} = 0$	†
5a	HDO_2	$\rightarrow OH + OD$			$\nu_{col} = 1.1 \times 10^{-8}$	†
5b		$\rightarrow DO_2 + H$			$\nu_{col} = 3.1 \times 10^{-10}$	†

Continued on next page

	Reaction		BR	MS	Rate or rate coefficient	Ref
5c		$\rightarrow HO_2 + D$			$\nu_{col} = 3.1 \times 10^{-10}$	†
5d		$\rightarrow HDO + O(^1D)$			$\nu_{col} = 0$	†
6a	OD	$\rightarrow O + D$			$\nu_{col} = 1.1 \times 10^{-9}$	NL84
6b		$\rightarrow O(^1D) + D$			$\nu_{col} = 1.6 \times 10^{-11}$	NL84
		Deuterated neutral-neutral reactions				
7	$CO + D$	$\rightarrow DCO$			See text $k_\infty = 1\,(T_n)^{0.2}$ $k_0 = 2.00 \times 10^{-35}\,(T_n)^{0.2}$	Est.
8a	$CO + OD$	$\rightarrow CO_2 + D$		$\sqrt{\frac{17}{18}}$	See text $k_\infty = 1.63 \times 10^{-6}\,(T_n)^{6.1}$ $k_0 = 4.90 \times 10^{-15}\,(T_n)^{0.6}$	Est.
8b		$\rightarrow DOCO$		$\sqrt{\frac{17}{18}}$	See text $k_\infty = 6.62 \times 10^{-16}\,(T_n)^{1.3}$ $k_0 = 1.73 \times 10^{-29}\,(T_n)^{-1.4}$	Est.
9	$D + H_2$	$\rightarrow HD + H$			$2.73 \times 10^{-17}\,(T_n)^{2.0}\,e^{-2700/T_n}$	NIST
10a	$D + H_2O_2$	$\rightarrow H_2O + OD$	0.5		$1.16 \times 10^{-11} e^{-2110/T_n}$	C10
10b		$\rightarrow HDO + OH$	0.5		$1.16 \times 10^{-11} e^{-2110/T_n}$	C10
11a	$D + HO_2$	$\rightarrow DO_2 + H$			1.00×10^{-10}	Y88
11b		$\rightarrow HD + O_2$			2.45×10^{-12}	Y88
11c		$\rightarrow HDO + O(^1D)$			1.14×10^{-12}	Y88
11d		$\rightarrow OH + OD$			5.11×10^{-11}	Y88
12	$D + O_2$	$\rightarrow DO_2$		$\sqrt{\frac{1}{2}}$	See text $k_\infty = 2.40 \times 10^{-11}\,(T_n)^{0.2}$ $k_0 = 1.46 \times 10^{-28}\,(T_n)^{-1.3}$	Est.
13	$D + O_3$	$\rightarrow OD + O_2$			$9.94 \times 10^{-11} e^{-470/T_n}$	NIST
14	$D + OH + CO_2$	$\rightarrow HDO + CO_2$		$\sqrt{\frac{1}{2}}$	$1.16 \times 10^{-25}\,(T_n)^{-2.0}$	Est.
15	$DCO + H$	$\rightarrow CO + HD$		$\sqrt{\frac{29}{30}}$	1.50×10^{-10}	Est.
16a	$DCO + O$	$\rightarrow CO + OD$		$\sqrt{\frac{29}{30}}$	5.00×10^{-11}	Est.

Continued on next page

	Reaction		BR	MS	Rate or rate coefficient	Ref
16b		$\rightarrow CO_2 + D$		$\sqrt{\frac{29}{30}}$	5.00×10^{-11}	Est.
17a	$DCO + O_2$	$\rightarrow CO_2 + OD$		$\sqrt{\frac{29}{30}}$	7.60×10^{-13}	Est.
17b		$\rightarrow DO_2 + CO$		$\sqrt{\frac{29}{30}}$	5.20×10^{-12}	Est.
18	$DCO + OH$	$\rightarrow HDO + CO$	0.5	$\sqrt{\frac{29}{30}}$	1.80×10^{-10}	Est.
19	$DO_2 + HO_2$	$\rightarrow HDO_2 + O_2$		$\sqrt{\frac{33}{34}}$	$3.00 \times 10^{-13} e^{460/T_n}$	Est.
20	$DO_2 + N$	$\rightarrow NO + OD$		$\sqrt{\frac{33}{34}}$	2.20×10^{-11}	Est.
21	$DO_2 + O_3$	$\rightarrow OD + O_2 + O_2$		$\sqrt{\frac{33}{34}}$	$1.00 \times 10^{-14} e^{-490/T_n}$	Est.
22	$DOCO + O_2$	$\rightarrow DO_2 + CO_2$		$\sqrt{\frac{45}{46}}$	2.09×10^{-12}	Est.
23	$DOCO + OH$	$\rightarrow CO_2 + HDO$		$\sqrt{\frac{45}{46}}$	1.03×10^{-11}	Est.
24	$H + D + M$	$\rightarrow HD + M$		$\sqrt{\frac{1}{2}}$	$6.62 \times 10^{-27} (T_n)^{-2.27}$	Est.
25a	$H + DO_2$	$\rightarrow HD + O_2$		$\sqrt{\frac{33}{34}}$	3.45×10^{-12}	Est.
25b		$\rightarrow HDO + O(^1D)$		$\sqrt{\frac{33}{34}}$	1.60×10^{-12}	Est.
25c		$\rightarrow HO_2 + D$			$1.85 \times 10^{-10} e^{-890/T_n}$	Y88
25d		$\rightarrow OH + OD$		$\sqrt{\frac{33}{34}}$	7.20×10^{-11}	Est.
26	$H + HD$	$\rightarrow H_2 + D$			$1.15 \times 10^{-11} e^{-3041/T_n}$	NIST
27a	$H + HDO_2$	$\rightarrow H_2O + OD$	0.5		$1.16 \times 10^{-11} e^{-2110/T_n}$	C10
27b		$\rightarrow HDO + OH$	0.5		$1.16 \times 10^{-11} e^{-2110/T_n}$	C10
28	$H + OD + CO_2$	$\rightarrow HDO + CO_2$		$\sqrt{\frac{17}{18}}$	$1.16 \times 10^{-25} (T_n)^{-2.0}$	Est.
29	$HCO + D$	$\rightarrow CO + HD$		$\sqrt{\frac{1}{2}}$	1.50×10^{-10}	Est.
30	$HCO + OD$	$\rightarrow HDO + CO$	0.5	$\sqrt{\frac{29}{30}}$	1.80×10^{-10}	Est.
31a	$HD + O$	$\rightarrow OD + H$			$1.68 \times 10^{-12} e^{-4400/T_n}$	NIST
31b		$\rightarrow OH + D$			$4.40 \times 10^{-12} e^{-4390/T_n}$	NIST
32	$HO_2 + DO_2 + M$	$\rightarrow HDO_2 + O_2 + M$		$\sqrt{\frac{33}{34}}$	$4.20 \times 10^{-33} e^{920/T_n}$	Est.
33	$HOCO + OD$	$\rightarrow CO_2 + HDO$		$\sqrt{\frac{17}{18}}$	1.03×10^{-11}	Est.
34	$O + D$	$\rightarrow OD$		$\sqrt{\frac{1}{2}}$	$8.65 \times 10^{-18} (T_n)^{-0.38}$	Est.
35	$O + DO_2$	$\rightarrow OD + O_2$		$\sqrt{\frac{33}{34}}$	$3.00 \times 10^{-11} e^{200/T_n}$	Est.
36a	$O + HDO_2$	$\rightarrow OD + HO_2$	0.5	$\sqrt{\frac{34}{35}}$	$1.40 \times 10^{-12} e^{-2000/T_n}$	Est.
36b		$\rightarrow OH + DO_2$	0.5	$\sqrt{\frac{34}{35}}$	$1.40 \times 10^{-12} e^{-2000/T_n}$	Est.

Continued on next page

	Reaction		BR	MS	Rate or rate coefficient	Ref
37	$O + OD$	$\rightarrow O_2 + D$		$\sqrt{\frac{17}{18}}$	$1.80 \times 10^{-11} e^{180/T_n}$	Est.
38a	$O(^1D) + HD$	$\rightarrow D + OH$			4.92×10^{-11}	Y88
38b		$\rightarrow H + OD$			4.92×10^{-11}	Y88
39	$O(^1D) + HDO$	$\rightarrow OD + OH$		$\sqrt{\frac{18}{19}}$	$1.63 \times 10^{-10} e^{60/T_n}$	Est.
40	$OD + H$	$\rightarrow OH + D$			$4.58 \times 10^{-9} \left(T_n\right)^{-0.63} e^{-717/T_n}$	Y88
41	$OD + H_2$	$\rightarrow HDO + H$			$2.80 \times 10^{-12} e^{-1800/T_n}$	Y88
42	$OD + H_2O_2$	$\rightarrow HDO + HO_2$		$\sqrt{\frac{17}{18}}$	$2.90 \times 10^{-12} e^{-160/T_n}$	Est.
43	$OD + HO_2$	$\rightarrow HDO + O_2$		$\sqrt{\frac{17}{18}}$	$4.80 \times 10^{-11} e^{250/T_n}$	Est.
44	$OD + O_3$	$\rightarrow DO_2 + O_2$		$\sqrt{\frac{17}{18}}$	$1.70 \times 10^{-12} e^{-940/T_n}$	Est.
45a	$OD + OH$	$\rightarrow HDO + O$		$\sqrt{\frac{17}{18}}$	1.80×10^{-12}	Est.
					See text	
45b		$\rightarrow HDO_2$		$\sqrt{\frac{17}{18}}$	$k_\infty = 2.60 \times 10^{-11}$	Est.
					$k_0 = 6.60 \times 10^{-29} \left(T_n\right)^{-0.8}$	
46	$OH + D$	$\rightarrow OD + H$			$3.30 \times 10^{-9} \left(T_n\right)^{-0.63}$	Y88
47	$OH + DO_2$	$\rightarrow HDO + O_2$		$\sqrt{\frac{33}{34}}$	$4.80 \times 10^{-11} e^{250/T_n}$	Est.
48a	$OH + HD$	$\rightarrow H_2O + D$			$4.20 \times 10^{-13} e^{-1800/T_n}$	Y88
48b		$\rightarrow HDO + H$			$5.00 \times 10^{-12} e^{-2130/T_n}$	S11
49a	$OH + HDO_2$	$\rightarrow H_2O + DO_2$	0.5	$\sqrt{\frac{34}{35}}$	$2.90 \times 10^{-12} e^{-160/T_n}$	Est.
49b		$\rightarrow HDO + HO_2$	0.5	$\sqrt{\frac{34}{35}}$	$2.90 \times 10^{-12} e^{-160/T_n}$	Est.
		Deuterated ion-neutral reactions				
50	$ArD^+ + CO$	$\rightarrow DCO^+ + Ar$			1.25×10^{-9}	A03
51	$ArD^+ + CO_2$	$\rightarrow DCO_2^+ + Ar$			1.10×10^{-9}	A03
52a	$ArD^+ + H_2$	$\rightarrow ArH^+ + HD$			4.50×10^{-10}	A03
52b		$\rightarrow H_2D^+ + Ar$			8.80×10^{-10}	A03
53	$ArD^+ + N_2$	$\rightarrow N_2D^+ + Ar$			6.00×10^{-10}	A03
54	$ArH^+ + HD$	$\rightarrow H_2D^+ + Ar$			8.60×10^{-10}	A03
55a	$Ar^+ + HD$	$\rightarrow ArD^+ + H$			3.84×10^{-10}	A03
55b		$\rightarrow ArH^+ + D$			3.68×10^{-10}	A03

Continued on next page

	Reaction		BR	MS	Rate or rate coefficient	Ref
55c		$\rightarrow HD^+ + Ar$			4.80×10^{-11}	A03
56a	$CO_2^+ + D$	$\rightarrow DCO^+ + O$			6.38×10^{-11}	A03
56b		$\rightarrow D^+ + CO_2$			2.02×10^{-11}	A03
57a	$CO_2^+ + HD$	$\rightarrow DCO_2^+ + H$	0.5	$\sqrt{\frac{2}{3}}$	2.35×10^{-10}	Est.
57b		$\rightarrow HCO_2^+ + D$	0.5	$\sqrt{\frac{2}{3}}$	2.35×10^{-10}	Est.
58a	$CO_2^+ + HDO$	$\rightarrow DCO_2^+ + OH$	0.5	$\sqrt{\frac{18}{19}}$	3.00×10^{-10}	Est.
58b		$\rightarrow HCO_2^+ + OD$	0.5	$\sqrt{\frac{18}{19}}$	3.00×10^{-10}	Est.
58c		$\rightarrow HDO^+ + CO_2$		$\sqrt{\frac{18}{19}}$	1.80×10^{-9}	Est.
59	$CO^+ + D$	$\rightarrow D^+ + CO$			9.00×10^{-11}	A03
60a	$CO^+ + HD$	$\rightarrow DCO^+ + H$	0.25	$\sqrt{\frac{2}{3}}$	7.50×10^{-10}	Est.
60b		$\rightarrow DOC^+ + H$	0.25	$\sqrt{\frac{2}{3}}$	7.50×10^{-10}	Est.
60c		$\rightarrow HCO^+ + D$	0.25	$\sqrt{\frac{2}{3}}$	7.50×10^{-10}	Est.
60d		$\rightarrow HOC^+ + D$	0.25	$\sqrt{\frac{2}{3}}$	7.50×10^{-10}	Est.
61a	$CO^+ + HDO$	$\rightarrow DCO^+ + OH$	0.5	$\sqrt{\frac{18}{19}}$	8.40×10^{-10}	Est.
61b		$\rightarrow HCO^+ + OD$	0.5	$\sqrt{\frac{18}{19}}$	8.40×10^{-10}	Est.
61c		$\rightarrow HDO^+ + CO$		$\sqrt{\frac{18}{19}}$	1.56×10^{-9}	Est.
62	$C^+ + HD$	$\rightarrow CH^+ + D$	0.17		1.20×10^{-16}	A03
63a	$C^+ + HDO$	$\rightarrow DCO^+ + H$	0.5	$\sqrt{\frac{18}{19}}$	$7.80 \times 10^{-9} \left(T_i\right)^{-0.5}$	Est.
63b		$\rightarrow DOC^+ + H$	0.5	$\sqrt{\frac{18}{19}}$	1.08×10^{-9}	Est.
63c		$\rightarrow HCO^+ + D$	0.5	$\sqrt{\frac{18}{19}}$	$7.80 \times 10^{-9} \left(T_i\right)^{-0.5}$	Est.
63d		$\rightarrow HDO^+ + C$			2.34×10^{-10}	Est.
63e		$\rightarrow HOC^+ + D$	0.5	$\sqrt{\frac{18}{19}}$	1.08×10^{-9}	Est.
64	$DCO_2^+ + CO$	$\rightarrow DCO^+ + CO_2$		$\sqrt{\frac{45}{46}}$	7.80×10^{-10}	Est.
65a	$DCO_2^+ + e^-$	$\rightarrow CO + O$	0.68		$4.62 \times 10^{-5} \left(T_i\right)^{-0.64}$	G05
65b		$\rightarrow CO + OD$	0.27		$4.62 \times 10^{-5} \left(T_i\right)^{-0.64}$	G05
65c		$\rightarrow CO_2 + D$	0.05		$4.62 \times 10^{-5} \left(T_i\right)^{-0.64}$	G05
66	$DCO_2^+ + H_2O$	$\rightarrow H_2DO^+ + CO_2$		$\sqrt{\frac{45}{46}}$	2.65×10^{-9}	Est.
67	$DCO_2^+ + O$	$\rightarrow DCO^+ + O_2$		$\sqrt{\frac{45}{46}}$	5.80×10^{-10}	Est.

Continued on next page

	Reaction		BR	MS	Rate or rate coefficient	Ref
68a	$DCO^+ + e^-$	$\rightarrow CO + D$	0.92		$9.02 \times 10^{-5}\,(T_i)^{-1.1}$	GK
68b		$\rightarrow OD + C$	0.07		$9.02 \times 10^{-5}\,(T_i)^{-1.1}$	GK
69	$DCO^+ + H$	$\rightarrow HCO^+ + D$			1.50×10^{-11}	A03
70	$DCO^+ + H_2O$	$\rightarrow H_2DO^+ + CO$		$\sqrt{\frac{29}{30}}$	2.60×10^{-9}	Est.
71	$DOC^+ + CO$	$\rightarrow DCO^+ + CO$		$\sqrt{\frac{29}{30}}$	6.00×10^{-10}	Est.
72	$DOC^+ + e^-$	$\rightarrow OD + C$		$\sqrt{\frac{29}{30}}$	$1.19 \times 10^{-8}\,(T_i)^{1.2}$	Est.
73a	$DOC^+ + H_2$	$\rightarrow H_2D^+ + CO$	0.57		6.20×10^{-10}	A03
73b		$\rightarrow HCO^+ + HD$	0.43		6.20×10^{-10}	A03
74a	$D^+ + CO_2$	$\rightarrow CO_2^+ + D$			3.50×10^{-9}	A03
74b		$\rightarrow DCO^+ + O$			2.60×10^{-9}	A03
75	$D^+ + H$	$\rightarrow D + H^+$	0.87		$6.50 \times 10^{-11}\,(T_i)^{0.5}$	Y89
76	$D^+ + H_2$	$\rightarrow H^+ + HD$			2.20×10^{-9}	A03
77a	$D^+ + H_2O$	$\rightarrow H_2O^+ + D$			5.20×10^{-9}	A03
77b		$\rightarrow HDO^+ + H$	0.5	$\sqrt{\frac{1}{2}}$	8.20×10^{-9}	Est.
78	$D^+ + NO$	$\rightarrow NO^+ + D$			1.80×10^{-9}	A03
79	$D^+ + O$	$\rightarrow D + O^+$			2.80×10^{-10}	A03
80	$D^+ + O_2$	$\rightarrow O_2^+ + D$			1.60×10^{-9}	A03
81a	$H_2DO^+ + e^-$	$\rightarrow H_2 + O$	0.5	$\sqrt{\frac{19}{20}}$	$9.68 \times 10^{-8}\,(T_i)^{-0.5}$	Est.
81b		$\rightarrow H_2O + D$	0.5	$\sqrt{\frac{19}{20}}$	$1.86 \times 10^{-6}\,(T_i)^{-0.5}$	Est.
81c		$\rightarrow HD + O$	0.5	$\sqrt{\frac{19}{20}}$	$9.68 \times 10^{-8}\,(T_i)^{-0.5}$	Est.
81d		$\rightarrow HDO + H$	0.5	$\sqrt{\frac{19}{20}}$	$1.86 \times 10^{-6}\,(T_i)^{-0.5}$	Est.
81e		$\rightarrow OD + H$	0.5	$\sqrt{\frac{19}{20}}$	$4.47 \times 10^{-6}\,(T_i)^{-0.5}$	Est.
81f		$\rightarrow OD + H_2$	0.5	$\sqrt{\frac{19}{20}}$	$1.04 \times 10^{-6}\,(T_i)^{-0.5}$	Est.
81g		$\rightarrow OH + D$	0.5	$\sqrt{\frac{19}{20}}$	$4.47 \times 10^{-6}\,(T_i)^{-0.5}$	Est.
81h		$\rightarrow OH + HD$	0.5	$\sqrt{\frac{19}{20}}$	$1.04 \times 10^{-6}\,(T_i)^{-0.5}$	Est.
82a	$H_2D^+ + CO$	$\rightarrow DCO^+ + H_2$	0.33		1.60×10^{-9}	A03
82b		$\rightarrow HCO^+ + HD$	0.67		1.60×10^{-9}	A03
83a	$H_2D^+ + e^-$	$\rightarrow H + H$	0.73		6.00×10^{-8}	L96

Continued on next page

	Reaction		BR	MS	Rate or rate coefficient	Ref
83b		$\rightarrow H_2 + D$	0.07		6.00×10^{-8}	L96
83c		$\rightarrow HD + H$	0.2		6.00×10^{-8}	L96
84	$H_2D^+ + H_2$	$\rightarrow H_3^+ + HD$			5.30×10^{-10}	A03
85a	$H_2O^+ + HD$	$\rightarrow H_2DO^+ + H$	0.5	$\sqrt{\frac{2}{3}}$	3.80×10^{-10}	Est.
85b		$\rightarrow H_3O^+ + D$	0.5	$\sqrt{\frac{2}{3}}$	3.80×10^{-10}	Est.
86	$HCO_2^+ + HDO$	$\rightarrow H_2DO^+ + CO_2$		$\sqrt{\frac{18}{19}}$	2.65×10^{-9}	Est.
87	$HCO^+ + D$	$\rightarrow DCO^+ + H$			4.25×10^{-11}	A03
88	$HCO^+ + HDO$	$\rightarrow H_2DO^+ + CO$		$\sqrt{\frac{18}{19}}$	2.60×10^{-9}	Est.
89a	$HDO^+ + CO$	$\rightarrow DCO^+ + OH$	0.5	$\sqrt{\frac{18}{19}}$	2.12×10^{-10}	Est.
89b		$\rightarrow HCO^+ + OD$	0.5	$\sqrt{\frac{18}{19}}$	2.12×10^{-10}	Est.
90a	$HDO^+ + e^-$	$\rightarrow HD + O$	0.1		1.50×10^{-7}	J99
90b		$\rightarrow O + D$	0.59		1.50×10^{-7}	J99
90c		$\rightarrow OD + H$	0.21		1.50×10^{-7}	J99
90d		$\rightarrow OH + D$	0.1		1.50×10^{-7}	J99
91a	$HDO^+ + H_2$	$\rightarrow H_2DO^+ + H$	0.5	$\sqrt{\frac{18}{19}}$	3.80×10^{-10}	Est.
91b		$\rightarrow H_3O^+ + D$	0.5	$\sqrt{\frac{18}{19}}$	3.80×10^{-10}	Est.
92a	$HDO^+ + N$	$\rightarrow HNO^+ + D$	0.5	$\sqrt{\frac{18}{19}}$	5.60×10^{-11}	Est.
92b		$\rightarrow NO^+ + HD$		$\sqrt{\frac{18}{19}}$	2.80×10^{-11}	Est.
93	$HDO^+ + NO$	$\rightarrow NO^+ + HDO$		$\sqrt{\frac{18}{19}}$	4.60×10^{-10}	Est.
94	$HDO^+ + O$	$\rightarrow O_2^+ + HD$		$\sqrt{\frac{18}{19}}$	4.00×10^{-11}	Est.
95	$HDO^+ + O_2$	$\rightarrow O_2^+ + HDO$		$\sqrt{\frac{18}{19}}$	3.30×10^{-10}	Est.
96a	$HD^+ + Ar$	$\rightarrow ArD^+ + H$	0.45	$\sqrt{\frac{2}{3}}$	2.10×10^{-9}	A03
96b		$\rightarrow ArH^+ + D$	0.55	$\sqrt{\frac{2}{3}}$	2.10×10^{-9}	Est.
97a	$HD^+ + CO$	$\rightarrow DCO^+ + H$	0.5	$\sqrt{\frac{2}{3}}$	1.45×10^{-9}	Est.
97b		$\rightarrow HCO^+ + D$	0.5	$\sqrt{\frac{2}{3}}$	1.45×10^{-9}	Est.
98a	$HD^+ + CO_2$	$\rightarrow DCO_2^+ + H$	0.5	$\sqrt{\frac{2}{3}}$	1.17×10^{-9}	Est.
98b		$\rightarrow HCO_2^+ + D$	0.5	$\sqrt{\frac{2}{3}}$	1.17×10^{-9}	Est.
99	$HD^+ + e^-$	$\rightarrow H + D$			$1.93 \times 10^{-6}\,(T_i)^{-0.853}\,e^{-43.3/T_i}$	KIDA

Continued on next page

	Reaction		BR	MS	Rate or rate coefficient	Ref
100	$HD^+ + HD$	$\rightarrow H_2D^+ + D$			8.42×10^{-10}	A03
101a	$HD^+ + N_2$	$\rightarrow N_2D^+ + H$	0.5	$\sqrt{\frac{2}{3}}$	1.00×10^{-9}	Est.
101b		$\rightarrow N_2H^+ + D$	0.5	$\sqrt{\frac{2}{3}}$	1.00×10^{-9}	Est.
102a	$HD^+ + O$	$\rightarrow OD^+ + H$	0.5	$\sqrt{\frac{2}{3}}$	7.50×10^{-10}	Est.
102b		$\rightarrow OH^+ + D$	0.5	$\sqrt{\frac{2}{3}}$	7.50×10^{-10}	Est.
103	$HD^+ + O_2$	$\rightarrow HO_2^+ + D$	0.5	$\sqrt{\frac{2}{3}}$	9.60×10^{-10}	Est.
104	$H^+ + HD$	$\rightarrow D^+ + H_2$			1.10×10^{-10}	A03
105a	$H^+ + HDO$	$\rightarrow H_2O^+ + D$	0.5	$\sqrt{\frac{18}{19}}$	8.20×10^{-9}	Est.
105b		$\rightarrow HDO^+ + H$	0.5	$\sqrt{\frac{18}{19}}$	8.20×10^{-9}	Est.
106	$N_2D^+ + CO$	$\rightarrow DCO^+ + N_2$		$\sqrt{\frac{29}{30}}$	8.80×10^{-10}	Est.
107	$N_2D^+ + e^-$	$\rightarrow N_2 + D$		$\sqrt{\frac{29}{30}}$	$6.60 \times 10^{-7} \left(T_i\right)^{-0.51}$	Est.
108	$N_2D^+ + H$	$\rightarrow N_2H^+ + D$			2.50×10^{-11}	A03
109	$N_2D^+ + O$	$\rightarrow OD^+ + N_2$		$\sqrt{\frac{29}{30}}$	1.40×10^{-10}	Est.
110	$N_2H^+ + D$	$\rightarrow N_2D^+ + H$			8.00×10^{-11}	A03
111	$N_2^+ + D$	$\rightarrow D^+ + N_2$			1.20×10^{-10}	A03
112a	$N_2^+ + HD$	$\rightarrow N_2D^+ + H$	0.51		1.34×10^{-9}	A03
112b		$\rightarrow N_2H^+ + D$	0.49		1.34×10^{-9}	A03
113a	$N_2^+ + HDO$	$\rightarrow HDO^+ + N_2$		$\sqrt{\frac{18}{19}}$	1.90×10^{-9}	Est.
113b		$\rightarrow N_2D^+ + OH$	0.5	$\sqrt{\frac{18}{19}}$	5.04×10^{-10}	Est.
113c		$\rightarrow N_2H^+ + OD$	0.5	$\sqrt{\frac{18}{19}}$	5.04×10^{-10}	Est.
114	$N^+ + HD$	$\rightarrow NH^+ + D$	0.25		3.10×10^{-10}	A03
115	$OD^+ + CO$	$\rightarrow DCO^+ + O$		$\sqrt{\frac{17}{18}}$	8.40×10^{-10}	Est.
116	$OD^+ + CO_2$	$\rightarrow DCO_2^+ + O$		$\sqrt{\frac{17}{18}}$	1.35×10^{-9}	Est.
117	$OD^+ + e^-$	$\rightarrow O + D$		$\sqrt{\frac{17}{18}}$	$6.50 \times 10^{-7} \left(T_i\right)^{-0.5}$	Est.
118a	$OD^+ + H_2$	$\rightarrow H_2O^+ + D$	0.5	$\sqrt{\frac{17}{18}}$	9.70×10^{-10}	Est.
118b		$\rightarrow HDO^+ + H$	0.5	$\sqrt{\frac{17}{18}}$	9.70×10^{-10}	Est.
119	$OD^+ + N$	$\rightarrow NO^+ + D$		$\sqrt{\frac{17}{18}}$	8.90×10^{-10}	Est.
120	$OD^+ + N_2$	$\rightarrow N_2D^+ + O$		$\sqrt{\frac{17}{18}}$	2.40×10^{-10}	Est.

Continued on next page

	Reaction		BR	MS	Rate or rate coefficient	Ref
121	$OD^+ + O$	$\rightarrow O_2^+ + D$		$\sqrt{\frac{17}{18}}$	7.10×10^{-10}	Est.
122	$OD^+ + O_2$	$\rightarrow O_2^+ + OD$		$\sqrt{\frac{17}{18}}$	3.80×10^{-10}	Est.
123a	$OH^+ + HD$	$\rightarrow H_2O^+ + D$		$\sqrt{\frac{2}{3}}$	9.70×10^{-10}	Est.
123b		$\rightarrow HDO^+ + H$		$\sqrt{\frac{2}{3}}$	9.70×10^{-10}	Est.
124	$O^+ + D$	$\rightarrow D^+ + O$		$\sqrt{\frac{1}{2}}$	6.40×10^{-10}	Est.
125a	$O^+ + HD$	$\rightarrow OD^+ + H$	0.46		1.25×10^{-9}	A03
125b		$\rightarrow OH^+ + D$	0.54		1.25×10^{-9}	A03
126	$O^+ + HDO$	$\rightarrow HDO^+ + O$		$\sqrt{\frac{18}{19}}$	2.60×10^{-9}	Est.

†: Cross section assumed same as H-analogue. A03: Anicich (2003).

C0499: B.-M. Cheng et al. (1999) and B. M. Cheng et al. (2004). C10: Cazaux et al. (2010).

G05: Geppert et al. (2005). K09: Korolov et al. (2009). GK: Rate from K09, branching ratio from G05.

J99: Jensen et al. (1999). KIDA: Wakelam et al. (2019). L96: Larsson et al. (1996).

NIST: Manion et al. (2015). NL84: Nee et al. (1984). S11: Sander et al. (2011).

Y88: Yung et al. (1988). Y89: Yung et al. (1989). Est: Estimated with mass scaling (see text).

Photodissociation and photoionization: Photodissociation and ionization of deuterated species is calculated using the solar spectrum (see Section 3.3.2.2), so the entry in the table under 'Rate or rate coefficient' represents the integrated column rate. The 'Ref' column refers to the source of the cross sections used. For photoionization cross sections of the H-analogue reactions, see Vuitton et al. (2019, and references therein).

Neutral and ion bimolecular and termolecular reactions: The rate coefficient used for a given reaction is the product of the 'BR', 'MS' and 'Rate coefficient' columns (empty fields are taken to be 1). 'BR', or branching ratio, accounts for the fact that deuteration of a reaction can create two or more branches with differing products where only one branch would exist for the H-analogue reaction. 'MS', or mass scaling, is a scaling factor equal to the square root of the mass ratio, $\sqrt{m_1/m_2}$, where m_2 is the mass of the deuterated species and m_1 the H-bearing species. This factor is applied to reactions for which we were not able to find a measurement in the literature to account for replacement of one reactant H atom with one D atom; a similar approach was used previously by V. A. Krasnopolsky (2002) for reactions of neutral HD with dominant ions and minor H-bearing ions.

Most reactions in these tables proceed using the listed rate coefficients. A few exceptions apply; the categorization Types and formulae mentioned below are the same as used by Vuitton et al. (2019). A more complete description of the formulae used can be found in their Appendix B.

Reaction 7: Similar to its analogue CO + H → HCO, this is a Type 4 (pressure dependent association) reaction. The Troe parameter for this reaction is 0, so we use the form:

$$k = k_R + \frac{(Mk_0 k_\infty)}{Mk_0 + k_\infty} \tag{3.1}$$

Where k_R is 0 in this case and M is the background atmospheric density.

Reactions 8a, 8b, 12, and 45b: These are Type 6 (CO + OD → CO_2 + D) and Type 5 (CO + OH → DOCO, D + O_2→ DO_2, OD + OH → HDO_2) pressure dependent bimolecular reactions, with the formulae originally given by Sander et al. (2011) and J. Burkholder et al. (2019). We use the same forms here, but multiplied by our mass scaling factor.

Ion reactions which produce a lone D or H atom have the potential to cause the produced atom to be “hot”, that is, gaining enough excess energy from the reaction that they can escape. We describe this in more detail in Section 3.3.1.4.

3.3.1.2 Ambipolar diffusion

The model employs ambipolar diffusion for all ions, using the Langevin-Gioumousis-Stevenson equation (Bauer 1973):

$$D_{ai} = \frac{k(T_i + T_e)}{m_i \sum \nu_{ij}} \tag{3.2}$$

$$\nu_{ij} = 2\pi \left(\frac{\alpha_j e^2}{\mu_{ij}} \right)^{1/2} n_j \tag{3.3}$$

Where D_{ai} is the ambipolar diffusion coefficient for ion i, ν_{ij} is the collision frequency of ion i with neutral j, α_j is the polarizability, e is the fundamental charge, and n is the neutral density.

Polarizability values for neutrals are collected from Manion et al. (2015). Where polarizability was not available either in data or models for a deuterated species we include, we assumed the same value as the H-bearing analogue.

3.3.1.3 Partially fixed water profile

We assume a constant abundance of water in the lower atmosphere, which approximates the average water available due to seasonal cycles of polar cap sublimation and transport. The mixing ratio is 1.3 $\times 10^{-4}$ up to the hygropause; in our model (which does not include cloud microphysics), this is the point at which the water mixing ratio begins to follow the saturation vapor pressure curve. We take the hygropause to be 40 km, between 25 km by V. A. Krasnopolsky (2002) and its enhanced altitude of 50-80 km during dust storms (Heavens et al. 2018) and roughly in the middle of the cloud-forming region (Neary et al. 2020; Daerden et al. 2022). At 72 km, a minimum of saturation is reached; above that level, the abundance of water is a free variable. This allows a more holistic understanding of water and water ion chemistry in the upper atmosphere, which has been shown to be an important tracer of seasonal H escape (Stone et al. 2020). The total amount of water in the atmosphere is 10.5 precipitable μm, in accordance with observations (Jakosky et al. 1982; M. D. Smith 2004).

3.3.1.4 Non-thermal escape

Although there are many non-thermal escape mechanisms, in this work, we focus on photochemical loss, i.e. the contribution to escape from chemistry and photochemistry. We neglect processes involving the solar wind such as sputtering, ion pickup, and charge exchange with the solar wind. Processes which depend upon the solar wind will primarily occur above the bow shock (which is far above our top boundary), where the solar wind can interact with the corona before being mostly deflected around the planet (Halekas et al. 2017). By focusing on planetary ionospheric reactions, we capture the non-thermal escape of H and D sourced from the atmosphere below the exobase.

We calculate the non-thermal escape of hot atoms created via ion-neutral chemistry as the product of the probability of escape and the volume production rate of hot atoms using the procedure described by Gregory et al. (2023a), using the collisional cross sections for D and H on O (lacking data on collision with CO_2) by P. Zhang et al. (2009). We have evaluated all ion-neutral reactions that produce H, D, H_2, or HD in the model for their exothermicity ($\Delta H^o_{\mathrm{f,products}} - \Delta H^o_{\mathrm{f,reactants}}$, following Fox (2015)) and only use those where the excess energy, equal to the difference in enthalpies of products and reactants, is positive and exceeds the energy required for H or D to escape to space. In reality, varying amounts of the excess heat produced can contribute to electronic and/or rovibrational excitations of the more massive second product molecule. A detailed analysis of these energy branches is beyond the scope of this work, in which we provide a first look at these reactions, so we neglect branching of energy into the non-H or D product, and assume that all excess energy ends up in the atomic H or D (see Appendix B). We use the escape probability curve calculated by Gregory et al. (2023a) for an H atom of excess energy 5 eV; this is a reasonable approximation of the actual mean excess energy in our model, which is 3.6 eV. At this time, escape probabilities for larger atoms and molecules have not been calculated, so we also apply the escape probability to D, H_2, and HD. We expect this may introduce no more than a few percent uncertainty in our calculation of the escape of these species. A more rigorous analysis of energy branching ratios and their effect on escape, as well as an update with probability curves for D, H_2, and HD, is a worthy subject for future work.

The resulting volume escape rate can be integrated to obtain an escape flux for the top boundary of the model. Although our focus is escape of atomic H and D, some loss does occur via loss of the molecular form, so we also include non-thermal escape of H_2 and HD. In these cases, we assume that $\sigma_{\mathrm{H_2}}$ is the same as for D due to the similar masses, and that σ_{HD} is larger than H_2 by the same amount that D is larger than H. Although this is not an ideal assumption if one is interested in highly accurate non-thermal H_2 and HD escape, it is acceptable for our purposes, as that escape is very small compared to atomic escape of H and D.

3.3.2 Model inputs

Because the importance of non-thermal escape is expected to vary with solar activity, we have constructed three sets of inputs representing solar minimum, mean, and maximum conditions. The only properties which we vary between these cases are the neutral exobase temperatures and the incoming solar flux. Figure 3.1 shows these inputs in the navy, purple, and yellow colors. The inputs represent a dayside mean atmosphere (solar zenith angle [SZA]=60°).

3.3.2.1 Atmospheric temperature profiles

Standard neutral temperatures were obtained from the Mars Climate Database (Millour et al. 2018) by several layers of averaging, in order of first to last: by longitude, local time (9, 12, and 3 pm local times, night excluded), latitude (weighted by encompassed surface area), and L_s. Over the solar cycle, the only significant change is to the exobase temperature, so we hold the surface and mesospheric temperature constant at 230 K and 130 K respectively.

In order to support modeling of ion chemistry, we use a piecewise fit to the new ion temperature profiles obtained at SZA=60° with the STATIC instrument by Hanley et al. (2022). These new data have overturned long-standing assumptions that the neutrals, ions, and electrons thermalize to the same temperature around 125 km (Schunk et al. 2009), and thus represent a significant update in Mars photochemistry. We also include a fit to the electron profile from the Mars Atmosphere and Volatile EvolutioN mission (MAVEN) Langmuir Probes and Waves (LPW) instrument (Ergun et al. 2015). Because it is difficult to associate ion temperatures with contemporary neutral temperatures due to the averaging required for the neutral profiles, and because the data are limited in time, we do not change the ion or electron profiles for the different solar cycle scenarios. Past work indicates relatively minor temperature differences due to solar cycle (Kim et al. 1998); further analysis of MAVEN STATIC data provides an opportunity to confirm or deny this. Any variation with solar cycle is likely to have a minor impact on our results.

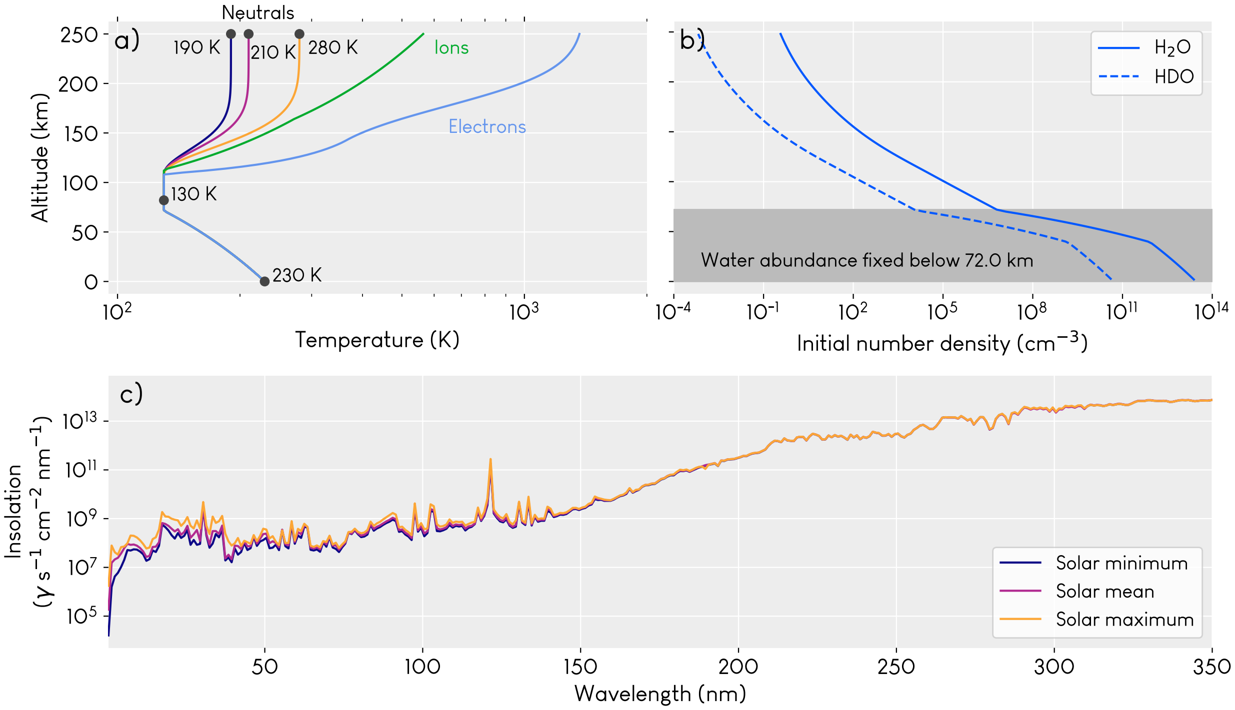

Figure 3.1: Main model inputs. a) Temperature profiles, with separate neutral exobase temperatures for each solar condition. Ion and electron temperatures are fits to data from MAVEN/STATIC as reported by Hanley et al. (2022) and MAVEN/LPW as reported by Ergun et al. (2015). b) Initial water profile. Above 72 km, water densities evolve according to the chemistry and transport. c) Insolation profiles from 0-350 nm for solar minimum, mean, and maximum. The full input spectrum goes out to 2400 nm, but the insolation there is relatively flat, with no variation due to solar cycle.

3.3.2.2 Insolation

Incoming solar photons are key reactants in photochemical reactions. For each solar case, we include photon fluxes from 0.5–2400 nm, binned in 1 nm increments. Total flux, once obtained, is scaled to Mars' orbit and SZA=60°.

We determined the dates of recent representative solar conditions by looking for periods when Ly α irradiance in the Lyman-alpha Model Solar Spectral Irradiance data set (Woods et al. 2019) reached a peak, average, or trough. Because solar maximum and mean in recent decades have been historically quiet, we chose dates from the early 2000s to get a more representative photon flux for maximum and mean (solar minimum has not changed much). The dates we used were February 25, 2019 for solar minimum; February 7, 2004 for mean; and March 22, 2002 for maximum.

For the insolation flux data, we use SORCE/SOLSTICE at solar minimum and mean, and a mix of SORCE/SOLSTICE and TIMED/SEE at solar maximum. There is an additional complication for solar maximum: SORCE/SOLSTICE began a year after our solar maximum date, but includes the longer wavelengths we need, while TIMED/SEE began before our solar maximum date, but only includes fluxes at wavelengths shortwards of 190 nm. We patched together these two datasets, using SORCE/SOLSTICE for wavelengths 190-2000 nm from June 4, 2015 and TIMED/SEE for wavelengths 0.5-189.5 nm from March 22, 2002.

Figure 3.1c shows the fluxes only from 0.5 to 350 nm for simplicity; longwards of 350 nm, the profile does not vary over the solar cycle. The region shortward of 350 nm is also more important for photochemistry as the photodissociation and photoionization cross sections are largest there. We use the same cross sections as E. M. Cangi et al. (2020), with the addition of new photoionization and a few neutral photodissociation cross sections, the same used by Vuitton et al. (2019).

3.3.3 Boundary conditions

We use mostly the same boundary conditions as E. M. Cangi et al. (2020). The key addition is an additional non-thermal flux boundary condition at the top of the model for H, D, H_2, and

HD, according to the functional form described by (Gregory et al. 2023a). Flux is zero at the top and bottom of the model for all ion species and any neutral species without a different boundary condition.

It is worth emphasizing that our flux boundary condition at the top of the model for atomic O is fixed at $1.2{\times}10^8$ $cm^{-2}s^{-1}$. This value has been used in past work (Nair et al. 1994) to ensure that equilibrium models would produce H escape rates similar to that calculated from Mariner data. Results from MAVEN (Brain et al. 2015; Dong et al. 2015; Leblanc et al. 2015; Lillis et al. 2017; Jakosky et al. 2018) indicate a present-day total O escape of closer to $3.8{\times}10^7$ $cm^{-2}s^{-1}$. We retain the use of $1.2{\times}10^8$ $cm^{-2}s^{-1}$ in this work, but in future work will explore the effect of the lower MAVEN-derived loss rates on H and D escape.

3.4 Results

3.4.1 What are the atmospheric densities of deuterated ions?

The general distribution of the deuterated ionospheric species is similar to that of their H-analogues. Vertical profiles for select species containing H or D are shown in Figure 3.2. Although they are calculated from surface to 250 km, the figure's lower boundary is placed at 80 km for legibility. The full image from surface to 250 km showing all species in the model appears in Figure B.1.

Primary peaks in the densities of deuterated ions occur between 150 and 200 km, with a minor peak near the top of the mesosphere, around 90-125 km. This structure does not hold for all species. H_3O^+ has its peak much lower down at about 90 km, which is in agreement with previous modeling (Molina-Cuberos et al. 2002; Fox et al. 2015). Unfortunately, comparisons with data are not feasible at this altitude because such data do not exist. Most ionic species, H- and D-bearing alike, also display a slight dip in density around 150 km, which is caused by a feature of the same shape in the electron temperature profile (see Figure 3.1a).

At solar maximum, greater insolation at short wavelengths enables more photoionization,

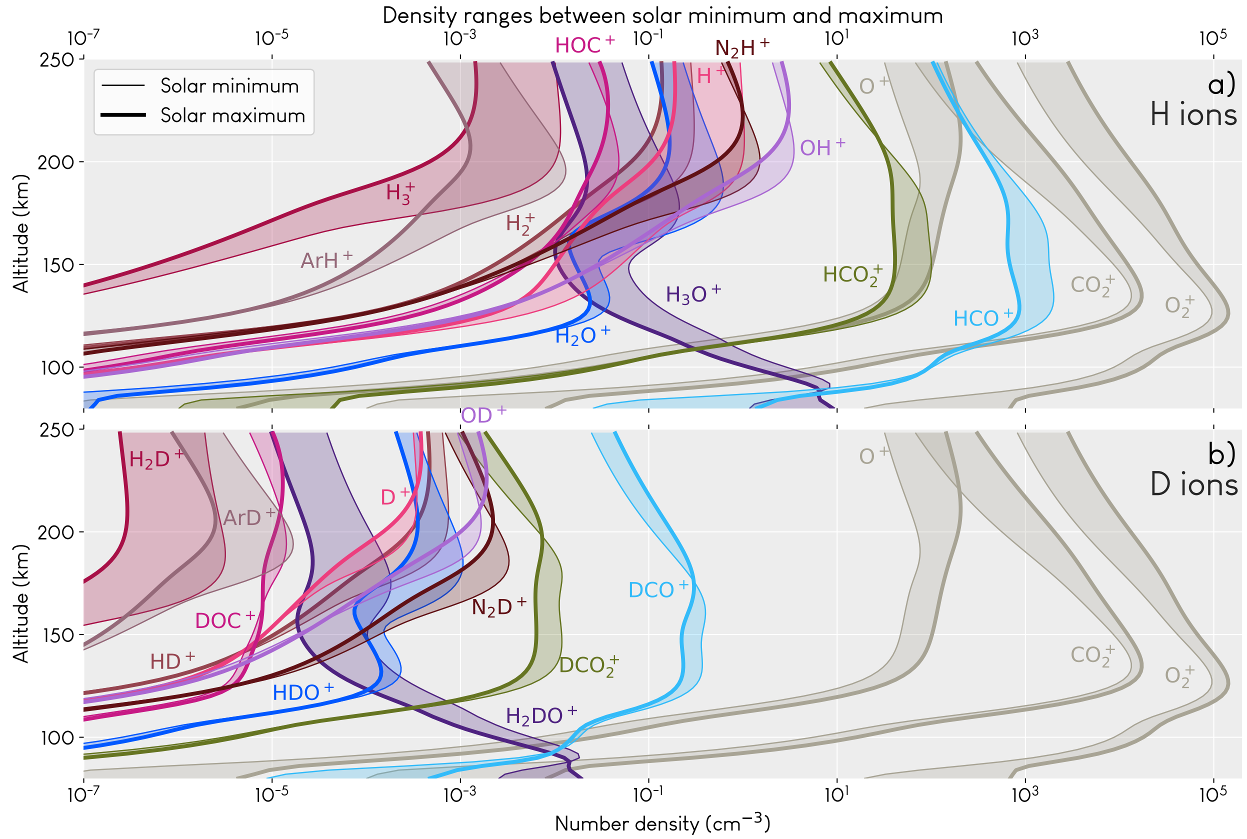

Figure 3.2: Densities of a) H-bearing ions and b) D-bearing (deuterated). Density ranges are bounded by their values at solar minimum (thin line) and solar maximum (thick line), with solar mean values falling within the shaded area. Gray lines show the primary ionospheric species for comparison.

increasing the abundances of primary species CO_2^+, O_2^+, and O^+ which are produced directly from the parent neutrals. But for the lighter (and often more minor) ions containing H and D, chemistry and/or transport is a more important driver than photoionization. Temperature-driven changes in the parent neutral densities propagate through to their ions; for example, H^+ abundance at the top of the atmosphere decreases as the temperature goes up because H escape is diffusion-limited, whereas the same is not true for D abundance (Zahnle et al. 2008; E. M. Cangi et al. 2020). For other minor species that are not diffusion-limited, higher temperatures can also stimulate faster chemical reactions, slightly enhancing production and therefore density at higher temperatures.

3.4.1.1 Comparisons with previous works

Here, we compare our results to modeling results by Fox et al. (2015, 2021) and measurements by MAVEN NGIMS (Benna et al. 2015; Fox et al. 2021). In this work, we have parameterized our atmosphere in order to obtain an understanding of the mean-field behavior in time and space. We have not attempted to match the same modeling input or the relevant atmospheric conditions of those studies. Our models differ substantially from those by Fox et al. (2015, 2021) in temperature structure, boundary conditions (especially for ions at the upper boundary), vertical extent, use of photochemical equilibrium, background atmosphere, SZA, included species, mean Mars-Sun distance, assumed eddy diffusion profile, and included processes (we do not model electron impact ionization or dissociation). Because of these differences, we provide these comparisons primarily for the reader's orientation.

Fox et al. (2015). For the major ions such as O^+, CO_2^+, and O_2^+, our density profiles are generally consistent with those modeled by Fox et al. (2015), as shown in Figure 3.3. They are also broadly similar for many of the minor ions, although in general, our profiles tend to show lower densities near 250 km by 1-2 orders of magnitude. There is a significant difference between our NO^+ profiles, which likely relates to differences between this work and that of Fox et al. (2015) in the nitrogen ion chemistry and included species. It should be noted that many of the ions for which we show a significantly different profile are quite minor, with populations never exceeding 100 cm^{-3},

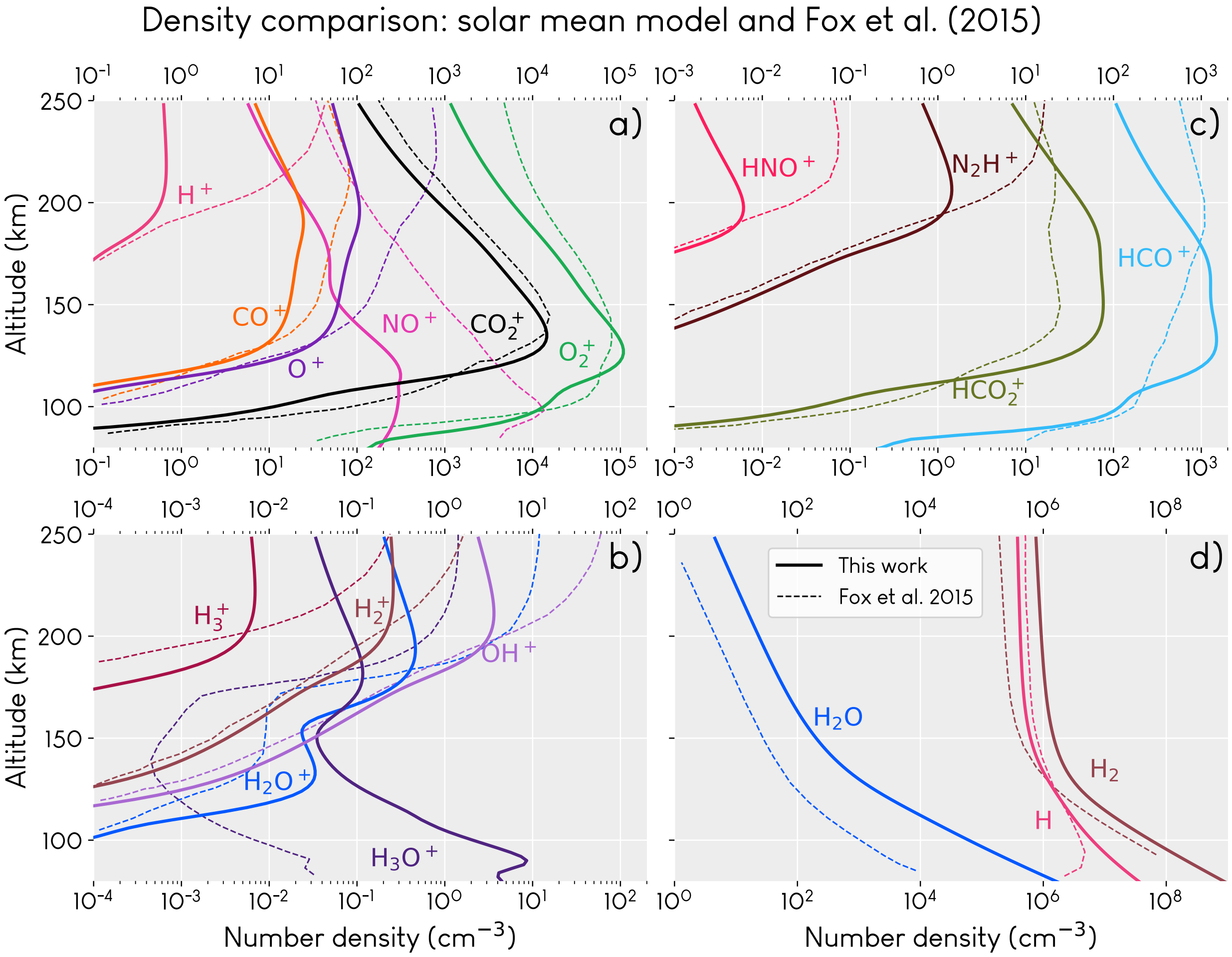

Figure 3.3: Ion and neutral densities computed by our model and compared with those computed by Fox et al. (2015). Species are divided amongst the four panels for legibility and compared with Figure 3 in Fox et al. (2015). Some minor species are omitted for clarity.

so the absolute differences as a percent of the total atmosphere are tiny, well within the absolute tolerance. Fox et al. (2015) make the point that their model calculates neutral H_2O produced only by ion-neutral reactions due to their choice of boundary conditions, whereas ours includes production by photodissociation and lower atmospheric neutral chemistry; it is then perhaps not surprising that our results include more water and different distributions of water-group ions and H-bearing species than theirs (see Figure 3.3d).

In Figure B.3, we also compare our results to Fox et al. (2021), which uses a similar model to Fox et al. (2015) and includes recent data from NGIMS for $CO_2{}^+$, $O_2{}^+$and O^+. Compared to that paper, our results are more dissimilar.

Benna et al. (2015), using MAVEN NGIMS. Figure 3.4 shows that our results are in reasonably good agreement with the initial NGIMS measurements at Mars (Benna et al. 2015), which occurred long enough into the mission that solar mean conditions would have prevailed. There continues to be a divergence between model and data for O^+in the upper atmosphere and an underprediction of NO^+, but considering we are using a 1D model that does not account for local and short-term variations and we have not made any model changes to match data, we find the output acceptable. Significant differences in minor H-bearing ions have a variety of explanations here. NGIMS has background noise typically at 0.01 cm^{-3} and below, and a random uncertainty of 50% at 0.1 cm^{-3} (Benna et al. 2015), which may explain the divergence in $H_3{}^+$and $H_2{}^+$; this difference could also result from the larger amount of the principal H_2O^+ion present in the data. $H_2{}^+$and $H_3{}^+$are also measured in the lowest mass channels that the instrument can access, where the instrument is less sensitive due to a correlation of sensitivity with cross section; there is also a possibility of H outgassing from the instrument fillament (Mahaffy et al. 2015b).

3.4.2 Are the dominant production mechanisms of hot H and D analogous or dissimilar?

Figure 3.5 shows the production mechanisms for hot H and D, which are mostly similar. The hot H production mechanisms are also calculated independently by Gregory et al. (2023b).

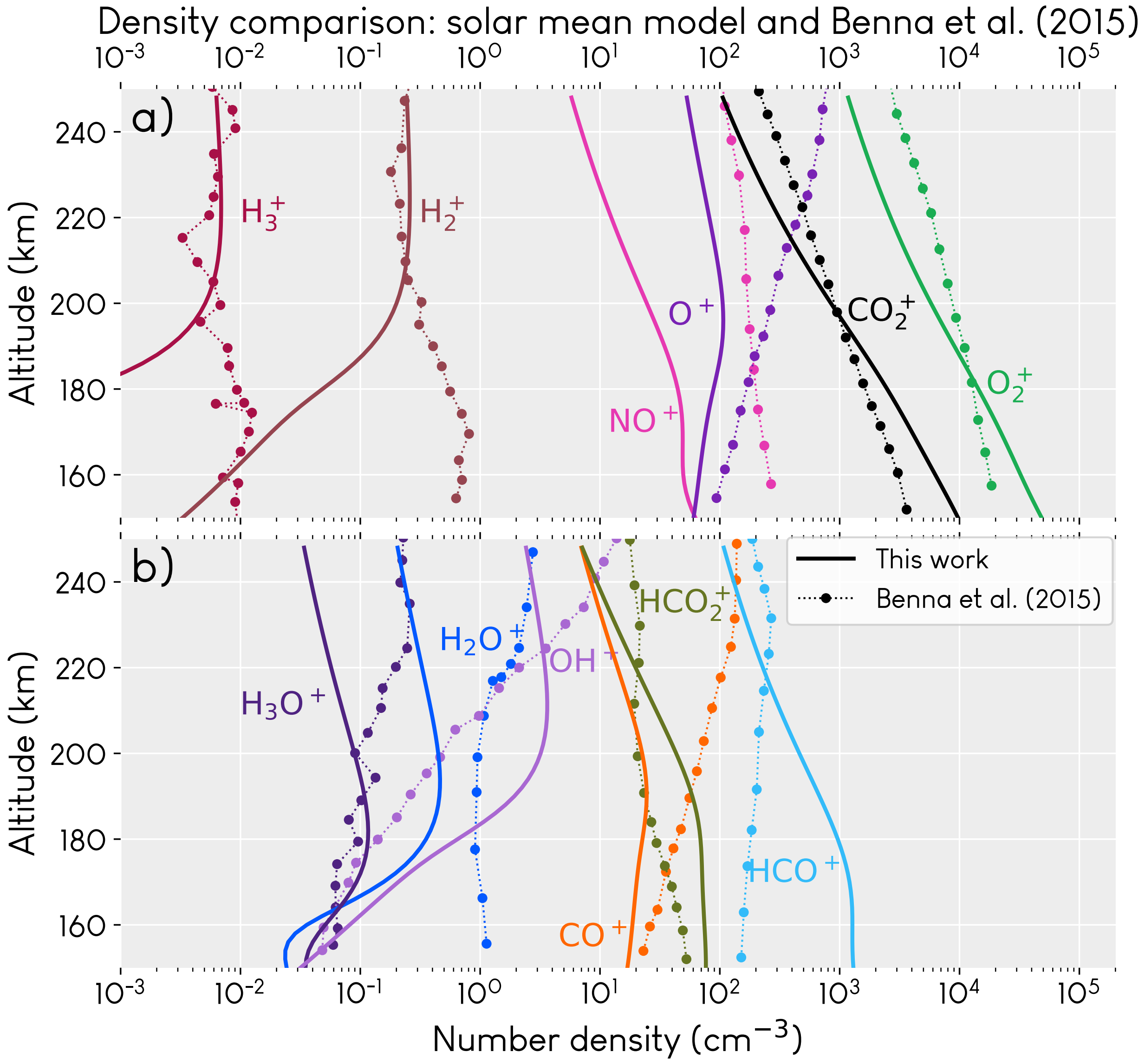

Figure 3.4: Ion and neutral densities computed by our model and compared with those computed by Benna et al. (2015). Species are divided amongst the two panels for legibility. HNO^+differs significantly from data and has been omitted; the measurements are known to be unreliable due to spacecraft potential.

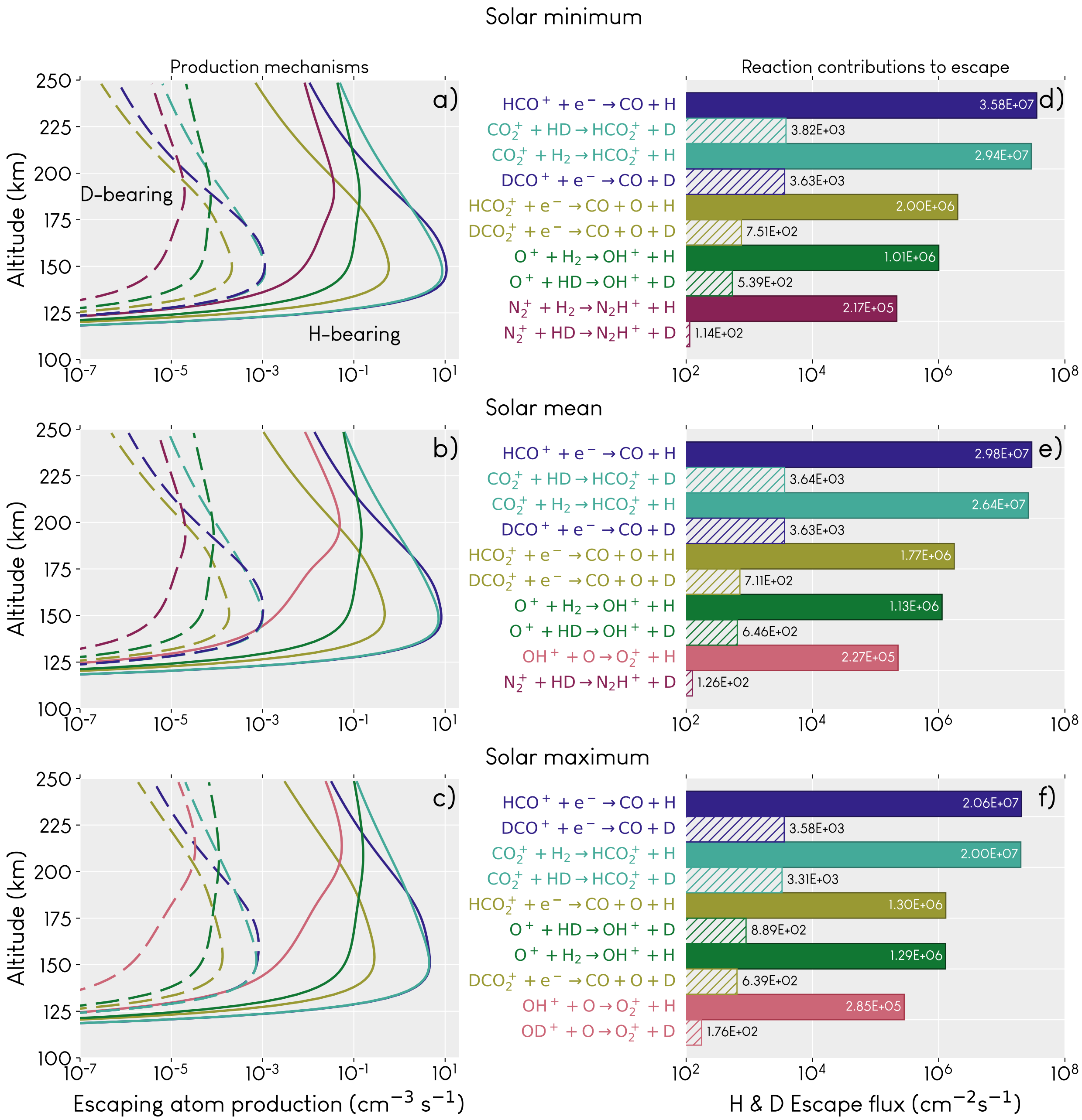

Figure 3.5: Volume production rates of escaping atoms (panels a, b, c) and integrated escape flux of the produced atomic H or D (d, e, f) for the dominant five chemical pathways producing hot H (solid lines/solid bars) and hot D (dashed lines/striped bars).

The most important reaction driving the production of hot D (H) below 200 km in solar mean and maximum is DCO^+(HCO^+) dissociative recombination (DR), with CO_2^++ HD (H_2) a close second. HCO^+ DR dominates for hot H under all solar conditions, but for hot D, CO_2^++ HD marginally dominates over DCO^+ DR during solar minimum at certain altitudes, making it the dominant source of escaping hot D at solar minimum. This is because the density of HD relative to DCO^+ is larger than H_2 relative to HCO^+. The rates of production from these two processes for hot D are very close; minor changes in conditions, including normal fluctuations in the real atmosphere, could likely change this relationship. Above 200 km, CO_2^++ H_2 dominates for hot H production, but high-altitude hot D comes mostly from O^++ HD.

DCO_2^+(HCO_2^+) DR is the third most important reaction during quiet solar conditions, but it is eclipsed by O+ + HD (H_2) during solar maximum. Under quieter solar conditions, the fifth place position is seized by N_2^++ HD (H_2). But as the thermosphere warms, OD (OH) + O claims the fifth place, first for the H species and then for the D species. This appears to be because the dominant reaction involving $OH^+$and $OD^+$is the reaction $O^+ + H_2\ (HD) \rightarrow OH^+(OD^+) + H$. This reaction also has a rate coefficient that is independent of temperature, whereas N_2^++ HD (H_2) has a rate coefficient which decreases with temperature.

3.4.3 What is the magnitude of non-thermal escape of D, and under which conditions does it dominate thermal escape?

Figure 3.6 shows the relative contributions of thermal and non-thermal escape of atomic H and D and thermal escape of the molecular species; the associated escape fluxes to space are given in Table 3.2. The density profiles of the neutral species, from which the escape is sourced, appear in Figure B.2; an upcoming publication will focus on variations in these neutral species and their D/H ratios. As in previous work, (e.g. V. A. Krasnopolsky 2002), thermal escape is the dominant loss process for atomic H, with non-thermal escape of H making up a gradually reducing share as solar activity increases. The picture looks very different for D, for which 62–99.3% of escape is non-thermal depending on solar conditions. Note that, as shown in Table 3.2, the total escape

	Thermal escape ($cm^{-2}s^{-1}$)				Non-thermal escape ($cm^{-2}s^{-1}$)				Total escape ($cm^{-2}s^{-1}$)		
	H	D	H_2	HD	H	D	H_2	HD	H	D	H + D
Solar minimum	1.70×10^8	62	1.66×10^5	0.1	6.92×10^7	9225	11871	7	2.39991×10^8	9295	2.4×10^8
Solar mean	1.79×10^8	243	5.43×10^5	0.9	6.02×10^7	9154	9491	7	2.39991×10^8	9405	2.4×10^8
Solar maximum	1.78×10^8	5415	8.92×10^6	104	4.43×10^7	9041	5473	4	2.39985×10^8	14564	2.4×10^8

Table 3.2: Amount of thermal and non-thermal escape of atomic and molecular H and D species for the three solar conditions. The total escape amounts to 2.4×10^8 $cm^{-2}s^{-1}$ because in the equilibrium atmosphere, the ratio ϕ_H/ϕ_O approaches 2, as O escape is fixed at $1.2\ \times10^8$ $cm^{-2}s^{-1}$ (see Section 3.3.3). Escaping atoms and molecules are sourced from the neutral species; densities for the associated species are shown in Figure B.2.

of H and D adds to 2.4×10^8 $cm^{-2}s^{-1}$ under all solar conditions due to the boundary condition on O escape. H and O escape are linearly related when the atmosphere is in equilibrium: the sum $\phi_{\mathrm{H}} + \phi_{\mathrm{D}}$ will naturally evolve to equal twice the O escape flux, since H_2O and HDO are the primary source of H and D in the model, and contain two H or D for every O. This relation does not necessarily hold over shorter timescales, when short-term perturbations can temporarily break this stoichiometric equilibrium.

Previous work has predicted that thermal escape of D should actually dominate at solar maximum (V. A. Krasnopolsky 2002) and that non-thermal escape of D in the form of larger molecules such as HD, OD, and HDO could be up to 15% (Gacesa et al. 2018), whereas our results show that non-thermal escape of HD is so negligible as to not appear at all in Figure 3.6. Besides the fact that we do not account for excited rotational states of HD, the discrepancy also likely arises from our chosen methods. Our non-thermal escape probability curve is valid for hot H atoms with 5 eV of energy, and we do not account at all for branching to excited internal states of the other products; we assume that all atomic H and D produced by exothermic reactions are produced "hot". In reality, not all exothermic heat is dumped directly into the lone atoms all the time. With proper accounting for these intricate branching ratios, our calculated total of non-thermally escaping atomic D would likely decrease. We also do not calculate non-thermal OD escape, as escape probabilities for a molecule of this mass are not available.

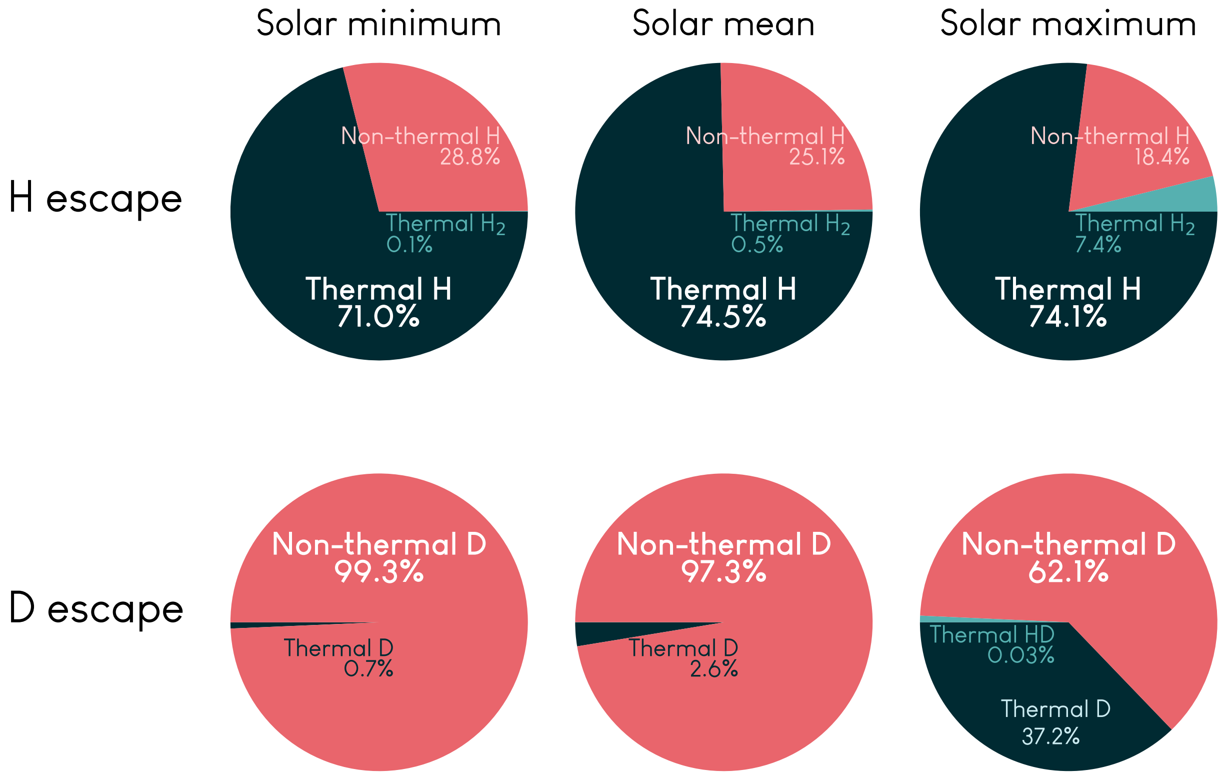

Figure 3.6: Relative escape contributions for H and D. As expected based on the literature, thermal escape dominates for H during all solar conditions, but non-thermal escape dominates D escape, even at solar maximum. Although we do model non-thermal escape of H_2 and HD, their contributions are completely negligible (see Table 3.2).

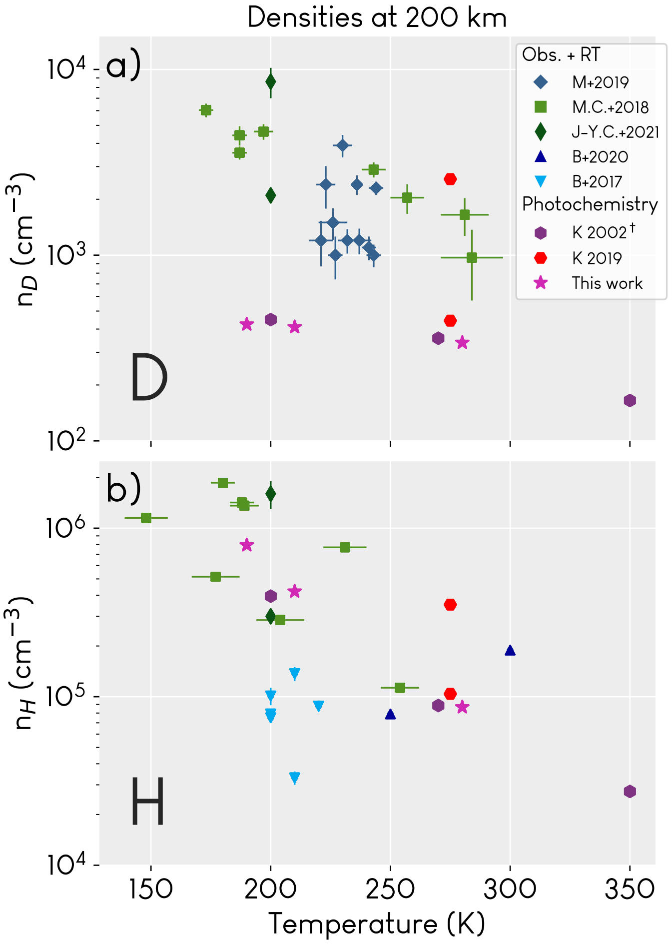

Figure 3.7: D and H densities at 200 km († 250 km) from multiple studies. Data represent multiple solar zenith angles, seasons, hemispheres, etc. M+2019: Mayyasi et al. (2019). M.C.+2018: Chaffin et al. (2018). J-Y.C.+2021: Chaufray et al. (2021a). B+2020, 2017: Bhattacharyya et al. (2017, 2020). K 2002, 2019: V. A. Krasnopolsky (2002, 2019). Entries under "Obs. + RT" used brightness observations from either HST (Bhattacharyya et al. 2017) or MAVEN IUVS (all others) with radiative transfer modeling for density retrievals. For these studies, invisible density error bars indicate uncertainty smaller than the marker size. Temperature error bars indicate that temperature was retrieved from spacecraft data, while missing temperature error bars mean it was a model parameter or output. Uncertainties for photochemistry studies are not calculated. Photochemical modeling typically reports an order of magnitude less D than other methods, which may be due to observation biases toward times of brighter D emission. There is no similar discrepancy in H densities.

3.5 Discussion

Figure 3.7 places our D and H densities in context with other studies. We have only consolidated reported densities; we make no attempt to filter by observation geometries. Nevertheless, there appears to be an inverse relationship of densities and temperature for both species. We can also see that photochemical models (red/purple/pink points) produce D densities that are an order of magnitude smaller than densities retrieved using observations and radiative transfer modeling; the same discrepancy does not occur for the H densities. Deuterium Lyman α is difficult to separate from hydrogen Lyman α; the D density discrepancy may potentially be explained by a systematic bias toward anomalously bright D emissions. One exception is the density of D at ~2500 and T=275 K in the work by V. A. Krasnopolsky (2019); this point represents a model run with a high amount of water in the thermosphere, whereas all the other photochemical results have a comparatively lower water abundance. This comparison demonstrates that our model output is in reasonable agreement with other works.

As mentioned previously, we do not include cloud or dust microphysics, although these processes do have an important effect on the water cycle. These effects are explored in two recent papers using the Laboratoire de Météorologie Dynamique Planetary Climate Model (LMD-PCM) to study the creation of water ice clouds and their role in controlling the D/H ratio (Rossi et al. 2022; Vals et al. 2022).

3.5.1 Can inclusion of non-thermal escape in the model yield an estimation of water loss similar to the amount calculated in geomorphological studies?

By considering both thermal and non-thermal escape, we can now compute the D/H fractionation factor, which represents the relative efficiency of D and H escape. It is defined as:

$$\mathrm{f} = \frac{\phi_{\mathrm{D}}/\phi_{\mathrm{H}}}{[\mathrm{HDO}]_{\mathrm{s}}/2[\mathrm{H_2O}]_{\mathrm{s}}} \tag{3.4}$$

Where $\phi_X = \phi_{X,t} + \phi_{X,n}$ is the rate at which species X (D or H) escapes from the top of the atmosphere due to both thermal (t) and non-thermal (n) processes. The denominator represents the D/H ratio in water measured at the surface (s), which is a proxy for the D/H ratio in the larger exchangeable reservoir.

The fractionation factor is important not only because it tells us how efficient loss of D is compared to loss of H, but also because it is useful for calculating the integrated water loss from a planet. Long-term enrichment of the heavy isotope (D) due to differential escape of D and H can be modeled using Rayleigh fractionation (Chamberlain et al. 1987; Yung et al. 1998):

$$\frac{(\mathrm{D/H})_{\mathrm{now}}}{(\mathrm{D/H})_{\mathrm{past}}} = \left(\frac{[\mathrm{H}]_{\mathrm{past}}}{[\mathrm{H}]_{\mathrm{now}}}\right)^{1-\mathrm{f}} \tag{3.5}$$

Equation 3.5 is used to calculate water loss from Mars. The D/H ratio on the left hand side represents the ratio measured in water in the exchangeable reservoir (the seasonal polar caps, near-surface ices, and atmospheric water vapor), and the ratio $\mathrm{H_2O_{past}/H_2O_{now}}$ can be substituted in on the righthand side and rearranged, obtaining (E. M. Cangi et al. 2020) (where W is water):

$$\mathrm{W}_{\mathrm{lost}} = \mathrm{W}_{\mathrm{now}}\left(\left(\frac{(\mathrm{D/H})_{\mathrm{now}}}{(\mathrm{D/H})_{\mathrm{past}}}\right)^{1/(1-\mathrm{f})} - 1\right) \tag{3.6}$$

Implicit in these equations is the assumption that $[\mathrm{H}] \gg [\mathrm{D}]$, so that the past and present abundances of H_2O are reasonable representations of the entire water budget. In the present day, the ratio of D/H is well constrained by many observational studies to be approximately 4-6 × standard mean ocean water (SMOW) (Villanueva et al. 2015; Encrenaz et al. 2018, and references therein). Current research also has identified a likely present-day exchangeable reservoir water budget of 20-30 m GEL (Lasue et al. 2013, and references therein). By obtaining a reliable value for f, we can combine all these values to calculate the inventory of water on ancient Mars.

E. M. Cangi et al. (2020) suggested that the difference between the mean atmospheric f_t (considering only thermal escape) and f_{tn} (considering both thermal and non-thermal escape) was several orders of magnitude. Because they did not directly model non-thermal escape, they arrived at this conclusion by incorporating the non-thermal escape velocity given by V. A. Krasnopolsky et al. (1998) into their model. We are now in a position to compare with those estimates; our

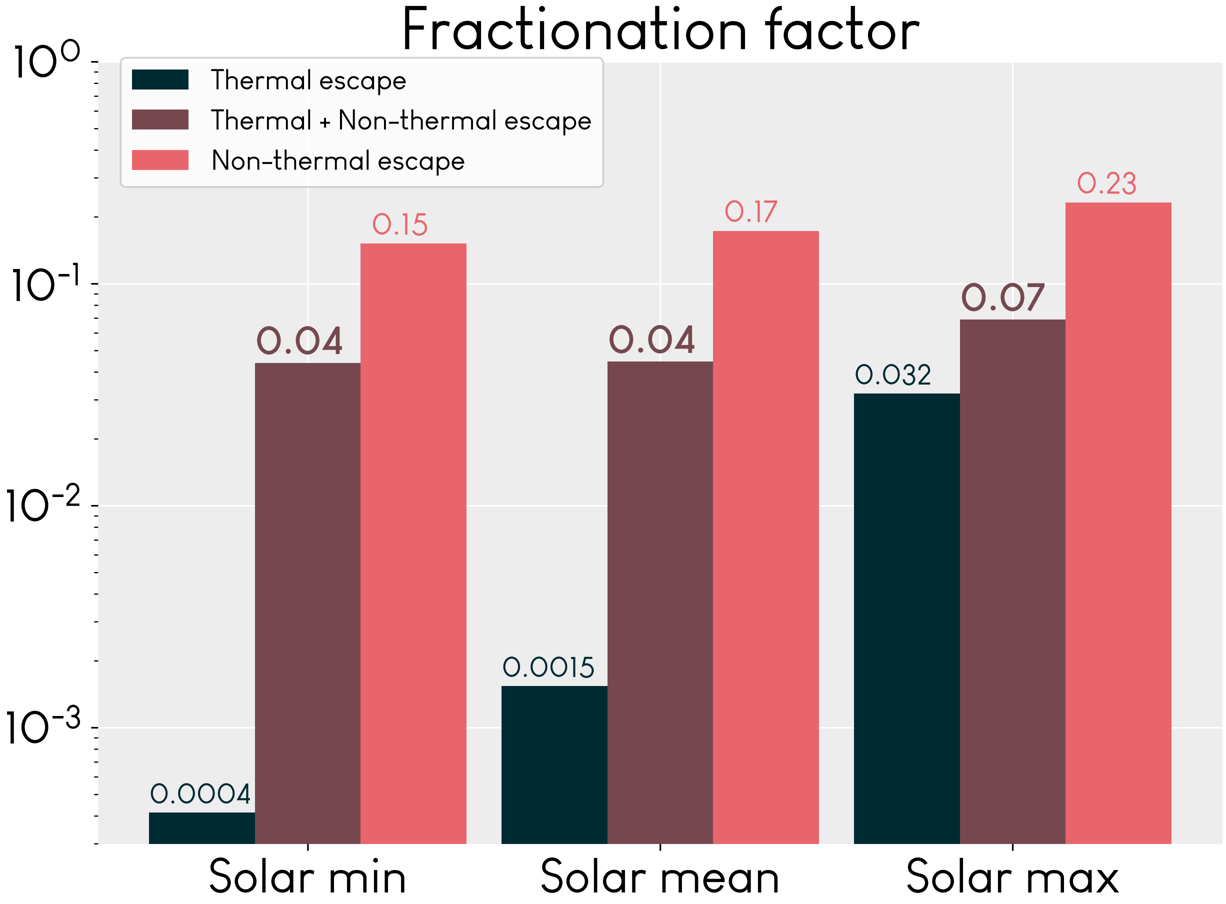

Figure 3.8: The fractionation factor f for three different modes of escape. Increased solar activity leads to amoderate increase in total f, and inclusion of non-thermal escape increases total f by 1-2 orders of magnitude during solar minimum and mean. Fractionation represents the escape efficiency of D compared to H, meaning that $f = 0.04$ represents a 4% escape efficiency of D. Non-thermal escape is an effective escape method for D under all solar conditions.

calculations of the fractionation factor are shown in Figure 3.8. E. M. Cangi et al. (2020) calculated $f = 0.06$ for their standard atmosphere, based on their modeled thermal escape and estimated non-thermal escape. We calculate a total escape fractionation of $f = 0.04$ for our solar mean atmosphere, which has the same insolation and similar temperatures, and is not far off from their 0.06. Our results are consistent with their thermal escape $f = 0.002$ for the standard atmosphere (roughly equivalent to our solar mean atmosphere). Our results show that while overall D escape at Mars is around 4–7% as efficient as H escape, non-thermal D escape is much more efficient, between 15–23% that of H.

Our results yield integrated water loss of 147–158 m GEL (present day exchangeable reservoir = 30 m GEL, $f = 0.04$–0.07, D/H=5.5×SMOW). This total loss still does not agree with the geological estimates of 500+ m GEL (Lasue et al. 2013). The discrepancy is summarized in Figure 3.9. Figure 3.9a shows the gap between the amount of water loss calculated by atmospheric models (Yung et al. 1988; Kass et al. 1999; V. Krasnopolsky 2000; V. A. Krasnopolsky 2002; E. M. Cangi et al. 2020) and that inferred from geomophological observations (Lasue et al. 2013, and references therein). The time-averaged H escape rate curve suggests that the rates observed today (Jakosky et al. 2018) are unlikely to be near the average, and that escape was likely higher in the distant past, enabling greater water loss. Plausible explanations could include periods of hydrodynamic escape, a more EUV-active young sun driving greater photochemistry, extreme obliquities (Laskar et al. 2004; R. Wordsworth 2016), or other as of yet unknown dynamics.

It is also possible that some water may have been sequestered into the surface. Recent work by Scheller et al. (2021) suggests that this amount may have accounted for between 30–99% of all missing water. More smaller-scale models and many observations will be needed to constrain this large range further. Hydrated minerals may contain 130–260 m GEL equivalent water Wernicke et al. (2021), but the time of emplacement and any fractionation of the process is unclear. In general, due to the chaotic evolution of obliquity (Laskar et al. 2004) over Mars' history, it is extremely difficult to qualitatively describe escape rates in the past. Although it is difficult to extrapolate much from the present-day rates, high loss of water via escape to space is not ruled out.

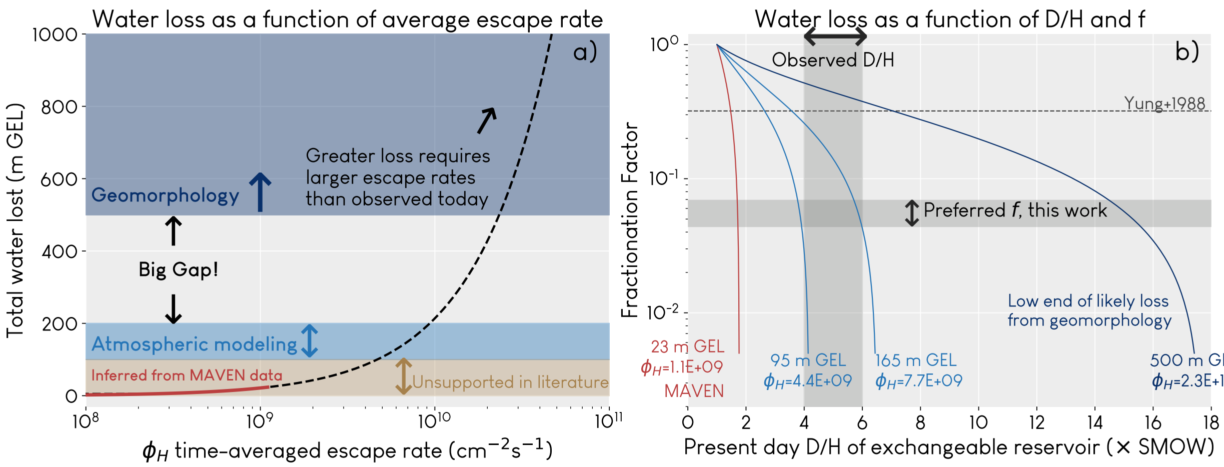

Figure 3.9: a): Possible water loss as a function of long-term average H escape rate ϕ_H, $\mathrm{W}_{\mathrm{lost}} = \bar{\phi}_{\mathrm{H}} t$, where $t = 4.5$ billion years. A significant gap separates the amount of water loss inferred from atmospheric modeling and geomorphological studies. Additionally, escape rates determined from MAVEN data enable very small amounts of water loss that are not consistent with the geological evidence. b): Water loss lines represent solutions to equation 3.6, assuming 30 m GEL in the present-day exchangeable reservoir. The regions matching the best values of D/H and f are shaded in gray, with the overlapped rectangle representing our best estimate of the present-day atmosphere. (The fractionation factor calculated by Yung et al. (1988) is shown for reference, though it is high due to the highly uncertain exospheric temperatures then used.)

Figure 3.9b also helps demonstrate when it is important to know the value of f rather precisely. Discriminating between $f = 0.04$ or $f = 0.07$ is not particularly important: below $f = 0.1$, water loss curves are relatively vertical, meaning that a change in f does not equate to a significant change in water loss, but this is less true the closer f gets to 1. (For another view, see Figure B.4 for water loss as a function of f for a single D/H ratio.)

Considered together, these insights tell us that non-thermal escape processes for D are important to model in order to accurately understand how D escapes from Mars. This conclusion may not hold for other planets, moons, or exoplanets; on bodies which are colder, larger, or otherwise less conducive to thermal escape, non-thermal escape may have a greater role to play.

3.5.2 Other non-thermal processes

As mentioned earlier, we do not model interactions with the solar wind. Lewkow et al. (2014) have calculated that penetrating solar wind protons can produce 4.18×10^4 cm^{-2}s^{-1} energetic neutral H atoms (ENAs) which escape. This is a negligible amount compared to our total non-thermal H escape, which is 6.5×10^7 cm^{-2}s^{-1}, so we do not expect it to change our results. Without a value for D ENAs, we cannot make an immediate comparison, but we can calculate what fraction of our total H column the H ENAs make up. For our solar mean model (Figure B.1), the fraction is 8×10^{-11}. If we multiply this fraction by our D column, we obtain an additional 25 cm^{-2}s^{-1} non-thermally escaping D atoms. Solar wind penetration should thus be negligible for the non-thermal escape we calculate at the altitudes we model, but an important interaction to consider during times of extreme solar activity or at higher altitudes in the exosphere. A future study on D ENA production would also help refine this contribution's value.

We do not account for the collision of hydrogen atoms or molecules with hot oxygen, which is another significant source of hot atoms in the martian atmosphere. Assuming an exospheric temperature of 240 K, Gacesa et al. (2012) calculated that 1.9×10^5 cm^{-2}s^{-1} H_2 molecules escape as a result of collision with hot oxygen, which is larger than our non-thermal H_2 flux by 1-2 orders of magnitude depending on solar conditions (see Table 3.2). They also estimate that 74 HD molecules

$cm^{-2}s^{-1}$ escape via this mechanism. This would bring our total HD escape to approximately 100 $cm^{-2}s^{-1}$, an order of magnitude larger than our current result. Other species may also play a role; Gacesa et al. (2017) calculate that the total non-thermal escape of OH is 1.07×10^{23} s^{-1}, i.e. 7.4×10^5 $cm^{-2}s^{-1}$. Even added together, these numbers are all still orders of magnitude smaller than the non-thermal atomic escape fluxes, and will not significantly affect our results. If we included them, the net effect would be to boost H escape, decreasing the fractionation factor and total water loss.

Energization of atomic H and D by collision with hot oxygen may be more significant. Shematovich (2013) estimates, for specific density profiles and temperatures, a total possible escape flux of hot H produced this way to be 6×10^6 $cm^{-2}s^{-1}$ at low solar activity. This is 9% of our non-thermal H escape (see Table 3.2). Our non-thermal D escape is 3 orders of magnitude lower than the H escape. If we apply this scaling relation to hot O collisions with D, we can expect that this pathway might produce D escape on the order of 10^3, which is the same order as our calculated non-thermal escape fluxes. If we instead generously assumed an extra 9×10^3 hot D atoms produced from collision with hot O, doubling our total, we would expect to also double our fractionation factor, to $f = 0.08 - 0.14$.

3.5.3 Future opportunities and directions

There are several things that could enhance our model. The first likely avenue worthy of exploration would be to perform a similar study, but with a more physically-motivated parameterization of atomic O escape. Fixing the O escape at 1.2×10^8 $cm^{-2}s^{-1}$ was sufficient for the scope of this work; our results represent long-term equilibrium, when it is possible to adopt reasonable means for parameters like O escape. Adding a dynamically evolving escape flux boundary condition for atomic O would enable a more comprehensive understanding of shorter-term variations in H and D escape rates, such as a result of regular seasonal cycles. This would better capture the interplay between the hydrogen species and CO_2, the main component of the atmosphere and a significant source of O. This would also present an opportunity to include processes more important to O loss, such as ion pickup, ion/polar outflow, and sputtering. We do not include these as we focus on H and D loss, which are dominated by other processes.

We have also been forced to make some unavoidable assumptions about the basic chemistry, owing to a lack of laboratory data. While we have made a best attempt to use existing reaction rate coefficient data from several different papers and databases, a comprehensive catalogue of rate coefficients, branching ratios, and cross sections for deuterated reactions is not available in the literature at this time. Most especially, future photochemical models would benefit from accurate photoabsorption cross sections for deuterated neutrals other than HDO (including OD and HD in particular), and measured reaction rate coefficients for as many of the deuterated reactions with estimated rates in Table 3.1 as possible. While not all reactions will significantly affect the chemistry, certain rates that dominate production or loss of a species can have strong effects, affecting densities up to a few orders of magnitude (see, for example, Fox et al. (2017)).

Photochemical modeling often entails excluding some important processes that are better captured in higher-dimensional models. Bluejay is the first photochemical model to couple the ion and neutral atmospheres from the upper atmosphere down to the surface, but there is still an opportunity for future work to give more attention to surface-atmosphere interactions. Our inclusion of surface-atmosphere interactions is primarily relegated to surface density boundary conditions for certain species. A more detailed parameterization of processes such as volcanic outgassing, major seasonal changes in the polar caps, water adsorption and desorption on dust grains and dust lifting, deposition of volatiles, and the role of non-volatiles such as perchlorates, salts, and other non-water ices could yield new insights into the planetary climate system as a whole.

Our results also have implications for the detectability of deuterated ions by present and future Mars missions. Using MAVEN's NGIMS instrument, the deuterated ions that we model typically occupy the same mass/charge ratio bin as a more prevalent H-bearing species. For example, D^+occupies the same bin as $H_2{}^+$, but the latter is far more abundant. The deuterated species in our model which do not overlap with an H-bearing species are H_2D^+(mass bin 4), $HD_2{}^+$(5),

H_2DO^+(20), $HDO_2{}^+$(35), and ArD^+(42). However, several of these species are expected to be very rarefied and thus difficult to detect, and others may overlap with species we do not model that do exist on Mars, such as helium in mass bin 4. These degeneracies make obtaining deuterated ion densities challenging; doing so will require inventive methods applied to existing data or new methods with new instruments.

3.6 Conclusions

We have used a 1D photochemical model, bluejay, that fully couples ions and neutrals from surface to space to study production of hot D from planetary ionospheric processes. We show that the deuterated ionosphere behaves relatively similar to the H-bearing ionosphere. This result is somewhat expected, as measurements of rate coefficients for deuterated reactions are much less available than the H-bearing counterpart reaction rate coefficients.

For the first time, we have self-consistently quantified, in raw flux and in percent of total escape, the thermal and non-thermal escape fluxes of H, D, H_2, and HD sourced from planetary ionospheric reactions under different solar conditions. We also show the first identification of the dominant chemical reactions which produce hot D. Our results confirm earlier suggestions that non-thermal escape dominates D escape at Mars, although our results have shown that this is true throughout the solar cycle rather than just during quiet solar conditions.

We also confirm an earlier prediction (E. M. Cangi et al. 2020) that including non-thermal escape when calculating the D/H fractionation factor will result in a fractionation factor several orders of magnitude higher than if it is neglected. However, the resulting fractionation factor is 0.04–0.07, meaning that D escape is only about 4-7% as efficient as H escape. If the fractionation has consistently been this small, and we also assume that ϕ_H has been similar to the value today through time, it is difficult to ascribe the large amount of water loss that we see indicated in the rock record to atmospheric escape alone. On the other hand, the dust storm season on Mars, as well as normal seasonal variations between perihelion and aphelion, are characterized by spatially and temporally localized enhancements of the D/H ratio, water abundance, and H escape (Chaffin et al. 2017; Heavens et al. 2018; Aoki et al. 2019; Vandaele et al. 2019; A. A. Fedorova et al. 2020; Stone et al. 2020; Chaffin et al. 2021; A. Fedorova et al. 2021; Holmes et al. 2021; Daerden et al. 2022; Villanueva et al. 2022, and references therein). It is not yet clear if enhanced D escape or a heightened fractionation factor also occur along with these seasonal changes, although it seems likely (Alday et al. 2021); if they do, then the assumption of a constant fractionation factor over time cannot hold, and we will have to introduce some additional nuance to our use of Rayleigh fractionation to estimate water loss.

Ongoing improvements in modeling, especially coupling between 1D and 3D models, as well as continual advancements in instrumentation for planetary missions will be necessary to continue putting together the puzzle of water on Mars throughout history.

Chapter 4

Seasonal enhancement in upper atmospheric D/H at Mars driven by both thermospheric temperature variations and mesospheric water

The contents of this chapter will be submitted soon to Geophysical Research Letters.

4.1 Abstract

The D/H ratio in water, R_{water}, on Mars is 4-6× the Earth ratio, signifying massive water loss to space. Recently, new measurements of the D/H ratio in hydrogen, R_{atomic}, have revealed that R_{atomic} in the thermosphere can reach 20× the Earth ratio during southern summer. Here, we use a fully coupled 1D photochemical model to provide a theoretical explanation for the drivers of R_{atomic}. We test three possible mechanisms for the enhancement: high thermospheric temperatures, excess mesospheric water, and changing insolation, and find that R_{atomic} can achieve values between 15× the Earth ratio (due to water) and 25× the Earth ratio (due to temperature). The root cause is that H escape is diffusion-limited, while D escape is energy-limited. Our results underscore how R_{atomic} reflects lower atmospheric dynamics, and the need for concurrent measurements of mesospheric water, thermospheric temperatures, and R_{atomic} to understand seasonal changes in Mars water loss.

4.2 Background and motivation

Ratios of isotopes and isotopologues in planetary atmospheres encode a history of changes to the atmospheric composition over time. On Mars, the argon isotope system reveals how sputtering has affected atmospheric loss (Slipski et al. 2016; Jakosky et al. 2017); the nitrogen isotope system is used to reconstruct potential past atmospheric compositions (e.g. Hu et al. 2022; Pieris et al. 2022); and the hydrogen isotope system is used to probe long-term integrated water loss (Owen et al. 1988; Yung et al. 1988; M. H. Carr 1990, and many others). Because of the interest in water loss from Mars, the isotopic ratio of deuterium (D) and hydrogen (H) is typically measured in water, and computed as

$$\mathrm{R}_{\mathrm{water}} = \frac{[\mathrm{HDO}]}{2[\mathrm{H_2O}]}, \tag{4.1}$$

where square brackets represents a number density (abundance). The mean value of $\mathrm{R}_{\mathrm{water}}$ is 4-6 × VSMOW (Vienna Standard Mean Ocean Water, the ratio measured in Earth's oceans), with local variations between 1–10× VSMOW (Villanueva et al. 2015; Encrenaz et al. 2018; Villanueva et al. 2021, 2022). The overall present-day enhancement relative to Earth is thought to be driven by escape to space of H and D, produced when atmospheric water dissociates.

Despite the key role of the atomic species in the parching of the planet, the atomic D/H ratio,

$$\mathrm{R}_{\mathrm{atomic}} = \frac{[\mathrm{D}]}{[\mathrm{H}]}, \tag{4.2}$$

has received considerably less attention than $\mathrm{R}_{\mathrm{water}}$. New results obtained with the MAVEN (Mars Atmosphere and Volatile EvolutioN) IUVS (Imaging UltraViolet Spectrograph) instrument indicate a strong seasonal component to enhancements in H and D brightness and $\mathrm{R}_{\mathrm{atomic}}$ (Chaufray et al. 2021a; Clarke et al. 2022), distinct from dust storm activity, meaning that the seasonal changes must have a repeatable, seasonal driver.

In this work, we use a fully coupled ion-neutral 1D photochemical model (E. M. Cangi et al. 2023) to explore three options for the driving parameter of $\mathrm{R}_{\mathrm{atomic}}$ enhancements: greater thermospheric temperatures, changing insolation, or increased mesospheric water abundance. We find that changing insolation throughout the Mars year has a negligible effect, and that the thermospheric temperature and mesospheric water can both enhance R_{atomic} up to values of 25× VSMOW. The thermospheric temperature does so by suppressing the ability of H to diffuse from the mesosphere up to the escape region, while mesospheric water enhances R_{atomic} by increasing the thermospheric reservoir of H & D above the cold trap. This work demonstrates that large variations in the upper atmospheric atomic D/H ratio are possible due to both temperature variations in the thermosphere and the dynamics of water in the mesosphere on seasonal timescales, suggesting a need for concurrent data from the surface to space to fully characterize martian atmospheric dynamics and escape.

4.3 Goals and modeling approach

The key question of this work is: How do seasonal changes in atmospheric conditions affect R_{atomic} and R_{water}, and what distinguishes the H and D responses? This question thus aims to understand the sub-annual response to seasonal perturbations. To answer it, we use the same modeling approach as (E. M. Cangi et al. 2023) to explore the role of three different atmospheric conditions in controling R_{atomic}. Full details are available in that paper and the archived code (E. M. Cangi et al. 2022), and the model parameters are summarized in Table S1. In this work, we run sequential simulations, using the output of one as the input for the next, so that we are able to examine the time-dependent photochemistry of the atmosphere.

We test three specific atmospheric conditions, which serve as our primary simulation variables:

(1) **Thermospheric temperature**: Past work has shown that the thermospheric temperature strongly affects D/H fractionation (E. M. Cangi et al. 2020) due to its relevance to Jeans escape. Our model uses a functional form for temperature as a function of altitude, and the thermospheric temperature is controlled by modifying T_{exo}, the temperature at top of the model (250 km).

(2) **Mesospheric water abundance**: Water in the mesosphere (above the cold trap), driving enhanced escape, has been demonstrated to occur either due to dust storms (Heavens et

al. 2018; Aoki et al. 2019; Vandaele et al. 2019; A. A. Fedorova et al. 2020; Stone et al. 2020; Chaffin et al. 2021; Holmes et al. 2021; Villanueva et al. 2021) or seasonal effects (Shaposhnikov et al. 2019; Neary et al. 2020).

(3) **Insolation**: Mars' orbit is reasonably eccentric, such that the orbital semi-major axis (sun-Mars distance) ranges from 1.38 AU at aphelion to 1.66 AU at perihelion, with a mean value of 1.524 AU. The incoming solar irradiation affects the dissociation of atmospheric molecules including water, and the different efficiency of photolysis of HDO compared to H_2O has been shown to be more important than condensation differences in fractionating the photolysis products (Alday et al. 2021).

The values of these three primary inputs according to simulation are described in Table 4.1. We run three sets of simulations: "Temperature", "Water", and "Insolation". In each set, we model an annual cycle by imposing the appropriate seasonal input parameters on the model, running it for one "season" (1/4 of a Mars year, 1.4838759×10^7 seconds), and then using the atmospheric state at the end of each simulation as the initial conditions for the next season in the cycle.

In all simulations, there are no sub-seasonal temperature profile variations; the temperature profile only changes at the start of a season. For the "Water" simulations, the water profile is modified below 72 km once at the season start and held fixed below that altitude for the duration of a season. Water densities above 72 km are solved for self-consistently (E. M. Cangi et al. 2023). In the "Insolation" set, insolation is also modified at the beginning of a season and then held fixed for that season.

We use logarithmically spaced timesteps in each simulation. Timesteps are small earlier in the simulation ($dt \approxeq 10^{-3}$ seconds) and large near the end ($dt \approxeq 10^7$ seconds). For the seasonal cycle simulations, we save the model state in quasi-logarithmically spaced points from 1 second to 1 day, then once per week after. This scheme is shown in Figure C.1.

In this work, we have used the best available photodissociation cross sections for HDO (B.-M. Cheng et al. 1999; Chung et al. 2001; B. M. Cheng et al. 2004), as well as assuming that HDO shares

		"Spring"	"Summer"	"Fall"	"Winter"
Set 1: Temperature	T_{exo} (K)	225	275	225	175
	Water	—	—	—	—
	Insolation	—	—	—	—
Set 2: Water	T_{exo} (K)	—	—	—	—
	Water	Mean	High	Mean	Low
	Insolation	—	—	—	—
Set 3: Insolation	T_{exo} (K)	—	—	—	—
	Water	—	—	—	—
	Insolation	Mean	High	Mean	Low

Table 4.1: Three simulation sets used in this work. To model long-term equilibrium, we run each of the mean case ("Spring"/"Fall"), high case ("Summer"), and low case ("Winter") to equilibrium in standalone simulations. To model a seasonal cycle, for each set, we run four sequential simulations in seasonal order, with the output of one serving as the starting input for the next. Because we model in 1D, the seasons are notional and do not specifically represent either northern or southern hemisphere, but rather a whole-planet mean. — represents the mean temperature (225 K), the mean insolation spectrum, or the mean water profile. See Figure 4.4 for the water profiles and Figure C.2 for the insolation spectra.

the H_2O cross section at Lyman α, where data are not available. We also ran several simulations in which both H_2O and HDO use the H_2O cross sections, resulting in a slightly larger D/H ratio (see Appendix C, Figures C.4 and C.10).

Our simulation results indicate that insolation changes have a negligible effect on the atomic D/H ratio (Figure C.2), so we will not discuss these results at length. We also explored adding additional water in the lower atmosphere (Figure C.7), with similarly small impacts on D/H.

4.4 Two limits on escape: the diffusion limit and the energy limit

Understanding the diffusion and energy limits of escape of light atoms from planets is critical to understanding the remainder of this paper. For that reason, we review here the key concepts.

Two major variables affect the escape of light atoms like H and D to space: the amount of energy available to be imparted to the atoms, and the total abundance of atoms near the exobase. In order to escape from the atmosphere, H and D must both gain enough energy to exceed escape velocity, and also travel from wherever they are first produced through chemistry up to the escape region.

As temperatures rise, densities of heavier species and their kinetic energies increase (Mayyasi et al. 2018), and it becomes harder for minor constituent atoms to diffuse through the atmosphere, creating a bottleneck defined by the limiting flux (Hunten 1973):

$$\phi_\ell \approxeq \frac{D_i n_i}{H_a}\left(1 - \frac{m_i}{m_a}\right) \tag{4.3}$$

where D_i, n_i and m_i are the diffusion coefficient, density, and mass of species i, and H_a and m_a are the mean scale height and molecular mass of the background atmosphere.

Figure 4.1 shows the limiting flux for H and D for typical Mars conditions ($T_{exo} = 225$ K). H is a relatively abundant trace gas, and is mostly produced in the lower atmosphere due to the abundance of water ice. However, $\phi_{\ell,H}$ in the mesosphere is lower than the typical maximum possible rate of H from the top of the atmosphere (right gray shaded area), so that typical escape rates tend to be similar to the diffusion rate through the mesosphere, ϕ_ℓ. H escape is thus diffusion-

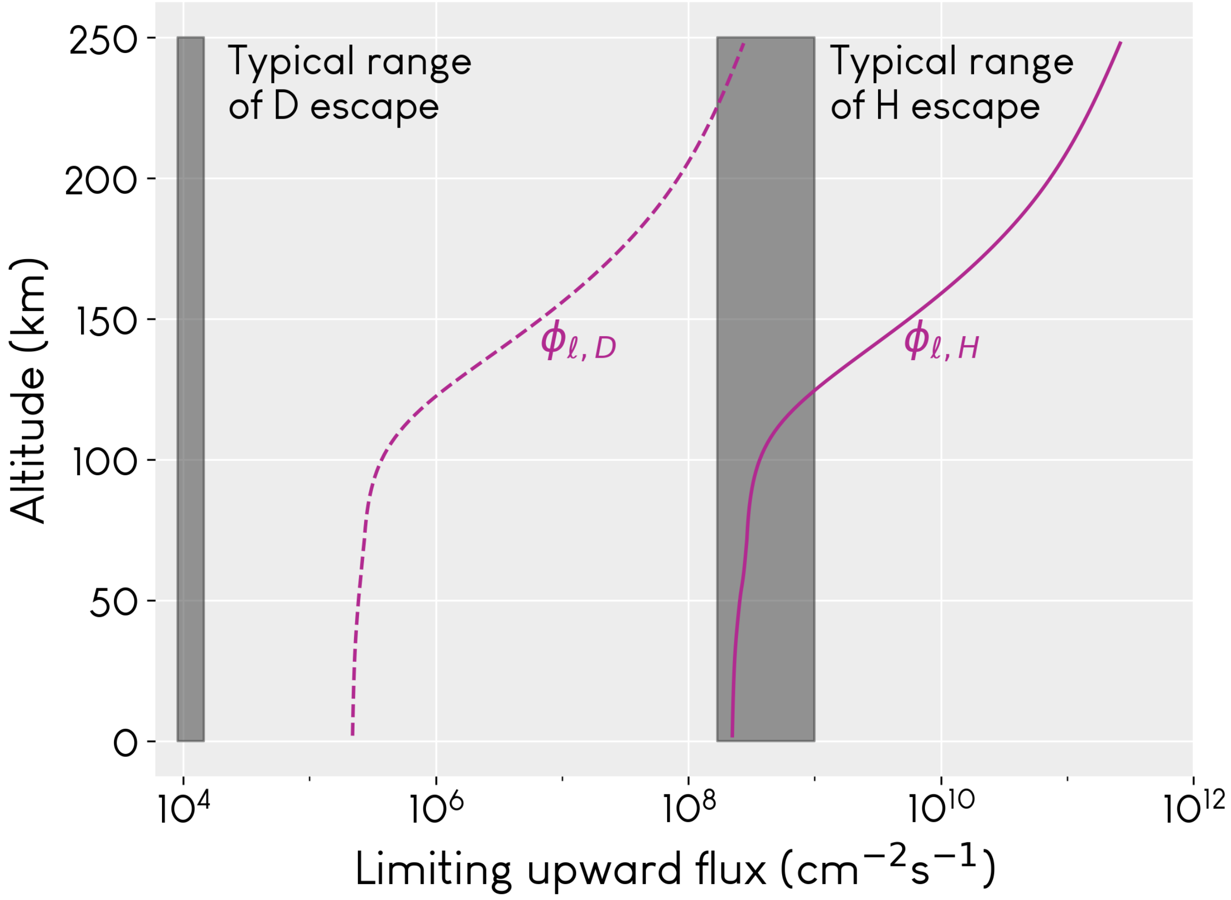

Figure 4.1: The limiting upward flux ϕ_ℓ (Hunten 1973) through the atmosphere for H+H_2+OH (solid line) and D+HD+OD (dashed line) at a typical exobase temperature of 225 K. Also plotted in gray are typical ranges of H escape (Jakosky et al. 2018) and D escape (E. M. Cangi et al. 2023). Since ϕ_H is comparable to or larger than the limiting flux in the mesosphere from 50-100 km, H escape is diffusion-limited: It typically does not occur at a rate higher than this mesospheric bottleneck rate (except for cases of impulsive changes in the atmosphere). On the other hand, ϕ_D is typically smaller than the peak mesospheric flux; D escape is thus not diffusion limited, but rather energy-limited at the top of the atmosphere.

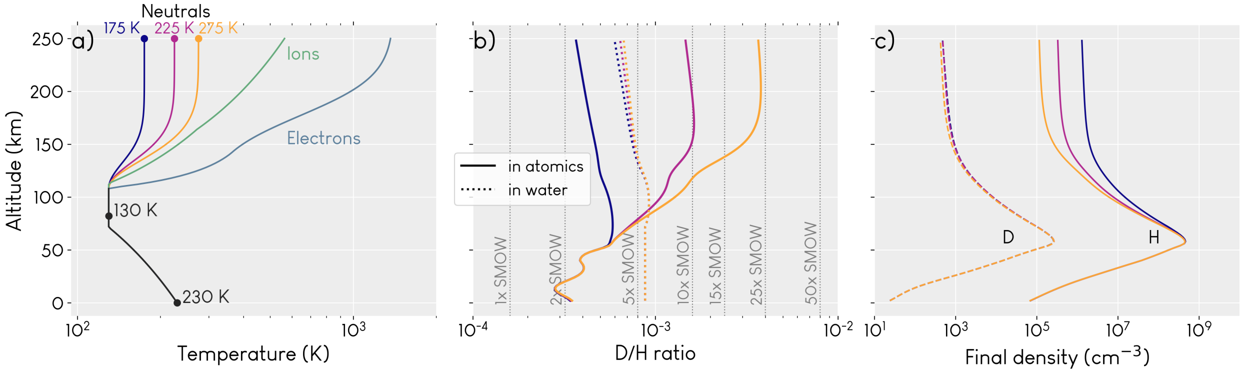

Figure 4.2: Input, atomic D/H ratio results, and associated H and D density profiles for the simulations with variable thermospheric temperatures. a) Temperature profiles adopted. b) Response of the D/H atmospheric profile (end of the season). c) D & H density profiles. Note that in panels b and c, the colors of the lines map to the neutral temperatures in panel a. Note also that SMOW is the same as VSMOW.

limited (Hunten 1973; Zahnle et al. 2008). In contrast, the limiting flux for D, $\phi_{\ell,D}$, is much higher than the maximum rates of escape (left gray shaded area). D escape is thus energy-limited.

In summary: H escape being diffusion-limited means that the main "roadblock" for H escape at Mars is the speed with which it can be supplied to the upper atmosphere from the lower atmosphere. D escape being energy-limited means that the main "roadblock" for D escape at Mars is the energy available at the exobase.

4.5 Exospheric temperature drives $\mathrm{R_{atomic}}$ enhancements by controlling H diffusion

Figures 4.2 and 4.3 show the model results from variation of the exobase temperature (which also changes the overall thermospheric temperature, due to the functional form we use for temperature), with altitude profiles of $\mathrm{R_{atomic}}$ and H and D densities shown in Figure 4.4 and time evolution of $\mathrm{R_{atomic}}$, the densities, and their escape fluxes shown in Figure 4.3.

Figure 4.2a shows the temperature profiles adopted. Ion and electron profiles are held fixed due to limited new data available to constrain them (Hanley et al. 2022; E. M. Cangi et al. 2023) and the fact that due to observing geometries and instrument pointing requirements, it is difficult to obtain simultaneous temperature measurements of different populations such as neutrals and ions (Gupta et al. 2022). The three different colors represent different adopted temperatures for the neutral exobase; here, the warmest temperature corresponds approximately to mean summer conditions, the coldest to mean winter, and the middle value to the global mean. The atmosphere is isothermal below about 110 km. Panel 4.2b shows how $\mathrm{R}_{\mathrm{atomic}}$ and $\mathrm{R}_{\mathrm{water}}$ respond; $\mathrm{R}_{\mathrm{water}}$ is mostly unaffected, while $\mathrm{R}_{\mathrm{atomic}}$ ranges from 2 to nearly 25× VSMOW in the upper atmosphere. Figure 4.2c shows that the change in upper atmospheric D is minimal, whereas a higher temperature leads to a 10× rarefaction of H, the same amount by which the D/H ratio increases.

Figure 4.3 shows the same information in an annual cycle by placing time on the x-axis. Panel 4.3c shows even more clearly that the primary driver of the increase in R_{atomic} is the large decrease of the H density. (D density also decreases, so it cannot be the primary driver of a D/H increase.)

The responses of D and H escape to temperature perturbations are dissimilar, as shown in panels 4.3d and e. As explained previously, H escape is diffusion-limited, while D escape is energy-limited. Thus, when the temperature rises, an additional fraction of upper atmospheric H suddenly has enough energy to escape. However, the resupply of H from below is not as rapid, so after a short time, H escape returns to a more nominal value. On the other hand, as long as the temperature is enhanced, so too is D escape enhanced. There was already plenty of D in the escape region that just needed extra energy before it could escape. These examples were given for “summer” when the temperature increases, but an analogous effect occurs when the exobase cools.

The uniqueness of H as a diffusion-limited species on Mars is important in understanding D/H variations and escape; the D/H ratio of other isotopologue pairs (see Figure C.3) do not show such dramatic temperature dependence, as heavier molecules in these other isotopologue pairs are less abundant and do not escape as readily as H or D.

H and D escape will be discussed further in the following section from a point of comparison with the results for the “Water” set.

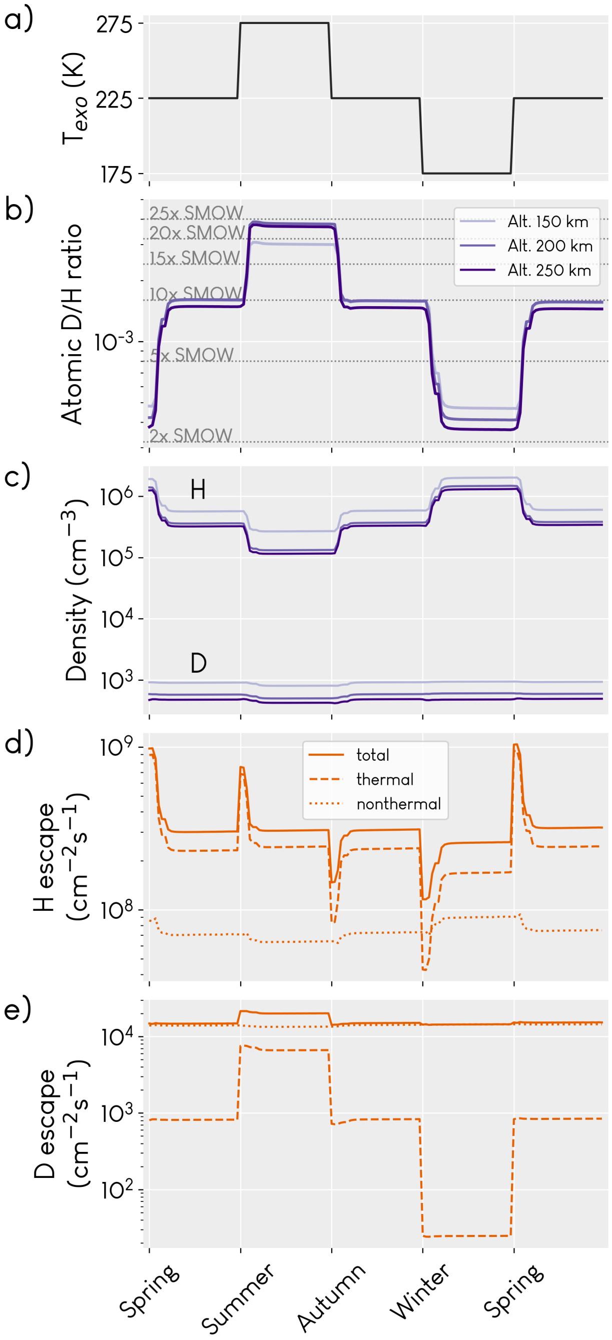

Figure 4.3: Atmospheric behavior over one Mars year. The length of each season is 1/4 Mars year, or 1.48 $\times 10^7$ seconds. a) Exospheric temperatures adopted during each "season". b) The seasonal response of R_{atomic} at three characteristic altitudes. c) Changes to H and D densities as a result of cycling of the inputs. d) H and e) D escape rates (total, thermal, and non-thermal) from the top of the atmosphere.

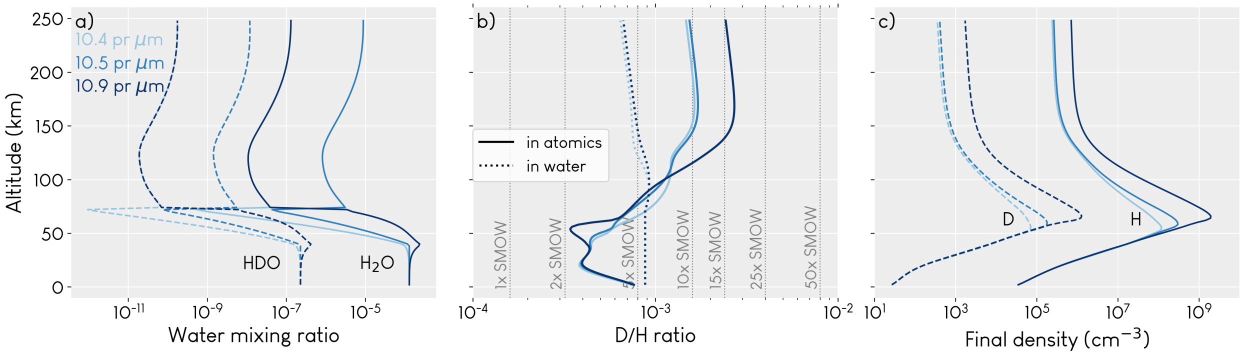

Figure 4.4: The same as Figure 4.2, but for different initial mesospheric water abundances. The profile with the most water has nearly 300 ppm of water at its peak, which is a little higher than has been observed during dust storms (e.g. Vandaele et al. 2019). In this scenario, H and D abundances in the mesosphere increase due to the additional supply of those atoms above the cold trap. Note here that the water profiles change as the simulation runs, meaning that the mean water profile (middle blue) begins with more water in the thermosphere due to chemistry that occurred in the previous, high-water season (dark blue profile).

4.6 Enhanced mesospheric water also drives R_{atomic} enhancements by supplying more H above the mesospheric diffusion bottleneck

Figure 4.4 shows the altitude profiles of R_{atomic} and D and H densities that result from varying the mesospheric water abundance. Changing the water abundance in the mesosphere also changes the total amount of water in the atmosphere (in precipitable micrometers, or pr μm, it is 10.4, 10.5, and 10.9 pr μm for the low, mean, and high water cases respectively). Note that because the outputs of one simulation are input for the next, the mean HDO and H_2O profiles in Figure 4.4a have significantly more water in the thermosphere and a sharp transition from the mesosphere. This occurs because chemistry and transport that occurred during the preceding season modify the water abundance above 72 km, below which we keep the water abundance fixed.

The largest amount of water introduced in the mesosphere is nearly 300 ppm at its peak, which is similar to observations during dust storms, (e.g. Vandaele et al. 2019) and was chosen to demonstrate an edge case of high water conditions. Perturbations of this magnitude to the water profile can also spur an enhancement of R_{atomic} (Figure 4.4b), but with a smaller magnitude (+5× VSMOW, compared with +15× VSMOW in Figure 4.3c). Figure C.8 also shows the D/H ratio in other species.

When water is introduced into the mesosphere, the D and H columns respond differently. The densities of both species peak at a higher altitude as mesospheric water increases, which is logical given the greater abundance of source water molecules at higher altitudes. The upper atmospheric D density also responds much more strongly to the perturbation than the H, whereas the opposite was true for the "Temperature" set due to the diffusion-limited nature of H escape.

Figure 4.5 shows the same results with time on the x-axis. This figure highlights the earlier point that escape depends on both the energy available to atoms and the abundance of atoms near the escape region. Adding water into the mesosphere has two main effects. First, the dissociated water supplies both D and H to the upper atmosphere. This additional supply enables a greater enhancement of H escape (150% increase) than D escape (85% increase). This is because H escape is most strongly controlled by the supply of escape-capable atoms due to the diffusion of H through the mesosphere, while the main control on D escape is the energy available. We have not changed the temperature (and therefore the energy) in this scenario, so the overall change to D escape is smaller than for H escape. Second, this preferential enhancement of H escape means that the change to the abundance of H (a 145% increase) in the upper atmosphere is less pronounced than the change in the abundance of D (a 282% increase).

Because of the greater relative enhancement of H escape, we should also expect to see a decreased fractionation factor (E. M. Cangi et al. 2020) when the mesosphere has extra water, and indeed we do (see Figure C.9).

4.7 Discussion and Conclusion

The key takeaway is: both thermospheric temperature variations and mesospheric water abundance variations can affect the value of R_{atomic} in the upper atmosphere. Extra water in the mesosphere affects R_{atomic} by enhancing both upper atmospheric D density and H escape, while higher thermospheric temperatures affect R_{atomic} by reducing the upper atmospheric H density. The reason for all these effects is the diffusion-limited nature of H escape contrasted with the

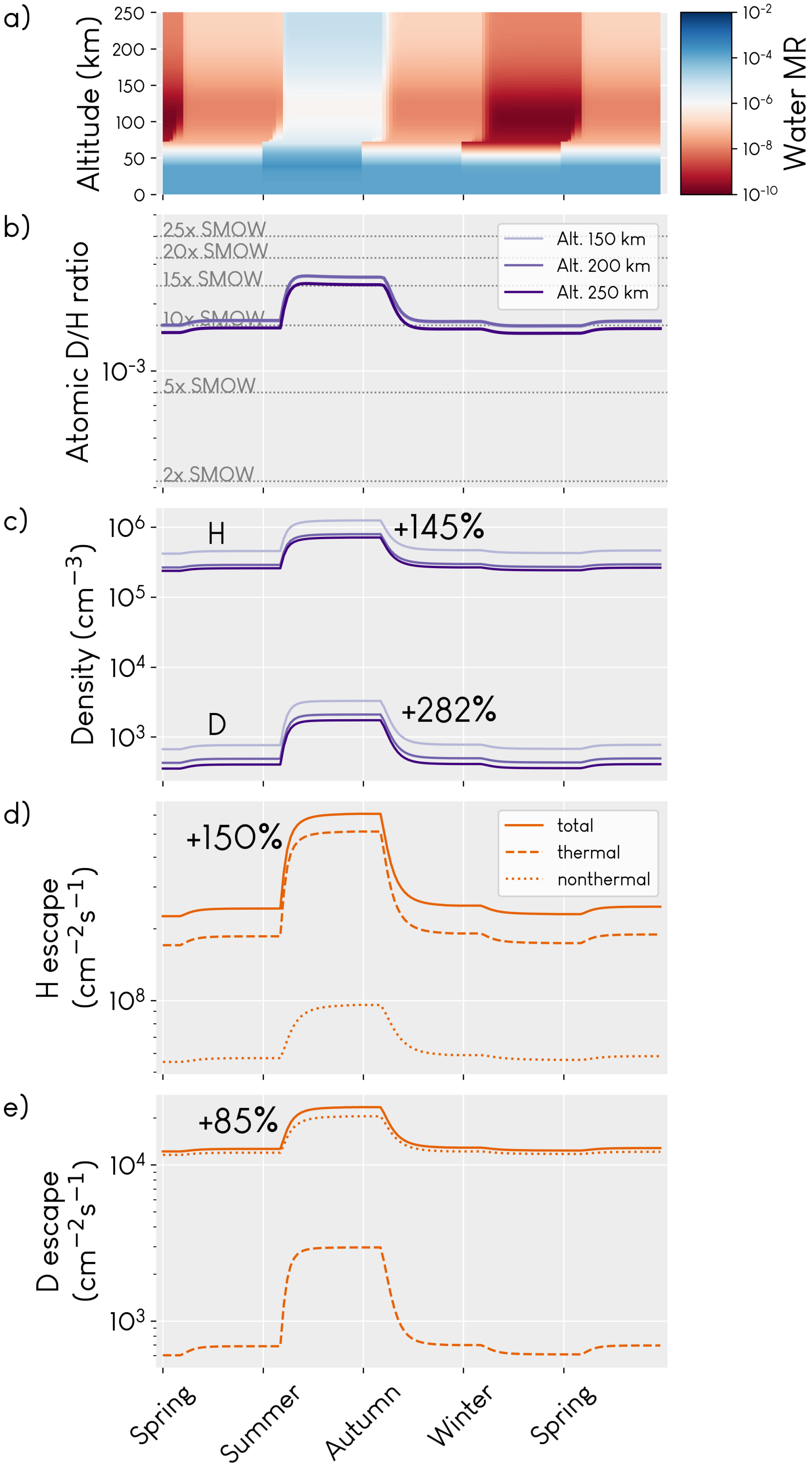

Figure 4.5: The same as Figure 4.3, but in response to changing water abundance in the mesosphere, which also propagates upwards. Because the water is supplied above the cold trap, both H and D escape in this scenario are sustained throughout the high water season ("summer"), and the D/H ratio also increases because H escape increases relatively more than D escape.

energy-limited nature of D escape. R_{atomic} is thus a tracer for the atmospheric dynamics of H and D from the mesosphere to the exobase, as well as escape to space.

Seasonal periods of high thermospheric temperatures chiefly alter R_{atomic} by suppressing upward diffusion of atomic H, leading to large differences in H density near the escape region but negligible difference to D density (Figures 4.2 and 4.3). Thermospheric temperature can also briefly enhance H escape when the temperature goes up (Figure 4.3d); the extra energy allows some more H to escape to space before the bottleneck of the diffusion limit kicks back in. This behavior is similar to behavior observed during space weather events with MAVEN. In September 2017, solar flares and a coronal mass ejection briefly enhanced thermospheric heating caused a 25% decrease in H density and 5× increase in H escape (Mayyasi et al. 2018), comparable to seasonal variations in H escape. D escape, which is energy-limited, can sustain a slightly higher level of escape as long as the temperature perturbation lasts (Figure 4.3e). A second version of Figure 4.1 appears as Figure C.6, showing the three exobase temperature profiles used in this work and the resulting escape calculations.

Seasonally increased mesospheric water abundance also affects R_{atomic}, but by acting as a supply of extra H in the mesosphere, providing more sustained enhancement of H escape, which also reduces H densities. Assuming that HDO is supplied in the same relative abundance, D escape also increases, but so too do the D densities due to the energy-limited nature of D escape. Close examination of Figure 4.5 will reveal that while thermal H escape increases by a factor of ∼2.5× after the introduction of mesospheric water, the same is not true for the non-thermal escape, which only increases by a factor of about 2. This is likely because the dissociation of water leads directly to the creation of neutral H (D), which can then escape thermally. But neutral H and D newly produced from the dissociation of water do not escape non-thermally. Rather, non-thermal escape occurs when hot H (D) is created in ionospheric reactions, primarily HCO^+ (DCO^+) dissociative recombination (E. M. Cangi et al. 2023; Gregory et al. 2023a). HCO^+ (DCO^+) is a terminal ion for H^+ (D^+), so neutral H (D) in the upper atmosphere that originally came from the extra mesospheric water must first undergo a variety of ion reactions to end up in HCO^+ (DCO^+) and then be freed as a hot atom before it can escape non-thermally; evidently, these chemical pathways are already saturated. Along the way, the neutral H (D) may also find its way into a number of other species; in essence, the path for H (D) to non-thermal escape is less direct than to thermal escape.

While we focus on the effect on escape, not all atoms escape. Some H and D may also mix downwards, which is a natural assumption, given that the exchangeable reservoir of water has an enriched D/H ratio. It is difficult to quantify the exact amounts which mix down, as we do not track the fates of individual atoms, but we can estimate the amount of escape relative to the total H and D columns. Figures C.5 and C.11 show the same information as Figures 4.3 and 4.5, but with an additional plotted line showing the fraction of the total H or D column which escapes; for H, this is $\sim 4 \times 10^{-5}\%$ (0.4 ppm) on average, and for D, $\sim 3 \times 10^{-6}\%$ (0.03 ppm, 30 ppb).

High R_{atomic} has been observed at Mars with the MAVEN IUVS instrument. Using the low resolution mode, (Chaufray et al. 2021a) calculated R_{atomic} at 200 km and T= 220 K up to $1.7 \pm 0.4 \times 10^{-2}$, or 106× VSMOW; other values range as low as 1× VSMOW, but frequently fall between 20–40× VSMOW. Through observations of the H corona, (Chaffin et al. 2018) calculated R_{atomic}=20-91×VSMOW. Measurements of R_{atomic} using the echelle channel (higher resolution) are also currently underway, with initial results hinting at a strong seasonal response in both D and H brightness and a related elevated R_{atomic} (Clarke et al. 2022). Past work by the same team has also revealed seasonal enhancement of atomic D brightness, although without a concurrent atomic D/H ratio calculation (Mayyasi et al. 2019). Our results generally agree with these measurements while also adding the important context of two distinct drivers of R_{atomic}: thermospheric temperature and mesospheric water.

Our results thus demonstrate that thermospheric R_{atomic}, more than R_{water}, is more reflective of present perturbations in the atmospheric system and the exchangeable reservoir. Apart from the causes we have discussed here, there are other fractionating processes that may add nuance and that warrant further research. One is the preferential condensation of HDO over H_2O (Fouchet et al. 2000; Lamb et al. 2017), which, although it is less impactful than photolysis differences (Alday et al. 2021), may have implications over geological time for exchange of the atmosphere with the seasonal water ice polar caps (Fisher 2007; Vos et al. 2022) and the creation of clouds (Moores et al. 2011a). Adsorption fractionation of water on dust grains is also potentially important. This adsorption fractionation factor has been found to be 1.97 ± 0.74, leading to a D/H ratio up to 21× VSMOW of adsorbed water (Moores et al. 2011b). Because of the lack of significant increases in dust content above 60 km, dust is not thought to be a direct delivery method for water above that altitude (A. Fedorova et al. 2018; Vandaele et al. 2019; Neary et al. 2020), but dedicated studies on fractionating adsorption and vertical transport of water on Mars are not available in the literature.

Cross-correlation of datasets of upper atmospheric R_{atomic} measurements, thermospheric temperatures, and mesospheric water abundance during non-dusty and dusty years would enhance our understanding of the martian climate and constitute a useful addition to martian water cycle literature. In particular, such studies may enable delineation of temperature and water abundance effects on R_{atomic}, providing a way to extract information about mesospheric dynamics even when direct information about the mesosphere is not available, whether due to a lack of attempted observations and measurements or climatic challenges such as severe dust storms.

Such work would also help provide context for present and future comparisons of spacecraft observations and GCM results. In our quest to understand the long-term evolution of the stability of water on and the habitability of terrestrial planets, we must continue working to both understand the specific effects of individual processes and to develop synoptic-scale understanding of the complex ways that surfaces and atmospheres interact and alter one another.

Chapter 5

Additional collaborations

During this thesis, substantial work went into developing the photochemical model into a robust and useful tool available to the community under open source software principles. The model is made available on my GitHub page (`https://github.com/emcangi`) and archived for associated publications on Zenodo (E. Cangi et al. 2020; E. M. Cangi et al. 2022).

5.1 Enhanced water loss from the martian atmosphere during a regional-scale dust storm and implications for long-term water loss (Holmes et al. 2021)

Authors: J.A. Holmes, S.R. Lewis, M.R. Patel, M.S. Chaffin, ***E.M. Cangi****, J. Deighan, N.M. Schneider, S. Aoki, A.A. Fedorova, D.M. Kass, A.C. Vandaele*

The original version of the model (E. Cangi et al. 2020), prior to the upgrade to include an ionosphere, was adapted and used in conjunction with the Open University Mars GCM by Holmes et al. (2021) to demonstrate the link between the Mars Year (MY) 34 regional "C" dust storm (Kass et al. 2016) and enhanced H escape. This study utilized the unique and powerful approach of integrating a GCM, a photochemical model, and assimilation of data from multiple spacecraft (the Trace Gas Orbiter, Mars Reconnaissance Orbiter, and MAVEN). With this approach, we were able to identify a substantial increase in upper atmospheric water and escape as a direct response to the MY 34 dust storm, much stronger than the response in MY 30, demonstrating that inter-annual variations can have a significant effect on water loss. For this paper, I advised James Holmes and

Manish Patel on the use of the model, providing support, and contributed to writing and editing of the final manuscript.

5.2 MAVEN/IUVS Observations of OH Prompt Emission: Daytime Water Vapor in the Thermosphere of Mars (Stevens et al., submitted 2023)

*M.H. Stevens, **E.M. Cangi**, J. Deighan, S.K. Jain, M.S. Chaffin, S. Gupta, J.S. Evans, N.M. Schneider*

I have also used the upgraded photochemical model (E. M. Cangi et al. 2022) to provide supporting theoretical analysis of recent observations of water by MAVEN/IUVS. This paper was submitted in June 2023, shortly before submission of this thesis.

In this paper, we have used MAVEN/IUVS observations of OH prompt emission as a direct detection of water. When H_2O photodissociates in the atmosphere, it can produce excited OH and atomic H. The excited OH can then de-excite, producing a photon at 308 nm (prompt emission) that is observable by IUVS:

$$\mathrm{H_2O + h\nu \rightarrow OH^* + H}$$

$$\mathrm{OH^* \rightarrow OH + h\nu}$$

The main portion of the paper, written by Mike Stevens, describes the use of multiple linear regressions to obtain the OH prompt and OH solar fluorescence signals, binning the residual brightnesses by altitude, and inversion of the brightness profiles to determine number densities of water and OH in the martian thermosphere; temperatures are also available from CO_2 observations.

Once the number densities of H_2O and temperatures were available, I incorporated them into the photochemical model as inputs, then ran it for a short amount of simulation time (one Mars season, about 6 Earth months) to determine the effect of the IUVS-observed water densities on the OH densities, as well as the timescale of changes. The full results will be available in the forthcoming paper. In addition to the data assimilation and model runs, I was responsible for writing the photochemical modeling results section and a portion of the discussion section, in which we show that the observed water densities can spur an order of magnitude increase in H escape on the timescale of hours to days. I also of course contributed to editing.

Chapter 6

Conclusion

This thesis has demonstrated the subtle differences prevalent in the chemistry, dynamics, and escape to space of D and H. An understanding of these effects is critical to a clear understanding of water loss from Mars, and the intuition and knowledge developed here can be extended to apply to other solar system bodies and/or exoplanets where mass fractionating processes such as atmospheric escape are ongoing (which is probably all of them). The parallels to Venus, another planet with a high D/H ratio, are intriguing; even on small bodies with thin exospheres and little water to speak of—such as Io or Triton—the principles explored here may be applied to other isotopic systems.

Most importantly for Mars, chapter 2 showed that the fractionation factor should not be considered to be a constant value, and that the cooler exobase temperatures measured by modern missions lead to a much smaller thermal escape fractionation factor than had been previously reported. It highlighted the need for more rigorous modeling of hot H and D production below the exobase, and the subsequent non-thermal escape.

Chapter 3 was a direct follow-on to chapter 2. Implementing the ion-neutral chemistry meant that one of the major results was simply the raw model output: the density profiles of deuterated ions, which have never been observed or predicted at Mars before. This paper thus provides a point of comparison for future observations of such ions. Here, we have also seen how the chemistry differs between H and D. We have seen not only the processes which control the production and loss of hot H and D, but also that the dominant process is not resonant charge exchange as has been expected; instead, it is the dissociative recombination of HCO^+/DCO^+, a terminal ion in the atmosphere. In the context of Figure 3.6, which shows that non-thermal escape is by far the largest loss vector for D, it is clear that it is important to get these hot production pathways right if we are to get an accurate assessment of water loss.

It is not just chemistry which affects the behavior of D, but also the dynamics. The upgraded photochemical model (E. M. Cangi et al. 2022) is the first surface-to-space photochemical model of the Mars atmosphere, and also the first to fully solve for the densities of all atmospheric constituents. This enabled the project described in Chapter 4, in which I was able to examine how exobase temperature and lower/middle atmospheric water vapor perturbations manifest in changes to the atomic D/H profile, meditated by differences in the dynamics of the two isotopes, especially with regard to the importance of the mesosphere. This chapter is not only the first dedicated investigation of the atomic D/H profile in modeling and the first model of seasonal D/H variations, but also one of the first such investigations on Mars at all, complementary to observations made with MAVEN/IUVS by Clarke et al. (2019), Chaufray et al. (2021a), and Clarke et al. (2022). The value of the atomic D/H ratio calculated in this chapter sits comfortably between several measurements made in the aforementioned observations with MAVEN/IUVS, as shown in Figure 6.1. The modeling results are not typically within the uncertainty ranges of the measurements, but this is not necessarily surprising as Chapter 4 does not examine how the combined variations of temperature, water vapor, and insolation affect the atomic D/H, and because the measurements are relatively few. Future more detailed modeling efforts, plus additional measurements, may lead to a convergence of modeling results and measured ratios in the future.

Throughout all of these projects, it is evident that even with the newly modeled non-thermal D escape processes, water loss calculated from the results (∼160 m GEL) is still a factor of ∼3 lower than the lowest bound of geomorphology estimates (∼500 m GEL at minimum). As Figure 1.13d shows, to match 500 m GEL, the lowest amount predicted by geomorphological studies, a fractionation factor of about 0.15 is required. Similar numbers to have been achieved before, but typically for much higher exobase temperatures than are observed by modern missions (V. Krasnopolsky 2000; V. A. Krasnopolsky 2002). The non-thermal escape fractionation factor (Figure

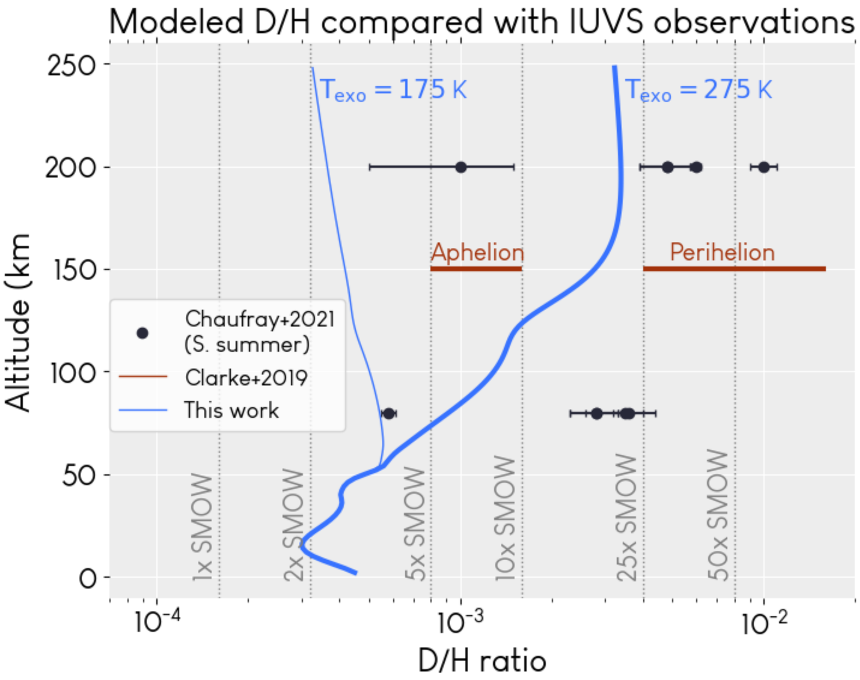

Figure 6.1: Variations of the atomic D/H ratio as calculated in Chapter 4 and from observations with MAVEN/IUVS. The modeling work is shown in blue, the ranges suggested by Clarke et al. (2019) are in the rust color, and measurements by Chaufray et al. (2021a) in the southern summer/near-perihelion season are in dark gray. Note that for the retrievals by Chaufray et al. (2021a), included data represent values based on a variety of different assumptions the exobase temperature and other model parameters.

3.8) is easily 0.15 or higher; thus, it seems likely that consideration of additional non-thermal processes not covered in this thesis (see section 1.2) will only serve to increase the calculated fractionation factor, escape of D, and integrated water loss. Other model aspects that, if improved, may change the picture include: 1) the parameterization of atomic O loss, which is intimately connected to H and D escape through the odd hydrogen cycle (M. B. McElroy et al. 1972; Liu et al. 1976; Chaffin 2015), and 2) vertical transport, which is captured in 1D photochemistry with diffusion, but is altogether more complicated in the real world due to horizontal transport, day-night cycles, waves, tides, and general 3D fluid dynamics.

However, this discussion tries to match the total loss from atmospheric modeling with the minimum geomorphological estimate of the ancient water inventory. The highest estimates range up to 2 km GEL lost (Lasue et al. 2013). In order to explain loss of that magnitude to space, several different hypotheses may be invoked:

- A much larger time-averaged fractionation factor of up to 0.6 (assuming 30 m GEL of water present today, and a total of 2 km GEL lost to space);
- Significant sequestration of water in the subsurface, removing it from the exchangeable reservoir (Lasue et al. 2013; Scheller et al. 2021; Wernicke et al. 2021);
- Periods of significant, non-fractionating loss, such as hydrodynamic escape on early Mars (Yoshida et al. 2020) or impact-induced escape (Schlichting et al. 2015).

The first hypothesis is not impossible, but given the well-known D/H ratio of ∼6× SMOW, would require a yet-unknown highly efficient present or past D removal process to be viable. The latter two hypotheses, if they really occurred in Mars' history, would reduce the amount of water loss needed to be accounted for with fractionating escape to space of H and D while upholding the larger estimates of past inventory. Subsurface sequestration may involve processes with their own fractionation factor, which would complicate our present implementation of equations 1.2, 1.3, and 1.5. Non-fractionating escape could effectively "hide" a large amount of water loss outside of the processes described by equations 1.2 and 1.3 (as applied to escape to space only). All together, significant amounts of water either lost to space in non-fractionating processes or locked away in the subsurface could reconcile the large estimates of the ancient water inventory with the comparatively small estimates of loss to space via fractionating escape.

An additional option that would connect lower estimates of escape to space with the geological evidence is the hypothesis that conditions on early Mars may have alternated between warm and wet and icy, thus possibly mobilizing a small amount of water around the planet in different forms. For example, Rosenberg et al. (2019) estimate that about 600 m GEL of water is the volume required to carve the valley networks, but they also state that the instantaneous inventory might have been smaller due to atmospheric recycling—i.e. the valley networks may not have required 600 *unique* m GEL of water. Atmospheric recycling could have mobilized a smaller amount of water around the planet at different times, carving the valley networks at different times. If this process operated on a grander scale, the ancient inventory of martian water could be smaller than we think; however, estimates of the past inventory required to carve surface features are typically conservative and representative of a minimum value (Lasue et al. 2013, and references therein), suggesting that the problem of explaining the fate of ancient martian water continues on.

The insights gained from chapters 2-4 point to many remaining open questions about atmospheric escape at Mars. Here are some of the most salient, arranged roughly in order how close in time their answers may be to the present day.

(1) How would inclusion of remaining loss processes change the D/H ratio?

As discussed in Section 1.2, in this thesis, I have focused on escape of D and H sourced from the atmosphere below 250 km through photochemical reactions and thermal escape. But D and H may also escape through other processes that I have neglected: for example, the neutral H and D atoms may escape through energization with hot oxygen (Shizgal 1999; Shematovich 2013) or by energy transfer from precipitating solar wind protons and other particles (Gronoff et al. 2020). Ion escape is also possible: D^+ and H^+ may escape via electron impact ionization (Lillis et al. 2021), pickup by the solar wind, or ion outflow (Gronoff et al. 2020).

A concern in accurately characterizing H and D escape is that some H and D atoms deemed to have "escaped" in models like ours may, in reality, enter the corona on ballistic or satellite trajectories (Chamberlain 1963), only to finally escape at a later time through one of the neglected processes mentioned above. In that sense, back-of-the-envelope calculations for these processes (e.g. V. A. Krasnopolsky et al. 1993) can provide an approximation of the total escape of hot H and D, but risk double-counting some atoms. Inclusion of these neglected processes in a model alongside the photochemistry would provide a more complete accounting of H and D escape.

(2) How does adsorption on dust grains affect the D/H ratio of the atmosphere and fractionating escape?

As has been discussed throughout this thesis, it is well-established that both regular seasonal cycles and dust storm activity can raise atmospheric temperatures, enabling more water to persist higher into the mesosphere, where it drives temporary increases in H escape. The effect on D escape, however, has not been studied. Unsurprisingly, dust storms lift dust into the atmosphere and close to the mesosphere, up to 60 km (e.g. Wu et al. 2020), providing another possible way to fractionate D and H due to differential adsorption rates. Moores et al. (2011b) showed that one martian regolith simulant has an adsorptive fractionation factor of 1.96 ± 0.74, implying a D/H ratio of adsorbed water on martian dust could be as high as $21 \pm 8\times$ SMOW. When adsorbed water on dust grains releases into the atmosphere after dust lifting, the abundance of atmospheric water may increase by as much as 20% (M. Stratton et al. 2020; A. Stratton et al. 2021). Significant dust injection into the mesosphere between 60-100 km has not been observed with concurrent water enhancement (A. Fedorova et al. 2018; Neary et al. 2020), so direct delivery via adsorption to those high altitudes may not be occurring, but the bottom of the mesosphere may still be a possible target for adsorptive water release. A detailed investigation of how water adsorbed on dust grains affects the total H_2O and HDO columns would certainly enhance our understanding of the lower atmosphere-mesosphere connection.

(3) How do D and H behave under other obliquity scenarios?

Mars' obliquity evolves chaotically, ranging between 0-60°, with solutions for its evolution earlier than a few to tens of millions of years before present functionally impossible (Laskar et al. 1993; Touma et al. 1993; Laskar et al. 2004). Yet, periods of high obliquity may drive significant sublimation and movement of water around the planet (Jakosky et al. 1995), enhanced dust lifting (Newman et al. 2005), or a moister atmosphere above the cold trap (Kang 2019), with potential implications for escape. It has also been indicated that the total water needed to carve the valley networks, 600 m GEL, (Rosenberg et al. 2019) could have been made up of recycled water over millions of years. If significant recycling of the overall martian water budget occurred over even longer time frames, the total initial inventory of unique water may be smaller than previous geomorphological estimates, potentially lining up more closely with atmospheric models. In any case, a greater understanding of H and D fractionation, the associated water loss, and the overall water cycle under different obliquity scenarios would fill a gap in the literature.

(4) How might conditions on early Mars change D and H escape?e

Water loss estimates made using Rayleigh fractionation are valid insofar as we trust that the Rayleigh fractionation equation encompasses all relevant processes. This in turn relies on good estimates of the average fractionation factor, as well as the past and present D/H ratios. Our understanding of these could be incomplete; if the D/H ratio of the atmosphere was regularly reset, either globally or locally, it's not guaranteed that estimating integrated water loss over all of Mars' history is the best approach. Our best understanding of the D/H ratio over time does not suggest this (see Figure 1.8), but admittedly, the amount of data is limited.

Noachian Mars was likely also exposed to different EUV conditions due to the greater activity of the young sun. Depending on the quantity of water originally present on Mars, this could have stimulated a period of hydrodynamic escape of H (Kulikov et al. 2007; Yoshida et al. 2020; Cassata et al. 2022). Hydrodynamic escape is expected to mainly fractionate mainly heavier molecules (Zahnle et al. 1990); Kasting et al. (1983) have shown that D would have been swept away along with the H outflow if the rate was high enough. Without significant fractionation from the actual escape, the only D/H fractionation in this scenario would come from either mass-dependent fractionation lower in the atmosphere, such as due to the vapor pressure isotope effect (Fouchet et al. 2000) or depletion due to preferential condensation of HDO (Bertaux et al. 2001). Depending on the efficiency of D escape in this scenario, an era of hydrodynamic escape could have been a potential avenue for loss of a large amount of water (e.g. V. A. Krasnopolsky 2015).

⁂

Mars is an intriguing, beautiful planet. With the highest mountain in the solar system and the deepest canyon, and the ongoing mystery of its transformation from a world with flowing water to a desert, its evolution is undeniably interesting in its own right, but it is even more interesting for what we can learn about the evolution of planetary habitability and climate. The more we explore Mars, our solar system, and beyond, the closer we come to finding out whether there life has arisen somewhere other than Earth.

For decades, we have invested time, money, and energy into studying the Red Planet; we have learned so much, and have much more to learn still. The work of this thesis has focused on incrementing our knowledge of Mars, but the principles and tools developed can be extended to other worlds with atmospheres, whether to understand water loss, atmospheric escape, or other isotope systems, and as a result, planetary evolution and habitability. In our own solar system, we already know of many unusual alien worlds, with methanological rather than hydrological systems (Titan), crushing atmospheres and searing temperatures (Venus), and worlds where tenuous atmospheres partially condense onto the surface at certain times (Io, Pluto). What other strange new worlds might atmospheric escape someday help us to understand? Amongst the infinite diversity of planets in our solar system and beyond, there are surely countless wonders in infinite combinations.

> We are a way for the cosmos to know itself.
>
> Carl Sagan, *Cosmos*

Bibliography

Adams, D. et al. (2021). “Nitrogen Fixation at Early Mars”. **Astrobiology** 21.8, pp. 968–980. DOI: `10.1089/ast.2020.2273`.

Alday, J. et al. (2021). “Isotopic fractionation of water and its photolytic products in the atmosphere of Mars”. **Nature Astronomy** 5, pp. 943–950. DOI: `10.1038/s41550-021-01389-x`.

AlMaazmi, H. et al. (2019). “C-Storm Effect on the Escape of Hydrogen in the Martian Atmosphere Using the LMD-GCM”. In: **Ninth International Conference on Mars**. Ed. by LPI Editorial Board. Vol. 2089. LPI Contributions, 6208, p. 6208.

Alsaeed, N. R. and B. M. Jakosky (2019). “Mars Water and D/H Evolution From 3.3 Ga to Present”. **Journal of Geophysical Research: Planets** 124.12, pp. 3344–3353. DOI: `10.1029/2019JE006066`.

Anderson, D. E. and C. W. Hord (1971). “Mariner 6 and 7 Ultraviolet Spectrometer Experiment: Analysis of hydrogen Lyman-alpha data”. **Journal of Geophysical Research** 76.28, pp. 6666–6673. DOI: `10.1029/ja076i028p06666`.

Anicich, V. G. (2003). **An index of the literature for bimolecular gas phase cation-molecule reaction kinetics**. JPL Publication 03-19. Pasadena: Jet Propulsion Laboratory.

— (1993). “Evaluated Bimolecular Ion-Molecule Gas Phase Kinetics of Positive Ions for Use in Modeling Planetary Atmospheres, Cometary Comae, and Interstellar Clouds”. **Journal of Physical and Chemical Reference Data** 22.6, pp. 1469–1569. DOI: `10.1063/1.555940`.

Aoki, S. et al. (2019). “Water Vapor Vertical Profiles on Mars in Dust Storms Observed by TGO/NOMAD”. **Journal of Geophysical Research (Planets)** 124.12, pp. 3482–3497. DOI: `10.1029/2019JE006109`.

Atkinson, R. et al. (1989). “Evaluated Kinetic and Photochemical Data for Atmospheric Chemistry: Supplement III. IUPAC Subcommittee on Gas Kinetic Data Evaluation for Atmospheric Chemistry”. **Journal of Physical and Chemical Reference Data** 18.2, pp. 881–1097. DOI: `10.1063/1.555832`.

Atreya, S. K. et al. (2013). “Primordial argon isotope fractionation in the atmosphere of Mars measured by the SAM instrument on Curiosity and implications for atmospheric loss”. **Geophysical Research Letters** 40.21, pp. 5605–5609. DOI: `10.1002/2013GL057763`.

Audouard, J. et al. (2016). “Analysis of Curiosity Surface Temperature Data”. In: **47th Lunar and Planetary Sciences Conference**.

Baker, V. R. and R. C. Kochel (1979). “Martian channel morphology: Maja and Kasei Valles”. **Journal of Geophysical Research: Solid Earth** 84.B14, pp. 7961–7983. DOI: `10.1029/JB084iB14p07961`.

Baker, V. R. and D. J. Milton (1974). “Erosion by catastrophic floods on Mars and Earth”. **Icarus** 23.1, pp. 27–41. DOI: `10.1016/0019-1035(74)90101-8`.

Banaszkiewicz, M. et al. (2000). “A Coupled Model of Titan’s Atmosphere and Ionosphere”. **Icarus** 147.2, pp. 386–404. DOI: `10.1006/icar.2000.6448`.

Bandfield, J. L. (2008). “High-silica deposits of an aqueous origin in western Hellas Basin, Mars”. **Geophysical Research Letters** 35.12. DOI: `10.1029/2008GL033807`.

Banks, P. M. and G. Kockarts (1973). **Aeronomy**. .B. 2 vols. New York: Academic Press, Inc., pp. 32–42.

Barabash, S. et al. (2007). “Martian Atmospheric Erosion Rates”. **Science** 315.5811, p. 501. DOI: `10.1126/science.1134358`.

Barfield, W., G. Koontz, and W. Huebner (1972). “Fits to new calculations of photoionization cross sections for low-Z elements”. **Journal of Quantitative Spectroscopy and Radiative Transfer** 12. DOI: `10.1016/0022-4073(72)90043-X`.

Barnes, J. J. et al. (2020). “Multiple early-formed water reservoirs in the interior of Mars”. **Nature Geoscience** 13.4, pp. 260–264. DOI: `10.1038/s41561-020-0552-y`.

Bauer, S. J. (1973). “Chemical Processes”. In: **Physics of Planetary Ionospheres**. Springer, pp. 82–95.

Baulch, D. L. et al. (1992). “Evaluated Kinetic Data for Combustion Modelling”. **Journal of Physical and Chemical Reference Data** 21.3, pp. 411–734. DOI: `10.1063/1.555908`.

Baulch, D. L. et al. (2005). “Evaluated Kinetic Data for Combustion Modeling: Supplement II”. **Journal of Physical and Chemical Reference Data** 34.3, pp. 757–1397. DOI: `10.1063/1.1748524`.

Benna, M. et al. (2015). “First measurements of composition and dynamics of the Martian ionosphere by MAVEN’s Neutral Gas and Ion Mass Spectrometer”. **Geophysical Research Letters** 42.21, pp. 8958–8965. DOI: `10.1002/2015GL066146`.

Bertaux, J.-L. and F. Montmessin (2001). “Isotopic fractionation through water vapor condensation: The Deuteropause, a cold trap for deuterium in the atmosphere of Mars”. **Journal of Geophysical Research (Planets)** 106.E12, pp. 32879–32884. DOI: `10.1029/2000JE001358`.

Bezanson, J. et al. (2017). “Julia: A fresh approach to numerical computing”. **SIAM review** 59.1, pp. 65–98.

Bhattacharyya, D. et al. (2017). “Seasonal Changes in Hydrogen Escape From Mars Through Analysis of HST Observations of the Martian Exosphere Near Perihelion”. **Journal of Geophysical Research (Space Physics)** 122.11, pp. 11, 756–11, 764. DOI: `10.1002/2017JA024572`.

Bhattacharyya, D. et al. (2020). “Two-dimensional model for the martian exosphere: Applications to hydrogen and deuterium Lyman α observations”. **Icarus** 339, p. 113573. DOI: `10.1016/j.icarus.2019.113573`.

Bibring, J.-P. et al. (2006). “Global Mineralogical and Aqueous Mars History Derived from OMEGA/Mars Express Data”. **Science** 312.5772, pp. 400–404. DOI: `10.1126/science.1122659`.

Biemann, K. et al. (1976). “The Atmosphere of Mars near the Surface: Isotope Ratios and Upper Limits on Noble Gases”. **Science** 194.4260, pp. 76–78.

Bierson, C. J. and X. Zhang (2020). “Chemical Cycling in the Venusian Atmosphere: A Full Photochemical Model From the Surface to 110 km”. **Journal of Geophysical Research: Planets** 125.7. DOI: `10.1029/2019JE006159`.

Bishop, J. L. et al. (2008). “Phyllosilicate Diversity and Past Aqueous Activity Revealed at Mawrth Vallis, Mars”. **Science** 321.5890, pp. 830–833. DOI: `10.1126/science.1159699`.

Bjoraker, G. L., M. Mumma, and H. P. Larson (1989). “Isotopic Abundance Ratios for Hydrogen and Oxygen in the Martian Atmosphere”. In: **Bulletin of the American Astronomical Society**. Vol. 21, p. 991.

Boesswetter, A. et al. (2010). “Non-thermal water loss of the early Mars: 3D multi-ion hybrid simulations”. **Planetary and Space Science** 58.14-15, pp. 2031–2043. DOI: `10.1016/j.pss.2010.10.003`.

Borodi, G., A. Luca, and D. Gerlich (2009). “Reactions of CO_2^+ with H, H_2 and deuterated analogues”. **International Journal of Mass Spectrometry** 280.1-3, pp. 218–225. DOI: `10.1016/j.ijms.2008.09.004`.

Bougher, S. W. et al. (2017). “The structure and variability of Mars dayside thermosphere from MAVEN NGIMS and IUVS measurements: Seasonal and solar activity trends in scale heights and temperatures”. **Journal of Geophysical Research: Space Physics** 122. DOI: `10.1002/2016JA023454`.

Brain, D. A. et al. (2015). “The spatial distribution of planetary ion fluxes near Mars observed by MAVEN”. **Geophysical Research Letters** 42.21, pp. 9142–9148. DOI: `10.1002/2015GL065293`.

Brian, J. and A. Mitchell (1990). “The dissociative recombination of molecular ions”. **Physics Reports** 186.5, pp. 215–248.

Brune, W. H., J. J. Schwab, and J. Anderson (1983). “Laser magnetic resonance, resonance fluorescence, resonance absorption studies of the reaction kinetics of $O + OH \rightarrow H + O_2$, $O + HO_2 \rightarrow OH + O_2$, $N + OH \rightarrow H + NO$, and $N + HO_2 \rightarrow$ products at 300 K between 1 and 5 torr”. **The Journal of Physical Chemistry** 87.22, pp. 4503–4514.

Burkholder, J. B. et al. (2015). **Chemical kinetics and photochemical data for use in atmospheric studies: evaluation number 18**. JPL Publication Publication 15-10. Pasadena: Jet Propulsion Laboratory.

Burkholder, J. et al. (2019). **Chemical kinetics and photochemical data for use in atmospheric studies, Evaluation No. 19**. JPL Publication Publication 19-5. Pasadena: Jet Propulsion Laboratory.

Campbell, I. M. and C. N. Gray (1973). "Rate constants for O(^{3}P) recombination and association with N(^{4}S)". **Chemical Physics Letters** 18.4, pp. 607–609. DOI: `10.1016/0009-2614(73)80479-8`.

Cangi, E., M. S. Chaffin, and J. Deighan (2020). **emcangi/dh_fractionation Mars D Photochemistry**. Version 1.0.4. DOI: `10.5281/zenodo.4110723`.

Cangi, E. M., M. S. Chaffin, and J. Deighan (2020). "Higher Martian Atmospheric Temperatures at All Altitudes Increase the D/H Fractionation Factor and Water Loss". **Journal of Geophysical Research: Planets** 125.12, 1–15. DOI: `10.1029/2020JE006626`.

Cangi, E. M. and M. Chaffin (2022). **bluejay: Atmospheric photochemistry in Julia**. Version v1.0. DOI: `10.5281/zenodo.7735302`.

Cangi, E. M. et al. (2023). "Fully Coupled Photochemistry of the Deuterated Ionosphere of Mars and Its Effects on Escape of H and D". **Journal of Geophysical Research: Planets** 128.7, e2022JE007713. DOI: `https://doi.org/10.1029/2022JE007713`.

Carr, M. H. and J. W. Head (2010). "Geologic history of Mars". **Earth and Planetary Science Letters** 294. DOI: `10.1016/j.epsl.2009.06.042`.

Carr, M. and J. Head (2019). "Mars: Formation and fate of a frozen Hesperian ocean". **Icarus** 319. DOI: `10.1016/j.icarus.2018.08.021`.

Carr, M. H. (1979). "Formation of Martian flood features by release of water from confined aquifers". **Journal of Geophysical Research** 84.B6, p. 2995. DOI: `10.1029/JB084iB06p02995`.

— (1990). "D/H on Mars: Effects of floods, volcanism, impacts, and polar processes". **Icarus** 87.1, pp. 210–227. DOI: `10.1016/0019-1035(90)90031-4`.

— (1995). "The Martian drainage system and the origin of valley networks and fretted channels". **Journal of Geophysical Research (Planets)** 100.E4, pp. 7479–7508. DOI: `10.1029/95JE00260`.

— (2012). "The fluvial history of Mars". **Philosophical Transactions of the Royal Society A: Mathematical, Physical and Engineering Sciences** 370.1966, pp. 2193–2215. DOI: `10.1098/rsta.2011.0500`.

Cassata, W. S. et al. (2022). "Xenon isotope constraints on ancient Martian atmospheric escape". **Earth and Planetary Science Letters** 580, 117349, p. 117349. DOI: `10.1016/j.epsl.2021.117349`.

Cazaux, S. et al. (2010). "Water formation on bare grains: When the chemistry on dust impacts interstellar gas". **Astronomy & Astrophysics** 522, A74, A74. DOI: `10.1051/0004-6361/201014026`.

Chaffin, M. S. et al. (2014). “Unexpected variability of Martian hydrogen escape”. **Geophysical Research Letters** 41, pp. 314–320. DOI: `10.1002/2013GL058578.Abstract`.

Chaffin, M. S. et al. (2017). “Elevated atmospheric escape of atomic hydrogen from Mars induced by high-altitude water”. **Nature Geoscience** 10.3, pp. 174–178. DOI: `10.1038/ngeo2887`.

Chaffin, M. S. et al. (2018). “Mars H Escape Rates Derived From MAVEN/IUVS Lyman Alpha Brightness Measurements and Their Dependence on Model Assumptions”. **Journal of Geophysical Research (Planets)** 123.8, pp. 2192–2210. DOI: `10.1029/2018JE005574`.

Chaffin, M. S. et al. (2021). “Martian water loss to space enhanced by regional dust storms”. **Nature Astronomy** 5, pp. 1036–1042. DOI: `10.1038/s41550-021-01425-w`.

Chaffin, M. S. (2015). “The H Corona of Mars”. PhD thesis. University of Colorado, Boulder.

Chamberlain, J. W. and D. M. Hunten (1987). **Theory of planetary atmospheres. An introduction to their physics andchemistry.** Vol. 36.

Chamberlain, J. W. (1963). “Planetary coronae and atmospheric evaporation”. **Planetary and Space Science** 11.8, pp. 901–960. DOI: `10.1016/0032-0633(63)90122-3`.

Chapman, M. G. et al. (2010). “Noachian–Hesperian geologic history of the Echus Chasma and Kasei Valles system on Mars: New data and interpretations”. **Earth and Planetary Science Letters**. Mars Express after 6 Years in Orbit: Mars Geology from Three-Dimensional Mapping by the High Resolution Stereo Camera (HRSC) Experiment 294.3, pp. 256–271. DOI: `10.1016/j.epsl.2009.11.032`.

Chaufray, J. Y. et al. (2021a). “Estimate of the D/H Ratio in the Martian Upper Atmosphere from the Low Spectral Resolution Mode of MAVEN/IUVS”. **Journal of Geophysical Research (Planets)** 126.4, e06814, e06814. DOI: `10.1029/2020JE006814`.

Chaufray, J. Y. et al. (2021b). “Study of the hydrogen escape rate at Mars during martian years 28 and 29 from comparisons between SPICAM/Mars express observations and GCM-LMD simulations”. **Icarus** 353, 113498, p. 113498. DOI: `10.1016/j.icarus.2019.113498`.

Cheng, B. M. et al. (2004). “Quantitative spectroscopic and theoretical study of the optical absorption spectra of H_2O, HOD, and D_2O in the 125-145 nm region”. **Journal of Chemical Physics** 120.1, pp. 224–229. DOI: `10.1063/1.1630304`.

Cheng, B.-M. et al. (1999). “Photo-induced fractionation of water isotopomers in the Martian atmosphere”. **Geophysical Research Letters** 26.24, pp. 3657–3660. DOI: `10.1029/1999GL008367`.

Chung, C.-Y. et al. (2001). “Temperature dependence of absorption cross-section of $H\ _2O$, HOD, and $D\ _2O$ in the spectral region 140-193 nm”. **Nuclear Instruments and Methods in Physics Research A** 467.2002, pp. 1572–1576. DOI: `10.1016/S0168-9002(01)00762-8`.

Clancy, R. T. et al. (2016). “Daily global mapping of Mars ozone column abundances with MARCI UV band imaging”. **Icarus** 266. DOI: `10.1016/j.icarus.2015.11.016`.

Clarke, J. T., M. Mayyasi, D. Bhattacharyya, et al. (2017). “Variability of D and H in the Martian upper atmosphere observed with the MAVEN IUVS echelle channel”. **Journal of Geophysical Research: Space Physics** 122. DOI: `10.1002/2016JA023479`.

Clarke, J. T. et al. (2014). “A rapid decrease of the hydrogen corona of Mars”. **Geophysical Research Letters** 41.22, pp. 8013–8020. DOI: `10.1002/2014GL061803`.

Clarke, J. T. et al. (2019). “The D/H Ratio in the Martian Upper Atmosphere”. In: **European Planetary Science Congress and AAS/Division for Planetary Sciences 2019 joint meeting**.

Clarke, J. T. et al. (2022). “Observations of H and D Densities and Escape Fluxes from the Upper Atmosphere of Mars with the MAVEN IUVS Echelle Channel”. In: **Seventh International Workshop on the Mars Atmosphere: Modelling and Observations**, 3101, p. 3101.

Cui, J. et al. (2019). “Photochemical escape of atomic C and N on Mars: clues from a multi-instrument MAVEN dataset”. **Astronomy & Astrophysics** 621, A23. DOI: `10.1051/0004-6361/201833749`.

Daerden, F. et al. (2022). “Explaining NOMAD D/H Observations by Cloud-Induced Fractionation of Water Vapor on Mars”. **Journal of Geophysical Research (Planets)** 127.2, e07079, e07079. DOI: `10.1029/2021JE007079`.

Davidson, J. A. et al. (1978). “Temperature dependence of the deactivation of O(^{1}D) by CO from 113-333 K”. **Journal of Chemical Physics** 69.3, pp. 1216–1217. DOI: `10.1063/1.436657`.

Deighan, J. et al. (2015). “MAVEN IUVS observation of the hot oxygen corona at Mars”. **Geophysical Research Letters** 42, pp. 9009–9014. DOI: `10.1002/2015GL065487.Received`.

Deighan, J. et al. (2018). “Discovery of a proton aurora at Mars”. **Nature Astronomy** 2, pp. 802–807. DOI: `10.1038/s41550-018-0538-5`.

Deighan, J. (2012). “The Effect of an Ozone Layer on Ancient Mars”. PhD thesis. University of Virginia.

Dobrijevic, M. et al. (2016). “1D-coupled photochemical model of neutrals, cations and anions in the atmosphere of Titan”. **Icarus** 268, pp. 313–339. DOI: `10.1016/j.icarus.2015.12.045`.

Domagal-Goldman, S. D. et al. (2016). “The astrobiology primer v2. 0”. **Astrobiology** 16.8, p. 561.

Dong, Y. et al. (2015). “Strong plume fluxes at Mars observed by MAVEN: An important planetary ion escape channel”. **Geophysical Research Letters** 42.21, pp. 8942–8950. DOI: `10.1002/2015GL065346`.

Dong, Y. et al. (2023). “The dependence of Martian ion escape on solar EUV irradiance as observed by MAVEN”. **Icarus** 393, 115288, p. 115288. DOI: `10.1016/j.icarus.2022.115288`.

Doroshenko, V., N. Kudryavtsev, and V. Smetanin (1992). “Quenching mechanisms for electronically excited species in partially dissociated air”. **HIGH ENERGY CHEMISTRY** 26.4, pp. 227–230.

Dunbar, B. (2023). **Thin Blue Line**. Ed. by Y. Smith. NASA. URL: `https://www.nasa.gov/multimedia/imagegallery/image_feature_1529.html`.

Dutuit, O. et al. (2013). “Critical Review of N, N^+, N_2^+, N++, and N_2++ Main Production Processes and Reactions of Relevance to Titan’s Atmosphere”. **Astrophysical Journal Supplement Series** 204.2, 20, p. 20. DOI: `10.1088/0067-0049/204/2/20`.

Ehlmann, B. L. and C. S. Edwards (2014). “Mineralogy of the Martian surface”. **Annual Review of Earth and Planetary Sciences** 42, pp. 291–315. DOI: `10.1146/annurev-earth-060313-055024`.

Ehlmann, B. L. et al. (2009). “Identification of hydrated silicate minerals on Mars using MRO-CRISM: Geologic context near Nili Fossae and implications for aqueous alteration”. **Journal of Geophysical Research: Planets** 114.E2. DOI: `10.1029/2009JE003339`.

Ehlmann, B. L. et al. (2011). “Subsurface water and clay mineral formation during the early history of Mars”. **Nature** 479.7371, pp. 53–60. DOI: `10.1038/nature10582`.

Elwood Madden, M. E., R. J. Bodnar, and J. D. Rimstidt (2004). “Jarosite as an indicator of water-limited chemical weathering on Mars”. **Nature** 431.7010, pp. 821–823. DOI: `10.1038/nature02971`.

Encrenaz, T. et al. (2018). “New measurements of D/H on Mars using EXES aboard SOFIA”. **Astronomy & Astrophysics** 612, A112, A112. DOI: `10.1051/0004-6361/201732367`.

Ergun, R. E. et al. (2015). “Dayside electron temperature and density profiles at Mars: First results from the MAVEN Langmuir probe and waves instrument”. **Geophysical Research Letters** 42.21, pp. 8846–8853. DOI: `10.1002/2015GL065280`.

Fassett, C. I. and J. W. Head (2008). “Valley network-fed, open-basin lakes on Mars: Distribution and implications for Noachian surface and subsurface hydrology”. **Icarus** 198.1, pp. 37–56. DOI: `10.1016/j.icarus.2008.06.016`.

Fedorova, A. et al. (2018). “Water vapor in the middle atmosphere of Mars during the 2007 global dust storm”. **Icarus** 300, pp. 440–457. DOI: `10.1016/j.icarus.2017.09.025`.

Fedorova, A. et al. (2021). “Multi-Annual Monitoring of the Water Vapor Vertical Distribution on Mars by SPICAM on Mars Express”. **Journal of Geophysical Research (Planets)** 126.1, e06616, e06616. DOI: `10.1029/2020JE006616`.

Fedorova, A. A. et al. (2020). “Stormy water on Mars: The distribution and saturation of atmospheric water during the dusty season”. **Science** 367.6475, pp. 297–300. DOI: `10.1126/science.aay9522`.

Fehsenfeld, F. C., D. B. Dunkin, and E. E. Ferguson (1970). “Rate constants for the reaction of CO_2^+ with O, O_2 and NO; N_2^+ with O and NO; and O_2^+ with NO”. **Planetary and Space Science** 18.8, pp. 1267–1269. DOI: `10.1016/0032-0633(70)90216-3`.

Fisher, D. A. (2007). “Mars’ water isotope (D/H) history in the strata of the North Polar Cap: Inferences about the water cycle”. **Icarus** 187.2, pp. 430–441. DOI: `10.1016/j.icarus.2006.10.032`.

Fletcher, I. and D. Husain (1976). “The collisional quenching of electronically excited oxygen atoms, O (21 D 2), by the gases NH3, H_2O_2, C2H6, C3H8, and C (CH3) 4, using time-resolved attenuation of atomic resonance radiation”. **Canadian Journal of Chemistry** 54.11, pp. 1765–1770.

Forget, F. et al. (2009). “Density and temperatures of the upper Martian atmosphere measured by stellar occultations with Mars Express SPICAM”. **Journal of Geophysical Research (Planets)** 114. DOI: `10.1029/2008JE003086`.

Fouchet, T. and E. Lellouch (1999). “Vapor Pressure Isotope Fractionation Effects in Planetary Atmospheres: Application to Deuterium”. **Icarus** 144. DOI: `10.1006/icar.1999.6264`.

Fouchet, T. and E. Lellouch (2000). “Vapor Pressure Isotope Fractionation Effects in Planetary Atmospheres: Application to Deuterium”. **Icarus** 144.1, pp. 114–123. DOI: `10.1006/icar.1999.6264`.

Fox, J. L. (1993). “The production and escape of nitrogen atoms on Mars”. **Journal of Geophysical Research** 98.E2, pp. 3297–3310. DOI: `10.1029/92JE02289`.

— (2003). “Effect of H_2 on the Martian ionosphere: Implications for atmospheric evolution”. **Journal of Geophysical Research** 108.A6, p. 1223. DOI: `10.1029/2001JA000203`.

— (2004). “CO_2^+ dissociative recombination: A source of thermal and nonthermal C on Mars”. **Journal of Geophysical Research: Space Physics** 109.A8. DOI: `10.1029/2004JA010514`.

Fox, J. L. and F. M. Bakalian (2001a). “Photochemical escape of atomic carbon from Mars”. **Journal of Geophysical Research: Space Physics** 106.A12, pp. 28785–28795. DOI: `10.1029/2001JA000108`.

Fox, J. L. and K. Y. Sung (2001b). “Solar activity variations of the Venus thermosphere/ionosphere”. **Journal of Geophysical Research: Space Physics** 106.A10, pp. 21305–21335. DOI: `10.1029/2001JA000069`.

Fox, J. L. (2009). “Morphology of the dayside ionosphere of Mars: Implications for ion outflows”. **Journal of Geophysical Research (Planets)** 114.E12, E12005, E12005. DOI: `10.1029/2009JE003432`.

— (2015). “The chemistry of protonated species in the martian ionosphere”. **Icarus** 252, pp. 366–392. DOI: `10.1016/j.icarus.2015.01.010`.

Fox, J. L. and A. B. Hać (2009a). “Photochemical escape of oxygen from Mars: A comparison of the exobase approximation to a Monte Carlo method”. **Icarus** 204.2, pp. 527–544. DOI: `10.1016/j.icarus.2009.07.005`.

— (2009b). “Photochemical escape of oxygen from Mars: A comparison of the exobase approximation to a Monte Carlo method”. **Icarus** 204.2, pp. 527–544. DOI: `10.1016/j.icarus.2009.07.005`.

Fox, J. L. et al. (2015). “Water and water ions in the Martian thermosphere/ionosphere”. **Geophysical Research Letters** 42.21, pp. 8977–8985. DOI: `10.1002/2015GL065465`.

Fox, J. L. et al. (2017). “Photochemical determination of O densities in the Martian thermosphere: Effect of a revised rate coefficient”. **Geophysical Research Letters** 44.16, pp. 8099–8106. DOI: `10.1002/2017GL074562`.

Fox, J. L. et al. (2021). “Rate coefficients for the reactions of CO_2^+ with O: Lessons from MAVEN at Mars”. **Icarus** 358, 114186, p. 114186. DOI: `10.1016/j.icarus.2020.114186`.

Gacesa, M., P. Zhang, and V. Kharchenko (2012). “Non-thermal escape of molecular hydrogen from Mars”. **Geophysical Research Letters** 39.10, p. L10203. DOI: `10.1029/2012GL050904`.

Gacesa, M., N. Lewkow, and V. Kharchenko (2017). “Non-thermal production and escape of OH from the upper atmosphere of Mars”. **Icarus** 284, pp. 90–96.

Gacesa, M. et al. (2018). “Non-thermal escape rates of light species from Mars using MAVEN in-situ measurements”. In: **European Planetary Science Congress**, EPSC2018–604.

Geiss, J. and H. Reeves (1981). “Deuterium in the solar system”. **Astronomy & Astrophysics** 93.

Geppert, W. D. et al. (2005). “Dissociative recombination branching ratios and their influence on interstellar clouds”. In: **Journal of Physics Conference Series**. Vol. 4. Journal of Physics Conference Series, pp. 26–31. DOI: `10.1088/1742-6596/4/1/004`.

Geppert, W. D. et al. (2000). “Comparison of the cross-sections and thermal rate constants for the reactions of C(3PJ) atoms with O_2 and NO”. **Physical Chemistry Chemical Physics (Incorporating Faraday Transactions)** 2.13, pp. 2873–2881. DOI: `10.1039/B002583F`.

Geppert, W. D. et al. (2004). “Extraordinary branching ratios in astrophysically important dissociative recombination reactions”. **Faraday Discussions** 127, p. 425. DOI: `10.1039/b314005a`.

Goudge, T. A. et al. (2017). “Sedimentological evidence for a deltaic origin of the western fan deposit in Jezero crater, Mars and implications for future exploration”. **Earth and Planetary Science Letters** 458, pp. 357–365. DOI: `10.1016/j.epsl.2016.10.056`.

Gregory, B. S. et al. (2023a). “HCO^+ Dissociative Recombination: A Significant Driver of Nonthermal Hydrogen Loss at Mars”. **Journal of Geophysical Research (Planets)** 128.1, e2022JE007576, e2022JE007576. DOI: `10.1029/2022JE007576`.

Gregory, B. S. et al. (2023b). “Nonthermal hydrogen loss at Mars: Contributions of photochemical mechanisms to escape and identification of key processes”. **Journal of Geophysical Research: Planets** n/a.n/a, e2023JE007802. DOI: `https://doi.org/10.1029/2023JE007802`. eprint: `https://agupubs.onlinelibrary.wiley.com/doi/pdf/10.1029/2023JE007802`.

Gröller, H. et al. (2014). “Hot oxygen and carbon escape from the martian atmosphere”. **Planetary and Space Science** 98, pp. 93–105. DOI: `10.1016/j.pss.2014.01.007`.

Gronoff, G. et al. (2020). “Atmospheric escape processes and planetary atmospheric evolution”. **Journal of Geophysical Research: Space Physics** 125.8, e2019JA027639.

Gu, H. et al. (2022). “Wind-Enhanced Hydrogen Escape on Mars”. **Geophysical Research Letters** 49.10, e98312, e98312. DOI: `10.1029/2022GL098312`.

Gupta, S. et al. (2022). “Thermal Structure of the Martian Upper Mesosphere/Lower Thermosphere From MAVEN/IUVS Stellar Occultations”. **Journal of Geophysical Research (Planets)** 127.11, e2022JE007534, e2022JE007534. DOI: 10.1029/2022JE007534.

Gustafsson, M. and G. Nyman (2015). “Radiative association rate constant for the formation of CO: the importance of the first excited $^1\Sigma^+$ state”. **Monthly Notices of the Royal Astronomical Society** 448.3, pp. 2562–2565. DOI: 10.1093/mnras/stv089.

Halekas, J. S. (2017). “Seasonal variability of the hydrogen exosphere of Mars”. **Journal of Geophysical Research (Planets)** 122.5, pp. 901–911. DOI: 10.1002/2017JE005306.

Halekas, J. S. et al. (2017). “Flows, Fields, and Forces in the Mars-Solar Wind Interaction”. **Journal of Geophysical Research (Space Physics)** 122.11, pp. 11, 320–11, 341. DOI: 10.1002/2017JA024772.

Hallis, L. J. (2017). “D/H ratios of the inner Solar System”. **Philosophical Transactions of the Royal Society A: Mathematical, Physical and Engineering Sciences** 375.2094, p. 20150390. DOI: 10.1098/rsta.2015.0390.

Hanley, K. G. et al. (2022). “MAVEN-STATIC Observations of Ion Temperature and Initial Ion Acceleration in the Martian Ionosphere”. **Geophysical Research Letters** 49.18, e2022GL100182. DOI: 10.1029/2022GL100182.

Heavens, N. G. et al. (2018). “Hydrogen escape from Mars enhanced by deep convection in dust storms”. **Nature Astronomy** 2.2, pp. 126–132. DOI: 10.1038/s41550-017-0353-4.

Herd, C. R., N. G. Adams, and D. Smith (1990). “OH Production in the Dissociative Recombination of H 3O +, HCO 2 +, and N 2OH +: Comparison with Theory and Interstellar Implications”. **Astrophysical Journal** 349, p. 388. DOI: 10.1086/168322.

Herron, J. T. (1999). “Evaluated Chemical Kinetics Data for Reactions of N(^{2}D) N(^{2}P), and $N_2(A^3\Sigma_u^+)$ in the Gas Phase”. **Journal of Physical and Chemical Reference Data** 28.5, pp. 1453–1483. DOI: 10.1063/1.556043.

Hierl, P. M., R. A. Morris, and A. A. Viggiano (1997). “Rate coefficients for the endothermic reactions $C^+(^2P) + H_2(D_2) \rightarrow CH^+(CD^+) + H(D)$ as functions of temperature from 400-1300 K”. **Journal of Chemical Physics** 106.24, pp. 10145–10152. DOI: 10.1063/1.474093.

Holmes, J. A. et al. (2021). “Enhanced water loss from the martian atmosphere during a regional-scale dust storm and implications for long-term water loss”. **Earth and Planetary Science Letters** 571, 117109, p. 117109. DOI: 10.1016/j.epsl.2021.117109.

Hu, R. and T. B. Thomas (2022). “A nitrogen-rich atmosphere on ancient Mars consistent with isotopic evolution models”. **Nature Geoscience** 15.2, pp. 106–111. DOI: 10.1038/s41561-021-00886-y. arXiv: 2202.04825 [astro-ph.EP].

Huebner, W. and J. Mukherjee (2015). **Photo Ionization/Dissociation Rates**.

Hughes, A. et al. (2019). “Proton Aurora on Mars: A Dayside Phenomenon Pervasive in Southern Summer”. **Journal of Geophysical Research (Space Physics)** 124.12, pp. 10, 533–10, 548. DOI: 10.1029/2019JA027140.

Hunten, D. M., R. O. Pepin, and J. C. G. Walker (1987). “Mass fractionation in hydrodynamic escape”. **Icarus** 69.3, pp. 532–549. DOI: `10.1016/0019-1035(87)90022-4`.

Hunten, D. M. (1973). “The escape of light gases from planetary atmospheres”. **Journal of Atmospheric Sciences** 30.8, pp. 1481–1494.

Hynek, B. M., M. Beach, and M. R. T. Hoke (2010). “Updated global map of Martian valley networks and implications for climate and hydrologic processes”. **Journal of Geophysical Research: Planets** 115.E9. DOI: `10.1029/2009JE003548`.

Ingersoll, A. P. (1969). “Mars: Occurrence of Liquid Water”. **Science** 129.13, pp. 1372–1372. DOI: `10.4045/tidsskr.09.0631`.

Inui, S. et al. (2018). “Cold Dense Ion Outflow Observed in the Martian-Induced Magnetotail by MAVEN”. **Geophysical Research Letters** 45.11, pp. 5283–5289. DOI: `10.1029/2018GL077584`.

Jain, S. K. et al. (2023). “Thermal structure of Mars’ middle and upper atmospheres: Understanding the impacts of dynamics and solar forcing”. **Icarus** 393, 114703, p. 114703. DOI: `10.1016/j.icarus.2021.114703`.

Jakosky, B. M. and C. B. Farmer (1982). “The seasonal and global behavior of water vapor in the Mars atmosphere - Complete global results of the Viking atmospheric water detector experiment”. **Journal of Geophysical Research** 87, pp. 2999–3019. DOI: `10.1029/JB087iB04p02999`.

Jakosky, B. M. and L. J. Hallis (2022). “The History and Inventory of Water on Mars”. In: **Seventh International Workshop on the Mars Atmosphere: Modelling and Observations**, 4205, p. 4205.

Jakosky, B. M. et al. (2017). “Mars’ atmospheric history derived from upper-atmosphere measurements of ^{38}Ar/^{36}Ar”. **Science** 355.6332, pp. 1408–1410. DOI: `10.1126/science.aai7721`.

Jakosky, B. M. et al. (2018). “Loss of the Martian atmosphere to space: Present-day loss rates determined from MAVEN observations and integrated loss through time”. **Icarus** 315, pp. 146–157. DOI: `10.1016/j.icarus.2018.05.030`.

Jakosky, B. M., B. G. Henderson, and M. T. Mellon (1995). “Chaotic obliquity and the nature of the Martian climate”. **Journal of Geophysical Research: Planets** 100.E1, pp. 1579–1584. DOI: `10.1029/94JE02801`.

Jeans, J. (1925). **The dynamical theory of gases**. University Press.

Jensen, M. J. et al. (1999). “Dissociative recombination and excitation of H_2O^+ and HDO^+”. **Physical Review A** 60.4, pp. 2970–2976. DOI: `10.1103/PhysRevA.60.2970`.

Jensen, M. J. et al. (2000). “Dissociative Recombination of H_3O^+, HD_2O^+, and D_3O^+”. **Astrophysical Journal** 543.2, pp. 764–774. DOI: `10.1086/317137`.

Kang, W. (2019). “Wetter Stratospheres on High-obliquity Planets”. **Astrophysical Journall** 877.1, L6, p. L6. DOI: `10.3847/2041-8213/ab1f79`. arXiv: `1904.04740 [astro-ph.EP]`.

Kass, D. M. et al. (2016). “Interannual similarity in the Martian atmosphere during the dust storm season”. **Geophysical Research Letters** 43.12, pp. 6111–6118. DOI: `10.1002/2016GL068978`.

Kass, D. M. and Y. L. Yung (1999). “Water on Mars: Isotopic constraints on exchange between the atmosphere and surface”. **Geophysical Research Letters** 26.24, pp. 3653–3656. DOI: `10.1029/1999GL008372`.

Kasting, J. F. and J. B. Pollack (1983). “Loss of water from Venus. I. Hydrodynamic escape of hydrogen”. **Icarus** 53.3, pp. 479–508. DOI: `10.1016/0019-1035(83)90212-9`.

Kasting, J. F., D. P. Whitmire, and R. T. Reynolds (1993). “Habitable Zones around Main Sequence Stars”. **Icarus** 101.1, pp. 108–128. DOI: `10.1006/icar.1993.1010`.

Kim, J. et al. (1998). “Solar cycle variability of hot oxygen atoms at Mars”. **Journal of Geophysical Research** 103.A12, pp. 29339–29342. DOI: `10.1029/98JA02727`.

Klingelhöfer, G. et al. (2004). “Jarosite and Hematite at Meridiani Planum from Opportunity’s Mössbauer Spectrometer”. **Science** 306. DOI: `10.1126/science.1104653`.

Klippenstein, S. J., Y. Georgievskii, and B. J. McCall (2010). “Temperature Dependence of Two Key Interstellar Reactions of H_3^+: $O(^3P) + H_3^+$ and $CO + H_3^+$”. **Journal of Physical Chemistry A** 114.1, pp. 278–290. DOI: `10.1021/jp908500h`.

Kong, T. Y. and M. B. McElroy (1977). “Photochemistry of the Martian atmosphere”. **Icarus** 32.2, pp. 168–189. DOI: `10.1016/0019-1035(77)90058-6`.

Korolov, I. et al. (2009). “Recombination of HCO^+ and DCO^+ ions with electrons”. **International Journal of Mass Spectrometry** 280.1-3, pp. 144–148. DOI: `10.1016/j.ijms.2008.07.023`.

Krasnopolsky, V. (1993). “Photochemistry of the Martian Atmosphere (Mean Conditions)”. **Icarus** 101. DOI: `10.1006/icar.1993.1027`.

Krasnopolsky, V. A. and P. D. Feldman (2001). “Detection of molecular hydrogen in the atmosphere of Mars”. **Science** 294.5548, pp. 1914–1917. DOI: `10.1126/science.1065569`.

Krasnopolsky, V. A. and V. A. Parshev (1979). “Ozone and photochemistry of the Martian lower atmosphere”. **Planetary and Space Science** 27.2, pp. 113–120. DOI: `10.1016/0032-0633(79)90040-0`.

Krasnopolsky, V. et al. (1997). “High-resolution spectroscopy of Mars at 3.7 and 8 μm:A sensitive search for H_2O_2, H_2CO, HCI, and CH_4, and detection of HDO”. **Journal of Geophysical Research** 102. DOI: `10.1029/96JE03766`.

Krasnopolsky, V. (2000). “NOTE: On the Deuterium Abundance on Mars and Some Related Problems”. **Icarus** 148.2, pp. 597–602. DOI: `10.1006/icar.2000.6534`.

Krasnopolsky, V. A. (2002). “Mars’ upper atmosphere and ionosphere at low, medium, and high solar activities: Implications for evolution of water”. **Journal of Geophysical Research (Planets)** 107.E12, p. 5128. DOI: `10.1029/2001JE001809`.

— (2006). “Photochemistry of the martian atmosphere: Seasonal, latitudinal, and diurnal variations”. **Icarus** 185.1, pp. 153–170. DOI: `10.1016/j.icarus.2006.06.003`.

Krasnopolsky, V. A. (2010). “Solar activity variations of thermospheric temperatures on Mars and a problem of CO in the lower atmosphere”. **Icarus** 207.2, pp. 638–647. DOI: `10.1016/j.icarus.2009.12.036`.

— (2012). “A photochemical model for the Venus atmosphere at 47–112km”. **Icarus** 218.1, pp. 230–246. DOI: `10.1016/j.icarus.2011.11.012`.

— (2013). “Nighttime photochemical model and night airglow on Venus”. **Planetary and Space Science** 85, pp. 78–88. DOI: `10.1016/j.pss.2013.05.022`.

— (2014). “Chemical composition of Titan’s atmosphere and ionosphere: Observations and the photochemical model”. **Icarus** 236, pp. 83–91. DOI: `10.1016/j.icarus.2014.03.041`.

— (2015). “Variations of the HDO/H_2O ratio in the martian atmosphere and loss of water from Mars”. **Icarus** 257, pp. 377–386. DOI: `10.1016/j.icarus.2015.05.021`.

— (2019). “Photochemistry of water in the martian thermosphere and its effect on hydrogen escape”. **Icarus** 321, pp. 62–70. DOI: `10.1016/j.icarus.2018.10.033`.

— (2020). “A photochemical model of Pluto’s atmosphere and ionosphere”. **Icarus** 335, p. 113374. DOI: `10.1016/j.icarus.2019.07.008`.

Krasnopolsky, V. A., S. Chakrabarti, and G. R. Gladstone (1993). “Helium in the Martian atmosphere”. **Journal of Geophysical Research: Planets** 98.E8, pp. 15061–15068. DOI: `10.1029/93JE00534`.

Krasnopolsky, V. A. and D. P. Cruikshank (1995). “Photochemistry of Triton’s atmosphere and ionosphere”. **Journal of Geophysical Research: Planets** 100.E10, pp. 21271–21286. DOI: `10.1029/95JE01904`.

Krasnopolsky, V. A., M. J. Mumma, and G. Randall Gladstone (1998). “Detection of Atomic Deuterium in the Upper Atmosphere of Mars”. **Science** 280, p. 1576. DOI: `10.1126/science.280.5369.1576`.

Kulikov, Y. N. et al. (2007). “A Comparative Study of the Influence of the Active Young Sun on the Early Atmospheres of Earth, Venus, and Mars”. **Space Science Reviews** 129.1, pp. 207–243. DOI: `10.1007/s11214-007-9192-4`.

Kumar, S. (1982). “Photochemistry of SO_2 in the atmosphere of Io and implications on atmospheric escape”. **Journal of Geophysical Research: Space Physics** 87.A3, pp. 1677–1684. DOI: `10.1029/JA087iA03p01677`.

Kurokawa, H. et al. (2014). “Evolution of water reservoirs on Mars: Constraints from hydrogen isotopes in martian meteorites”. **Earth and Planetary Science Letters** 394. DOI: `10.1016/j.epsl.2014.03.027`.

Lamb, K. D. et al. (2017). “Laboratory measurements of HDO/H_2O isotopic fractionation during ice deposition in simulated cirrus clouds”. **Proceedings of the National Academy of Science** 114.22, pp. 5612–5617. DOI: `10.1073/pnas.1618374114`. arXiv: `1508.01139 [physics.ao-ph]`.

Lammer, H. et al. (2003a). "Estimation of the past and present Martian water-ice reservoirs by isotopic constraints on exchange between the atmosphere and the surface". **International Journal of Astrobiology** 2.3, pp. 195–202.

Lammer, H. et al. (2003b). "Loss of water from Mars:. Implications for the oxidation of the soil". **Icarus** 165.1, pp. 9–25. DOI: `10.1016/S0019-1035(03)00170-2`.

Larsson, M. et al. (1996). "Dissociative recombination of H_2D^+ and the cosmic abundance of deuterium." **Astronomy and Astrophysics, v.309, p.L1-L3** 309, p. L1.

Laskar, J. and P. Robutel (1993). "The chaotic obliquity of the planets". **Nature** 361.6413, pp. 608–612. DOI: `10.1038/361608a0`.

Laskar, J. et al. (2004). "Long term evolution and chaotic diffusion of the insolation quantities of Mars". **Icarus** 170.2, pp. 343–364. DOI: `10.1016/J.ICARUS.2004.04.005`.

Lasue, J. et al. (2013). "Quantitative Assessments of the Martian Hydrosphere". **Space Science Reviews** 174, pp. 155–212. DOI: `10.1007/s11214-012-9946-5`.

Le Garrec, J. .-. et al. (2003). "The ion-molecule reaction of O $^+$ with N $_2$ measured down to 23 K". **Chemical Physics Letters** 372.3, pp. 485–488. DOI: `10.1016/S0009-2614(03)00377-4`.

Leblanc, F. et al. (2015). "Mars heavy ion precipitating flux as measured by Mars Atmosphere and Volatile EvolutioN". **Geophysical Research Letters** 42.21, pp. 9135–9141. DOI: `10.1002/2015GL066170`.

Lee, Y. et al. (2015). "Hot oxygen corona at Mars and the photochemical escape of oxygen: Improved description of the thermosphere, ionosphere, and exosphere". **Journal of Geophysical Research: Planets** 120.11, pp. 1880–1892. DOI: `10.1002/2015JE004890`.

Leshin Watson, L. et al. (1994). "Water on Mars: Clues from Deuterium/Hydrogen and Water Contents of Hydrous Phases in SNC Meteorites". **Science** 265.5168, pp. 86–90. DOI: `10.1126/science.265.5168.86`.

Lewkow, N. R. and V. Kharchenko (2014). "Precipitation of Energetic Neutral Atoms and Induced Non-thermal Escape Fluxes from the Martian Atmosphere". **Astrophysical Journal** 790.2, 98, p. 98. DOI: `10.1088/0004-637X/790/2/98`. arXiv: `1404.5986 [astro-ph.EP]`.

Liang, M.-C. and Y. L. Yung (2009). "Modeling the distribution of H_2O and HDO in the upper atmosphere of Venus". **Journal of Geophysical Research: Planets** 114.E5. DOI: `10.1029/2008JE003095`.

Lillis, R. J. et al. (2017). "Photochemical escape of oxygen from Mars: First results from MAVEN in situ data". **J. Geophys. Res. Space Physics** 122.3, pp. 3815–3836. DOI: `10.1002/2016JA023525`.

Lillis, R. J. et al. (2021). "Ionization Efficiency in the Dayside Ionosphere of Mars: Structure and Variability". **Journal of Geophysical Research (Planets)** 126.12, e06923, e06923. DOI: `10.1029/2021JE006923`.

Liu, S. C. and T. M. Donahue (1976). "The regulation of hydrogen and oxygen escape from Mars". **Icarus** 28.2, pp. 231–246. DOI: `10.1016/0019-1035(76)90035-X`.

Lo, D. Y., R. V. Yelle, and R. J. Lillis (2020). "Carbon photochemistry at Mars: Updates with recent data". **Icarus** 352.July. DOI: `10.1016/j.icarus.2020.114001`.

Lo, D. Y. et al. (2021). "Carbon photochemical escape rates from the modern Mars atmosphere". **Icarus** 360, p. 114371. DOI: `10.1016/j.icarus.2021.114371`.

Lo, D. Y. et al. (2022). "MAVEN/IUVS observations of C I 156.1 nm and 165.7 nm dayglow: Direct detection of carbon and implications on photochemical escape". **Icarus** 371, p. 114664. DOI: `10.1016/j.icarus.2021.114664`.

Lowell, P. (1908). **Mars as the Abode of Life**. Macmillan.

Luhmann, J. G. (1990). "A model of the ion wake of Mars". **Geophysical Research Letters** 17.6, pp. 869–872. DOI: `10.1029/GL017i006p00869`.

Luhmann, J. G., R. E. Johnson, and M. H. G. Zhang (1992). "Evolutionary impact of sputtering of the Martian atmosphere by O+ pickup ions". **Geophysical Research Letters** 19.21, pp. 2151–2154. DOI: `10.1029/92GL02485`.

Lunine, J. I. et al. (2003). "The origin of water on Mars". **Icarus** 165.1, pp. 1–8.

Ma, Y.-J. and A. F. Nagy (2007). "Ion escape fluxes from Mars". **Geophysical Research Letters** 34, p. L08201. DOI: `10.1029/2006GL029208`.

Maes, L. et al. (2021). "Escape of CO_2^+ and Other Heavy Minor Ions From the Ionosphere of Mars". **Journal of Geophysical Research (Space Physics)** 126.1, e28608, e28608. DOI: `10.1029/2020JA028608`.

Mahaffy, P. R. et al. (2015a). "The imprint of atmospheric evolution in the D/H of hesperian clay minerals on Mars". **Science** 347.6220, pp. 412–414. DOI: `10.1126/science.1260291`.

Mahaffy, P. R. et al. (2013). "Abundance and Isotopic Composition of Gases in the Martian Atmosphere from the Curiosity Rover". **Science** 341.6143, pp. 263–266. DOI: `10.1126/science.1237966`.

Mahaffy, P. R. et al. (2015b). "The Neutral Gas and Ion Mass Spectrometer on the Mars Atmosphere and Volatile Evolution Mission". **Space Science Reviews** 195.1-4, pp. 49–73. DOI: `10.1007/s11214-014-0091-1`.

Maltagliati, L. (2011). "Evidence of Water Vapor in Excess of Saturation in the Atmosphere of Mars". **Science** 333. DOI: `10.1126/science.1207957`.

Manion, J. A. et al. (2015). **NIST Chemical Kinetics Database. NIST Standard Reference Database 17**. Release 1.6.8. Version 2015.09.

Marti, J. and K. Mauersberger (1993). "A Survey and New Measurements of Ice Vapor Pressure at Temperatures Between 170 and 250K". **Geophysical Research Letters** 20. DOI: `10.1029/93GL00105`.

Masson, P. et al. (2001). “Geomorphologic Evidence for Liquid Water”. **Space Science Reviews** 96.1, pp. 333–364. DOI: `10.1023/A:1011913809715`.

Matta, M., P. Withers, and M. Mendillo (2013). “The composition of Mars’ topside ionosphere: Effects of hydrogen”. **Journal of Geophysical Research (Space Physics)** 118.5, pp. 2681–2693. DOI: `10.1002/jgra.50104`.

Mayyasi, M. et al. (2018). “Significant Space Weather Impact on the Escape of Hydrogen From Mars”. **Geophysical Research Letters** 45.17, pp. 8844–8852. DOI: `10.1029/2018GL077727`.

Mayyasi, M. et al. (2019). “Seasonal Variability of Deuterium in the Upper Atmosphere of Mars”. **Journal of Geophysical Research (Space Physics)** 124.3, pp. 2152–2164. DOI: `10.1029/2018JA026244`.

McCauley, J. F. et al. (1972). “Preliminary Mariner 9 Report on the Geology of Mars (A 4. 3)”. **Icarus** 17.2, pp. 289–327. DOI: `10.1016/0019-1035(72)90003-6`.

McElroy, D. et al. (2013). “The UMIST database for astrochemistry 2012”. **Astronomy & Astrophysics** 550, A36, A36. DOI: `10.1051/0004-6361/201220465`. eprint: `1212.6362`.

McElroy, M. B. and T. M. Donahue (1972). “Stability of the Martian Atmosphere”. **Science** 177.13, pp. 986–988. DOI: `10.1007/978-3-642-70401-7_3`.

McElroy, M. B., T. Y. Kong, and Y. L. Yung (1977). “Photochemistry and evolution of Mars’ atmosphere: A Viking perspective”. **Journal of Geophysical Research** 82.28, pp. 4379–4388. DOI: `10.1029/js082i028p04379`.

Milligan, D. B. and M. J. McEwan (2000). “$H_3{}^+$+O: an experimental study.” **Chemical Physics Letters** 319.5, pp. 482–485. DOI: `10.1016/S0009-2614(00)00154-8`.

Millour, E. and F. Forget (2018). **Mars Climate Database**. Version 5.3. LATMOS.

Mitchell, J. B. A. et al. (2005). “LETTER TO THE EDITOR: Dissociative recombination of rare gas hydride ions: II. ArH^+”. **Journal of Physics B Atomic Molecular Physics** 38.10, pp. L175–L181. DOI: `10.1088/0953-4075/38/10/L07`.

Molina-Cuberos, G. J. et al. (2002). “Ion-neutral chemistry model of the lower ionosphere of Mars”. **Journal of Geophysical Research (Planets)** 107.E5, 5027, p. 5027. DOI: `10.1029/2000JE001447`.

Montmessin, F., T. Fouchet, and F. Forget (2005). “Modeling the annual cycle of HDO in the Martian atmosphere”. **Journal of Geophysical Research E: Planets** 110. DOI: `10.1029/2004JE002357`.

Moores, J. E. et al. (2011a). “Stratification of HDO During Cloud Formation on Mars”. In: **42nd Annual Lunar and Planetary Science Conference**. Lunar and Planetary Science Conference, p. 1402.

Moores, J. E., P. H. Smith, and W. V. Boynton (2011b). “Adsorptive fractionation of HDO on JSC MARS-1 during sublimation with implications for the regolith of Mars”. **Icarus** 211.2, pp. 1129–1149. DOI: `10.1016/j.icarus.2010.10.020`.

Moses, J., M. Zolotov, and B. Fegley (2002). "Photochemistry of a Volcanically Driven Atmosphere on Io: Sulfur and Oxygen Species from a Pele-Type Eruption". **Icarus** 156.1, pp. 76–106. DOI: `10.1006/icar.2001.6758`.

Mustard, J. F. et al. (2008). "Hydrated silicate minerals on Mars observed by the Mars Reconnaissance Orbiter CRISM instrument". **Nature** 454.7202, pp. 305–309. DOI: `10.1038/nature07097`.

Nagy, A., J. Kim, and T. Cravens (1990). "Hot hydrogen and oxygen atoms in the upper atmospheres of Venus and Mars". **Annales geophysicae. Atmospheres, hydrospheres and space sciences** 8.4, pp. 251–256.

Nahar, S. N. and A. K. Pradhan (1997). "Electron-Ion Recombination Rate Coefficients, Photoionization Cross Sections, and Ionization Fractions for Astrophysically Abundant Elements. I. Carbon and Nitrogen". **Astrophysical Journals** 111.1, pp. 339–355. DOI: `10.1086/313013`.

Nair, H. et al. (1994). "Photchemical Model of the Martian Atmosphere". **Icarus** 111.1, pp. 124–150. DOI: `10.1006/icar.1994.1137`.

Neary, L. et al. (2020). "Explanation for the Increase in High-Altitude Water on Mars Observed by NOMAD During the 2018 Global Dust Storm". **Geophysical Research Letters** 47.7, e84354, e84354. DOI: `10.1029/2019GL084354`.

Nee, J. B. and L. C. Lee (1984). "Photoabsorption cross section of OD at 115-180 nm". **The Journal of Chemical Physics** 81.9, pp. 3811–3813. DOI: `10.1063/1.448183`.

Newman, C. E., S. R. Lewis, and P. L. Read (2005). "The atmospheric circulation and dust activity in different orbital epochs on Mars". **Icarus** 174.1, pp. 135–160. DOI: `10.1016/j.icarus.2004.10.023`.

Nier, A. O. and M. B. Mcelroy (1977). "Composition and Structure of the neutral upper atmosphere of mars: Results from Viking 1 and Viking 2". **Science** 194.4271, pp. 1298–1300. DOI: `10.1126/science.194.4271.1298`.

Niles, P. B. et al. (2010). "Stable Isotope Measurements of Martian Atmospheric CO_2 at the Phoenix Landing Site". **Science** 329.5997, pp. 1334–1337. DOI: `10.1126/science.1192863`.

Okabe, H. (1978). **Photochemistry of Small Molecules**. A Wiley-Interscience publication. Wiley. ISBN: 9780471653042.

Owen, T. et al. (1977). "The composition of the atmosphere at the surface of Mars". **Journal of Geophysical Research** 82.B28, pp. 4635–4640. DOI: `10.1029/JS082i028p04635`.

Owen, T. et al. (1988). "Deuterium on Mars: The Abundance of HDO and the Value of D/H". **Science** 240.4860, pp. 1767–1770. DOI: `10.1126/science.240.4860.1767`.

Pacifici, A., G. Komatsu, and M. Pondrelli (2009). "Geological evolution of Ares Vallis on Mars: Formation by multiple events of catastrophic flooding, glacial and periglacial processes". **Icarus** 202.1, pp. 60–77. DOI: `10.1016/j.icarus.2009.02.029`.

Pickett, N. B. et al. (2022). “Carbon Ion Fluxes at Mars: First Results of Tailward Flows From MAVEN-STATIC”. **Journal of Geophysical Research (Space Physics)** 127.1, e29635, e29635. DOI: `10.1029/2021JA029635`.

Pieris, H. and B. M. Jakosky (2022). “Understanding the Evolution of the Martian Atmosphere Through Nitrogen Isotopes”. In: **Seventh International Workshop on the Mars Atmosphere: Modelling and Observations**, p. 3557.

Plaut, J. J. et al. (2007). “Subsurface Radar Sounding of the South Polar Layered Deposits of Mars”. **Science** 316. DOI: `10.1126/science.1139672`.

Poulet, F. et al. (2005). “Phyllosilicates on Mars and implications for early martian climate”. **Nature** 438.7068, pp. 623–627. DOI: `10.1038/nature04274`.

Praxmarer, C., A. Hansel, and W. Lindinger (1994). “Interaction between the ion dipole and the ion-induced dipole in reactions of the polar ion $ArH^{+}{}_3$”. **Journal of Chemical Physics** 100.12, pp. 8884–8889. DOI: `10.1063/1.466691`.

Rahmati, A. et al. (2017). “MAVEN measured oxygen and hydrogen pickup ions: Probing the Martian exosphere and neutral escape”. **Journal of Geophysical Research: Space Physics** 122.3, pp. 3689–3706. DOI: `10.1002/2016JA023371`.

Rahmati, A. et al. (2018). “Seasonal Variability of Neutral Escape from Mars as Derived From MAVEN Pickup Ion Observations”. **Journal of Geophysical Research (Planets)** 123.5, pp. 1192–1202. DOI: `10.1029/2018JE005560`.

Ramstad, R. et al. (2023). “Solar wind driven influences on the Martian oxygen corona: Constraints on atmospheric sputtering from a synthesis of MAVEN measurements during solar minimum”. **Icarus** 397, p. 115491.

Rosén, S. et al. (1998). “Absolute cross sections and final-state distributions for dissociative recombination and excitation of CO^{+}(v=0) using an ion storage ring”. **Physical Review A: General Physics** 57.6, pp. 4462–4471. DOI: `10.1103/PhysRevA.57.4462`.

Rosén, S. et al. (2000). “Recombination of simple molecular ions studied in storage ring: dissociative recombination of H_2O^{+}”. **Faraday Discussions** 115, pp. 295–302. DOI: `10.1039/a909314a`.

Rosenberg, E. N. et al. (2019). “The volume of water required to carve the martian valley networks: Improved constraints using updated methods”. **Icarus** 317.August 2017, pp. 379–387. DOI: `10.1016/j.icarus.2018.07.017`.

Rossi, L. et al. (2022). “The HDO Cycle on Mars: Comparison of ACS Observations With GCM Simulations”. **Journal of Geophysical Research (Planets)** 127.8, e07201, e07201. DOI: `10.1029/2022JE007201`.

Sagan, C. (1971). “The long winter model of Martian biology: A speculation”. **Icarus** 15.3, pp. 511–514. DOI: `10.1016/0019-1035(71)90131-X`.

Sander, S. P. et al. (2011). **Chemical Kinetics and Photochemical Data for Use in Atmospheric Studies Evaluation No. 17**. JPL Publication 10-6. Pasadena: Jet Propulsion Laboratory.

Savijärvi, H. et al. (2019). “Water vapor mixing ratios and air temperatures for three martian years from Curiosity”. **Icarus** 326. DOI: `10.1016/j.icarus.2019.03.020`.

Scheller, E. L. et al. (2021). “Long-term drying of Mars by sequestration of ocean-scale volumes of water in the crust”. **Science** 372.6537, pp. 56–62. DOI: `10.1126/science.abc7717`.

Scheller, E. L. et al. (2022). “Aqueous alteration processes in Jezero crater, Mars—Implications for organic geochemistry”. **Science** 378.6624, pp. 1105–1110.

Schlichting, H. E., R. Sari, and A. Yalinewich (2015). “Atmospheric mass loss during planet formation: The importance of planetesimal impacts”. **Icarus** 247, pp. 81–94. DOI: `10.1016/j.icarus.2014.09.053`.

Schunk, R. and A. Nagy (2009). **Ionospheres: Physics, Plasma Physics, and Chemistry**. DOI: `10.1017/CBO9780511635342`.

Scott, G. B. et al. (1997). “Gas phase reactions of some positive ions with atomic and molecular hydrogen at 300 K”. **Journal of Chemical Physics** 106.10, pp. 3982–3987. DOI: `10.1063/1.473116`.

Scott, G. B. I. et al. (1998). “Gas-phase reactions of some positive ions with atomic and molecular nitrogen”. **Journal of Chemical Physics** 109.20, pp. 9010–9014. DOI: `10.1063/1.477571`.

Seiff, A. (1982). “Post-Viking models for the structure of the summer atmosphere of Mars”. **Advances in Space Research** 2. DOI: `10.1016/0273-1177(82)90102-8`.

Shaposhnikov, D. S. et al. (2019). “Seasonal Water ”Pump” in the Atmosphere of Mars: Vertical Transport to the Thermosphere”. **Geophysical Research Letters** 46. DOI: `10.1029/2019GL082839`.

Shematovich, V. I. (2013). “Suprathermal oxygen and hydrogen atoms in the upper Martian atmosphere”. **Solar System Research** 47.6, pp. 437–445. DOI: `10.1134/S0038094613060087`.

Shizgal, B. D. (1999). “Escape of H and D from Mars and Venus by energization with hot oxygen”. **Journal of Geophysical Research: Space Physics** 104.A7, pp. 14833–14846. DOI: `10.1029/1999JA900157`.

Slade, M. A., B. J. Butler, and D. O. Muhleman (1992). “Mercury Radar Imaging: Evidence for Polar Ice”. **Science** 258.5082, pp. 635–640. DOI: `10.1126/science.258.5082.635`.

Slipski, M. and B. M. Jakosky (2016). “Argon isotopes as tracers for Martian atmospheric loss”. **Icarus** 272, pp. 212–227.

Smith, M. A. et al. (2002). “$HOC^+ + H_2$ Isomerization Rate at 25 K: Implications for the Observed $[HCO^+]/[HOC^+]$ Ratios in the Interstellar Medium”. **Astrophysical Journall** 578.1, pp. L87–L90. DOI: `10.1086/344404`.

Smith, M. D. (2004). “Interannual variability in TES atmospheric observations of Mars during 1999-2003”. **Icarus** 167.1, pp. 148–165. DOI: `10.1016/j.icarus.2003.09.010`.

Smith, M. D. et al. (2006). “One Martian year of atmospheric observations using MER Mini-TES”. **Journal of Geophysical Research E: Planets** 111. DOI: `10.1029/2006JE002770`.

Smyth, W. H. and M. C. Wong (2004). “Impact of electron chemistry on the structure and composition of Io’s atmosphere”. **Icarus** 171.1, pp. 171–182. DOI: `10.1016/j.icarus.2004.04.001`.

Španěl, P., L. Dittrichová, and D. Smith (1993). “FALP studies of the dissociative recombination coefficients for O_2^+ and NO^+ within the electron temperature range 300-2000 K”. **International Journal of Mass Spectrometry and Ion Processes** 129, pp. 183–191. DOI: `10.1016/0168-1176(93)87041-P`.

Squyres, S. W. et al. (2004). “In Situ Evidence for an Ancient Aqueous Environment at Meridiani Planum, Mars”. **Science** 306. DOI: `10.1126/science.1104559`.

Stone, S. W. et al. (2018). “Thermal Structure of the Martian Upper Atmosphere From MAVEN NGIMS”. **Journal of Geophysical Research: Planets**. DOI: `10.1029/2018JE005559`.

Stone, S. W. et al. (2020). “Hydrogen escape from Mars is driven by seasonal and dust storm transport of water”. **Science** 370.6518, pp. 824–831. DOI: `10.1126/science.aba5229`.

Stratton, A. and B. Jakosky (2021). “Influence of Dust Storm Adsorptive Properties on the Atmospheric Water Content of Mars”. In: **AGU Fall Meeting Abstracts**. Vol. 2021, P31B-03, P31B–03.

Stratton, M. and B. Jakosky (2020). “Influence of Dust Adsorption Effects on the Martian Water Cycle”. In: **51st Annual Lunar and Planetary Science Conference**. 2326, p. 2484.

Thiemann, E. M. B. et al. (2018). “Mars Thermospheric Variability Revealed by MAVEN EUVM Solar Occultations: Structure at Aphelion and Perihelion and Response to EUV Forcing”. **Journal of Geophysical Research (Planets)** 123. DOI: `10.1029/2018JE005550`.

Touma, J. and J. Wisdom (1993). “The Chaotic Obliquity of Mars”. **Science** 259.5099, pp. 1294–1297. DOI: `10.1126/science.259.5099.1294`.

Trainer, M. G. et al. (2019). “Seasonal Variations in Atmospheric Composition as Measured in Gale Crater, Mars”. **Journal of Geophysical Research: Planets** 124. DOI: `10.1029/2019JE006175`.

Tsang, W. and R. F. Hampson (1986). “Chemical Kinetic Data Base for Combustion Chemistry. Part I. Methane and Related Compounds”. **Journal of Physical and Chemical Reference Data** 15.3, pp. 1087–1279. DOI: `10.1063/1.555759`.

Tsang, W. and J. T. Herron (1991). “Chemical Kinetic Data Base for Propellant Combustion I. Reactions Involving NO, NO_2, HNO, HNO_2, HCN and N_2O”. **Journal of Physical and Chemical Reference Data** 20.4, pp. 609–663. DOI: `10.1063/1.555890`.

Tully, J. C. (1975). “Reactions of $O(^1D)$ with atmospheric molecules”. **Journal of Chemical Physics** 62.5, pp. 1893–1898. DOI: `10.1063/1.430675`.

Usui, T. et al. (2012). “Evidence from Olivine-Hosted Melt Inclusions that the Martian Mantle has a Chondritic D/H Ratio and that Some Young Basalts have Assimilated Old Crust”. In: **Lunar and Planetary Science Conference**, 1341.

Vals, M. et al. (2022). “Improved Modeling of Mars’ HDO Cycle Using a Mars’ Global Climate Model”. **Journal of Geophysical Research (Planets)** 127.8, e07192, e07192. DOI: `10.1029/2022JE007192`.

Vandaele, A. C. et al. (2019). “Martian dust storm impact on atmospheric H 2 O and D/H observed by ExoMars Trace Gas Orbiter”. **Nature** 568.7753, pp. 521–525. DOI: `10.1038/s41586-019-1097-3`.

Vasavada, A. R. et al. (2016). “Thermophysical properties along Curiosity’s traverse in Gale crater, Mars, derived from the REMS ground temperature sensor”. **Icarus** 284. DOI: `10.1016/j.icarus.2016.11.035`.

Viggiano, A. A. et al. (1980). “Laboratory studies of some ion-atom reactions related to interstellar molecular synthesis.” **Astrophysical Journal** 236, pp. 492–497. DOI: `10.1086/157766`.

Viggiano, A. A. et al. (2005). “Rate constants and branching ratios for the dissociative recombination of ${CO_2}^{+}$”. **Journal of Chemical Physics** 122.22, pp. 226101–226101. DOI: `10.1063/1.1926283`.

Villanueva, G. L. et al. (2015). “Strong water isotopic anomalies in the martian atmosphere: Probing current and ancient reservoirs”. **Science** 348.6231, pp. 218–221. DOI: `10.1126/science.aaa3630`.

Villanueva, G. L., G. Liuzzi, M. M. Crismani, et al. (2019). “Strong seasonal and diurnal variabilityof water D/H on Marsas revealed with ExoMars/NOMAD”. In: **EPSC Abstracts**.

Villanueva, G. L. et al. (2021). “Water heavily fractionated as it ascends on Mars as revealed by ExoMars/NOMAD”. **Science Advances** 7.7, eabc8843. DOI: `10.1126/sciadv.abc8843`.

Villanueva, G. L. et al. (2022). “The Deuterium Isotopic Ratio of Water Released From the Martian Caps as Measured With TGO/NOMAD”. **Geophysical Research Letters** 49.12, e98161, e98161. DOI: `10.1029/2022GL098161`.

Volkov, A. N. et al. (2011). “Thermally driven atmospheric escape: Transition from hydrodynamic to Jeans escape”. **The Astrophysical Journal Letters** 729.2, p. L24.

Vos, E. et al. (2022). “Stratigraphic and Isotopic Evolution of the Martian Polar Caps From Paleo-Climate Models”. **Journal of Geophysical Research (Planets)** 127.3, e07115, e07115. DOI: `10.1029/2021JE007115`. eprint: `2203.10471`.

Vuitton, V. et al. (2019). “Simulating the density of organic species in the atmosphere of Titan with a coupled ion-neutral photochemical model”. **Icarus** 324, pp. 120–197. DOI: `10.1016/j.icarus.2018.06.013`.

Wakelam, V. and P. Gratier (2019). **Kinetic Database for Astrochemistry**.

Webster, C. R. et al. (2013). “Isotope Ratios of H, C, and O in CO_2 and H $_2$ O of the Martian Atmosphere”. **Science** 341.6143, pp. 260–263. DOI: `10.1126/science.1237961`.

Wernicke, L. J. and B. M. Jakosky (2021). “Martian Hydrated Minerals: A Significant Water Sink”. **Journal of Geophysical Research (Planets)** 126.3, e06351, e06351. DOI: `10.1029/2019JE006351`.

Williams, R. M. E. et al. (2013). “Martian Fluvial Conglomerates at Gale Crater”. **Science** 340.6136, pp. 1068–1072. DOI: `10.1126/science.1237317`.

Wong, M. C. and R. E. Johnson (1996). “A three-dimensional azimuthally symmetric model atmosphere for Io 1. Photochemistry and the accumulation of a nightside atmosphere”. **Journal of Geophysical Research** 101.E10, pp. 23243–23060. DOI: `10.1029/96JE02510`.

Wong, M. C. and W. H. Smyth (2000). “Model Calculations for Io’s Atmosphere at Eastern and Western Elongations”. **Icarus** 146.1, pp. 60–74. DOI: `10.1006/icar.2000.6362`.

Wong, M. H. et al. (2013). “Isotopes of nitrogen on Mars: Atmospheric measurements by Curiosity’s mass spectrometer”. **Geophysical Research Letters** 40.23, pp. 6033–6037. DOI: `10.1002/2013GL057840`.

Wong, M. L., Y. L. Yung, and G. Randall Gladstone (2015). “Pluto’s implications for a Snowball Titan”. **Icarus**. Special Issue: The Pluto System 246, pp. 192–196. DOI: `10.1016/j.icarus.2014.05.019`.

Wong, M. L. et al. (2017). “The photochemistry of Pluto’s atmosphere as illuminated by New Horizons”. **Icarus**. Special Issue: The Pluto System 287, pp. 110–115. DOI: `10.1016/j.icarus.2016.09.028`.

Woods, T. N. et al. (2019). **LISIRD (LASP Interactive Solar Irradiance Datacenter)**. Version 3.30.0.

Wordsworth, R. (2016). “The Climate of Early Mars”. **Annual Review of Earth and Planetary Sciences** 44, pp. 381–408. DOI: `10.1146/annurev-earth-060115-012355`.

Wordsworth, R. D. et al. (2015). “Comparison of ”warm and wet” and ”cold and icy” scenarios for early Mars in a 3D climate model”. **Journal of Geophysical Research: Planets**. DOI: `10.1002/2015JE004787`.

Wu, Z. et al. (2020). “Dust tides and rapid meridional motions in the Martian atmosphere during major dust storms”. **Nature Communications** 11.1, pp. 1–10. DOI: `10.1038/s41467-020-14510-x`.

Yiğit, E. (2021). “Martian water escape and internal waves”. **Science** 374.6573, pp. 1323–1324. DOI: `10.1126/science.abg5893`.

Yiğit, E. et al. (2021). “Dust Storm Enhanced Gravity Wave Activity in the Martian Thermosphere Observed by MAVEN and Implication for Atmospheric Escape”. **Geophysical Research Letters** 48.5, e92095, e92095. DOI: `10.1029/2020GL092095`. eprint: `2101.07698`.

Yoshida, T. and K. Kuramoto (2020). “Sluggish hydrodynamic escape of early Martian atmosphere with reduced chemical compositions”. **Icarus** 345, 113740, p. 113740. DOI: `10.1016/j.icarus.2020.113740`.

Yu, H.-G., J. T. Muckerman, and J. S. Francisco (2005). “Direct ab initio dynamics study of the OH+ HOCO reaction”. **The Journal of Physical Chemistry A** 109.23, pp. 5230–5236.

Yung, Y. L. and W. B. DeMore (1998). **Photochemistry of Planetary Atmospheres**. Oxford University Press.

Yung, Y. L. and W. Demore (1982). “Photochemistry of the stratosphere of Venus: Implications for atmospheric evolution”. **Icarus** 51.2, pp. 199–247. DOI: `10.1016/0019-1035(82)90080-X`.

Yung, Y. L. et al. (1988). “HDO in the Martian atmosphere: Implications for the abundance of crustal water”. **Icarus** 76.1, pp. 146–159. DOI: `10.1016/0019-1035(88)90147-9`.

Yung, Y. L. et al. (1989). “Hydrogen and deuterium loss from the terrestrial atmosphere: A quantitative assessment of nonthermal escape fluxes”. **Journal of Geophysical Research** 94.D12, pp. 14971–14989. DOI: `10.1029/JD094iD12p14971`.

Yung, Y. L. et al. (2009). “Evidence for carbonyl sulfide (OCS) conversion to CO in the lower atmosphere of Venus”. **Journal of Geophysical Research** 114, E00B34. DOI: `10.1029/2008JE003094`.

Zahnle, K., J. F. Kasting, and J. B. Pollack (1990). “Mass fractionation of noble gases in diffusion-limited hydrodynamic hydrogen escape”. **Icarus** 84.2, pp. 502–527. DOI: `10.1016/0019-1035(90)90050-J`.

Zahnle, K. et al. (2008). “Photochemical instability of the ancient Martian atmosphere”. **Journal of Geophysical Research E: Planets** 113.E11, pp. 1–16. DOI: `10.1029/2008JE003160`.

Zanchet, A. et al. (2009). “Study of the $C(^3P) + OH(X^2\Pi) \rightarrow CO(a^3\Pi) + H(^2S)$ reaction: fully global ab initio potential energy surfaces of the 12A” and 14A” excited states and non adiabatic couplings”. **Physical Chemistry Chemical Physics (Incorporating Faraday Transactions)** 11.29, p. 6182. DOI: `10.1039/b903829a`.

Zhang, P. et al. (2009). “Energy relaxation in collisions of hydrogen and deuterium with oxygen atoms: OH AND OD COLLISION ENERGY RELAXATION”. **J. Geophys. Res.** 114.A7, pp. 1–14. DOI: `10.1029/2009JA014055`.

Zhang, X. et al. (2012). “Sulfur chemistry in the middle atmosphere of Venus”. **Icarus** 217.2, pp. 714–739. DOI: `10.1016/j.icarus.2011.06.016`.

Zuber, M. T. et al. (1998). “Observations of the North Polar Region of Mars from the Mars Orbiter Laser Altimeter”. **Science** 282. DOI: `10.1126/science.282.5396.2053`.

Appendix A

Supporting Information for Chapter 2

This text was originally published as the Supporting Information companion document to chapter 2, “Higher Martian Atmospheric Temperatures at All Altitudes Increase the D/H Fractionation Factor and Water Loss.”

- Text S1: Photodissociation cross sections
- Text S2: Vertical transport
- Text S3: Boundary conditions
- Table A.1: H chemistry reaction list
- Table A.2: D chemistry reaction list
- Table A.3: Boundary conditions
- Table A.4: Temperature profile parameters
- Table A.5: Fractionation factor results
- Figure A.1: HDO Photodissociation cross section
- Figure A.2: OH and OD Photodissociation cross section
- Figure A.3: Reproductions of past studies
- Figure A.4: Contributions of atomic and molecular H, D to loss of H, D

- Figure A.5: Thermal and non-thermal contributions to escape fluxes of H and D for tropopause and exobase temperature variations
- Figure A.6: Changes in transport flux and chemical production/loss of D and H by altitude and tropopause temperature
- Figure A.7: Changes in transport flux and chemical production/loss of D and H by altitude and exobase temperature

Introduction

This Supporting Information file provides additional information on parameters of the model in Text S1-S3, Figures A.1–A.3, and Tables A.1–A.4. A numerical table of the results in Figure 2.4 appears in Table A.5. Figures A.4–A.7 provide additional context supporting the discussion points and conclusions.

Text S1. Photodissociation cross sections

Photodissociation is the process by which molecules are dissociated due to absorption of incoming solar photons. A key parameter that governs absorption of these photons is the photochemical cross section of the absorber; unfortunately, measurements on photochemical cross sections for D-bearing species are rare and incomplete in the literature. In this work, we have included cross sections for semi-heavy water (HDO) (B.-M. Cheng et al. 1999; B. M. Cheng et al. 2004), shown in Figure A.1, and deuterated hydroxyl (OD) (Nee et al. 1984), shown in Figure A.2. The OD cross sections are only available for a small wavelength range compared to OH, so we fill in gaps for OD using the OH data. For the HDO cross sections, we use the measurements valid for 298-300 K, which are the most complete available B.-M. Cheng et al. (1999) and B. M. Cheng et al. (2004). A less complete data set exists for 250 K. Ideally, HDO cross section data in the range of 150-250 K would be used, but these measurements do not exist in the literature. For our purposes, the 300 K cross sections are sufficient, at least until some point in the future when more measurements will hopefully be made.

Text S2. Vertical transport

In terms of modeling the martian atmosphere, the most important distinction between eddy and molecular diffusion are the regimes in which they dominate. Turbulent mixing dominates in the lower atmosphere, and is approximated using eddy diffusion. In this regime, molecular species are intermixed and do not stratify due to their masses. We use the following piece-wise equation for eddy diffusion:

$$K = \begin{cases} 10^6 & z < 60 \text{ km} \\ 2 \times 10^{13} n^{-1/2} & z > 60 \text{ km} \end{cases}$$

Where n is the total number of particles in the atmosphere layer. A similar equation is used by V. Krasnopolsky (2000) and Chaffin et al. (2017).

Above the homopause (about 120 km), molecular diffusion dominates, meaning that molecular species diffusively separate and follow their own scale heights. Molecular diffusion is described by the following equation from Banks et al. (1973):

$$D = \frac{AT^s}{n} \tag{A.1}$$

The values of A and s for H and H_2 through CO_2 have been experimentally determined (Hunten 1973): $A_H = 8.4 \times 10^{17}$, $s_H = 0.597$, $A_{H_2} = 2.23 \times 10^{17}$, $s_{H_2} = 0.75$. For D and HD, we used the theoretical framework for determining A and s given by Banks et al. (1973). This framework applied to H and H_2 results in values of A that disagree with experiment, so we first calculate A and s for D and HD, then use the ratio of the experimental and theoretical values for H and H_2 to scale them, giving the results: $A_D = 5.98 \times 10^{17}$, $A_{HD} = 1.84 \times 10^{17}$. For s_D and s_{HD}, we use the same values as the H-bearing species. For other species, experimental data of A and s are not readily available. We set A and s for other species to 1 and 0.75 respectively, as they should diffuse less easily compared to H, D, H_2 and HD.

Text S3. Boundary conditions

In general, we use the same boundary conditions used by Chaffin et al. (2017), given in Table

A.3. Densities of Ar and N_2 are fixed to be 2% and 1.9% of the CO_2 density respectively. All surface-ward fluxes are fixed to be 0 as we do not account for surface deposition in our model; surface deposition is likely an important process, however, and has been explored in other studies (Zahnle et al. 2008). Because we are only modeling thermal escape, we assume that no species more massive than HD is able to escape to space, and therefore flux to space for more massive species is 0 (except for the flux of O, which is fixed as shown in the table).

Table A.1: H-bearing chemical reactions used in the model. For the photodissociation reactions (unimolecular reactions), the entry in the rate coefficient column is the total model-calculated rate at the top of the equilibrated atmosphere for the standard temperature profile, as reference. For bimolecular reactions, the rate coefficient is in units of cm^3 $molecule^{-1}$ s^{-1}. For termolecular reactions, the unit is cm^6 $molecule^{-1}$ s^{-1}.

Number	Reaction	Rate coefficient	Ref
R1a	$CO_2 \rightarrow CO + O$	6.1×10^{-8}	
R1b	$\rightarrow CO + O(^1D)$	2.4×10^{-7}	
R2a	$O_2 \rightarrow O + O$	2.3×10^{-8}	
R2b	$\rightarrow O + O(^1D)$	4.7×10^{-7}	
R3a	$O_3 \rightarrow O_2 + O$	2.5×10^{-4}	
R3b	$\rightarrow O_2 + O(^1D)$	1.5×10^{-3}	
R4	$H_2 \rightarrow H + H$	1.2×10^{-8}	
R5a	$OH \rightarrow O + H$	1.4×10^{-6}	
R5b	$\rightarrow O(^1D) + H$	4.2×10^{-8}	
R6	$HO_2 \rightarrow OH + O$	1.0×10^{-4}	
R7a	$H_2O \rightarrow H + OH$	1.9×10^{-6}	

Continued on next page

Table A.1 – continued from previous page

Number	**Reaction**	**Rate coefficient**	**Ref**
R7b	$\rightarrow H_2 + O(^1D)$	1.2×10^{-7}	
R8a	$H_2O_2 \rightarrow OH + OH$	1.8×10^{-5}	
R8b	$\rightarrow HO_2 + H$	9.4×10^{-7}	
R9	$O + O + M \rightarrow O_2 + M$	$5.4 \times 10^{-33}(300/T)^{3.25}$	*d*
R10	$O + O_2 + N_2 \rightarrow O_3 + N_2$	$5 \times 10^{-35}e^{724/T}$	*a*
R11	$O + O_2 + CO_2 \rightarrow O_3 + CO_2$	$1.5 \times 10^{-33}(300/T)^{2.4}$	*a*
R12	$O + O_3 \rightarrow O_2 + O_2$	$8.0 \times 10^{-12}e^{-2060/T}$	*a*
R13	$O + CO + M \rightarrow CO_2 + M$	$2.2 \times 10^{-33}e^{-1780/T}$	*d*
R14	$O(^1D) + O_2 \rightarrow O + O_2$	$3.2 \times 10^{-11}e^{70/T}$	*a*
R15	$O(^1D) + O_3 \rightarrow O_2 + O_2$	1.2×10^{-10}	*a*
R16	$\rightarrow O + O + O_2$	1.2×10^{-10}	*a*
R17	$O(^1D) + CO_2 \rightarrow O + CO_2$	$7.5 \times 10^{-11}e^{115/T}$	*a*
R18	$O(^1D) + H_2 \rightarrow H + OH$	1.2×10^{-10}	*a*
R19	$O(^1D) + H_2O \rightarrow OH + OH$	$1.63 \times 10^{-10}e^{60/T}$	*a*
R20	$H_2 + O \rightarrow OH + H$	$6.34 \times 10^{-12}e^{-4000/T}$	*b*
R21	$OH + H_2 \rightarrow H_2O + H$	$2.8 \times 10^{-12}e^{-1800/T}$	*a*
R22	$H + H + M \rightarrow H_2 + M$	$1.6 \times 10^{-32}\left(\frac{298}{T}\right)^{2.27}$	*d*
R23	$H + OH + CO_2 \rightarrow H_2O + CO_2$	$1.292 \times 10^{-30}\left(\frac{300}{T}\right)^{2}$	*c*
R24a	$H + HO_2 \rightarrow OH + OH$	7.2×10^{-11}	*a*
R24b	$\rightarrow H_2 + O_2$	3.45×10^{-12}	*a*
R24c	$\rightarrow H_2O + O(^1D)$	1.6×10^{-12}	*a*
R25a	$H + H_2O_2 \rightarrow HO_2 + H_2$	$2.81 \times 10^{-12}e^{-1890/T}$	*c*
R25b	$\rightarrow H_2O + OH$	$1.7 \times 10^{-11}e^{-1800/T}$	*c*
R26	$H + O_2 \rightarrow HO_2$	$k_0 = 8.8 \times 10^{-32}\left(\frac{T}{300}\right)^{-1.3}$	*ad*

Continued on next page

Table A.1 – continued from previous page

Number	Reaction	Rate coefficient	Ref
		$k_\infty = 7.5 \times 10^{-11} \left(\frac{T}{300}\right)^{0.2}$	*ad*
R27	$H + O_3 \rightarrow OH + O_2$	$1.4 \times 10^{-10} e^{-470/T}$	*c*
R28	$O + OH \rightarrow O_2 + H$	$1.8 \times 10^{-11} e^{180/T}$	*a*
R29	$O + HO_2 \rightarrow OH + O_2$	$3.0 \times 10^{-11} e^{200/T}$	*a*
R30	$O + H_2O_2 \rightarrow OH + HO_2$	$1.4 \times 10^{-12} e^{-2000/T}$	*a*
R31a	$OH + OH \rightarrow H_2O + O$	$4.2 \times 10^{-12} e^{-240/T}$	*c*
R31b	$\rightarrow H_2O_2$	$k_0 = 8.97 \times 10^{-31} \left(\frac{T}{300}\right)^{-1.0}$	*ad*
		$k_\infty = 2.6 \times 10^{-11}$	*ad*
R32	$OH + O_3 \rightarrow HO_2 + O_2$	$1.7 \times 10^{-12} e^{-940/T}$	*a*
R33	$OH + HO_2 \rightarrow H_2O + O_2$	$4.8 \times 10^{-11} e^{250/T}$	*a*
R34	$OH + H_2O_2 \rightarrow H_2O + HO_2$	$2.9 \times 10^{-12} e^{-160/T}$	*c*
R35	$HO_2 + O_3 \rightarrow OH + O_2 + O_2$	$1.0 \times 10^{-14} e^{-490/T}$	*a*
R36	$HO_2 + HO_2 \rightarrow H_2O_2 + O_2$	$3.0 \times 10^{-13} e^{460/T}$	*a*
R37	$HO_2 + HO_2 + M \rightarrow H_2O_2 + O_2 + M$	$4.2 \times 10^{-33} e^{920/T}$	*a*
R38	$CO + OH \rightarrow CO_2 + H$	$k_0 = 1.5 \times 10^{-13} \left(\frac{T}{300}\right)^{0.6}$	*a*
		$k_\infty = 2.1 \times 10^{9} \left(\frac{T}{300}\right)^{6.1}$	*a*
R39	$OH + CO \rightarrow CO_2H$	$k_0 = 5.9 \times 10^{-33} \left(\frac{T}{300}\right)^{-1.4}$	*a*
		$k_\infty = 1.1 \times 10^{-12} \left(\frac{T}{300}\right)^{1.3}$	*a*
R40	$CO_2H + O_2 \rightarrow HO_2 + CO_2$	2.09×10^{-12}	*c*
R41	$CO_2^+ + H_2 \rightarrow CO_2 + H + H$	8.7×10^{-10}	*e*

[a]Sander et al. (2011). [b]KIDA database (Wakelam et al. 2019).

[c]NIST database (Manion et al. 2015). [d] Deighan (2012). [e]V. A. Krasnopolsky (2010).

Table A.2: The same as Table A.1, but for D-bearing chemistry. Where we cite *a*, we multiply the H-bearing reaction in Table A.1 by the multiplier specified in *a*. If the reference specifies a different rate entirely, we use it. Reaction numbers have been chosen so that the reaction of the same number in Table A.1 is the H-bearing analogue reaction.

Number	**Reaction**	**Rate**	**Ref**
DR4	$HD \rightarrow H + D$	1.2×10^{-8}	
DR5a	$OD \rightarrow O + D$	2.3×10^{-6}	
DR5b	$\rightarrow O(^1D) + D$	4.2×10^{-8}	
DR6	$DO_2 \rightarrow OD + O$	1.0×10^{-4}	
DR7a	$HDO \rightarrow H + OD$	6.3×10^{-7}	
DR7b	$\rightarrow D + OH$	6.3×10^{-7}	
DR7c	$\rightarrow HD + O(^1D)$	4.3×10^{-8}	
DR8a	$HDO_2 \rightarrow OH + OD$	1.8×10^{-5}	
DR8b	$\rightarrow DO_2 + H$	4.7×10^{-7}	
DR8c	$\rightarrow HO_2 + D$	4.7×10^{-7}	
DR18a	$O(^1D) + HD \rightarrow H + OD$	4.92×10^{-11}	*a*
DR18b	$\rightarrow D + OH$	4.92×10^{-11}	*a*
DR19	$O(^1D) + HDO \rightarrow OD + OH$	$1.63 \times 10^{-10} e^{60/T}$	*a*
DR20a	$HD + O \rightarrow OH + D$	$4.40 \times 10^{-12} e^{-4390/T}$	*b*
DR20b	$\rightarrow OD + H$	$1.68 \times 10^{-12} e^{-4400/T}$	*b*
DR21a	$OH + HD \rightarrow HDO + H$	$(3/20) 2.8 \times 10^{-12} e^{-1800/T}$	*a*
DR21b	$\rightarrow H_2O + D$	$(3/20) 2.8 \times 10^{-12} e^{-1800/T}$	*a*
DR21c	$OD + H_2 \rightarrow HDO + H$	$2.8 \times 10^{-12} e^{-1800/T}$	*a*
DR22	$H + D + M \rightarrow HD + M$	$1.6 \times 10^{-32} \left(\frac{298}{T}\right)^{2.27}$	*a*

Continued on next page

Table A.2 – continued from previous page

Number	Reaction	Rate	Ref
DR23a	$H + OD + CO_2 \rightarrow HDO + CO_2$	$1.292 \times 10^{-30} \left(\frac{300}{T}\right)^2$	*
DR23b	$D + OH + CO_2 \rightarrow HDO + CO_2$	$1.292 \times 10^{-30} \left(\frac{300}{T}\right)^2$	*
DR24a	$H + DO_2 \rightarrow OH + OD$	7.2×10^{-11}	a
DR24b	$\rightarrow HD + O_2$	3.45×10^{-12}	a
DR24c	$\rightarrow HDO + O(^1D)$	1.6×10^{-12}	a
DR24d	$\rightarrow HO_2 + D$	$1 \times 10^{-10}/(0.54e^{890/T})$	a
DR24e	$D + HO_2 \rightarrow OH + OD$	5.112×10^{-11}	a
DR24f	$\rightarrow HD + O_2$	2.4495×10^{-12}	a
DR24g	$\rightarrow HDO + O(^1D)$	1.136×10^{-12}	a
DR24h	$\rightarrow DO_2 + H$	1.0×10^{-10}	a
DR25a	$H + HDO_2 \rightarrow HDO + OH$	$5.8 \times 10^{-10}e^{-2110/T}$	c
DR25b	$\rightarrow H_2O + OD$	$5.8 \times 10^{-10}e^{-2110/T}$	c
DR25c	$D + H_2O_2 \rightarrow HDO + OH$	$5.8 \times 10^{-10}e^{-2110/T}$	c
DR25d	$\rightarrow H_2O + OD$	$5.8 \times 10^{-10}e^{-2110/T}$	c
DR25e	$D + HDO_2 \rightarrow OD + HDO$	$5.8 \times 10^{-10}e^{-2110/T}$	c
DR26	$D + O_2 \rightarrow DO_2$	$k_0 = 8.8 \times 10^{-32} \left(\frac{T}{300}\right)^{-1.3}$	a
		$k_\infty = 7.5 \times 10^{-11} \left(\frac{T}{300}\right)^{0.2}$	a
DR27	$D + O_3 \rightarrow OD + O_2$	$9.94 \times 10^{-11}e^{-470/T}$	a
DR28	$O + OD \rightarrow O_2 + D$	$1.8 \times 10^{-11}e^{180/T}$	a
DR29	$O + DO_2 \rightarrow OD + O_2$	$3.0 \times 10^{-11}e^{200/T}$	a
DR30a	$O + HDO_2 \rightarrow OD + HO_2$	$0.7 \times 10^{-12}e^{-2000/T}$	a
DR30b	$\rightarrow OH + DO_2$	$0.7 \times 10^{-12}e^{-2000/T}$	a
DR31a	$OD + OH \rightarrow HDO + O$	$4.2 \times 10^{-12}e^{-240/T}$	a
DR31b	$\rightarrow HDO_2$	$k_0 = 8.97 \times 10^{-31} \left(\frac{T}{300}\right)^{-1.0}$	a

Continued on next page

Table A.2 – continued from previous page

Number	**Reaction**	**Rate**	**Ref**
		$k_\infty = 2.6 \times 10^{-11}$	^{a}
DR32	$OD + O_3 \rightarrow DO_2 + O_2$	$1.7 \times 10^{-12} e^{-940/T}$	^{a}
DR33a	$OH + DO_2 \rightarrow HDO + O_2$	$4.8 \times 10^{-11} e^{250/T}$	^{a}
DR33b	$OD + HO_2 \rightarrow HDO + O_2$	$4.8 \times 10^{-11} e^{250/T}$	^{a}
DR34a	$OD + H_2O_2 \rightarrow HDO + HO_2$	$2.9 \times 10^{-12} e^{-160/T}$	^{a}
DR34b	$OH + HDO_2 \rightarrow HDO + HO_2$	$1.45 \times 10^{-12} e^{-160/T}$	^{a}
DR34c	$\rightarrow H_2O + DO_2$	$1.45 \times 10^{-12} e^{-160/T}$	^{a}
DR35	$DO_2 + O_3 \rightarrow OD + O_2 + O_2$	$1.0 \times 10^{-14} e^{-490/T}$	^{a}
DR36	$DO_2 + HO_2 \rightarrow HDO_2 + O_2$	$3.0 \times 10^{-13} e^{460/T}$	^{a}
DR37	$HO_2 + DO_2 + M \rightarrow HDO_2 + O_2 + M$	$4.2 \times 10^{-33} e^{920/T}$	*
DR38	$CO + OD \rightarrow CO_2 + D$	$k_0 = 1.5 \times 10^{-13} \left(\frac{T}{300}\right)^{0.6}$	^{a}
		$k_\infty = 2.1 \times 10^{-9} \left(\frac{T}{300}\right)^{6.1}$	^{a}
DR39	$CO + OD \rightarrow CO_2D$	$k_0 = 5.9 \times 10^{-33} \left(\frac{T}{300}\right)^{-1.4}$	*
		$k_\infty = 1.1 \times 10^{-12} \left(\frac{T}{300}\right)^{1.3}$	*
DR40	$CO_2D + O_2 \rightarrow DO_2 + CO_2$	2.09×10^{-12}	*
DR41	$CO_2^+ + HD \rightarrow CO_2^+ + H + D$	$(2/5)\, 8.7 \times 10^{-10}$	^{a}
DR42a	$H + HD \rightarrow H_2 + D$	$6.31 \times 10^{-11} e^{-4038/T}$	^{d}
DR42b	$D + H_2 \rightarrow HD + H$	$6.31 \times 10^{-11} e^{-3821/T}$	^{b}
DR43a	$OD + H \rightarrow OH + D$	$3.3 \times 10^{-9} (T^{-0.63})/(0.72 e^{717/T})$	^{a}
DR43b	$OH + D \rightarrow OD + H$	$3.3 \times 10^{-9} T^{-0.63}$	^{a}

[a] Yung et al. (1988). [b] NIST database (Manion et al. 2015). [c] (Cazaux et al. 2010).

[d] (Yung et al. 1989). *No source found. Assumed same rate as H-bearing reaction.

Species	Surface density (cm^{-3})	Surface flux ($cm^{-2}s^{-1}$)	Flux to space ($cm^{-2}s^{-1}$)	Outgoing velocity^a (cm/s)
CO_2	2.1×10^{17}	-	0	-
Ar	$2.0 \times 10^{-2}(2.1 \times 10^{17})$	-	0	-
N_2	$1.9 \times 10^{-2}(2.1 \times 10^{17})$	-	0	-
H_2O	Set by vapor pressure	-	0	-
HDO	Set by vapor pressure	-	0	-
O	-	0	1.2×10^8	-
H	-	0	-	402
D	-	0	-	0.5
H_2	-	0	-	0.5
HD	-	0	-	6×10^{-4}

[a] Outgoing velocity is fixed to the effusion velocity (Hunten 1973), which depends on the exobase temperature. Values quoted here are for the nominal exobase temperature used in the model, $T_{exo} = 205$K, but each model run uses an effusion velocity appropriate to its exobase temperature.

Table A.3: Boundary conditions

Profile	T_{surf} (K)	T_{tropo} (K)	T_{exo} (K)
Mean	216	130	205
Cold surface	160	130	205
Warm surface	270	130	205
Cold tropopause	216	100	205
Warm tropopause	216	160	205
Cold exobase	216	130	150
Warm exobase	216	130	250

Table A.4: Parameters for temperature profiles

	Thermal		Non-thermal		All escape	
Parameter varied	f_{min}	f_{max}	f_{min}	f_{max}	f_{min}	f_{max}
Surface temperature	0.0014	0.0020	0.34	0.50	0.04	0.06
Tropopause temperature	0.0009	0.0035	0.26	0.86	0.03	0.10
Exobase temperature	3.3×10^{-5}	0.0172	0.48	0.81	0.06	0.1
Water vapor	0.0015	0.0020	0.39	0.50	0.05	0.06

Table A.5: Fractionation factor results as a function of atmospheric parameter. Reported values of f are the minimum and maximum calculated within the range of the varied parameter.

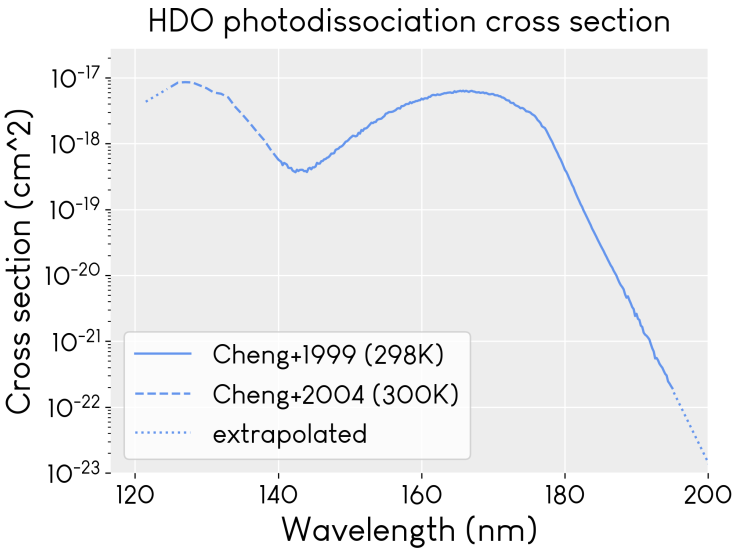

Figure A.1: HDO cross sections used in this work, collected from B.-M. Cheng et al. (1999) and B. M. Cheng et al. (2004), the studies with the most complete data available, despite the temperature of measurement (298-300 K) being a bit high for the Martian atmosphere. We extrapolate the data at the edges of the data set in order to have cross sections available for all necessary wavelengths in the model.

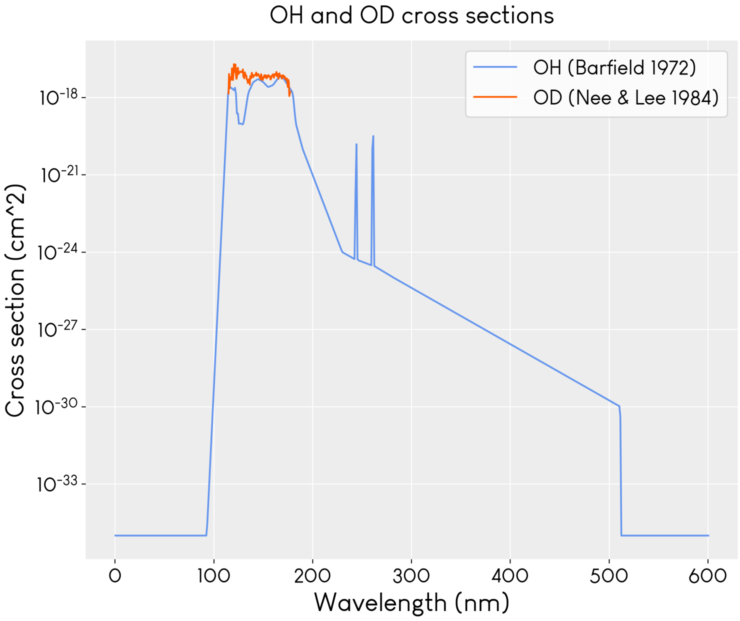

Figure A.2: OD and OH cross sections used in this work. The OH cross sections are from Barfield et al. (1972), while the few OD cross sections are from Nee et al. (1984). We use cross section data for OD in the wavelengths available, and the OH cross section everywhere else.

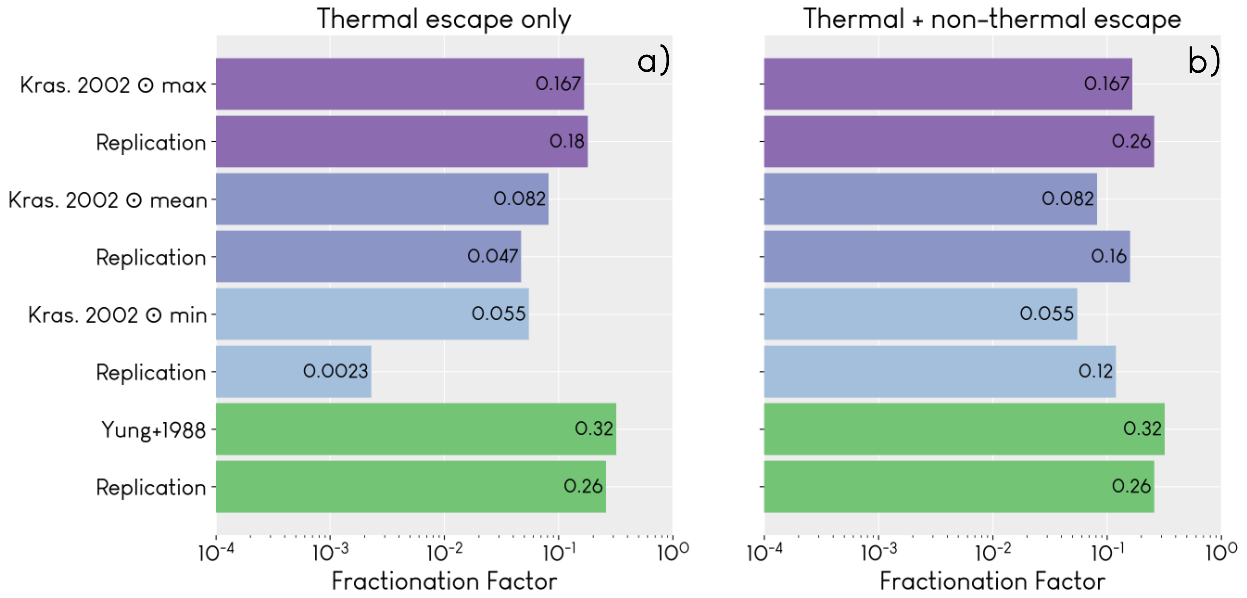

Figure A.3: Reproductions of past studies that obtained a value of the fractionation factor. (left) For thermal escape only. The best agreement is with Yung et al. (1988), which also only considered thermal escape. (right) For both thermal and non-thermal escape. The non-thermal escape contribution is the same as in V. A. Krasnopolsky (2002), and is added on to this study's thermal-only reproduction. Inclusion of non-thermal escape improves the agreement with V. A. Krasnopolsky (2002) at solar minimum, when the exobase is cold (below 270 K) and non-thermal escape processes dominate for D, HD, and H_2.

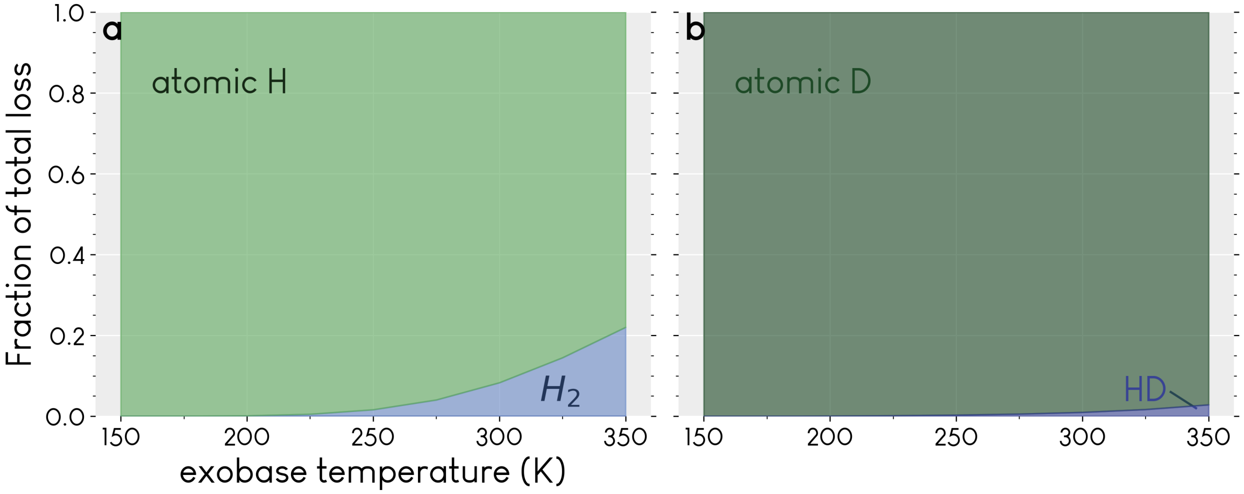

Figure A.4: Contributions of the atomic and molecular forms to the overall thermal escape of (a) H and (b) D. High temperatures are required to remove the molecular forms, whereas at low temperatures, loss via the atomic forms is near 100%. HD can contribute to H loss, but the fraction is so small ($\sim 10^{-10}$) as to be completely negligible.

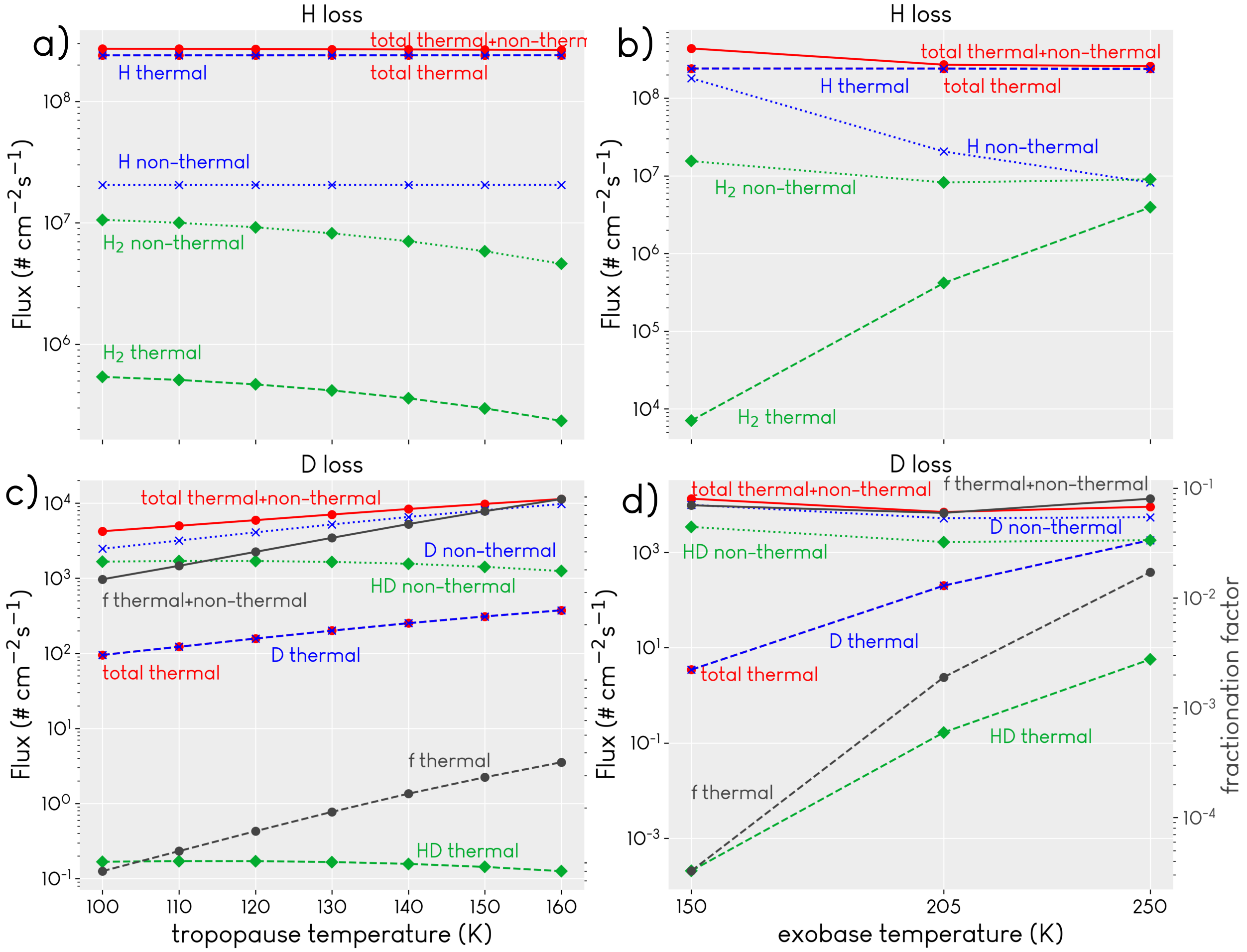

Figure A.5: Modeled thermal and estimated non-thermal contributions to escape fluxes of H and D (panels a and b) for simulations where either the tropopause (panels a and c) or exobase (panels b and d) temperatures were varied. Each point represents a single simulation. The simulation's calculated fractionation factor f is plotted on the secondary (gray) axis of panels c and d. In panels a and c, each simulation uses standard atmosphere exobase temperature (205 K). In panels b and d, each simulation uses the standard atmosphere tropopause temperature (130 K). Because the exobase temperature varies in panels b and d, and because our estimates for non-thermal escape were based on other simulations by V. A. Krasnopolsky (2002) (which did not extend down below 200 K), it is likely that our estimates for non-thermal escape at low exobase temperatures are artificially high.

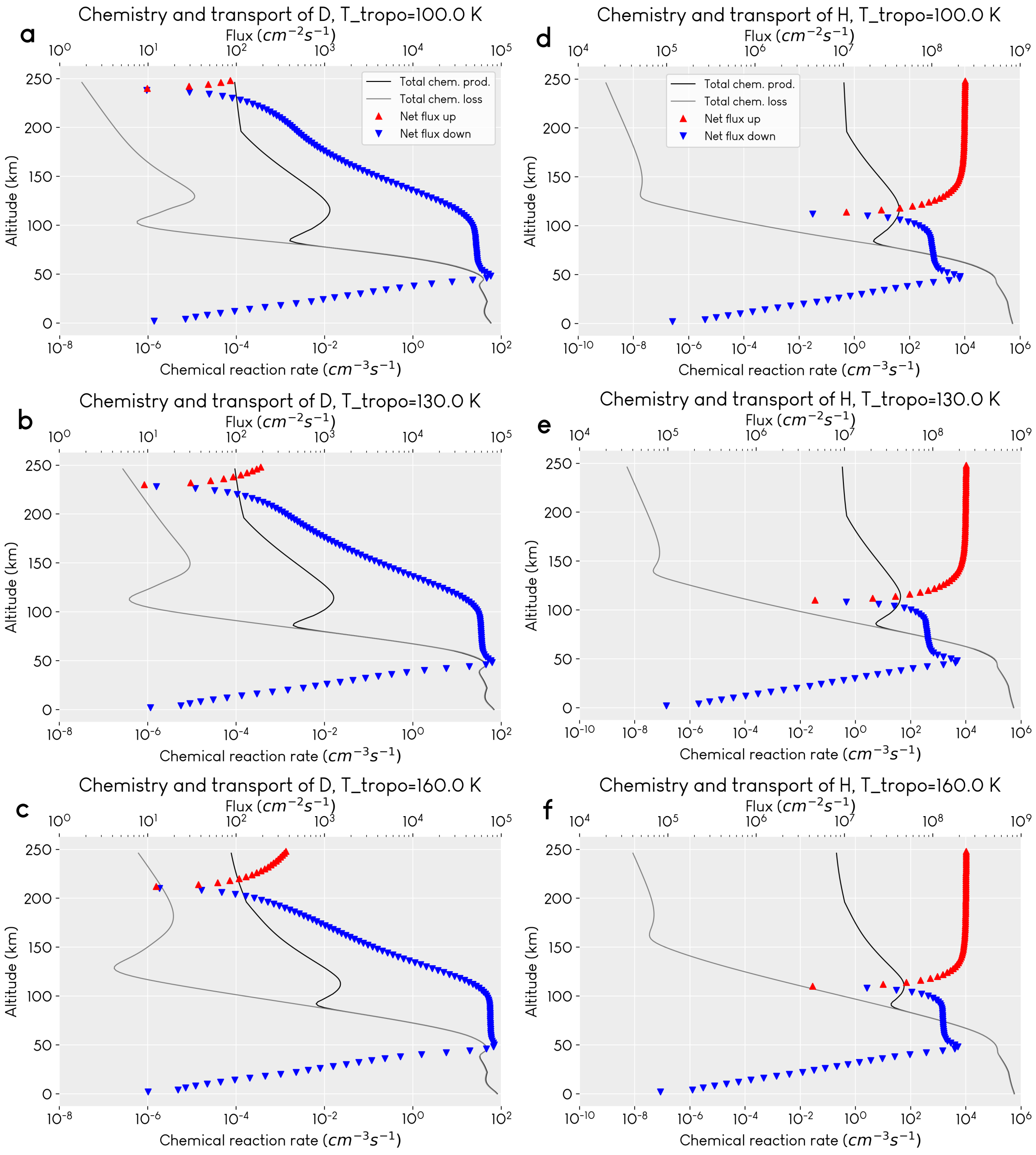

Figure A.6: Chemical production and loss (bottom axis) and net flux (top axis) of atomic D (panels a, b, and c) and H (panels d, e, and f) as a function of the tropopause temperature T_{tropo}. As T_{tropo} increases and T_{exo} remains fixed, the thermosphere also warms, enabling greater upward flux (red triangles) at lower altitudes. D, which is not diffusion limited, responds strongly with increased escape flux and very weakly with increased loss via photochemistry. Because H takes up the lion's share of the $\phi_D + \phi_H = 2\phi_O$ required balance, its response is a relatively weak decrease (not visible in plot), to "make room" for the increased ϕ_D.

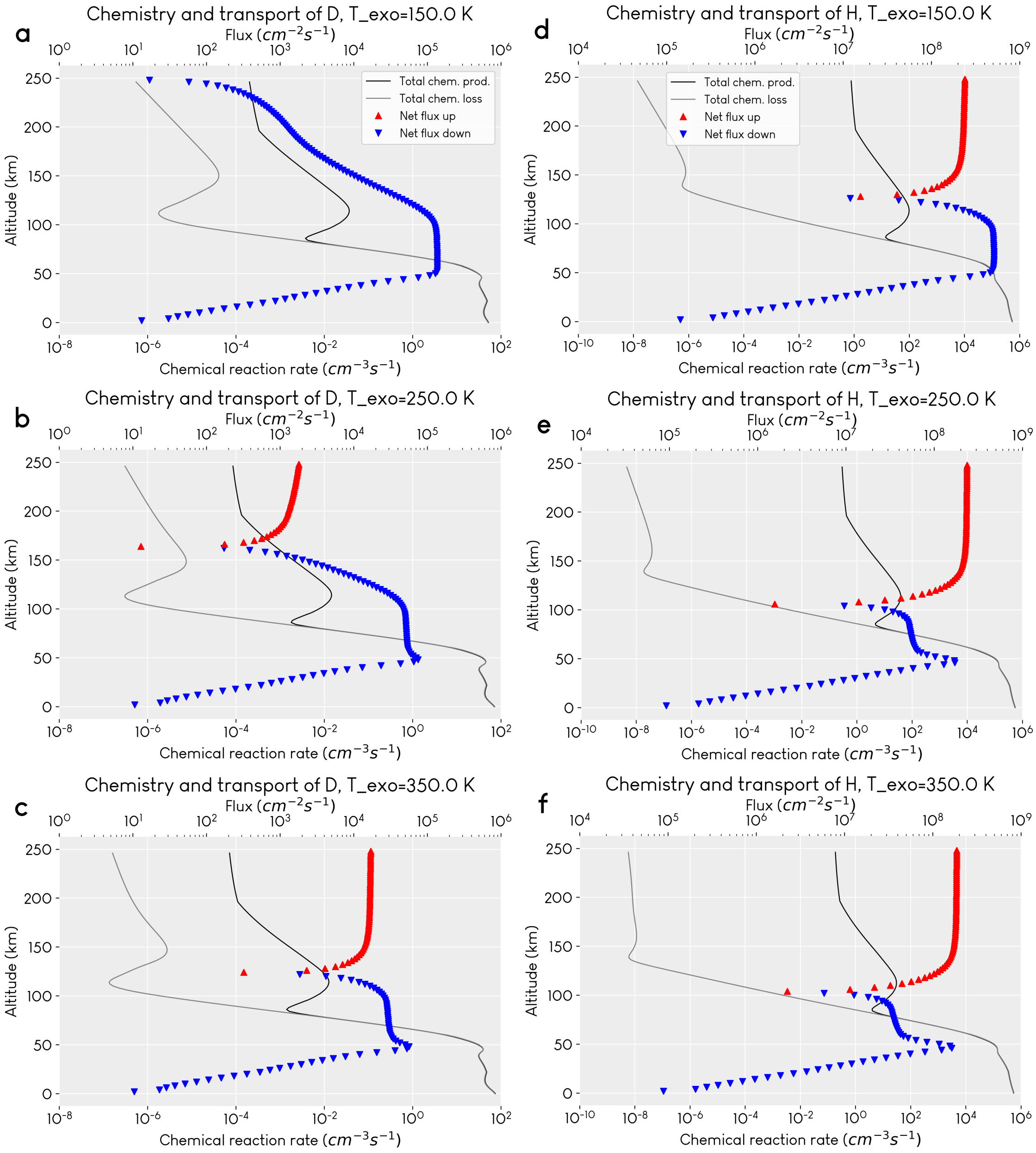

Figure A.7: The same as Figure A.6, but for T_{exo}. Here, the same mechanisms are more prominently shown, and the decrease in ϕ_{H} to "make room" for the increased ϕ_{D} according to the stoichiometric balance is just visible.

Appendix B

Supporting Information for Chapter 3

This text will be originally published as the Supporting Information companion document to Chapter 3, “Fully coupled photochemistry of the deuterated ionosphere of Mars and its effects on escape of H and D”.

Contents of this file

- Text S1: Using the reaction network spreadsheet and comments on Table B.2
- Text S2: Reasonableness of the assumption that all excess energy in a non-thermal reaction ends up in produced atomic H or D
- Figure B.1: Vertical density profiles of all modeled species
- Figure B.2: Density profiles of neutral deuterated species and their H-bearing analogues as a function of solar cycle
- Figure B.3: Comparison of densities with Fox et al. (2021)
- Figure B.4: Water loss as a function of fractionation factor
- Table B.1: Complete input for the reaction network (separate Excel file—not included in this thesis due to format and size. See E. M. Cangi et al. (2022) for the file.)
- Table B.2: Human readable table of the non-deuterated reaction network
- Table B.3: Citations for Table B.2

Introduction

These supplementary figures and table add additional details about the model inputs and results. We hope that other photochemical modelers looking for rate coefficient sources, or anyone interested in the details of the chemistry, will find the complete table of reactions and rate coefficients useful.

Text S1: Using the reaction network spreadsheet and comments on Table B.2

The non-deuterated reaction network is printed in Table B.2, complementary to Table 3.1. The reaction network can be also be viewed in Table B.1 (Excel spreadsheet). All reactions used in the model are shown there, both deuterated and non-deuterated. Table B.1 can be read into the model; for details, see the Zenodo repository (E. M. Cangi et al. 2022).

The spreadsheet has four sheets: **Neutral reactions**, **Ion reactions**, **Photodissociation**, and **Photoionization**. The column name meanings common to all sheets are as follows:

- R1, R2, R3: Reactant species names. “pl” indicates $^+$ for cations. E here is electron.
- P1, P2, P3: Product species names
- M2, M1, pow: Heavy isotopologue mass, light isotopologue mass, and power, used for estimating unmeasured reaction rate coefficients of deuterated reactions by assuming proportionality to the mass ratio of the deuterated isotopologue and its hydrogen analogue (see main text). Please note that in the spreadsheet, “pow” is usually equal to -0.5 because the calculation as performed in the model is $\left(\frac{M_2}{M_1}\right)^{-0.5}$, but we print it in the main paper text as the more easily readable $\sqrt{\frac{M_1}{M_2}}$.
- BR: Branching ratio, used for reactions with identical reactants but differing products to identify percent of reactions which lead to each unique product set.
- kA, kB, kC: coefficients used for the standard Arrhenius equation (equation B.1), i.e. k_{inf}, the rate in the high-pressure limit.

- k0A, k0B, k0C: coefficients for the low-pressure limit used with certain equations which use either the Troe form or the termolecular expression (J. Burkholder et al. 2019).
- kradA, kradB, kradC: coefficients used for the Troe form
- F: Troe parameter
- Trange: Range of temperatures for which reaction is valid. Not always guaranteed to match perfectly with Mars temperatures.
- Reference: Citation for rate in short form (AuthorYear, method description, or database acronym)
- Notes: Additional caveats or usage notes

The neutral spreadsheet contains the following information in the type column:

- 1: Pressure-independent unimolecular reactions, such as spontaneous de-excitation.
- 2: Pressure-independent bimolecular neutral-neutral reactions.
- 4: Pressure-dependent association reactions, as described by Vuitton et al. (2019)
- 5 and 6: OH + CO or OD + CO bimolecular, pressure-dependent association reactions, as described by Vuitton et al. (2019)

For the Troe form and termolecular equations, the reader is directed to Appendix B of Vuitton et al. (2019).

The ion reaction sheet also contains:

- Type:
    - ∗ -2: Bimolecular ion-neutral reactions
    - ∗ -4: Dissociative recombination reactions

- excessE (eV): excess energy computed by taking the difference $\Delta H_f^{\text{products}} - \Delta H_f^{\text{reactants}} - E$, where E is the escape energy of either atomic H or D. If positive, this number indicates that the reaction can produce a hot atom.
- NTEscape: Whether the reaction contributes to non-thermal escape of H, D, H_2 or HD by virtue of being exothermic.
- hotH, hotD, hotH2, hotHD: Flags to indicate what types of hot atoms/molecules are produced by the reaction, for use internally by the model.

Bimolecular reaction rate coefficients for neutrals and ions are computed using the entries in the columns described above with the equation:

$$k = BR \left(\frac{M_2}{M_1} \right)^{pow} AT^B e^{C/T} \tag{B.1}$$

For non-deuterated reactions, M2=M1=1 and pow=0. For reactions with only one unique product set, BR=1.

Photodissociation and photoionization reactions do not have specific rate coefficients because they are computed for a given altitude as a function of the insolation by wavelength and overhead column density. Some, however, use the branching ratio term.

We note the references for the reaction rate coefficients in the table, with the keys described in Table B.3. In some cases, reaction rate coefficient information was collected directly from databases such as the UMIST database (D. McElroy et al. 2013), or the KIDA database (Wakelam et al. 2019). These databases may reference papers which we also reference directly here. Some reactions have many sources available for rate coefficient measurements. We have generally tried to use the more recent sources when available, and mostly use sources similar to those used by other recent works in Mars photochemical literature (e.g. Fox 2015; Fox et al. 2021).

For O_2^+ dissociative recombination, a key process in the ionosphere, we have selected the rate coefficient identified by Španěl et al. (1993), which is valid for a broad range of temperatures

(300K $\leq T_e \leq$ 2000K). In contrast, Fox (2009) previously used a combination of other rates for different temperature regimes. At present, our model does not have the functionality to impose different rate coefficients at different temperatures, so we use the more broadly applicable rate coefficient. As pointed out by Fox (2009), the resulting rate of O_2^+ dissociative recombination is not terribly sensitive to minor variations in the selected rate coefficient, so we do not anticipate any significant effect to our results as a result of this rate coefficient choice. Our O_2^+ profile also agrees reasonably well with those published by Fox (2009) and Fox et al. (2015), with differences attributable to different choices of boundary conditions, included reactions, and model extent.

Some reactions listed in Table B.2 also have special forms, as described in the main text. As in the main text, the types are fully described by Vuitton et al. (2019). We list them here:

- Type 4 (pressure dependent association): Reactions 14, 15, 58, 89b
- Type 5 (pressure dependent bi-molecular): Reactions 16b, 22
- Type 6 (pressure dependent bi-molecular): Reaction 16a

Text S2: Reasonableness of the assumption that all excess energy in a non-thermal reaction ends up in produced atomic H or D

We can show this to be reasonable by calculating a ratio of the velocity of the light product (atomic H or D) in the case where (1) it gains all the excess energy to a case where (2) both products acquire excess energy. By assuming conservation of energy and momentum, the ratio of the light product velocity in case (1) to case (2) can be shown to be

$$\frac{v_1}{v_2} = \sqrt{\frac{R}{R+1}}, \tag{B.2}$$

where $\mathrm{R} = \mathrm{m}_{\mathrm{product2}}/\mathrm{m}_{\mathrm{H,D}}$. If the product set consists of H and the heaviest species in the model, O_3, then $v_1/v_2 = 0.99$, that is, the velocity of atomic H if it gains all excess energy is 99% of what we would otherwise calculate if we allowed O_3 to also gain excess energy. On the other end of the spectrum, the product set with the smallest value of R would be H and H ($R = 1$). In that

Table B.1: Complete reaction rate coefficient input spreadsheet (attached; also see E. M. Cangi et al. (2022, 2023))

case, energy is shared equally between the two produced H atoms, but $v_1/v_2 = 0.70$, which is close to what it would be if energy were not split at all.

Table B.2: Non-deuterated reactions used in the model. Reactions 1-13b: column rate ν in $\text{cm}^{-2}\text{s}^{-1}$. Reactions 14-298b: rate coefficients in units of cm^3 molecule^{-1} s^{-1} for bimolecular reactions and cm^6 molecule^{-1} s^{-1} for termolecular reactions. BR = branching ratio; MS = mass scaling, F = Troe parameter (only relevant for certain neutral reactions). For Reactions 1-13b, the Ref column refers to the reference for the cross section.

		Reaction	BR	MS	Rate coefficient	F	Ref
		Photodissociation and photoionization					
1a	CO	$\rightarrow CO^+$			$\nu_{\text{col}} = 2.6 \times 10^{-11}$		V19
1b		$\rightarrow C + O$			$\nu_{\text{col}} = 2.4 \times 10^{-12}$		V19
1c		$\rightarrow O + C^+$			$\nu_{\text{col}} = 2.3 \times 10^{-12}$		V19
1d		$\rightarrow C + O^+$			$\nu_{\text{col}} = 1.8 \times 10^{-12}$		V19
2a	CO_2	$\rightarrow CO + O(^1D)$			$\nu_{\text{col}} = 1.0 \times 10^{-10}$		SwRI
2b		$\rightarrow CO_2^+$			$\nu_{\text{col}} = 5.6 \times 10^{-11}$		V19
2c		$\rightarrow CO + O$			$\nu_{\text{col}} = 2.1 \times 10^{-11}$		SwRI
2d		$\rightarrow O^+ + CO$			$\nu_{\text{col}} = 4.5 \times 10^{-12}$		V19
2e		$\rightarrow C + O_2$			$\nu_{\text{col}} = 3.6 \times 10^{-12}$		V19
2f		$\rightarrow CO^+ + O$			$\nu_{\text{col}} = 3.0 \times 10^{-12}$		V19
2g		$\rightarrow C^+ + O_2$			$\nu_{\text{col}} = 2.3 \times 10^{-12}$		V19
2h		$\rightarrow C + O + O$			$\nu_{\text{col}} = 2.2 \times 10^{-14}$		V19
3	H	$\rightarrow H^+$			$\nu_{\text{col}} = 7.5 \times 10^{-12}$		V19

Continued on next page

	Reaction		BR	MS	Rate coefficient	F	Ref
4a	H_2	$\rightarrow H_2^+$			$\nu_{col} = 6.2 \times 10^{-12}$		V19
4b		$\rightarrow H + H$			$\nu_{col} = 3.8 \times 10^{-12}$		SwRI
4c		$\rightarrow H^+ + H$			$\nu_{col} = 6.9 \times 10^{-13}$		V19
5a	H_2O	$\rightarrow H + OH$			$\nu_{col} = 9.0 \times 10^{-10}$		SwRI
5b		$\rightarrow H_2 + O(^1D)$			$\nu_{col} = 5.7 \times 10^{-11}$		SwRI
5c		$\rightarrow H_2O^+$			$\nu_{col} = 3.3 \times 10^{-11}$		V19
5d		$\rightarrow OH^+ + H$			$\nu_{col} = 6.4 \times 10^{-12}$		V19
5e		$\rightarrow H^+ + OH$			$\nu_{col} = 2.9 \times 10^{-12}$		V19
5f		$\rightarrow O^+ + H_2$			$\nu_{col} = 3.8 \times 10^{-13}$		V19
5g		$\rightarrow H + H + O$			$\nu_{col} = 0$		SwRI
6a	H_2O_2	$\rightarrow OH + OH$			$\nu_{col} = 1.1 \times 10^{-8}$		SwRI
6b		$\rightarrow HO_2 + H$			$\nu_{col} = 6.3 \times 10^{-10}$		SwRI
6c		$\rightarrow H_2O + O(^1D)$			$\nu_{col} = 0$		SwRI
7	HO_2	$\rightarrow OH + O$			$\nu_{col} = 6.9 \times 10^{-8}$		SwRI
8a	N_2	$\rightarrow N_2^+$			$\nu_{col} = 3.2 \times 10^{-11}$		V19
8b		$\rightarrow N^+ + N$			$\nu_{col} = 4.5 \times 10^{-12}$		V19
9a	NO	$\rightarrow N + O$			$\nu_{col} = 4.6 \times 10^{-9}$		V19
9b		$\rightarrow NO^+$			$\nu_{col} = 1.5 \times 10^{-10}$		V19
10	O	$\rightarrow O^+$			$\nu_{col} = 1.9 \times 10^{-11}$		V19
11a	O_2	$\rightarrow O + O(^1D)$			$\nu_{col} = 2.0 \times 10^{-10}$		SwRI
11b		$\rightarrow O + O$			$\nu_{col} = 1.2 \times 10^{-11}$		SwRI
11c		$\rightarrow O_2^+$			$\nu_{col} = 1.2 \times 10^{-11}$		V19
12a	O_3	$\rightarrow O_2 + O(^1D)$			$\nu_{col} = 9.3 \times 10^{-7}$		SwRI
12b		$\rightarrow O_2 + O$			$\nu_{col} = 1.6 \times 10^{-7}$		SwRI
12c		$\rightarrow O + O + O$			$\nu_{col} = 0$		SwRI
13a	OH	$\rightarrow O + H$			$\nu_{col} = 6.6 \times 10^{-10}$		SwRI
13b		$\rightarrow O(^1D) + H$			$\nu_{col} = 1.6 \times 10^{-11}$		SwRI

Neutral-neutral reactions

Continued on next page

	Reaction		BR	MS	Rate coefficient	F	Ref
14	$CO + H$	$\rightarrow HCO$			See text $k_\infty = 1\,(T_n)^{0.2}$ $k_0 = 2.00 \times 10^{-35}\,(T_n)^{0.2}$		B05
15	$CO + O$	$\rightarrow CO_2$			See text $k_\infty = 1e^{-1509/T_n}$ $k_0 = 1.70 \times 10^{-33}e^{-1509/T_n}$	0.4	Ts86
16a	$CO + OH$	$\rightarrow CO_2 + H$			See text $k_\infty = 1.63 \times 10^{-6}\,(T_n)^{6.1}$ $k_0 = 4.90 \times 10^{-15}\,(T_n)^{0.6}$		S11
16b		$\rightarrow HOCO$			See text $k_\infty = 6.62 \times 10^{-16}\,(T_n)^{1.3}$ $k_0 = 1.73 \times 10^{-29}\,(T_n)^{-1.4}$		S15
17	$CO_2 + H$	$\rightarrow CO + OH$			$3.38 \times 10^{-10}e^{-13163/T_n}$		UMIST
18	$CO_2 + N$	$\rightarrow NO + CO$			$3.20 \times 10^{-13}e^{-1710/T_n}$		UMIST
19	$CO_2 + O$	$\rightarrow O_2 + CO$			$2.46 \times 10^{-11}e^{-26567/T_n}$		UMIST
20	$H + H + M$	$\rightarrow H_2 + M$			$6.62 \times 10^{-27}\,(T_n)^{-2.27}$		D12
21a	$H + H_2O_2$	$\rightarrow H_2O + OH$			$1.70 \times 10^{-11}e^{-1800/T_n}$		NIST
21b		$\rightarrow HO_2 + H_2$			$2.81 \times 10^{-12}e^{-1890/T_n}$		NIST
22	$H + O_2$	$\rightarrow HO_2$			See text $k_\infty = 2.40 \times 10^{-11}\,(T_n)^{0.2}$ $k_0 = 1.46 \times 10^{-28}\,(T_n)^{-1.3}$		S11
23	$H_2 + O$	$\rightarrow OH + H$			$6.34 \times 10^{-12}e^{-4000/T_n}$		KIDA
24	$H_2O + H$	$\rightarrow OH + H_2$			$1.69 \times 10^{-14}\,(T_n)^{1.2}\,e^{-9610/T_n}$		UMIST
25	$H_2O + O$	$\rightarrow OH + OH$			$8.20 \times 10^{-14}\,(T_n)^{0.95}\,e^{-8571/T_n}$		UMIST
26a	$H_2O_2 + H$	$\rightarrow H_2O + OH$			$1.70 \times 10^{-11}e^{-1800/T_n}$		B05
26b		$\rightarrow HO_2 + H_2$			$2.80 \times 10^{-12}e^{-1890/T_n}$		B92
27	$H_2O_2 + O$	$\rightarrow HO_2 + OH$			$1.40 \times 10^{-12}e^{-2000/T_n}$		S15
28	$HCO + H$	$\rightarrow CO + H_2$			1.50×10^{-10}		B05

Continued on next page

	Reaction		BR	MS	Rate coefficient	F	Ref
29	$HCO + HCO$	$\rightarrow CO + CO + H_2$			7.35×10^{-12}		B05
30a	$HCO + O$	$\rightarrow CO + OH$			5.00×10^{-11}		B05
30b		$\rightarrow CO_2 + H$			5.00×10^{-11}		B05
31a	$HCO + O_2$	$\rightarrow CO_2 + OH$			7.60×10^{-13}		UMIST
31b		$\rightarrow HO_2 + CO$			5.20×10^{-12}		S15
32	$HCO + OH$	$\rightarrow H_2O + CO$			1.80×10^{-10}		B05
33	$HO_2 + CO$	$\rightarrow CO_2 + OH$			$5.60 \times 10^{-10} e^{-12160/T_n}$		UMIST
34a	$HO_2 + H$	$\rightarrow H_2O + O(^1D)$			1.60×10^{-12}		S15
34b		$\rightarrow O_2 + H_2$			3.45×10^{-12}		S15
34c		$\rightarrow OH + OH$			7.20×10^{-11}		S15
35	$HO_2 + H_2$	$\rightarrow H_2O_2 + H$			$5.00 \times 10^{-11} e^{-13110/T_n}$		Ts86
36	$HO_2 + H_2O$	$\rightarrow H_2O_2 + OH$			$4.65 \times 10^{-11} e^{-16500/T_n}$		UMIST
37	$HO_2 + HO_2 + M$	$\rightarrow H_2O_2 + O_2 + M$			$4.20 \times 10^{-33} e^{920/T_n}$		Bu20
38	$HO_2 + HO_2$	$\rightarrow H_2O_2 + O_2$			$3.00 \times 10^{-13} e^{460/T_n}$		S15
39	$HO_2 + N$	$\rightarrow NO + OH$			2.20×10^{-11}		Br83
40	$HO_2 + O$	$\rightarrow O_2 + OH$			$3.00 \times 10^{-11} e^{200/T_n}$		S15
41	$HO_2 + OH$	$\rightarrow H_2O + O_2$			$4.80 \times 10^{-11} e^{250/T_n}$		S15
42	$HOCO + O_2$	$\rightarrow CO_2 + HO_2$			2.00×10^{-12}		S15
43	$HOCO + OH$	$\rightarrow CO_2 + H_2O$			1.03×10^{-11}		Yu05
44	$NO + C$	$\rightarrow CO + N$			$2.24 \times 10^{-10} \left(T_n\right)^{-0.16}$		UMIST
45	$NO + N$	$\rightarrow N_2 + O$			$2.10 \times 10^{-11} e^{100/T_n}$		S15
46	$NO + O$	$\rightarrow O_2 + N$			$1.18 \times 10^{-11} e^{-20413/T_n}$		UMIST
47	$N(^2D) + CO$	$\rightarrow CO + N$			1.90×10^{-12}		Her99
48	$N(^2D) + CO_2$	$\rightarrow NO + CO$			3.60×10^{-13}		Her99
49	$N(^2D) + H_2O$	$\rightarrow NO + H_2$			1.30×10^{-11}		Her99
50	$N(^2D) + N_2$	$\rightarrow N_2 + N$			1.70×10^{-14}		Her99
51	$N(^2D) + NO$	$\rightarrow N_2 + O$			6.00×10^{-11}		Her99
52	$N(^2D) + O$	$\rightarrow O + N$			$3.30 \times 10^{-12} e^{-260/T_n}$		Her99

Continued on next page

	Reaction		BR	MS	Rate coefficient	F	Ref
53	$N(^2D) + O_2$	$\rightarrow NO + O$			$9.70 \times 10^{-12} e^{-185/T_n}$		Her99
54	$N(^2D)$	$\rightarrow N$			2.30×10^{-5}		O78
55	$O + C$	$\rightarrow CO$			$1.75 \times 10^{-19} (T_n)^{0.705} e^{-136/T_n}$		Gu15
56	$O + H$	$\rightarrow OH$			$8.65 \times 10^{-18} (T_n)^{-0.38}$		UMIST
57	$O + H_2O_2$	$\rightarrow OH + HO_2$			$1.40 \times 10^{-12} e^{-2000/T_n}$		S11, NIST
58	$O + N$	$\rightarrow NO$			See text $k_\infty = 1$ $k_0 = 5.46 \times 10^{-33} e^{155/T_n}$	0.4	Cam73
59	$O + O + M$	$\rightarrow O_2 + M$			$6.07 \times 10^{-25} (T_n)^{-3.25}$		D12
60a	$O(^1D) + CO$	$\rightarrow CO + O$			$4.70 \times 10^{-11} e^{63/T_n}$		Da78
60b		$\rightarrow CO_2$			8.00×10^{-11}		Tu75
61	$O(^1D) + CO_2$	$\rightarrow CO_2 + O$			$7.50 \times 10^{-11} e^{115/T_n}$		S15, Bu20
62	$O(^1D) + H_2$	$\rightarrow OH + H$			1.20×10^{-10}		S15, Bu20
63	$O(^1D) + H_2O$	$\rightarrow OH + OH$			$1.63 \times 10^{-10} e^{60/T_n}$		S15, Bu20
64	$O(^1D) + H_2O_2$	$\rightarrow H_2O_2 + O$			5.20×10^{-10}		Fl76
65	$O(^1D) + N_2$	$\rightarrow N_2 + O$			$2.15 \times 10^{-11} e^{110/T_n}$		S15
66	$O(^1D) + NO$	$\rightarrow NO + O$			4.00×10^{-11}		Do92
67	$O(^1D) + O_2$	$\rightarrow O_2 + O$			$3.30 \times 10^{-11} e^{55/T_n}$		S15, Bu20
68a	$O(^1D) + O_3$	$\rightarrow O_2 + O + O$			2.40×10^{-10}		Bu20
68b		$\rightarrow O_2 + O_2$			2.40×10^{-10}		Bu20
69	$O(^1D)$	$\rightarrow O$			5.10×10^{-3}		O78
70	$O_2 + C$	$\rightarrow CO + O$			$3.03 \times 10^{-10} (T_n)^{-0.32}$		G00
71	$O_2 + CO$	$\rightarrow CO_2 + O$			$5.99 \times 10^{-12} e^{-24075/T_n}$		UMIST

Continued on next page

	Reaction		BR	MS	Rate coefficient	F	Ref
72	$O_2 + H$	$\rightarrow OH + O$			$2.61 \times 10^{-10} e^{-8156/T_n}$		UMIST
73a	$O_2 + H_2$	$\rightarrow HO_2 + H$			$2.40 \times 10^{-10} e^{-28500/T_n}$		UMIST
73b		$\rightarrow OH + OH$			$3.16 \times 10^{-10} e^{-21890/T_n}$		UMIST
74	$O_2 + N$	$\rightarrow NO + O$			$1.50 \times 10^{-11} e^{-3600/T_n}$		S15
75	$O_2 + O + CO_2$	$\rightarrow O_3 + CO_2$			$1.32 \times 10^{-27} (T_n)^{-2.4}$		Bu20
76	$O_2 + O + N_2$	$\rightarrow O_3 + N_2$			$5.00 \times 10^{-35} e^{724/T_n}$		Ch17
77	$O_3 + H$	$\rightarrow O_2 + OH$			$1.40 \times 10^{-10} e^{-470/T_n}$		S15
78	$O_3 + HO_2$	$\rightarrow O_2 + O_2 + OH$			$1.00 \times 10^{-14} e^{-490/T_n}$		S15
79	$O_3 + N$	$\rightarrow O_2 + NO$			1.00×10^{-16}		At89
80	$O_3 + O$	$\rightarrow O_2 + O_2$			$8.00 \times 10^{-12} e^{-2060/T_n}$		S15, Bu20
81	$O_3 + OH$	$\rightarrow HO_2 + O_2$			$1.70 \times 10^{-12} e^{-940/T_n}$		S15
82	$OH + C$	$\rightarrow CO + H$			$7.98 \times 10^{-10} (T_n)^{-0.34} e^{-0.108/T_n}$		Z09
83	$OH + H + CO_2$	$\rightarrow H_2O + CO_2$			$1.16 \times 10^{-25} (T_n)^{-2.0}$	0.4	NIST
84	$OH + H$	$\rightarrow H_2 + O$			$8.10 \times 10^{-21} (T_n)^{2.8} e^{-1950/T_n}$		UMIST
85	$OH + H_2$	$\rightarrow H_2O + H$			$2.80 \times 10^{-12} e^{-1800/T_n}$		S15, Bu20
86	$OH + H_2O_2$	$\rightarrow H_2O + HO_2$			$2.90 \times 10^{-12} e^{-160/T_n}$		NIST, KIDA
87	$OH + N$	$\rightarrow NO + H$			$1.80 \times 10^{-10} (T_n)^{-0.2}$		B05
88	$OH + O$	$\rightarrow O_2 + H$			$1.80 \times 10^{-11} e^{180/T_n}$		S15
89a	$OH + OH$	$\rightarrow H_2O + O$			1.80×10^{-12}		S15
89b		$\rightarrow H_2O_2$			See text $k_\infty = 2.60 \times 10^{-11}$ $k_0 = 6.60 \times 10^{-29} (T_n)^{-0.8}$	0.5	B05
					Ion-neutral reactions		
90	$ArH^+ + C$	$\rightarrow CH^+ + Ar$			1.02×10^{-9}		Est.
91	$ArH^+ + CO$	$\rightarrow HCO^+ + Ar$			1.25×10^{-9}		A93

Continued on next page

	Reaction		BR	MS	Rate coefficient	F	Ref
92	$ArH^+ + CO_2$	$\rightarrow HCO_2^+ + Ar$			1.10×10^{-9}		A93
93	$ArH^+ + e^-$	$\rightarrow Ar + H$			1.00×10^{-9}		Mi05
94	$ArH^+ + H_2$	$\rightarrow H_3^+ + Ar$			6.30×10^{-10}		A93
95	$ArH^+ + N_2$	$\rightarrow N_2H^+ + Ar$			8.00×10^{-10}		A93
96	$ArH^+ + O$	$\rightarrow OH^+ + Ar$			5.90×10^{-10}		Est.
97	$ArH^+ + O_2$	$\rightarrow HO_2^+ + Ar$			5.05×10^{-10}		A93
98	$Ar^+ + CO$	$\rightarrow CO^+ + Ar$			4.40×10^{-11}		A93
99	$Ar^+ + CO_2$	$\rightarrow CO_2^+ + Ar$			4.80×10^{-10}		A93
100	$Ar^+ + e^-$	$\rightarrow Ar$			$4.00 \times 10^{-12} \, (T_i)^{0.6}$		Est.
101a	$Ar^+ + H_2$	$\rightarrow ArH^+ + H$			8.72×10^{-10}		A93
101b		$\rightarrow H_2^+ + Ar$			1.78×10^{-11}		A93
102a	$Ar^+ + H_2O$	$\rightarrow ArH^+ + OH$			3.24×10^{-10}		A93
102b		$\rightarrow H_2O^+ + Ar$			1.30×10^{-9}		A93
103	$Ar^+ + N_2$	$\rightarrow N_2^+ + Ar$			1.10×10^{-11}		A93
104	$Ar^+ + NO$	$\rightarrow NO^+ + Ar$			3.10×10^{-10}		A93
105	$Ar^+ + O_2$	$\rightarrow O_2^+ + Ar$			4.60×10^{-11}		A93
106	$CH^+ + CO$	$\rightarrow HCO^+ + C$			$7.00 \times 10^{-12} \, (T_i)^{-0.5}$		A93
107	$CH^+ + CO_2$	$\rightarrow HCO^+ + CO$			1.60×10^{-9}		A93
108	$CH^+ + e^-$	$\rightarrow C + H$			$1.65 \times 10^{-6} \, (T_i)^{-0.42}$		Mi90
109	$CH^+ + H$	$\rightarrow C^+ + H_2$			7.50×10^{-10}		A93
110a	$CH^+ + H_2O$	$\rightarrow H_3O^+ + C$			1.45×10^{-9}		A93
110b		$\rightarrow HCO^+ + H_2$			$5.02 \times 10^{-8} \, (T_i)^{-0.5}$		UMIST
111	$CH^+ + O$	$\rightarrow CO^+ + H$			3.50×10^{-10}		V80
112	$CH^+ + O_2$	$\rightarrow HCO^+ + O$			8.73×10^{-10}		A93
113	$CH^+ + OH$	$\rightarrow CO^+ + H_2$			$1.30 \times 10^{-8} \, (T_i)^{-0.5}$		UMIST
114	$CO_2^+ + e^-$	$\rightarrow CO + O$			$3.03 \times 10^{-5} \, (T_i)^{-0.75}$		V05
115a	$CO_2^+ + H$	$\rightarrow HCO^+ + O$			4.50×10^{-10}		Bo09
115b		$\rightarrow H^+ + CO_2$			5.53×10^{-11}		A93

Continued on next page

	Reaction		BR	MS	Rate coefficient	F	Ref
116	$CO_2^+ + H_2$	$\rightarrow HCO_2^+ + H$			$2.24 \times 10^{-9}\,(T_i)^{-0.15}$		Bo09
117a	$CO_2^+ + H_2O$	$\rightarrow H_2O^+ + CO_2$			$1.80 \times 10^{-9}\,(T_i)^{-0.15}$		A93
117b		$\rightarrow HCO_2^+ + OH$			6.00×10^{-10}		A93
118	$CO_2^+ + N$	$\rightarrow CO^+ + NO$			3.40×10^{-10}		Sc98
119	$CO_2^+ + NO$	$\rightarrow NO^+ + CO_2$			1.23×10^{-10}		A93
120a	$CO_2^+ + O$	$\rightarrow O_2^+ + CO$			1.60×10^{-10}		Feh70
120b		$\rightarrow O^+ + CO_2$			9.60×10^{-11}		Feh70
121	$CO_2^+ + O_2$	$\rightarrow O_2^+ + CO_2$			5.50×10^{-11}		A93
122	$CO^+ + C$	$\rightarrow C^+ + CO$			1.10×10^{-10}		UMIST
123	$CO^+ + CO_2$	$\rightarrow CO_2^+ + CO$			1.10×10^{-9}		A93
124a	$CO^+ + e^-$	$\rightarrow O + C$			$4.82 \times 10^{-6}\,(T_i)^{-0.55}$		R98
124b		$\rightarrow O(^1D) + C$			$2.48 \times 10^{-8}\,(T_i)^{-0.55}$		R98
125	$CO^+ + H$	$\rightarrow H^+ + CO$			4.00×10^{-10}		Sc97
126a	$CO^+ + H_2$	$\rightarrow HCO^+ + H$			7.50×10^{-10}		Sc97
126b		$\rightarrow HOC^+ + H$			7.50×10^{-10}		Sc97
127a	$CO^+ + H_2O$	$\rightarrow H_2O^+ + CO$			1.56×10^{-9}		A93
127b		$\rightarrow HCO^+ + OH$			8.40×10^{-10}		A93
128	$CO^+ + HCO$	$\rightarrow HCO^+ + CO$			$1.28 \times 10^{-8}\,(T_i)^{-0.5}$		UMIST
129	$CO^+ + N$	$\rightarrow NO^+ + C$			8.20×10^{-11}		Sc98
130	$CO^+ + NO$	$\rightarrow NO^+ + CO$			4.20×10^{-10}		A93
131	$CO^+ + O$	$\rightarrow O^+ + CO$			1.40×10^{-10}		A93
132	$CO^+ + O_2$	$\rightarrow O_2^+ + CO$			1.50×10^{-10}		A93
133a	$CO^+ + OH$	$\rightarrow HCO^+ + O$			$5.37 \times 10^{-9}\,(T_i)^{-0.5}$		UMIST
133b		$\rightarrow OH^+ + CO$			$5.37 \times 10^{-9}\,(T_i)^{-0.5}$		UMIST
134a	$C^+ + CO_2$	$\rightarrow CO_2^+ + C$			1.10×10^{-10}		A93
134b		$\rightarrow CO^+ + CO$			9.90×10^{-10}		A93
135	$C^+ + e^-$	$\rightarrow C$			$6.28 \times 10^{-10}\,(T_i)^{-0.59}$		N97
136	$C^+ + H$	$\rightarrow CH^+$			1.70×10^{-17}		UMIST

Continued on next page

	Reaction		BR	MS	Rate coefficient	F	Ref
137	$C^+ + H_2$	$\rightarrow CH^+ + H$			$7.40 \times 10^{-10} e^{-4537/T_i}$		Hierl1997
138a	$C^+ + H_2O$	$\rightarrow H_2O^+ + C$			2.40×10^{-10}		A93
138b		$\rightarrow HCO^+ + H$			$1.56 \times 10^{-8}\,(T_i)^{-0.5}$		UMIST
138c		$\rightarrow HOC^+ + H$			2.16×10^{-9}		A93
139a	$C^+ + HCO$	$\rightarrow CH^+ + CO$			$8.31 \times 10^{-9}\,(T_i)^{-0.5}$		UMIST
139b		$\rightarrow HCO^+ + C$			$8.31 \times 10^{-9}\,(T_i)^{-0.5}$		UMIST
140	$C^+ + NO$	$\rightarrow NO^+ + C$			7.50×10^{-10}		A93
141	$C^+ + O$	$\rightarrow CO^+$			$7.39 \times 10^{-18}\,(T_i)^{-0.15}\,e^{-68/T_i}$		UMIST
142a	$C^+ + O_2$	$\rightarrow CO^+ + O$			3.48×10^{-10}		A93
142b		$\rightarrow O^+ + CO$			5.22×10^{-10}		A93
143	$C^+ + OH$	$\rightarrow CO^+ + H$			$1.33 \times 10^{-8}\,(T_i)^{-0.5}$		UMIST
144	$H_2O^+ + C$	$\rightarrow CH^+ + OH$			1.10×10^{-9}		UMIST
145	$H_2O^+ + CO$	$\rightarrow HCO^+ + OH$			4.25×10^{-10}		A93
146a	$H_2O^+ + e^-$	$\rightarrow H_2 + O$			$2.64 \times 10^{-6}\,(T_i)^{-0.74}$		R00
146b		$\rightarrow O + H$			$2.08 \times 10^{-5}\,(T_i)^{-0.74}$		R00
146c		$\rightarrow OH + H$			$5.86 \times 10^{-6}\,(T_i)^{-0.74}$		R00
147	$H_2O^+ + H_2$	$\rightarrow H_3O^+ + H$			7.60×10^{-10}		A93
148	$H_2O^+ + H_2O$	$\rightarrow H_3O^+ + OH$			1.85×10^{-9}		A93
149a	$H_2O^+ + HCO$	$\rightarrow H_3O^+ + CO$			$4.85 \times 10^{-9}\,(T_i)^{-0.5}$		UMIST
149b		$\rightarrow HCO^+ + H_2O$			$4.85 \times 10^{-9}\,(T_i)^{-0.5}$		UMIST
150a	$H_2O^+ + N$	$\rightarrow HNO^+ + H$			1.12×10^{-10}		Sc98
150b		$\rightarrow NO^+ + H_2$			2.80×10^{-11}		Sc98
151	$H_2O^+ + NO$	$\rightarrow NO^+ + H_2O$			4.60×10^{-10}		A93
152	$H_2O^+ + O$	$\rightarrow O_2^+ + H_2$			4.00×10^{-11}		UMIST
153	$H_2O^+ + O_2$	$\rightarrow O_2^+ + H_2O$			3.30×10^{-10}		A93
154	$H_2O^+ + OH$	$\rightarrow H_3O^+ + O$			$1.20 \times 10^{-8}\,(T_i)^{-0.5}$		UMIST
155	$H_2^+ + Ar$	$\rightarrow ArH^+ + H$			2.10×10^{-9}		A93
156	$H_2^+ + C$	$\rightarrow CH^+ + H$			2.40×10^{-9}		UMIST

Continued on next page

	Reaction		BR	MS	Rate coefficient	F	Ref
157a	$H_2^+ + CO$	$\rightarrow CO^+ + H_2$			6.44×10^{-10}		UMIST
157b		$\rightarrow HCO^+ + H$			2.90×10^{-9}		A93
158	$H_2^+ + CO_2$	$\rightarrow HCO_2^+ + H$			2.35×10^{-9}		A93
159	$H_2^+ + e^-$	$\rightarrow H + H$			$1.86 \times 10^{-7} \, (T_i)^{-0.43}$		Mi90
160	$H_2^+ + H$	$\rightarrow H^+ + H_2$			6.40×10^{-10}		A93
161	$H_2^+ + H_2$	$\rightarrow H_3^+ + H$			2.00×10^{-9}		A93
162a	$H_2^+ + H_2O$	$\rightarrow H_2O^+ + H_2$			3.87×10^{-9}		A93
162b		$\rightarrow H_3O^+ + H$			3.43×10^{-9}		A93
163a	$H_2^+ + HCO$	$\rightarrow H_3^+ + CO$			$1.73 \times 10^{-8} \, (T_i)^{-0.5}$		UMIST
163b		$\rightarrow HCO^+ + H_2$			$1.73 \times 10^{-8} \, (T_i)^{-0.5}$		UMIST
164	$H_2^+ + N$	$\rightarrow NH^+ + H$			1.90×10^{-9}		UMIST
165	$H_2^+ + N_2$	$\rightarrow N_2H^+ + H$			2.00×10^{-9}		A93
166a	$H_2^+ + NO$	$\rightarrow HNO^+ + H$			1.10×10^{-9}		UMIST
166b		$\rightarrow NO^+ + H_2$			1.10×10^{-9}		UMIST
167	$H_2^+ + O$	$\rightarrow OH^+ + H$			1.50×10^{-9}		UMIST
168a	$H_2^+ + O_2$	$\rightarrow HO_2^+ + H$			1.92×10^{-9}		A93
168b		$\rightarrow O_2^+ + H_2$			7.83×10^{-10}		A93
169a	$H_2^+ + OH$	$\rightarrow H_2O^+ + H$			$1.32 \times 10^{-8} \, (T_i)^{-0.5}$		UMIST
169b		$\rightarrow OH^+ + H_2$			$1.32 \times 10^{-8} \, (T_i)^{-0.5}$		UMIST
170	$H_3O^+ + C$	$\rightarrow HCO^+ + H_2$			1.00×10^{-11}		UMIST
171a	$H_3O^+ + e^-$	$\rightarrow H_2 + O$			$9.68 \times 10^{-8} \, (T_i)^{-0.5}$		J00
171b		$\rightarrow H_2O + H$			$1.86 \times 10^{-6} \, (T_i)^{-0.5}$		J00
171c		$\rightarrow OH + H$			$4.47 \times 10^{-6} \, (T_i)^{-0.5}$		J00
171d		$\rightarrow OH + H_2$			$1.04 \times 10^{-6} \, (T_i)^{-0.5}$		J00
172	$H_3^+ + Ar$	$\rightarrow ArH^+ + H_2$			3.65×10^{-10}		A93
173	$H_3^+ + C$	$\rightarrow CH^+ + H_2$			2.00×10^{-9}		UMIST
174a	$H_3^+ + CO$	$\rightarrow HCO^+ + H_2$			$3.06 \times 10^{-9} \, (T_i)^{-0.142} \, e^{3.41/T_i}$		A93,Kl10
174b		$\rightarrow HOC^+ + H_2$			$5.82 \times 10^{-10} \, (T_i)^{0.0661} \, e^{-5.21/T_i}$		A93

Continued on next page

	Reaction		BR	MS	Rate coefficient	F	Ref
175	$H_3^+ + CO_2$	$\rightarrow HCO_2^+ + H_2$			2.50×10^{-9}		A93
176a	$H_3^+ + e^-$	$\rightarrow H + H$			$8.46 \times 10^{-7}\,(T_i)^{-0.52}$		UMIST
176b		$\rightarrow H_2 + H$			$4.54 \times 10^{-7}\,(T_i)^{-0.52}$		UMIST
177	$H_3^+ + H_2O$	$\rightarrow H_3O^+ + H_2$			5.30×10^{-9}		A93
178	$H_3^+ + N$	$\rightarrow NH^+ + H_2$			2.60×10^{-10}		A93
179	$H_3^+ + N_2$	$\rightarrow N_2H^+ + H_2$			1.63×10^{-9}		Sc98
180	$H_3^+ + NO$	$\rightarrow HNO^+ + H_2$			1.94×10^{-9}		Pr94
181a	$H_3^+ + O$	$\rightarrow H_2O^+ + H$			$8.33 \times 10^{-10}\,(T_i)^{-0.156}\,e^{-1.4/T_i}$		M00,Kl10
181b		$\rightarrow OH^+ + H_2$			$1.94 \times 10^{-9}\,(T_i)^{-0.156}\,e^{-1.4/T_i}$		M00,Kl10
182	$H_3^+ + O_2$	$\rightarrow HO_2^+ + H_2$			6.70×10^{-10}		A93
183	$H_3^+ + OH$	$\rightarrow H_2O^+ + H_2$			$2.25 \times 10^{-8}\,(T_i)^{-0.5}$		UMIST
184	$HCO_2^+ + C$	$\rightarrow CH^+ + CO_2$			1.00×10^{-9}		UMIST
185	$HCO_2^+ + CO$	$\rightarrow HCO^+ + CO_2$			7.80×10^{-10}		UMIST
186a	$HCO_2^+ + e^-$	$\rightarrow CO + O$			$4.12 \times 10^{-6}\,(T_i)^{-0.5}$		G04,H90
186b		$\rightarrow CO + OH$			$1.64 \times 10^{-6}\,(T_i)^{-0.5}$		G04,H90
186c		$\rightarrow CO_2 + H$			$3.03 \times 10^{-7}\,(T_i)^{-0.5}$		G04,H90
187	$HCO_2^+ + H_2O$	$\rightarrow H_3O^+ + CO_2$			2.65×10^{-9}		A93
188	$HCO_2^+ + O$	$\rightarrow HCO^+ + O_2$			5.80×10^{-10}		Est.
189	$HCO^+ + C$	$\rightarrow CH^+ + CO$			1.10×10^{-9}		UMIST
190a	$HCO^+ + e^-$	$\rightarrow CO + H$	0.92		$1.06 \times 10^{-5}\,(T_i)^{-0.64}$		G05
190b		$\rightarrow OH + C$	0.07		$8.08 \times 10^{-7}\,(T_i)^{-0.64}$		G05
191	$HCO^+ + H_2O$	$\rightarrow H_3O^+ + CO$			2.60×10^{-9}		A93
192a	$HCO^+ + OH$	$\rightarrow H_2O^+ + CO$			$1.07 \times 10^{-8}\,(T_i)^{-0.5}$		UMIST
192b		$\rightarrow HCO_2^+ + H$			$1.73 \times 10^{-8}\,(T_i)^{-0.5}$		UMIST
193	$HNO^+ + C$	$\rightarrow CH^+ + NO$			1.00×10^{-9}		UMIST
194	$HNO^+ + CO$	$\rightarrow HCO^+ + NO$			8.60×10^{-10}		F15
195	$HNO^+ + CO_2$	$\rightarrow HCO_2^+ + NO$			9.40×10^{-10}		Est.
196	$HNO^+ + e^-$	$\rightarrow NO + H$			$5.20 \times 10^{-6}\,(T_i)^{-0.5}$		UMIST

Continued on next page

	Reaction		BR	MS	Rate coefficient	F	Ref
197	$HNO^+ + H_2O$	$\rightarrow H_3O^+ + NO$			2.30×10^{-9}		A93
198	$HNO^+ + N_2$	$\rightarrow N_2H^+ + NO$			1.00×10^{-11}		UMIST
199	$HNO^+ + OH$	$\rightarrow H_2O^+ + NO$			$1.07 \times 10^{-8}\,(T_i)^{-0.5}$		UMIST
200	$HO_2^+ + C$	$\rightarrow CH^+ + O_2$			1.00×10^{-9}		UMIST
201	$HO_2^+ + CO$	$\rightarrow HCO^+ + O_2$			8.40×10^{-10}		UMIST
202	$HO_2^+ + CO_2$	$\rightarrow HCO_2^+ + O_2$			1.10×10^{-9}		A93
203	$HO_2^+ + e^-$	$\rightarrow O_2 + H$			$5.20 \times 10^{-6}\,(T_i)^{-0.5}$		UMIST
204	$HO_2^+ + H_2$	$\rightarrow H_3^+ + O_2$			3.30×10^{-10}		A93
205	$HO_2^+ + H_2O$	$\rightarrow H_3O^+ + O_2$			$1.42 \times 10^{-8}\,(T_i)^{-0.5}$		UMIST
206	$HO_2^+ + N_2$	$\rightarrow N_2H^+ + O_2$			8.00×10^{-10}		A93
207	$HO_2^+ + NO$	$\rightarrow HNO^+ + O_2$			7.70×10^{-10}		UMIST
208	$HO_2^+ + O$	$\rightarrow OH^+ + O_2$			6.20×10^{-10}		UMIST
209	$HO_2^+ + OH$	$\rightarrow H_2O^+ + O_2$			$1.06 \times 10^{-8}\,(T_i)^{-0.5}$		UMIST
210	$HOC^+ + CO$	$\rightarrow HCO^+ + CO$			6.00×10^{-10}		A93
211	$HOC^+ + CO_2$	$\rightarrow HCO_2^+ + CO$			9.45×10^{-10}		A93
212a	$HOC^+ + e^-$	$\rightarrow CO + H$			$3.30 \times 10^{-5}\,(T_i)^{-1.0}$		UMIST
212b		$\rightarrow OH + C$			$1.19 \times 10^{-8}\,(T_i)^{1.2}$		Est. (HCO^+)
213a	$HOC^+ + H_2$	$\rightarrow H_3^+ + CO$			2.68×10^{-10}		A93
213b		$\rightarrow HCO^+ + H_2$			3.80×10^{-10}		Sm02
214	$HOC^+ + N_2$	$\rightarrow N_2H^+ + CO$			6.70×10^{-10}		A93
215	$HOC^+ + NO$	$\rightarrow HNO^+ + CO$			7.10×10^{-10}		A93
216	$HOC^+ + O_2$	$\rightarrow HO_2^+ + CO$			1.90×10^{-10}		A93
217	$H^+ + CO_2$	$\rightarrow HCO^+ + O$			3.80×10^{-9}		A93
218	$H^+ + e^-$	$\rightarrow H$			$6.46 \times 10^{-14}\,(T_i)^{0.7}$		KIDA
219a	$H^+ + H$	$\rightarrow H + H^+$			$6.50 \times 10^{-11}\,(T_i)^{0.5}$		Y89
219b		$\rightarrow H_2^+$			$2.34 \times 10^{-22}\,(T_i)^{1.49}\,e^{-228/T_i}$		UMIST
220	$H^+ + H_2O$	$\rightarrow H_2O^+ + H$			8.20×10^{-9}		A93

Continued on next page

	Reaction		BR	MS	Rate coefficient	F	Ref
221a	$H^+ + HCO$	$\rightarrow CO^+ + H_2$			$1.63 \times 10^{-8}\,(T_i)^{-0.5}$		UMIST
221b		$\rightarrow H_2^+ + CO$			$1.63 \times 10^{-8}\,(T_i)^{-0.5}$		UMIST
221c		$\rightarrow HCO^+ + H$			$1.63 \times 10^{-8}\,(T_i)^{-0.5}$		UMIST
222	$H^+ + NO$	$\rightarrow NO^+ + H$			1.90×10^{-9}		A93
223	$H^+ + O$	$\rightarrow O^+ + H$			3.75×10^{-10}		A93
224	$H^+ + O_2$	$\rightarrow O_2^+ + H$			1.17×10^{-9}		A93
225	$H^+ + OH$	$\rightarrow OH^+ + H$			$3.64 \times 10^{-8}\,(T_i)^{-0.5}$		UMIST
226	$N_2H^+ + C$	$\rightarrow CH^+ + N_2$			1.10×10^{-9}		UMIST
227	$N_2H^+ + CO$	$\rightarrow HCO^+ + N_2$			8.80×10^{-10}		A93
228	$N_2H^+ + CO_2$	$\rightarrow HCO_2^+ + N_2$			1.07×10^{-9}		A93
229	$N_2H^+ + e^-$	$\rightarrow N_2 + H$	0.93		$3.01 \times 10^{-5}\,(T_i)^{-0.84}$		F15
230	$N_2H^+ + H_2$	$\rightarrow H_3^+ + N_2$			5.10×10^{-18}		A93
231	$N_2H^+ + H_2O$	$\rightarrow H_3O^+ + N_2$			2.60×10^{-9}		A93
232	$N_2H^+ + NO$	$\rightarrow HNO^+ + N_2$			3.40×10^{-10}		A93
233	$N_2H^+ + O$	$\rightarrow OH^+ + N_2$			1.40×10^{-10}		A93
234	$N_2H^+ + OH$	$\rightarrow H_2O^+ + N_2$			$1.07 \times 10^{-8}\,(T_i)^{-0.5}$		UMIST
235	$N_2^+ + Ar$	$\rightarrow Ar^+ + N_2$			2.00×10^{-13}		A93
236	$N_2^+ + C$	$\rightarrow C^+ + N_2$			1.10×10^{-10}		UMIST
237	$N_2^+ + CO$	$\rightarrow CO^+ + N_2$			7.30×10^{-11}		A93
238	$N_2^+ + CO_2$	$\rightarrow CO_2^+ + N_2$			8.00×10^{-10}		SN09
239a	$N_2^+ + e^-$	$\rightarrow N + N$			$5.09 \times 10^{-7}\,(T_i)^{-0.39}$		Du13
239b		$\rightarrow N(^2D) + N(^2D)$			$1.42 \times 10^{-6}\,(T_i)^{-0.39}$		Du13
240	$N_2^+ + H_2$	$\rightarrow N_2H^+ + H$			$1.87 \times 10^{-9} e^{-54.7/T_i}$		Du13
241a	$N_2^+ + H_2O$	$\rightarrow H_2O^+ + N_2$			1.90×10^{-9}		A93
241b		$\rightarrow N_2H^+ + OH$			5.04×10^{-10}		A93
242a	$N_2^+ + HCO$	$\rightarrow HCO^+ + N_2$			$6.41 \times 10^{-9}\,(T_i)^{-0.5}$		UMIST
242b		$\rightarrow N_2H^+ + CO$			$6.41 \times 10^{-9}\,(T_i)^{-0.5}$		UMIST
243	$N_2^+ + N$	$\rightarrow N^+ + N_2$			1.40×10^{-11}		Sc98

Continued on next page

	Reaction		BR	MS	Rate coefficient	F	Ref
244	$N_2^+ + NO$	$\rightarrow NO^+ + N_2$			4.40×10^{-10}		UMIST
245a	$N_2^+ + O$	$\rightarrow NO^+ + N$			$1.72 \times 10^{-9}\,(T_i)^{-0.44}$		F93
245b		$\rightarrow O^+ + N_2$			9.80×10^{-12}		SN09
246	$N_2^+ + O_2$	$\rightarrow O_2^+ + N_2$			5.00×10^{-11}		A93
247	$N_2^+ + OH$	$\rightarrow OH^+ + N_2$			$1.09 \times 10^{-8}\,(T_i)^{-0.5}$		UMIST
248	$NH^+ + C$	$\rightarrow CH^+ + N$			1.60×10^{-9}		UMIST
249	$NH^+ + CO$	$\rightarrow HCO^+ + N$			4.41×10^{-10}		A93
250a	$NH^+ + CO_2$	$\rightarrow HCO_2^+ + N$			3.85×10^{-10}		A93
250b		$\rightarrow HNO^+ + CO$			3.85×10^{-10}		A93
250c		$\rightarrow NO^+ + HCO$			3.30×10^{-10}		A93
251	$NH^+ + e^-$	$\rightarrow N + H$			$7.45 \times 10^{-7}\,(T_i)^{-0.5}$		Mi90
252	$NH^+ + H_2$	$\rightarrow H_3^+ + N$			1.85×10^{-10}		A93
253a	$NH^+ + H_2O$	$\rightarrow H_3O^+ + N$			1.05×10^{-9}		A93
253b		$\rightarrow HNO^+ + H_2$			3.50×10^{-10}		A93
254	$NH^+ + N$	$\rightarrow N_2^+ + H$			1.30×10^{-9}		UMIST
255	$NH^+ + N_2$	$\rightarrow N_2H^+ + N$			6.50×10^{-10}		A93
256	$NH^+ + NO$	$\rightarrow N_2H^+ + O$			1.78×10^{-10}		A93
257	$NH^+ + O$	$\rightarrow OH^+ + N$			1.00×10^{-9}		UMIST
258a	$NH^+ + O_2$	$\rightarrow HO_2^+ + N$			1.64×10^{-10}		A93
258b		$\rightarrow NO^+ + OH$			2.05×10^{-10}		A93
259	$NH^+ + OH$	$\rightarrow H_2O^+ + N$			$1.73 \times 10^{-8}\,(T_i)^{-0.5}$		UMIST
260a	$NO^+ + e^-$	$\rightarrow O + N$	0.05		$6.93 \times 10^{-6}\,(T_i)^{-0.5}$		F15
260b		$\rightarrow O + N(^2D)$	0.95		$6.93 \times 10^{-6}\,(T_i)^{-0.5}$		F15
261a	$N^+ + CO$	$\rightarrow CO^+ + N$			4.93×10^{-10}		A93
261b		$\rightarrow C^+ + NO$			5.60×10^{-12}		A93
261c		$\rightarrow NO^+ + C$			6.16×10^{-11}		A93
262a	$N^+ + CO_2$	$\rightarrow CO_2^+ + N$			9.18×10^{-10}		A93
262b		$\rightarrow CO^+ + NO$			2.02×10^{-10}		A93

Continued on next page

	Reaction		BR	MS	Rate coefficient	F	Ref
263	$N^+ + e^-$	$\rightarrow N$			$1.90 \times 10^{-10}\,(T_i)^{-0.7}$		Du13
264	$N^+ + H_2$	$\rightarrow NH^+ + H$			$5.00 \times 10^{-10} e^{-85/T_i}$		A93
265	$N^+ + H_2O$	$\rightarrow H_2O^+ + N$			2.70×10^{-9}		A93
266a	$N^+ + HCO$	$\rightarrow HCO^+ + N$			$7.79 \times 10^{-9}\,(T_i)^{-0.5}$		UMIST
266b		$\rightarrow NH^+ + CO$			$7.79 \times 10^{-9}\,(T_i)^{-0.5}$		UMIST
267	$N^+ + N$	$\rightarrow N_2^+$			$9.44 \times 10^{-19}\,(T_i)^{0.24}\,e^{-26.1/T_i}$		UMIST
268a	$N^+ + NO$	$\rightarrow N_2^+ + O$			8.33×10^{-11}		A93
268b		$\rightarrow NO^+ + N$			4.72×10^{-10}		A93
269a	$N^+ + O_2$	$\rightarrow NO^+ + O$			2.32×10^{-10}		A93
269b		$\rightarrow O_2^+ + N$			3.07×10^{-10}		A93
269c		$\rightarrow O^+ + NO$			4.64×10^{-11}		A93
270	$N^+ + OH$	$\rightarrow OH^+ + N$			$6.41 \times 10^{-9}\,(T_i)^{-0.5}$		UMIST
271a	$O_2^+ + C$	$\rightarrow CO^+ + O$			5.20×10^{-11}		UMIST
271b		$\rightarrow C^+ + O_2$			5.20×10^{-11}		UMIST
272	$O_2^+ + e^-$	$\rightarrow O + O$			$8.15 \times 10^{-6}\,(T_i)^{-0.65}$		Sp93
273a	$O_2^+ + HCO$	$\rightarrow HCO^+ + O_2$			$6.24 \times 10^{-9}\,(T_i)^{-0.5}$		UMIST
273b		$\rightarrow HO_2^+ + CO$			$6.24 \times 10^{-9}\,(T_i)^{-0.5}$		UMIST
274	$O_2^+ + N$	$\rightarrow NO^+ + O$			1.00×10^{-10}		Sc98
275	$O_2^+ + NO$	$\rightarrow NO^+ + O_2$			4.60×10^{-10}		A93
276	$OH^+ + C$	$\rightarrow CH^+ + O$			1.20×10^{-9}		UMIST
277	$OH^+ + CO$	$\rightarrow HCO^+ + O$			8.40×10^{-10}		A93
278	$OH^+ + CO_2$	$\rightarrow HCO_2^+ + O$			1.35×10^{-9}		A93
279	$OH^+ + e^-$	$\rightarrow O + H$			$6.50 \times 10^{-7}\,(T_i)^{-0.5}$		Mi90
280	$OH^+ + H_2$	$\rightarrow H_2O^+ + H$			9.70×10^{-10}		A93
281a	$OH^+ + H_2O$	$\rightarrow H_2O^+ + OH$			1.59×10^{-9}		A93
281b		$\rightarrow H_3O^+ + O$			1.30×10^{-9}		A93
282a	$OH^+ + HCO$	$\rightarrow H_2O^+ + CO$			$4.85 \times 10^{-9}\,(T_i)^{-0.5}$		UMIST
282b		$\rightarrow HCO^+ + OH$			$4.85 \times 10^{-9}\,(T_i)^{-0.5}$		UMIST

Continued on next page

	Reaction		BR	MS	Rate coefficient	F	Ref
283	$OH^+ + N$	$\rightarrow NO^+ + H$			8.90×10^{-10}		UMIST
284	$OH^+ + N_2$	$\rightarrow N_2H^+ + O$			2.40×10^{-10}		A93
285a	$OH^+ + NO$	$\rightarrow HNO^+ + O$			6.11×10^{-10}		UMIST
285b		$\rightarrow NO^+ + OH$			8.15×10^{-10}		A93
286	$OH^+ + O$	$\rightarrow O_2^+ + H$			7.10×10^{-10}		UMIST
287	$OH^+ + O_2$	$\rightarrow O_2^+ + OH$			3.80×10^{-10}		A93
288	$OH^+ + OH$	$\rightarrow H_2O^+ + O$			$1.21 \times 10^{-8}\,(T_i)^{-0.5}$		UMIST
289	$O^+ + CO_2$	$\rightarrow O_2^+ + CO$			1.10×10^{-9}		A93
290	$O^+ + e^-$	$\rightarrow O$			$1.40 \times 10^{-10}\,(T_i)^{-0.66}$		UMIST
291	$O^+ + H$	$\rightarrow H^+ + O$			6.40×10^{-10}		A93
292	$O^+ + H_2$	$\rightarrow OH^+ + H$			1.62×10^{-9}		A93
293	$O^+ + H_2O$	$\rightarrow H_2O^+ + O$			2.60×10^{-9}		A93
294a	$O^+ + HCO$	$\rightarrow HCO^+ + O$			$7.45 \times 10^{-9}\,(T_i)^{-0.5}$		UMIST
294b		$\rightarrow OH^+ + CO$			$7.45 \times 10^{-9}\,(T_i)^{-0.5}$		UMIST
295	$O^+ + N_2$	$\rightarrow NO^+ + N$			$4.58 \times 10^{-9}\,(T_i)^{-1.37}\,e^{-28.592/T_i}$		L03
296	$O^+ + NO$	$\rightarrow NO^+ + O$			8.00×10^{-13}		A93
297	$O^+ + O_2$	$\rightarrow O_2^+ + O$			2.10×10^{-11}		A93
298a	$O^+ + OH$	$\rightarrow O_2^+ + H$			$6.24 \times 10^{-9}\,(T_i)^{-0.5}$		UMIST
298b		$\rightarrow OH^+ + O$			$6.24 \times 10^{-9}\,(T_i)^{-0.5}$		UMIST

Table B.3: Reference keys for Table B.2.

Short code	Reference
A03	Anicich (2003)
A93	Anicich (1993)
At89	Atkinson et al. (1989)
B05	Baulch et al. (2005)
B05	Baulch et al. (2005)

Continued on next page

Short code	Reference
B92	Baulch et al. (1992)
Bo09	Borodi et al. (2009)
B15	J. B. Burkholder et al. (2015)
Bu19	J. Burkholder et al. (2019)
Br83	Brune et al. (1983)
Cam73	Campbell et al. (1973)
C10	Cazaux et al. (2010)
Ch17	Chaffin et al. (2017)
D12	Deighan (2012)
Da78	Davidson et al. (1978)
Do92	Doroshenko et al. (1992)
Du13	Dutuit et al. (2013)
Feh70	Fehsenfeld et al. (1970)
Fl76	Fletcher et al. (1976)
F93	Fox (1993)
F15	Fox (2015)
G04	Geppert et al. (2004)
G05	Geppert et al. (2005)
G00	Geppert et al. (2000)
Gu15	Gustafsson et al. (2015)
He90	Herd et al. (1990)
Her99	Herron (1999)
Hi97	Hierl et al. (1997)
J00	Jensen et al. (2000)
KIDA	Wakelam et al. (2019)
K09	Korolov et al. (2009)
Kl10	Klippenstein et al. (2010)
L03	Le Garrec et al. (2003)

Continued on next page

Short code	Reference
M00	Milligan et al. (2000)
Mi05	Mitchell et al. (2005)
Mi90	Brian et al. (1990)
N97	Nahar et al. (1997)
NIST	Manion et al. (2015)
O78	Okabe (1978)
Pr94	Praxmarer et al. (1994)
R98	Rosén et al. (1998)
R00	Rosén et al. (2000)
S11	Sander et al. (2011)
Sc97	G. B. Scott et al. (1997)
Sc98	G. B. I. Scott et al. (1998)
SN09	Schunk et al. (2009)
Sm02	M. A. Smith et al. (2002)
Sp93	Španěl et al. (1993)
SwRI	Huebner et al. (2015)
Tu75	Tully (1975)
Ts86	Tsang et al. (1986)
Ts91	Tsang et al. (1991)
UMIST	D. McElroy et al. (2013)
V80	Viggiano et al. (1980)
V05	Viggiano et al. (2005)
V19	Vuitton et al. (2019)
Y88	Yung et al. (1988)
Y89	Yung et al. (1989)
Yu05	Yu et al. (2005)
Z09	Zanchet et al. (2009)
Est.	Estimated.

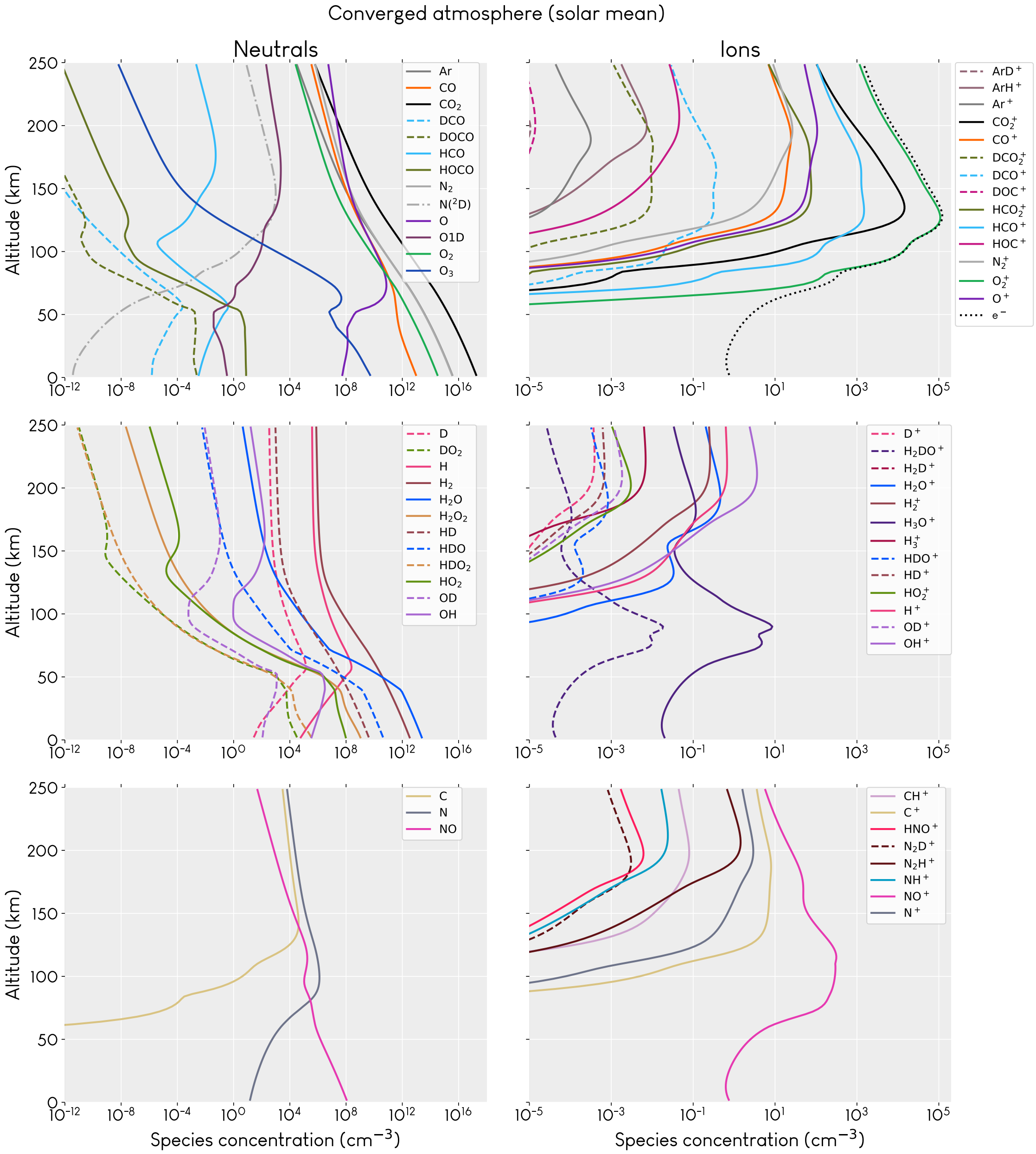

Figure B.1: The complete atmosphere, with all species, at the end of the solar mean simulation.

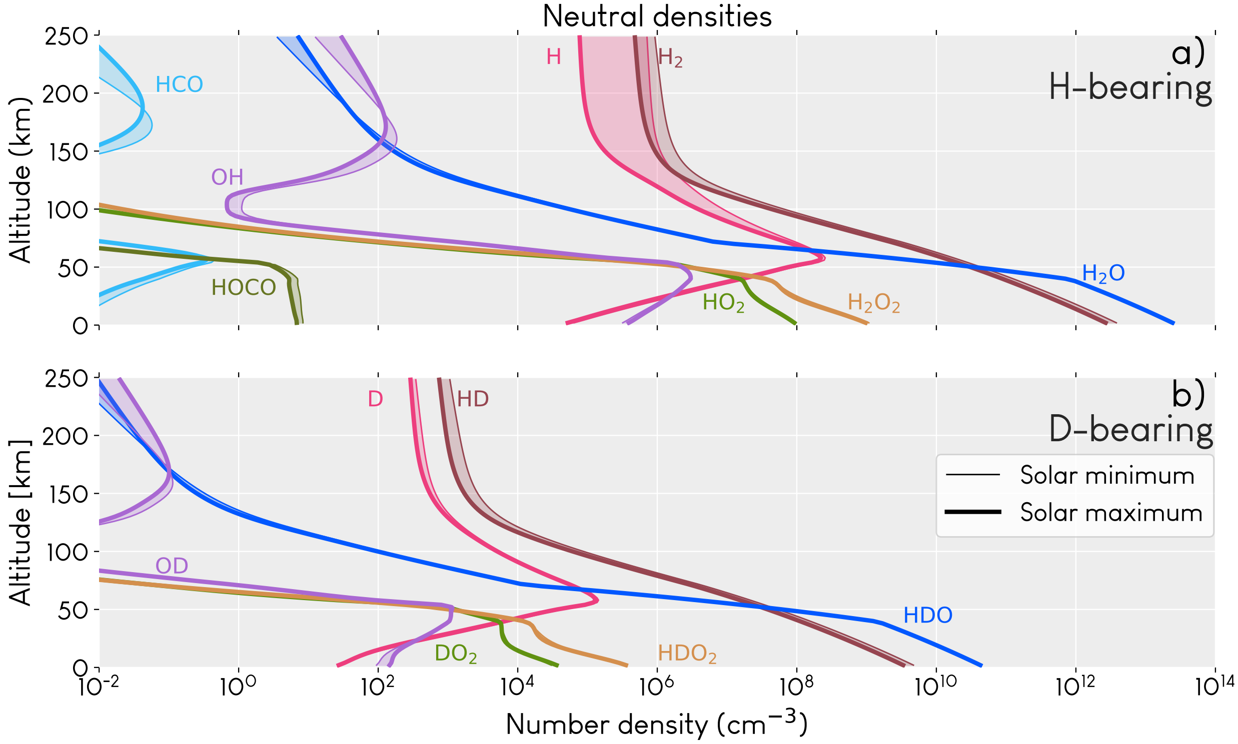

Figure B.2: Densities of neutral deuterated species and their H-bearing analogues. Some minor species are not plotted in order to maintain legibility of the more abundant species.

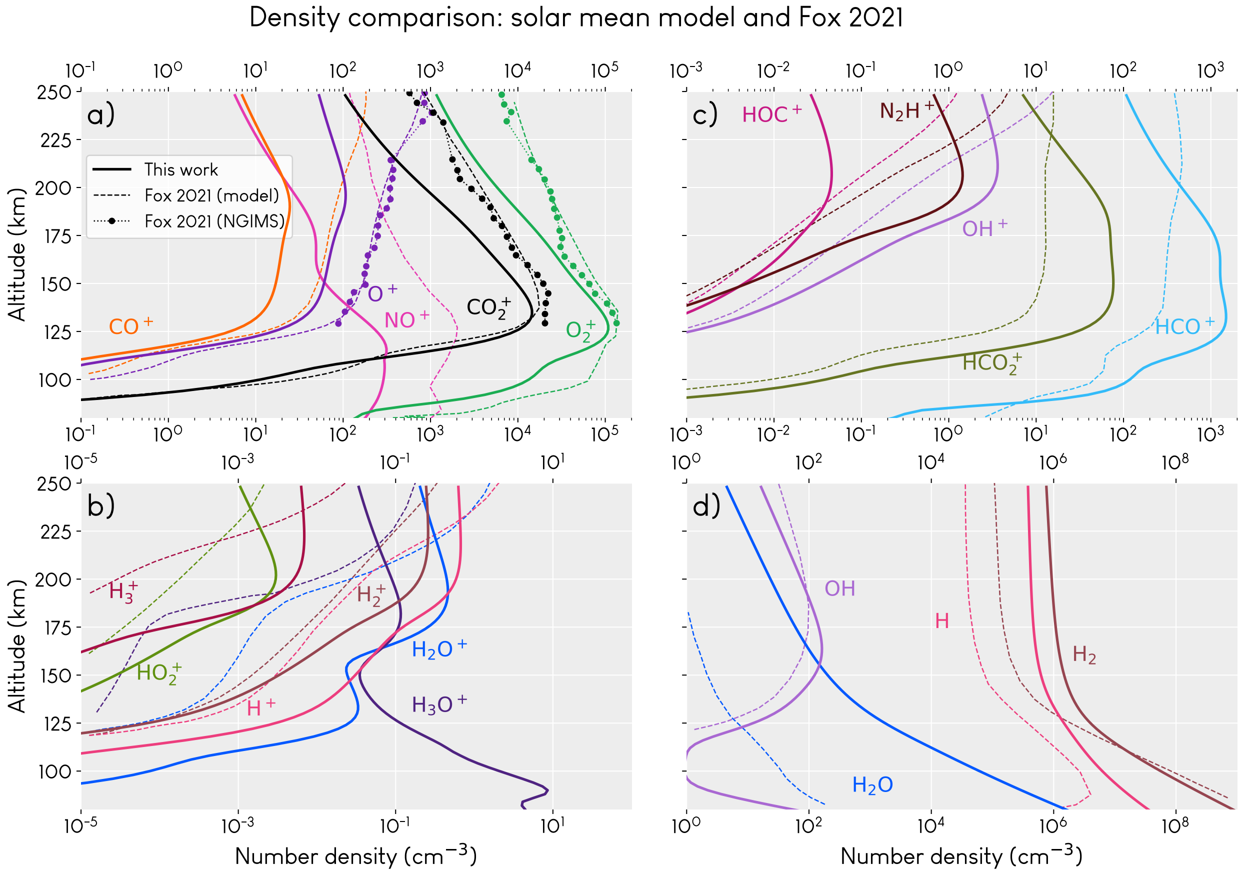

Figure B.3: Comparison of model output with Fox et al. (2021), their model output and NGIMS densities for three principal ions.

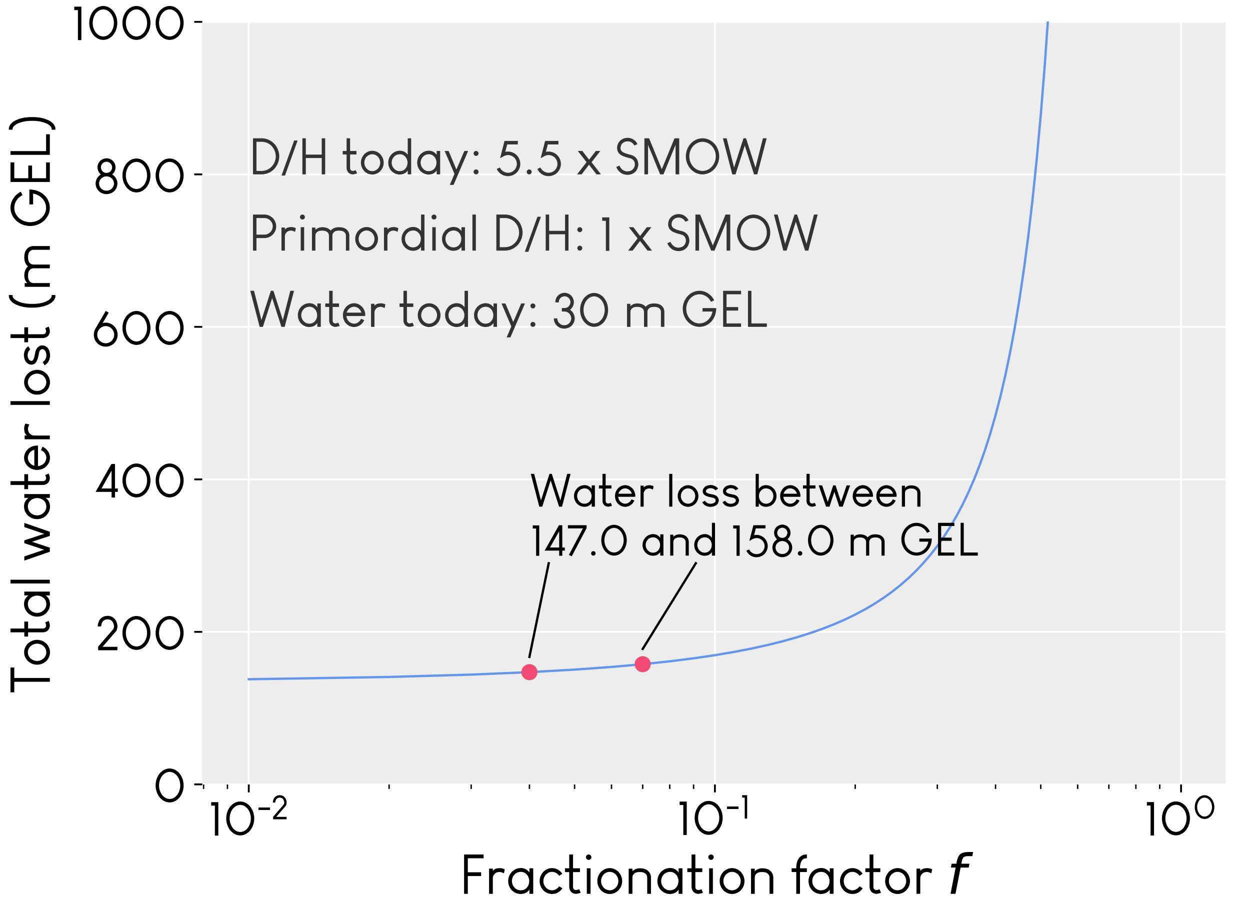

Figure B.4: Water loss as a function of fractionation factor for D/H = 5.5× SMOW, primordial D/H = 1 × SMOW., and 30 m GEL present-day water inventory.

Appendix C

Supporting Information for Chapter 4

This text will be originally published as the Supporting Information companion document to Chapter 4.

Supporting Tables

Table C.1: Model parameters.

Supporting Figures

- Figure C.1 Timesteps

Insolation figures

- Figure C.2: The effect of insolation on the atomic D/H ratio

Supplemental exobase temperature variation figures

- Figure C.3: The effect of thermospheric temperature on the D/H ratios of 6 isotopologue pairs
- Figure C.4: The same as Figure 4.2, but with HDO cross sections equal to the H_2O cross sections
- Figure C.5: The same as Figure 4.3, but also showing the percent of the total H and D column which escape.

- Figure C.6: The same as Figure 4.1 but with more detail, using the temperatures and escape rates calculated in this work.

Supplemental mesospheric water vapor variation figures

- Figure C.7: The effect of low altitude water on the atomic D/H ratio
- Figure C.8: The effect of mesospheric water on the D/H ratios of 6 isotopologue pairs
- Figure C.9: The effect of mesospheric water on the D/H fractionation factor
- Figure C.10: The same as Figure 4.4, but with HDO cross sections equal to the H_2O cross sections
- Figure C.11: The same as Figure 4.5, but also showing the percent of the total H and D column which escape.

Included neutrals (28)	Ar, C, CO, CO_2, D, DCO, DO_2, DOCO, H, H_2, H_2O, H_2O_2, HCO, HD, HDO, HDO_2, HO_2, HOCO, N, N_2, NO, $N(^2D)$, O, $O(^1D)$, O_2, O_3, OD, OH
Included ions (35)	ArD^+, ArH^+, Ar^+, CH^+, CO_2^+, CO^+, C^+, DCO_2^+, DCO^+, DOC^+, D^+, H_2DO^+, H_2D^+, H_2O^+, H_2^+, H_3O^+, H_3^+, HCO_2^+, HCO^+, HDO^+, HD^+, HNO^+, HO_2^+, HOC^+, H^+, N_2D^+, N_2H^+, N_2^+, NH^+, NO^+, N^+, O_2^+, OD^+, OH^+, O^+
Basic output format	Number density at each altitude
Vertical extent	0-250 km; spacing 2 km
SZA	60° (dayside mean)
Chemistry	∼600 reactions including photodissociation, photoionization, bimolecular and termolecular reactions, dissociative recombination
Electron density treatment	Sum of the local ion density (Quasineutral)
Photochemical equilibrium	Not assumed
Background atmosphere	Argon at all altitudes; water below 72 km
Escape types	Thermal and non-thermal (due to ion-neutral reations)
Escaping species	H, D, H_2, HD
Boundary conditions	Surface density: CO_2, N_2
	Exobase flux: O (fixed at 1.2×10^8), H, D, H_2, HD (all non-thermal, function of atmospheric state)
	Exobase velocity: H, D, H_2, HD (thermal escape; effusion velocity)

Table C.1: High-level summary of model characteristics

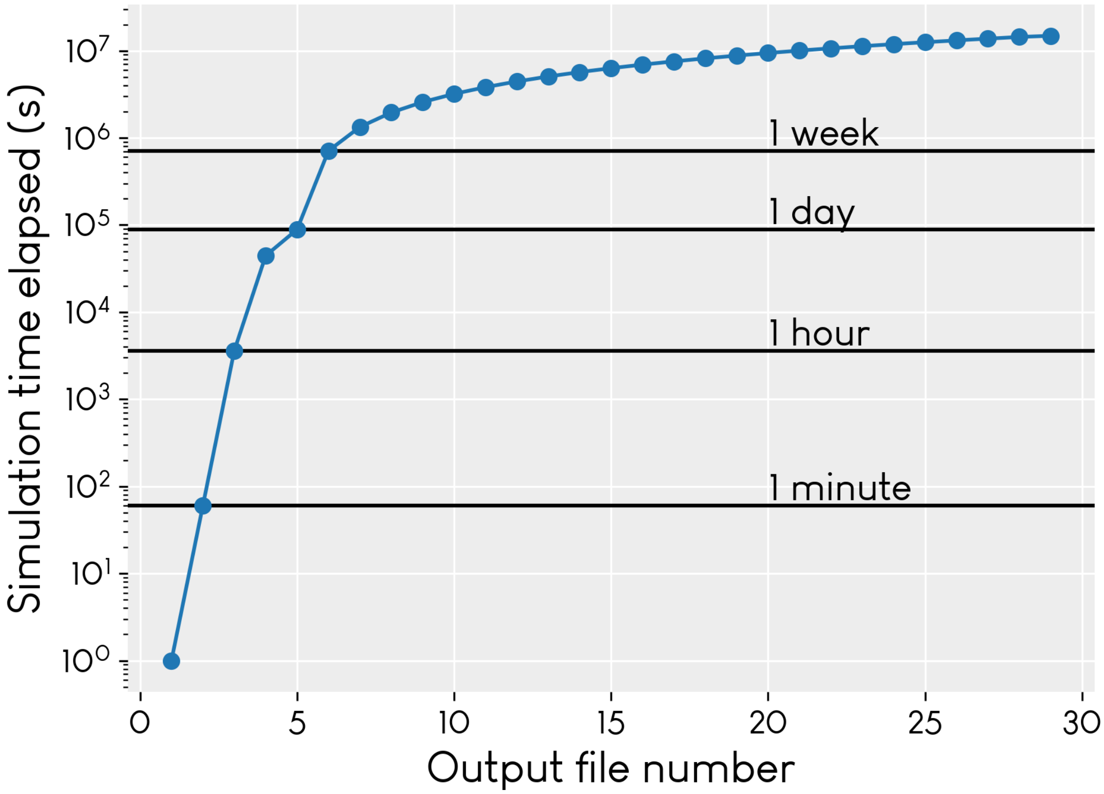

Figure C.1: Times at which we save the model state for the seasonal cycle simulations. Note the small non-linearity caused by changing from logarithmically spaced steps between 1s-1 day to linearly spaced steps (every week). This appears as an artifact in Figure 4.3.

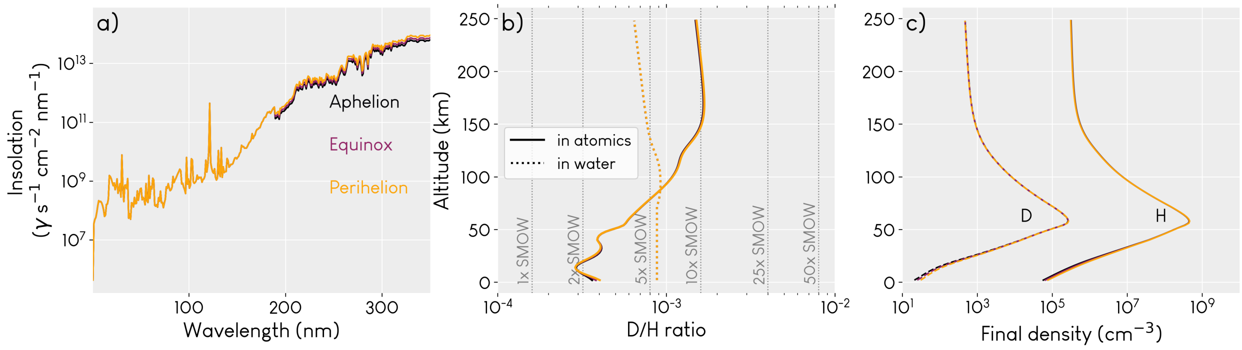

Figure C.2: a) Three different possible insolation profiles adopted for three different model runs. The profiles extend out to 2000 nm, but here we only show out to 350 nm for legibility. b) Resulting D/H profiles in atomic hydrogen and water. Insolation has very little effect. c) The associated density profiles for D and H, demonstrating very little variation.

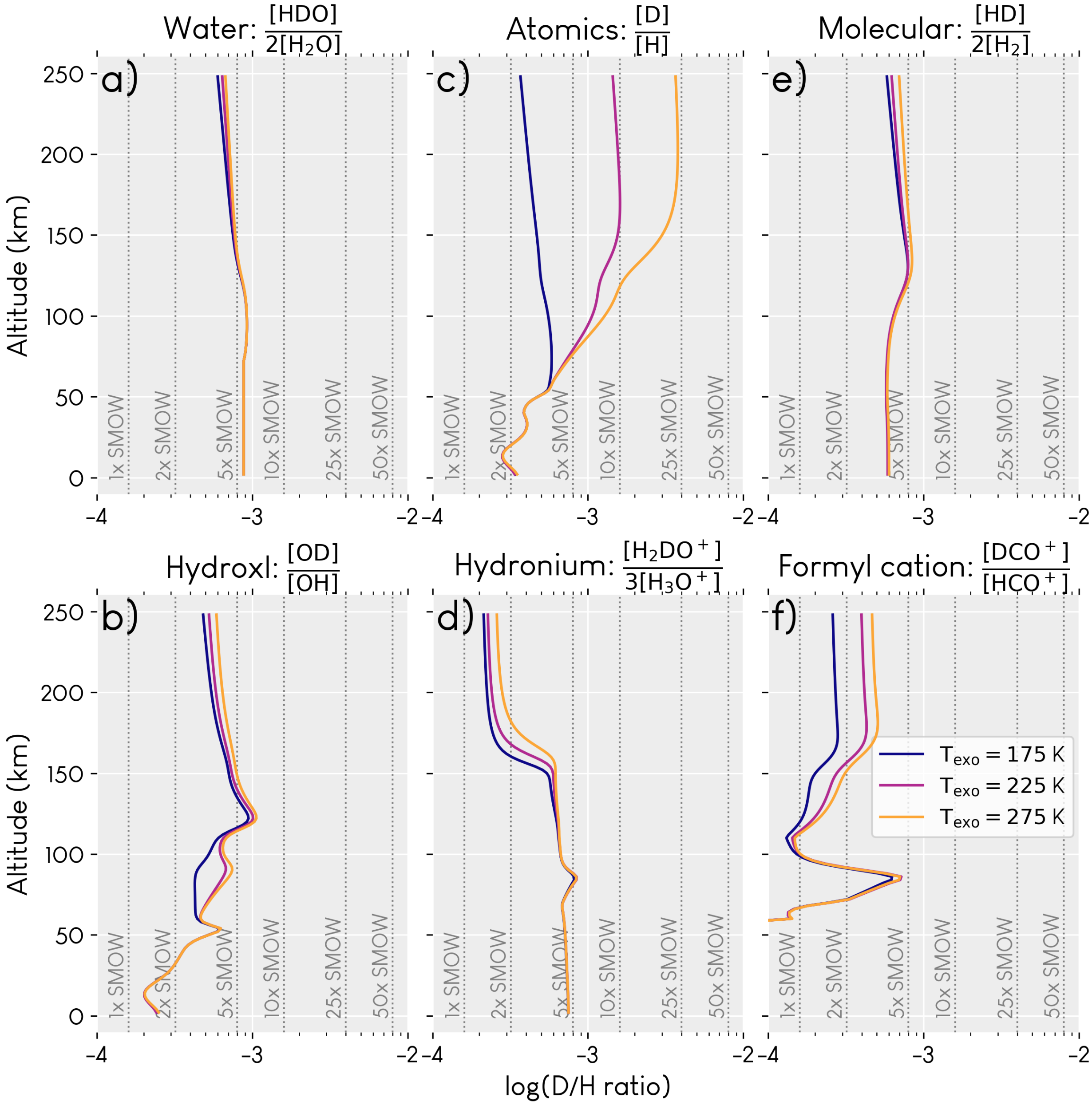

Figure C.3: The D/H ratio in several different H- and D-bearing species, with thermospheric temperature as the variable. No species shows as much variation in the D/H ratio as the atomics. Hydronium and the formyl cation show moderate variation, likely because these are terminal ions: the base species (CO and H_2O) have the highest proton affinities in the atmosphere (Fox 2015).

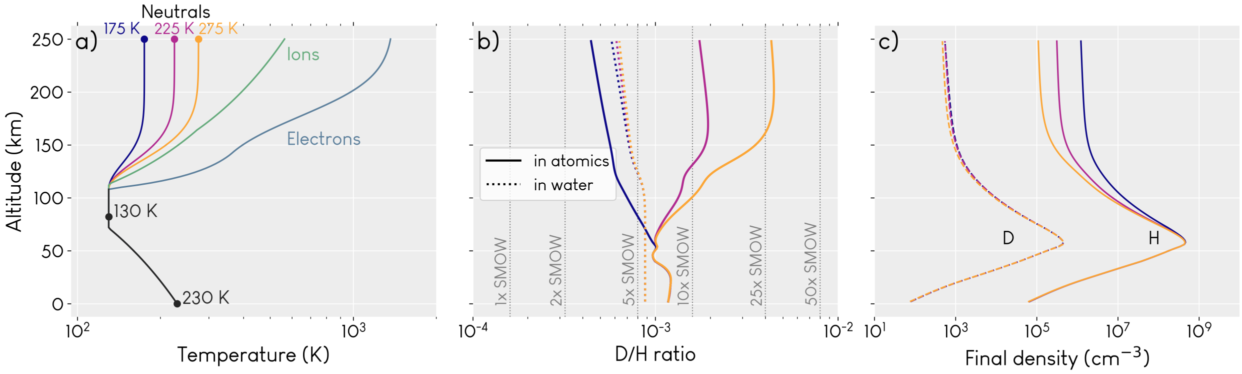

Figure C.4: The same as Figure 4.2, but with both HDO and H_2O set to use the H_2O photochemical cross sections. Inaccurately assuming the same cross sections for HDO and H_2O can artificially increase the calculated atomic D/H ratio by a factor of 2, even with a coarse wavelength resolution of 1 nm (the scale at which we bin our cross sections).

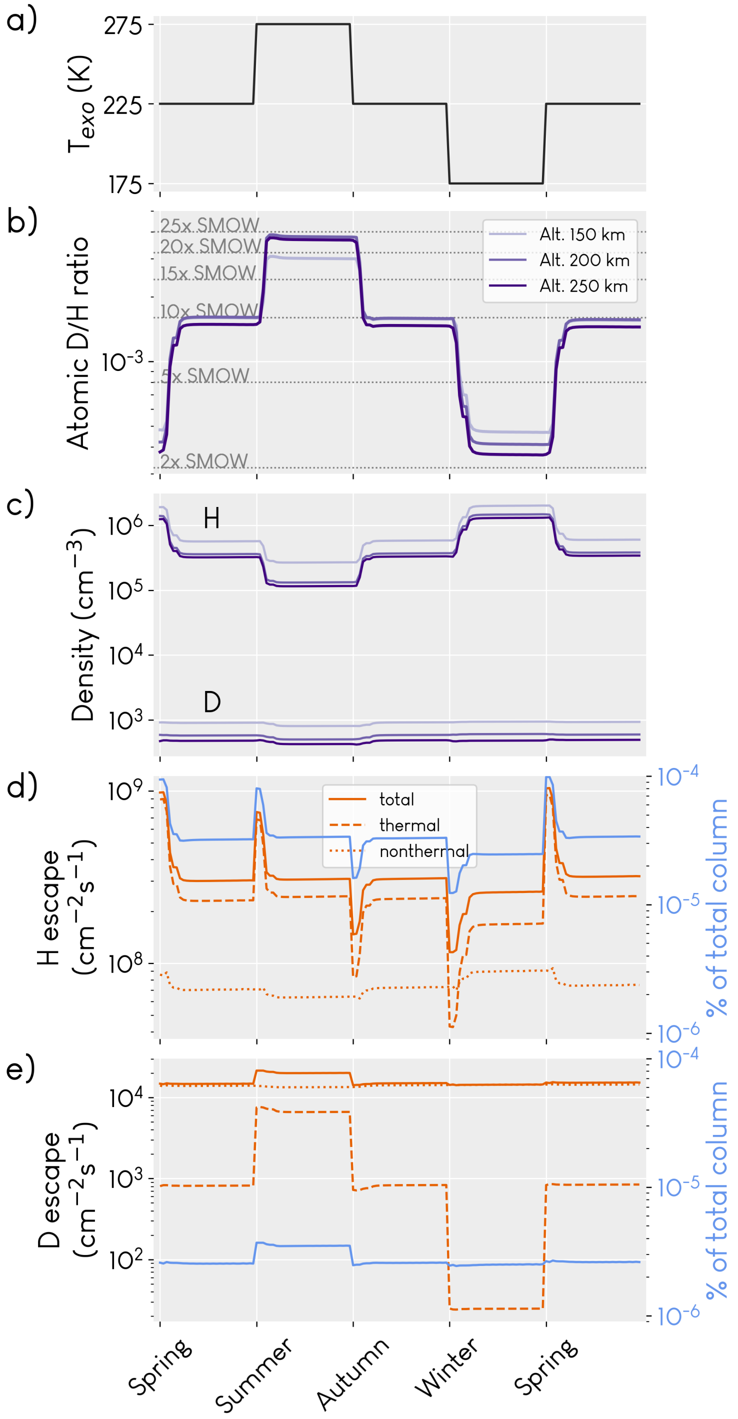

Figure C.5: The same as Figure 4.3, but also showing the percent of the total H and D column which escape.

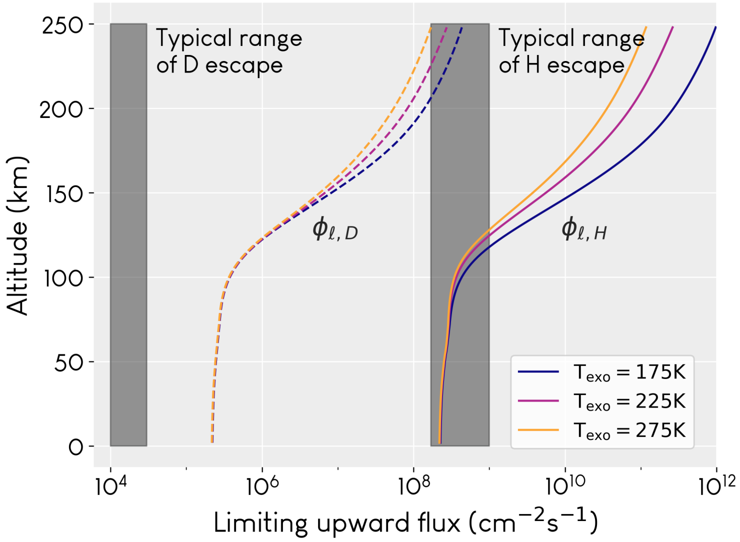

Figure C.6: The same as Figure 4.1, but with the three exobase temperatures adopted in this chapter and the range of escape calculated in this chapter.

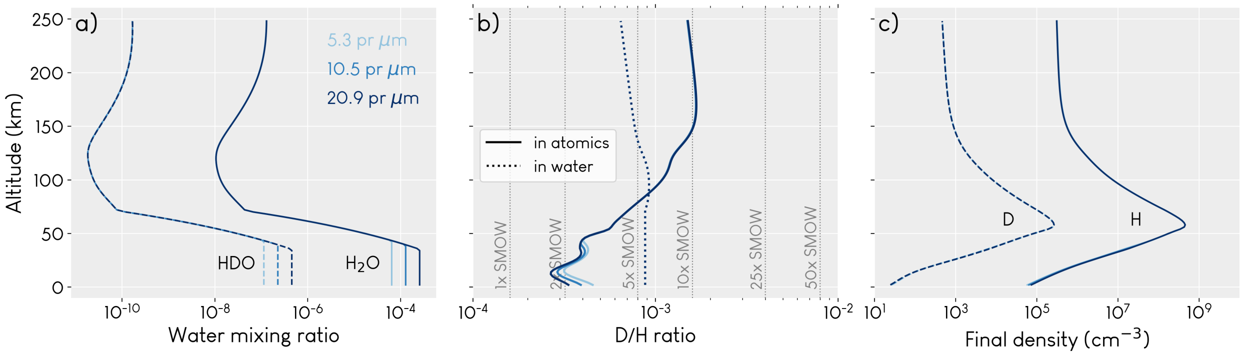

Figure C.7: The same as Figures 4.2 and 4.4, but here showing how variation of lower atmospheric water content has a negligible effect on atomic D/H.

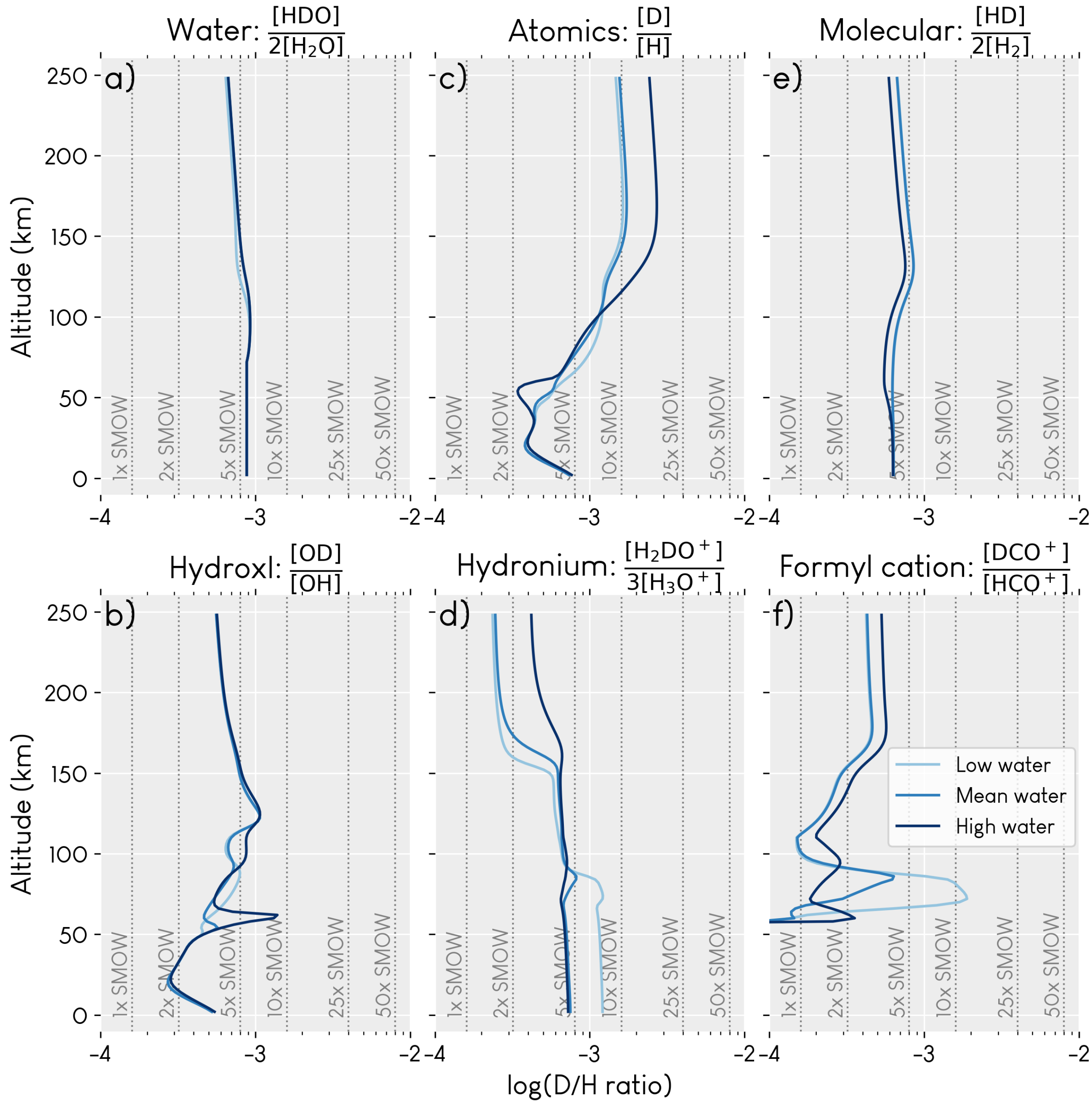

Figure C.8: The same as Figure C.3, but here showing how excess mesospheric water affects the D/H ratios in several isotopologue pairs.

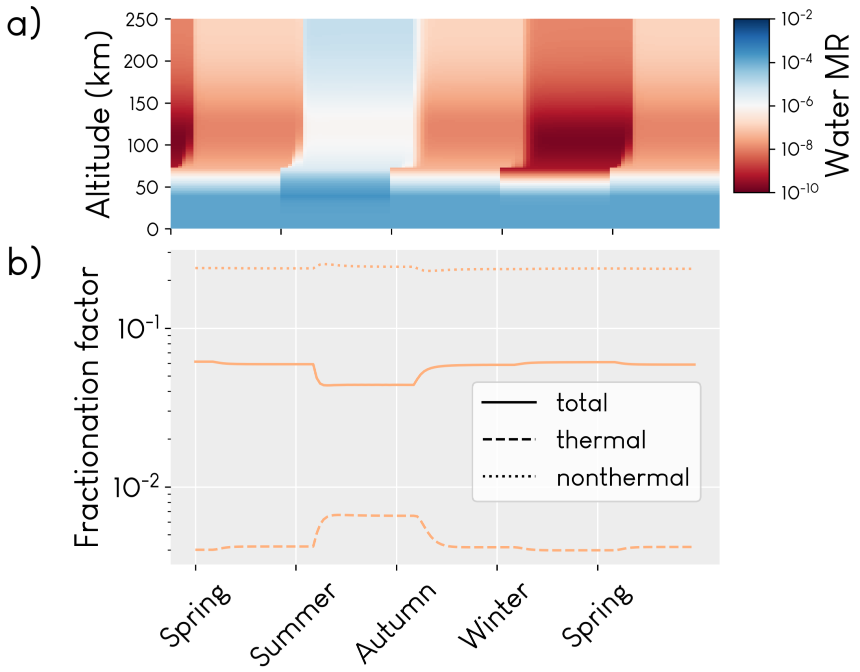

Figure C.9: The D/H fractionation factor as a function of the atmospheric water content over time. The smaller value during high water conditions ("summer") occurs because the extra water in the mesosphere overcomes the diffusion limit bottleneck, enabling much higher H escape, but with little effect to the D escape, which is energy-limited.

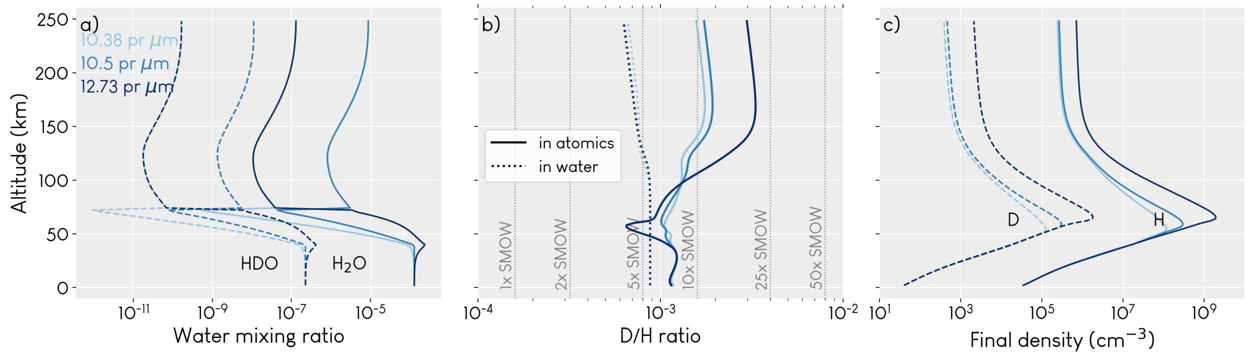

Figure C.10: The same as Figure 4.4, but with both HDO and H_2O set to use the H_2O photochemical cross sections. Here, inaccurately assuming the same cross sections for HDO and H_2O increases the calculated atomic D/H ratio by a factor of 2-10. A wetter atmosphere is much less sensitive to the water photodissociation cross sections (the D/H ratio changes very little by comparison).

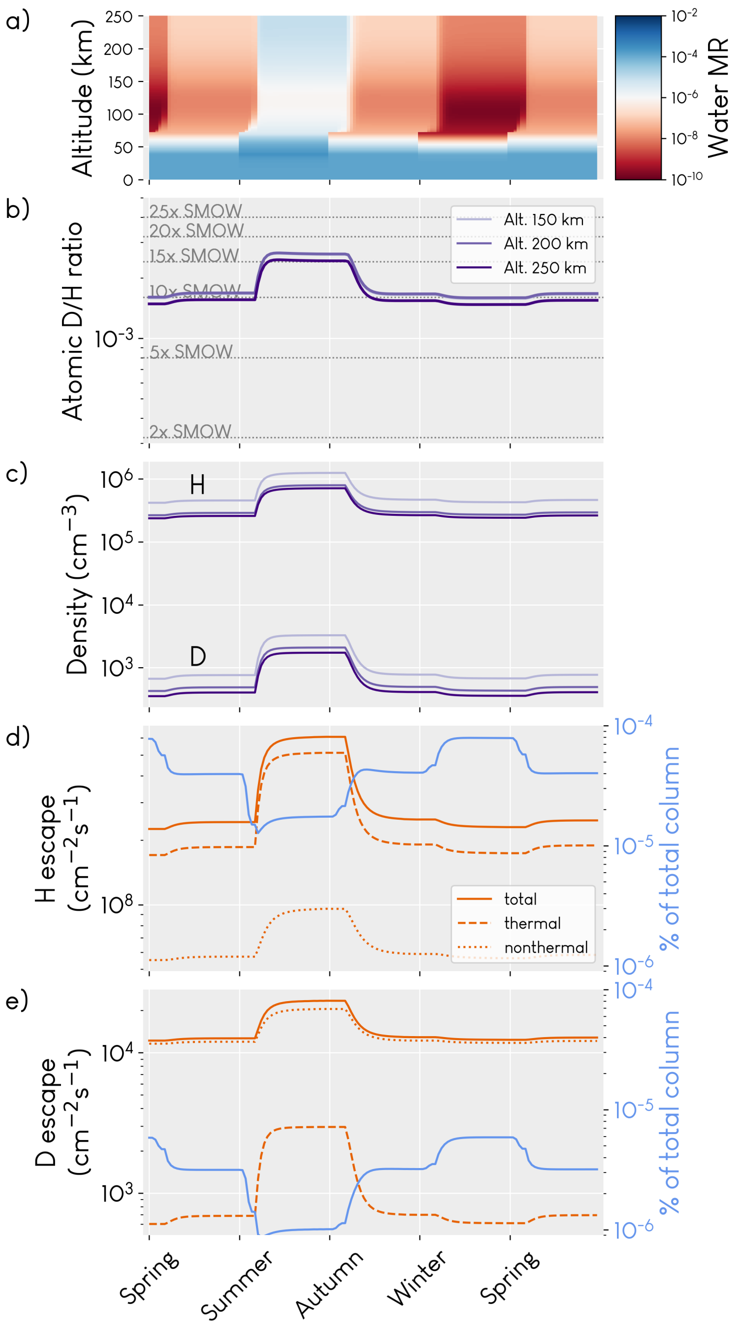

Figure C.11: The same as Figure 4.5, but also showing the percent of the total H and D column which escape.